ISBN 978-82-326-0936-9 (printed version)
ISBN 978-82-326-0937-6 (electronic version)
ISSN 1503-8181

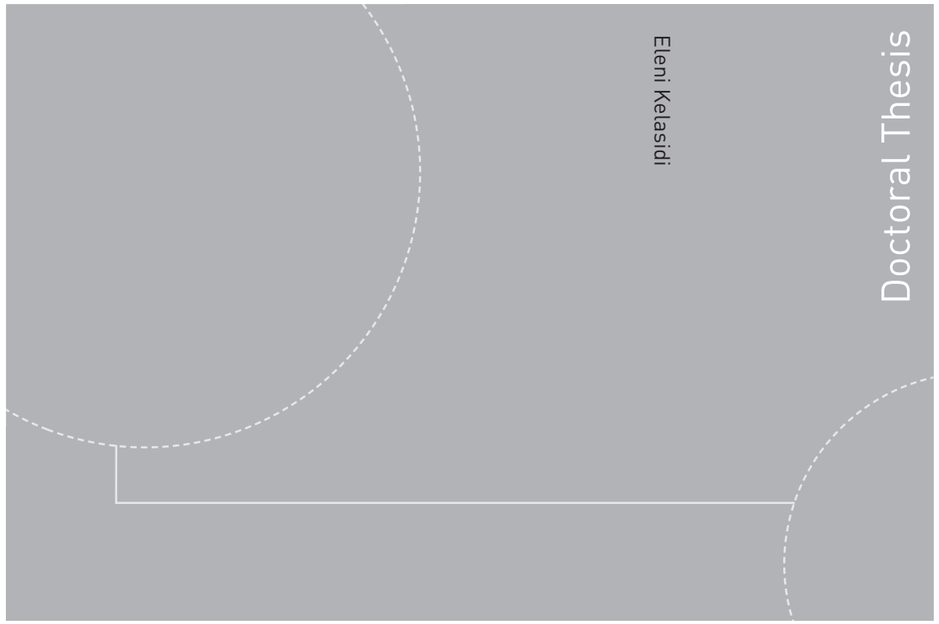

Doctoral theses at NTNU, 2015:140

Eleni Kelasidi

Modeling, Control and Energy Efficiency of Underwater Snake Robots

NTNU
Norwegian University of
Science and Technology

NTNU
Norwegian University of
Science and Technology
Faculty of Information Technology,
Mathematics and Electrical Engineering
Department of Engineering Cybernetics

NTNU
Norwegian University of
Science and Technology

Doctoral theses at NTNU, 2015:140

NTNU

Eleni Kelasidi

Modeling, Control and Energy Efficiency of Underwater Snake Robots

Thesis for the degree of Philosophiae Doctor

Trondheim, December 2015

Norwegian University of Science and Technology
Faculty of Information Technology,
Mathematics and Electrical Engineering
Department of Engineering Cybernetics

NTNU
Norwegian University of
Science and Technology

NTNU
Norwegian University of Science and Technology

Thesis for the degree of Philosophiae Doctor

Faculty of Information Technology,
Mathematics and Electrical Engineering
Department of Engineering Cybernetics

ISBN 978-82-326-0936-9 (printed version)
ISBN 978-82-326-0937-6 (electronic version)
ISSN 1503-8181

Doctoral theses at NTNU, 2015:140

Printed by Skipnes Kommunikasjon as

To my family and my friend Fani

Summary

This thesis is mainly motivated by the attribute of the snake robots that they are able to move over land as well as underwater while the physiology of the robot remains the same. This adaptability to different motion demands depending on the environment is one of the main characteristics of the snake robots. In particular, this thesis targets several interesting aspects regarding the modeling, control and energy efficiency of the underwater snake robots.

This thesis addresses the problem of modeling the hydrodynamic effects with an analytical perspective and a primary objective to conclude in a closed-form solution for the dynamic model of an underwater snake robot. Two mathematical models of the kinematics and dynamics of underwater snake robots swimming in virtual horizontal and vertical planes aimed at control design are presented. The presented models are derived in a closed-form and can be utilized in modern model-based control schemes. In addition, these proposed models comprise snake robots moving both on land and in water which makes the model applicable for unified control methods for amphibious snake robots moving both on land and in water. The third model presented in this thesis is based on simplifying assumptions in order to derive a control-oriented model of an underwater snake robot moving in a virtual horizontal plane that is well-suited for control design and stability analysis.

The models are analysed using several techniques. An extensive analysis of the model of a fully immersed underwater snake robot moving in a virtual horizontal plane is conducted. Based on this analysis, a set of essential properties that characterize the overall motion of underwater snake robots is derived. An averaging analysis reveals new fundamental properties of underwater snake robot locomotion that are useful from a motion planning perspective.

In this thesis, both the motion analysis and control strategies are conducted based on a general sinusoidal motion pattern which can be used for a broad class of motion patterns including lateral undulation and eel-like motion. This thesis proposes and experimentally validates solutions to the path following control problem for biologically inspired swimming snake robots. In particular, line-of-sight (LOS) and integral line-of-sight (I-LOS) guidance laws, which are combined with a sinusoidal gait pattern and a directional controller that steers the robot towards and along the desired path are proposed. An I-LOS path following controller for steering an underwater snake robot along a straight line path in the presence of ocean currents of unknown direction and magnitude is presented and by using a Poincaré map, it is shown that all state variables of an underwater snake robot, except for the position along the desired path, trace out an exponentially stable

periodic orbit. Moreover, this thesis presents the combined use of an artificial potential fields-based path planner with a new waypoint guidance strategy for steering an underwater snake robot along a path defined by waypoints interconnected by straight lines. The waypoints are derived by using a path planner based on the artificial potential field method in order to also address the obstacle avoidance problem.

Furthermore, this thesis considers the energy efficiency of underwater snake robots. In particular, the relationship between the parameters of the gait patterns, the forward velocity and the energy consumption for the different motion patterns for underwater snake robots is investigated. Based on simulation results, this thesis presents empirical rules to choose the values for the parameters of the motion gait pattern of underwater snake robots. The experimental results support the derived properties regarding the relationship between the gait parameters and the power consumption both for lateral undulation and eel-like motion patterns. Moreover, comparison results are obtained for the total energy consumption and the cost of transportation of underwater snake robots and remotely operated vehicles (ROVs). Furthermore, in this thesis a multi-objective optimization problem is developed with the aim of maximizing the achieved forward velocity of the robot and minimizing the corresponding average power consumption of the system.

Contents

List of figures

List of tables

Preface

In my life I have learned to set goals, work hard in order to achieve them and never give up. One of the major goals was to complete my doctoral dissertation. In order to achieve this goal, I realized that except from studying and working hard every single day, I should have patience and persistence as well as make fruitful collaborations and move abroad. Certainly, these would not be enough without the assistance and support from a number of people. During my PhD I had great collaborations with several people and I can not describe how much they have contributed during these three years of my doctoral studies. Through this dissertation, I would like to express my deepest gratitude to these people for their direct or indirect assistance, support and encouragement.

First of all, I am especially grateful to my supervisors Professor Kristin Ytterstad Pettersen, Professor Jan Tommy Gravdahl and Associate Professor Øyvind Stavdahl for giving me the opportunity to be part of an amazing group and do research on snake robots at NTNU. Especially, I would like to thank Professor Kristin Ytterstad Pettersen for her excellent supervision during my PhD research. The completeness of my doctoral thesis would be unattainable without her scientific guidance, her invaluable feedback on my publications, her support and her confidence in me and my work. I learned from Professor Kristin Ytterstad Pettersen how important it is to spend some time and give positive feedback to people that you collaborate with or supervise. It is hard to explain how much this contributed to make me more productive by giving me the right motivation to work harder and harder every day. It would be at least ungrateful to argue that I could imagine having better supervision. In addition, I would like to thank Professor Jan Tommy Gravdahl for his scientific guidance and his constructive feedback on my ideas and works. His support, his encouragement, his invaluable inputs and discussions during our meetings, his trust in my research all these years helped me accomplish my goals. I thank my co-supervisor Associate Professor Øyvind Stavdahl for his support and guidance during the first months of my PhD and for the fruitful and inspiring discussions that we had during the last years.

During my PhD I was extremely lucky to meet and collaborate with an extremely intelligent and nice person, Pål Liljebäck. He was always there to show me that there is light at the end of the tunnel which I was not able to see because I was too tired or too disappointed at that moment. Thank you so much Pål for always being positive, for always being polite and patient to discuss for hours my crazy ideas, for always being available to help me with the experiments, for always supporting and trusting me during these years. It was a great pleasure to work with

you and Mamba during my PhD. It is really hard to count how much I have learned through our collaboration. In addition, I would like to thank Anna Kohl, Aksel A. Transeth, Ehsan Rezapour, Christian Holden and Jørgen Sverdrup-Thygeson for having really interesting discussions and nice collaborations in our snake robotics group. I also thank Terje Haugen and Glenn Angel at the mechanical workshop of the department for their effort and help preparing the experimental systems needed for my PhD. None of the experimental results of this thesis would be achieved on time without their great work.

I would like to thank my former supervisors Professors Antony Tzes and Stamatios Manesis from the University of Patras for inspiring me to start doing research on snake robots. In particular, I am really grateful to Professor Antony Tzes for making me realize that there is no easy path to be walked in research and for always advising me as he does with his own children. Of course, I could not forget all my former friends and colleagues from the University of Patras, Nancy Panousopoulou, Vasso Reppa, Themis Kolyvas, Yannis Koveos, Nikos Athanasopoulos, John Stergiopoulos, Kostas Alexis, Christos Papachristos and John Arvanitakis. Especially, I would like to thank my friend Rania for her support and help all these years even from a long distance.

I was very fortunate to work in a very pleasant environment, created by the former and current colleagues at the department of Engineering Cybernetics at NTNU. I would like to thank all of them for the very pleasant coffee and lunch breaks, their support and help. Especially, I would like to thank Marialena Vagia, Mansoureh Jesmani, Christoph Josef Backi and Giancarlo Marafioti for supporting me and for taking care of me in Norway. Their friendship is invaluable for me. Thank you Marialena for always counting me as a member of your beautiful family. I thank my officemate Lorenzo Fusini for really nice discussions that we had during the last years. I owe many thanks to Mutaz Tuffaha for really relaxing short breaks all these years. Furthermore, I am thankful to my Brazilian friends and of course to my incredible flatmates Sigrun Husø Haugtrø and Nefeli Novak not only for their support during my PhD but also for the special moments we shared together. I can not forget my friend Eirini and her invaluable support and help during the last year of my PhD. It is so important when your friends are happy when you succeed and they are supportive when you fail. I am extremely lucky having a friend like her.

I am grateful that my doctoral studies were the reason for knowing new people, getting closer to some others and making very good collaborations. However, the people that I met in my school and undergraduate years were always by my side. I would like to thank my friends Niki, Poulia, Eleni, Katerina, Dimitri, Stathi, Jenny, Thodori, Grigori, Ioanna and Fani for their long friendship, but also because they remind me that life is not only working and studying. Thank you so much all of you for being my friends and for your support and trust. Jenny and Thodori thank you for never counting on the distance in order to be part of my life. Especially, I would like to thank Fani for inspiring me to work with robots from the high school. She is always there for me, always encouraging me, always giving me the right advices, always supporting me, being strict with me when needed and being proud of everything I have accomplished. I really hope that I will one day manage to reach her expectations and that I will be able to follow her attitude of being

an incredibly generous and useful person for the society. I will always remember Fani's motto: *Knowledge that you keep for yourself is useless, spread it.*

Last but not least, I would like to express my deepest gratitude to my parents, Antzela and Christoforos. I thank them for the values with which they raised me and the sacrifices they made in order to accomplish my goals and for always helping me pursue my dreams. I would like to thank my brothers Giorgos and Michalis for always being there for me, for supporting my choices and mostly for their love. It would be almost impossible to complete this thesis without the support of my family.

Trondheim, December 2015 Eleni Kelasidi

Publications

The results presented in this thesis are based on the following conference and journal papers:

Journal Papers (First Author)

- E. Kelasidi, P. Liljebäck, K. Y. Pettersen, and J. T. Gravdahl, "Experimental Investigation of Efficient Locomotion of Underwater Snake Robots for Lateral Undulation and Eel-like Motion Patterns," in Robotics and Biomimetics, 2015, (Accepted).
- E. Kelasidi, P. Liljebäck, K. Y. Pettersen, and J. T. Gravdahl, "Biologically inspired swimming snake robots: Modeling, control and experimental investigation," in IEEE Robotics and Automation Magazine, 2015, (Conditionally Accepted).
- E. Kelasidi, P. Liljebäck, K. Y. Pettersen, and J. T. Gravdahl, "Integral line-of-sight guidance for path following control of underwater snake robots: Theory and experiments," in IEEE Transactions on Robotics, 2014, (Submitted).

Conference Papers (First Author)

- E. Kelasidi, M. Jesmani, K. Y. Pettersen, and J. T. Gravdahl, "Multi-objective optimization for efficient motion of underwater snake robots," in Proc. The First International Symposium on Swarm Behavior and Bio-Inspired Robotics (SWARM), Kyoto, Japan, Oct. 28- 30 2015.
- E. Kelasidi, K. Y. Pettersen, and J. T. Gravdahl, "Energy efficiency of underwater robots," in Proc. 10th IFAC Conference on Manoeuvring and Control of Marine Craft (MCMC), Copenhagen, Denmark, Aug. 24-26 2015.
- E. Kelasidi, K. Y. Pettersen, and J. T. Gravdahl, "Energy efficiency of underwater snake robot locomotion," in Proc. 23th Mediterranean Conference on Control and Automation (MED), Torremolinos, Spain, June 16-19 2015.
- E. Kelasidi, K. Y. Pettersen, and J. T. Gravdahl, "Stability analysis of underwater snake robot locomotion based on averaging theory," in Proc. IEEE International Conference on Robotics and Biomimetics (ROBIO), pp. 574-581, Bali, Indonesia, Dec. 5-10 2014.

- E. Kelasidi, K. Y. Pettersen, and J. T. Gravdahl, "A control-oriented model of underwater snake robots," in Proc. IEEE International Conference on Robotics and Biomimetics (ROBIO), pp. 753-760, Bali, Indonesia, Dec. 5-10 2014.
- E. Kelasidi, K. Y. Pettersen, P. Liljebäck, and J. T. Gravdahl, "Integral line-of-sight for path-following of underwater snake robots," in Proc. IEEE Multi-Conference on Systems and Control, pp. 1078 – 1085, Juan Les Antibes, France, Oct. 8-10 2014.
- E. Kelasidi, K. Y. Pettersen, and J. T. Gravdahl, "A waypoint guidance strategy for underwater snake robots," in Proc. IEEE 22nd Mediterranean Conference on Control and Automation (MED), pp. 1512 – 1519, Palermo, Italy, June 16-19 2014.
- E. Kelasidi, K. Pettersen, and J. Gravdahl, "Modeling of underwater snake robots moving in a vertical plane in 3D," in Proc. IEEE/RSJ International Conference on Intelligent Robots and Systems (IROS), pp. 266–273, Chicago, Illinois, Sept. 14-18 2014.
- E. Kelasidi, K. Y. Pettersen, J. T. Gravdahl, and P. Liljebäck, "Modeling of underwater snake robots," in Proc. IEEE International Conference on Robotics and Automation (ICRA), pp. 4540–4547, Hong Kong, China, May 31-June 7 2014.

Patent

- E. Kelasidi, K. Y. Pettersen, J. T. Gravdahl and P. Liljebäck, "Guidance of Underwater Snake Robots", Patent Application No. 1417625.9, Sept. 25 2014 (submitted).

Other publications, not part of this thesis

Journal Papers

- E. Rezapour, K. Y. Pettersen, P. Liljebäck, J. T. Gravdahl, and E. Kelasidi, "Path Following Control of Planar Snake Robots Using Virtual Holonomic Constraints: Theory and Experiments", Robotics and Biomimetics, SpringerOpen, 1:3, 2014.
- E. Kelasidi, G. Andrikopoulos, G. Nikolakopoulos, and S. Manesis, "A survey on pneumatic muscle actuators modeling," Journal of Energy and Power Engineering, 6 (9), pp. 1442–1452, 2012.

Conference Papers

- A. M. Kohl, K. Y. Pettersen, E. Kelasidi, and J. T. Gravdahl, "Analysis of underwater snake robot locomotion based on a control-oriented model", in Proc. International Conference on Robotics and Biomimetics, Zhuhai, China, Dec. 6-9 2015 (Accepted).

- A. M. Kohl, E. Kelasidi, K. Pettersen, and J. Gravdahl, "A control-oriented model of underwater snake robots exposed to currents", in Proc. IEEE Multi-Conference on Systems and Control, Sydney Australia, Sept. 21-23 2015.
- E. Kelasidi and A. Tzes. "Serpentine motion control of snake robots for curvature and heading based trajectory - parameterization", in Proc. IEEE 20th Mediterranean Conference on Control Automation (MED), pp 536-541, Barcelona, Spain, July 3-6 2012.
- P. Giataganas, N. Evangeliou, Y. Koveos, E. Kelasidi, and A. Tzes, "Design and Experimental Evaluation of an Innovative SMA-Based Tendon-Driven Redundant Endoscopic Robotic Surgical Tool", in Proc. 19th Mediterranean Conference on Control and Automation, pp. 1071-1075, Corfu, Greece, June 20-23 2011
- E. Kelasidi, G. Andrikopoulos, G. Nikolakopoulos and S. Manesis, "A Survey on Modeling Pneumatic Muscle Actuators", in Proc. 20th IEEE International Symposium on Industrial Electronics ISIE 2011, pp. 1263 - 1269, Gdansk, Poland, June 27-30 2011

Chapter 1

Introduction

1.1 Background and Motivation

For centuries, engineers and scientists have gained inspiration from the natural world in their search for solutions to technical problems, and this process is termed biomimetics. Mobile robots continue to challenge researchers with new applications in a variety of environments [100]. A recent fields of interest includes the integration of robotic technology into underwater exploration, monitoring, and surveillance. Bio-inspired robotic systems that mimic the motion of biological snakes or fish can be considered good candidates for these kind of application. Previous studies of hyper-redundant mechanisms (HRMs) have largely restricted themselves to land-based studies, for which several models for snake robots have been proposed [101]. Empirical and analytic studies of snake locomotion were reported by Gray [41], while the work of Hirose [51] was among the first approaches to develop a snake robot prototype. Comparing amphibious snake robots to the traditional snake robots, the amphibious robots have the advantage of adaptability to aquatic environments. Research on amphibious snake robots (also referred to as lamprey robots or eel-like robots) is, however, much less extensive than for the traditional types and fewer prototypes have been developed [29, 102, 138]. Several results have been reported in the related field of design, modeling and control of underwater robots that mimic the movement of fish [26]. Note that one of the main characteristics of snake robots is their adaptability to different motion demands. This attribute is extremely important for snake robots, since they have the ability to move over land as well underwater, while the physiology remains the same. Biological snakes, that are able to move only on the ground, are simply called land snakes while biological snakes that are able to move both on the ground and in water are referred to as amphibious snakes. Additionally, biological snakes that are able to move only in water are referred to as swimming snakes.

The use of underwater vehicles has rapidly increased the last decades since these systems are able to operate in deep and high risk areas which humans can not reach. Nowadays, autonomous underwater vehicles (AUVs) and remotely operated vehicles (ROVs) are widely used in the subsea environment for different challenging tasks [38]. These vehicles are suitable for various work assignments such as inspec-

tion, surveillance, maintenance, repairing equipment, building structures, and data collection, and they are extensively used in the subsea oil and gas industry and by the science community. In addition, swimming snake robots represent an interesting alternative to conventional ROVs and AUVs. These mechanisms have a long, slender and flexible body which enable them to reach and operate in locations not accessible by larger and more conventional underwater vehicles. At the same time, a swimming snake robot carries manipulation capabilities as an inherent part of its body since it is essentially a mobile manipulator arm. Underwater snake robots thus bring a promising prospective to improve the efficiency and maneuverability of modern-day underwater vehicles [15, 69, 83, 135]. A particularly relevant application concerns inspection and maintenance of subsea oil and gas installations, where the ability to reach tight locations in between pipe structures is important. Moreover, for the biological community and marine archeology, snake robots that can swim smoothly with limited noise, and that can navigate in difficult environments such as ship wrecks, are very interesting. However, in order to study these properties an accurate dynamic model of the hydrodynamic forces during the motion under the water it is essential.

Modeling and control of underwater snake robots is quite challenging mainly because these systems have many degrees of freedom. In addition, for the swimming robots, the dynamic modeling of the contact forces is more complicated compared to the modeling of the overall rigid motion and the dynamics of the body deformation. Hence, the hydrodynamic modeling task presents a major challenge. The hydrodynamic forces induced by the motion of a rigid body in an underwater environment are very complex and highly nonlinear. Generally, the modeling of the environmental forces is more complicated for underwater snake robots compared to ground snake robots. The derived dynamic model of underwater snake robots is thus quite complex due to the many degrees of freedom of the robot combined with a highly nonlinear model of the hydrodynamic effects and dynamic coupling between the links. This complexity is the main reason that makes the control design for underwater snake robots challenging. Furthermore, it is of great interest to investigate the energy efficiency of underwater snake robots, which can provide both inspection and intervention capabilities and can be good candidates for the next generation inspection and intervention AUVs, compared to those of the widely used robots for subsea operations which are the remotely operated vehicles (ROVs).

In this thesis, we will explore some of the challenges for underwater snake robots mentioned above. The main goal of the thesis is to investigate and gain deeper theoretical insights regarding the modeling, control and energy efficiency of underwater snake robots in the subsea environment. Generally the modeling for control design purposes poses different challenges than hydrodynamic modeling for simulations. When modeling for model-based control design purposes, the model needs to be well-suited for analytical analysis while only the significant hydrodynamic effects need to be included. To this end, in this thesis, we will first address the problem of modeling the hydrodynamic effects with a primary goal of finding a closed-form solution for the dynamic model of underwater snake robots. In addition, based on the kinematics and dynamics of underwater snake robot locomotion, we will propose control strategies for these systems. In particular, we will investigate the ability of an underwater snake robot to follow a path, compensating the environmental dis-

turbances (i.e. the current effects). The proposed path following control strategies will be validated through simulations and experiments which are obtained using a physical underwater snake robot. Note that the overall future goal is to realize operational snake robots for underwater applications. In order to achieve this, a number of different control design challenges must first be solved. An important control problem concerns the ability to achieve efficient motion with preferably a minimum amount of consumed energy in order to be able to undertake longer missions. Hence, for the long term autonomy of underwater vehicles, energy efficiency is one of the main challenges. This is the main motivation behind the investigation of the energy efficiency of underwater snake robots in this thesis.

1.2 Biologically Inspired Locomotion of Robots

The last decades, a large amount of research has been done regarding bio-inspired robots. More specifically, the overall idea of bio-inspired robots is to make systems that are inspired by biological ones, to learn the concepts of the locomotion from nature and apply them to the design and the locomotion of the robotic systems. Snake robots are robotic systems where both design and locomotion are inspired by biological snakes. For the underwater robots it is crucial to increase the efficiency by improving the locomotion methods. Increased agility and maneuverability are connected to a general decrease in the size of the robot, as well as more flexibility in its internal shape. In order to improve these properties, researchers began studying aquatic biological systems and their methods of locomotion [12, 26, 126, 129]. However, since land and water are two completely different environments, the same gaits of the robots will not give the same results on ground as in water. To this end, in this section, we briefly review the locomotion methods of the biologically inspired locomotion of snake-like and fish-like robots.

1.2.1 Biologically inspired locomotion of snake-like robots

Research on snake robots is inspired by the robust motion capabilities of biological snakes. As it is already mentioned, empirical and analytical studies of snake locomotion were reported by Gray [43]. Moreover, mathematical descriptions of the forces acting on a snake are proposed in [43] and used to reenact the attributes of snake locomotion. It is shown in [43] that the forward motion of a snake moving in the plane on the ground requires the existence of external forces that act in the normal direction to the body of the snake. Hirose [51] studied biological snakes moving on the ground and modeled the body of the snake as a continuous curve that could move sideways with or without sideslip constraints. The serpenoid curve was then formulated, which is a mathematical description of lateral undulation, which is the most common form of snake locomotion. In particular, Hirose found out that a close approximation to the shape of a biological snake during lateral undulation, is given by a planar curve with its curvature varying sinusoidally [51]. An alternative description of lateral undulation–the serpentine curve–was introduced by Ma [103]. Ma concludes that snake-like robots moving on the ground have higher locomotive efficiency using the serpentine curve compared to those using the serpenoid curve.

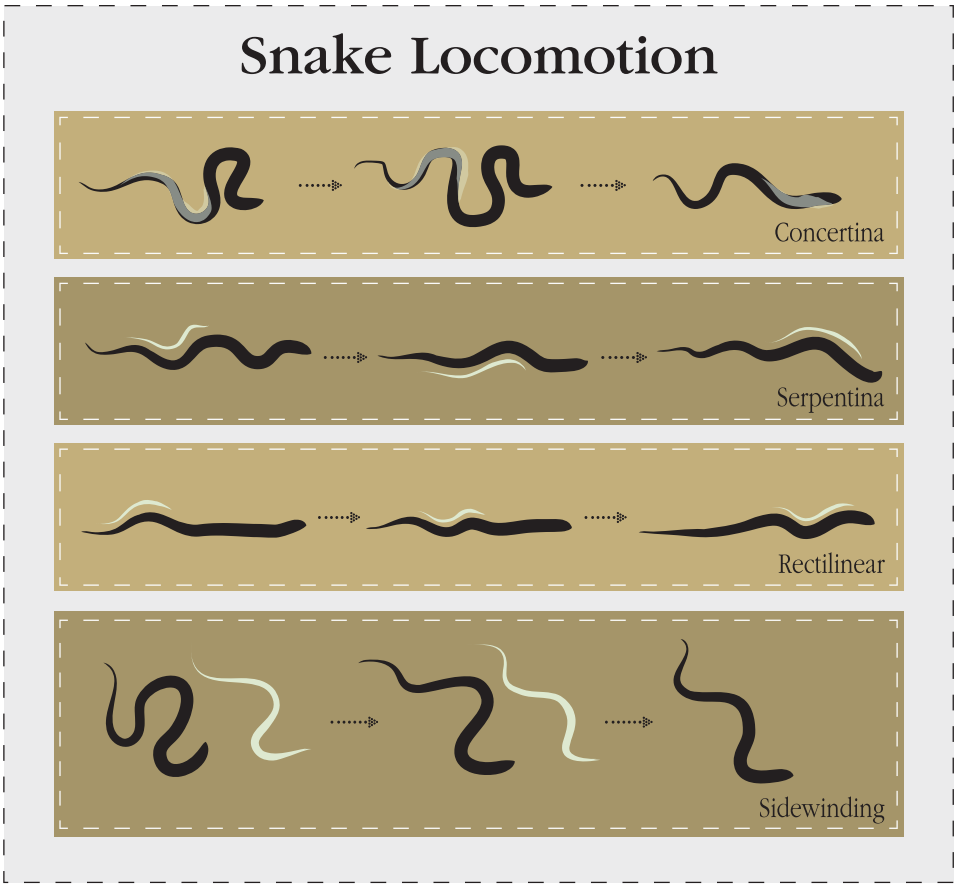

Figure 1.1: Different forms of locomotion modes for biological snakes.

In addition, the frictional properties of snake skin was studied in [53]. This work shows that in order to achieve undulatory locomotion on the ground, an issue of fundamental importance is that the friction coefficients between the snake and the ground have to be directional. In particular, there must be a low friction coefficient in the tangential direction and a high friction coefficient in the perpendicular one in order to achieve forward motion. Relevant results can be found in the biological literature about behaviors that have been observed by biologists in qualitative studies of lampreys and other anguilliform swimmers in nature [106].

Four main different locomotion modes have been documented for biological snakes: *lateral undulation (serpentine locomotion)*, *concertina*, *sidewinding* and *rectilinear* locomotion. Illustrations of the different locomotion models are shown in Fig. 1.1. The lateral undulatory mode, characterized by a lateral wave travelling from head to tail, is the most common and efficient one, and almost all biological snakes use it. A detailed presentation of these modes can be found in [101].

1.2.2 Biologically inspired locomotion of fish-like robots

Swimming snakes move the body practically in the same way as snakes on land [57]. Researchers have developed many theories and numerous robotic fish prototypes to study and mimic the way that real fish moves. Swimming behavior of flexible elongate fish was first described as the *anguilliform* mode by Breder, who categorized these fish under the genus name *Anguilla* [18]. Simulations indicate that aquatic locomotion is possible because water gives higher resistance to motions that are perpendicular to the direction of travel than to parallel motions due to the shape of the organism, so eels push their curves against the resistance of the water. During the last decades the academic community has dealt with the locomotive abilities of eel-like swimming robots, which is one of the major issues in this area of research [126, 128, 129]. However, the majority of the scientific studies about these robotic systems are largely concentrated on forward swimming locomotion, while backward swimming has received far less attention [143]. Gray [41] presented an approximate analysis of the fluid mechanics of several species of fish, making the qualitative assessment that anguilliform swimming operates by passing traveling waves down the body, such that the wavelength is approximately equal to the length of the animal. Further research on elongated fish was done by Grillner [44, 45] and Kashin [61] who studied the much simpler nervous system of lampreys. This study clarified the neural network that underlies the undulatory axial muscle motions. It was noticed that motoneuronal activity that oscillates on either side of the spinal cord as the body travels caudally causes the body undulations [45]. Additionally, a range of carangiform (fish-like) robots were studied and implemented by researchers.

Subsequently, more recent research, such as Williams [137], Cohen [25] and Grillner [44, 46–48] studied the motion control in animals. Lampreys, once again, were the inspiration because of the forward swimming problem and its neural network model, leading to a central pattern generator (CPG) that could control the eel-like robot's locomotion. Swimming frequency, in particular, seems to be a key issue to imitate animal movement. Gray [41] observed a linear relationship between swimming frequency and body velocity for anguilliform swimming, while Grillner [48] noticed that the phase delay between segments of the lamprey remains constant over a wide range of swimming frequencies. Grillner [48] has observed that backward swimming qualitatively matches forward swimming. Grillner [46] suggested modelling lamprey's central pattern generator (CPG) based on the amino acid excitation over a chain of coupled oscillators. In this way, one oscillator leads the rest in the chain, resulting in the phasing of the oscillation. Williams [137] argued that this prediction is biologically implausible, and counter-proposed a model based on varying strength of excitatory synapses.

Turning and steering locomotion have received far less attention from the biological community than forward/backward swimming. However, some qualitative results are available. In his study of directional control in fish [42], Gray describes the turning gait of the anguilliform swimmer as passing a traveling wave down one side of its body. This wave is similar, in nature, to that which affects normal locomotion, but has an abnormally large amplitude on the side of the desired direction. The solution was given by Ekeberg [33] by constant tonic (rhythmic) excitation to the spinal neurons along only one side of the animal, which allowed this turning

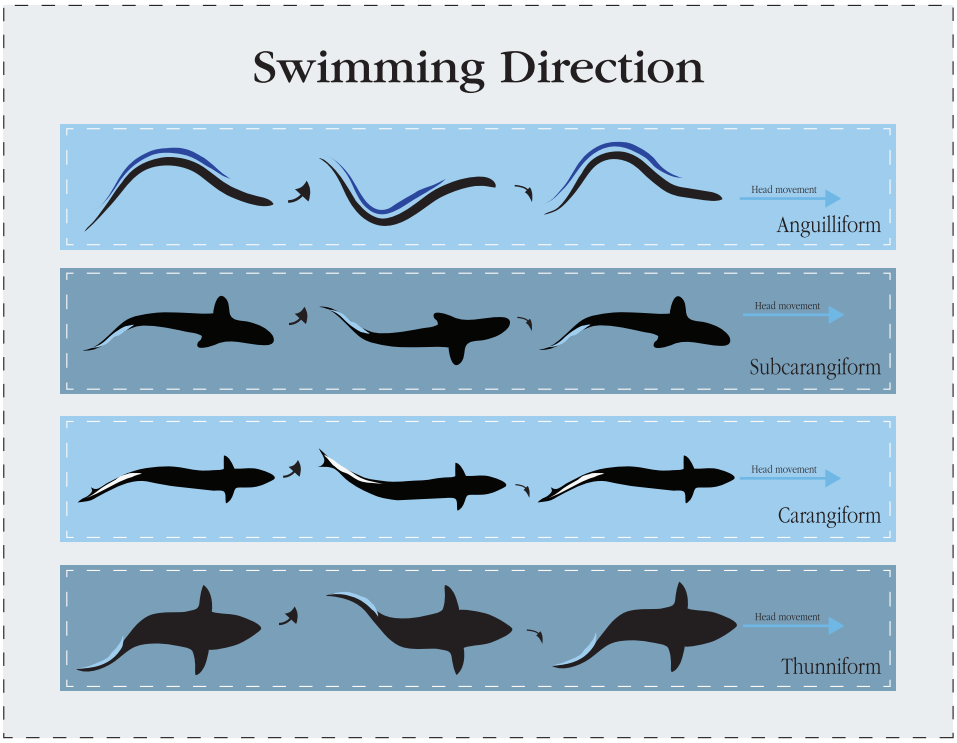

Figure 1.2: Different forms of biological locomotion of fish.

behavior in his neural network swimming model. A typical example of CPG for anguilliform swimming is found in the lamprey [137]. The CPG is a double chain of oscillators. In this case, the chain is designed to generate a traveling wave, from the head to the tail of the robot. Researchers use this wave to achieve anguilliform swimming in water and serpentine locomotion on ground.

Generally, swimming modes of fish are classified according to four main categories: *Anguilliform*, *Subcarangiform*, *Carangiform* and *Thunniform*. Illustrations of these modes are shown in Fig. 1.2. In *Anguilliform* mode, the whole body participates in large amplitude undulations. In *Subcarangiform* mode, approximately, 2/3 to 1/2 of whole body is used to produce the propulsive wave responsible for forward motion. Side to side movement of the head is reduced, while in Carangiform swimming, the fish body undulations are confined to the last third of the body length. *Carangiform* swimmers generally have rapidly oscillating tails. Finally in *Thunniform*, the undulation proportion is even less (confined mostly to the caudal fin). For amphibious robots, the serpentine motion is the most common mode of locomotion in order to traverse any uneven terrain or confined spaces, like tunnels or pipes, whereas for locomotion in three-dimensional dynamic aquatic environments the eel-like motions is the most common.

Various methods have been proposed in the literature regarding amphibious snake-like robots gait generation [27, 29]. Reviewing these methods, three categories

can be identified: motion control based on kinematic or dynamic models of the amphibious snake-like robot, motion equations derived from the Serpenoid Curve or formed by sinusoidal functions, and motions activated by biomimetic neural networks like Central Pattern Generators (CPG) [27, 141]. Gait generation by the serpenoid curve has a relatively simple mathematical form. In addition, it avoids complicated calculations of kinematic and dynamic models and the problem of environment interaction for a CPG controller. A review on CPG for locomotion control in animals and robots can be found in [55].

1.3 Previous Work on Modeling, Development, Control and Energy Efficiency of Underwater Snake Robots

In this section, we present an overview of previous literature regarding the modeling, control and energy efficiency of underwater snake robots. In addition, this section provides an overview of previous research efforts related to implementation of underwater snake robots (also referred to as eel-like robots).

1.3.1 Modeling and Analysis of Underwater Snake Robots

There exist many underwater robots, and these can be classified into autonomous underwater vehicles (AUVs), remotely-operated underwater vehicles (ROVs), and bottom-crawling-legged underwater robots. As it is already mentioned, more recently, there has been growing interest in the design, modeling and control of underwater robots that propel themselves and maneuver by mimicking the movement of a fish. Researchers have developed analytical models for the forces generated during the motion of these devices in the water [26].

The dynamics of snake robots moving on land have been derived by utilizing various modeling techniques [100, 101]. The friction between the snake robot and the ground significantly affects its motion. In addition to many models of snake robots that consider sideslip constraints, there have been reported cases with anisotropic ground friction properties similar to biological snakes, providing the opportunity to model lateral undulation locomotion patterns. In [100], the authors provide an overview on modeling and analysis of snake robot locomotion emphasizing the growing trend toward locomotion in unknown and challenging environments. When it comes to swimming snake robots, only a few modeling approaches have been presented for eel-like robots [15, 106, 135].

For swimming robots, the dynamic modeling of the contact forces is most complicated compared to the modeling of the overall rigid motion and dynamics of the body deformation. Hence, the hydrodynamic modeling task presents a major challenge. Classical works by Taylor [126] and Lighthill [95] provide analytic models of fluid forces acting on the body during undulatory swimming. However, the validity of Taylor's resistive [126] and Lighthill's reactive [95] model assumptions varies significantly depending on the flow regime and geometry of the swimmer, as it is pointed in [135]. Generally, for slow swimming devices at low Reynolds numbers, the viscous forces become dominant. Hence, in this case, the Taylor's resistive model is most applicable. For larger swimmers in which the added-mass effects

dominate, Lighthill argues that reactive forces are the primary source of thrust and the resistive ones can be neglected. For, underwater snake robots, which lie in between these two extremes, both the resistive forces (drag forces) and reactive ones (added mass affects) need to be modeled, since both play a critical role in underwater swimming robotic systems propulsion (see e.g. [58]). Generally, for underwater snake robotic systems that swim at a Reynolds number of approximately 10^4 to 10^5, a detailed model of the fluid effects can only be achieved through a full numerical solution to the Navier-Stokes equations [135]. Unfortunately, due to prohibitive computational costs of such methods they are not suitable for real time control, and the resulting models would not be suited for analytical analysis.

To sum up, the hydrodynamic forces (fluid forces) induced by the motion of a rigid body in an underwater environment are very complex and highly nonlinear [146]. Furthermore, as it is already mentioned, Navier-Stokes equations are very difficult to solve and quite unsuited for robotics control design purposes. Hence, as far as the fluid effects are considered, for control design purposes, the hydrodynamic phenomena should be modeled in a sufficiently simple manner while taking into account all the hydrodynamic effects that are significant for the control design [32]. It is important to notice that modeling for control design purposes poses different challenges than hydrodynamic modeling for simulations. In the latter, high accuracy and modeling of all hydrodynamic effects are important, while the model does not need to be in a form suited for analytical analysis. When modeling for model-based control design purposes, however, the model needs to be well-suited for analytical analysis while only the significant hydrodynamic effects need to be included. The closed-loop control system provides robustness to the less-significant unmodeled hydrodynamics, cf. for instance [38] and [37].

Consequently, solving the hydrodynamic modeling problem by using an analytical simplified form suited for the design of online control is essential for underwater snake robots. The literature provides three simple analytical models suitable for control design purposes. All of them are based on the fluid mechanics theory of slender bodies. The biomechanics community suggests the first one, the second one is offered by the oceanic engineering community and the third one is a model that is mostly used in the robotics community. In particular,

- the first model is a result of the Large Amplitude Elongated Body Theory (LAEBT) of fish locomotion by Lighthill [95],
- the second model is devoted to the dynamics of underwater flexible cables [15] and
- the third one is based on the Morison's equations and models the forces between the fluid and the cylindrical links of underwater snake robots [36, 111].

Different modeling approaches for underwater snake robots are presented in previous literature. A dynamic simulation of an underwater snake-like robot was developed by the biorobotic laboratory EPFL using Webots Dynamics [5]. In [31], Crespi *et. al.* have developed a simulation tool for the underwater swimming robots Amphibot I and II in order to test controllers on a physics-based model of the robot. This dynamic simulation has the same mechanical and physical properties as the real robot. During swimming, the hydrodynamic forces applied to each element

of the robot are the buoyancy and drag forces. Although this model is relatively simple (e.g., it does not take into account the turbulence generated in the water by the movement of the robot), it is adequate for a qualitative analysis of the swimming motion. In this model, the anisotropic friction property used in order to achieve undulation locomotion on the ground. In addition, due to the elongate shape, propulsion is produced by the combination of a low drag coefficient in the tangential direction and a higher one in the perpendicular direction in order to achieve the anisotropic property during locomotion underwater [27, 31].

Another approach to modeling an eel-like robot was presented in [108]. In [108], McIsaac *et. al.* proposed basic viscous and fluid drag models to capture the effect of external forces acting on the bodies of land-based snakes and eels. In this geometric approach, the authors made tree assumptions: 1) the fluid is stationary, so the force of the fluid on a given link is due to the motion of that link, 2) the Reynolds number is high enough that inertial forces dominate over viscous effects and 3) the drag forces parallel to the link have negligible effects and can be excluded. In this paper, a new approach of modeling of snake and eel-like robots from a geometric perspective was proposed, while [106] presents a discrete model of the eel-like robot using a geometric approach to show that the dynamics of eel locomotion can be decomposed into motions in the position and orientation of the overall system and changes in its internal shape. However, the model does not place sideslip constraints on the robot. Instead, the eel-like mechanism was propelled by hydrodynamic forces modeled by a viscous friction model. The basic viscous and fluid drag models were presented to capture the effect of external forces acting on the bodies of land-based snakes and aquatic eels. To simulate the forces in the water, a simple fluid mechanical model that has been used by Ekeberg [33], was adopted.

In order to realize the remarkable features of the snake-like robot's serpentine locomotion in water, Zuo et. al. [146] developed an amphibious snake-like robot which can adapt to terrestrial and underwater environments. They derived the dynamic equations for the serpentine locomotion of the underwater robot and simulated the dynamic model using ADAMS software [1]. In water, a snake-like robot generates force from serpentine locomotion to push its body forward. As it is observed by researchers in the biomimetics literature, the flow field around the snake-like robot is distributed. The traditional method to solve the distributed problem by replacing parameters cannot produce a closed-form solution. Hence, it is very difficult to derive the dynamic model. To solve this problem, Zuo *et. al.* [146] used a direct method in order to incorporate external environmental forces into the model, which includes four major hydrodynamic forces: added mass, drag, fluid acceleration and buoyancy. In particular, the net effect of added mass, buoyancy, fluid acceleration, and drag are often treated as the superposition of each individual force. Zuo *et. al.* derived all of the generalized inertia forces and generalized active forces for the amphibious snake-like robot. Using these generalized forces the equation of motion was derived.

Ayers *et. al.* [9] studied a lamprey-based undulatory vehicle. They observed that during migration lampreys encounters a variety of obstacles and hydrodynamic conditions. Different habitats through which lampreys travel include streams, rivers, falls, rapids, lakes, estuaries, inter tidal zones and the open ocean. In addition to its high adaptability, lampriform swimming affords an additional advantage of en-

ergetic efficiency. Lampreys swim by rhythmic lateral undulations of the body axis. Also, lampreys swim forward by propagating lateral axial undulations that increase in amplitude from nose to tail [9]. To evaluate how lamprey swimming movements are modulated by hydrodynamic load, researchers analyzed high-frequency forward swimming of the lamprey in a shallow, wet pan sans water. They adapted a conservative command neuron, coordinating neuron, central pattern generator (CPG) architecture to realize a finite state machine that generates an alternating bilateral pattern that propagates along the body axis. Initially, they modeled the hydrodynamics of the robot and optimized the hydrodynamics for wakeless propulsion by first comparing lamprey swimming to a hydrodynamic model of a wakeless propulsor. After that, a beam model was developed for the undulatory robot. The beam model was coupled with the 3D slender-body hydrodynamic model for external hydrodynamic loads. This coupled model can be used for the prediction and/or evaluation of the external hydrodynamic loads, the internal load (stress), the input power, the propulsion efficiency, and the motion of the undulator. In addition to this, sensory feedback was used to elicit behavioral changes due to environmental perturbations. For example, the robot will need to increase its swim speed when it encounters strong currents, turn away from or into obstacles, dive and climb according to static pressure changes therefore maintaining a constant depth in the water column [9, 136].

Unlike most lampreys, the pacific lamprey is capable of climbing vertical wetted surfaces through a two-phase (bending and stretching) locomotion mode using the oral disc for adherence. Among all the climbers, the pacific lamprey is unusual both in its ability to climb sheer, vertical wetted surfaces in air and in its unique mode of locomotion. Zhu et. al. [145] developed a continuous beam model based on Euler-Bernoulli beam theory to simulate the structural response and the body displacement during one climbing step of a pacific lamprey. They created a continuous model of the lamprey body by idealizing it as a uniform elastic beam with circular cross-sections. In [145], a nonlinear beam model was implemented to solve the mechanical responses of the aforementioned fish body. Mathematically, this model consists of a set of fully nonlinear governing partial differential equations representing the conservation of translational momentum, the conservation of angular momentum, and the continuity of the configuration. The external force includes contributions from the fluid drag caused by the thin layer of fluid on the wetted surface. The fluid drag in the vertical direction and the horizontal drag were imposed on the head. From simulations Zue *et. al.* [145] observed that the climbing capacity of the lamprey, with its simplistic efficiency, may inspire biomimetic design of fish-like swimming devices capable of overcoming steep obstacles. As a suggested direct application, Zue *et. al.* mention the development of anguilliform swimming machines.

Khalil *et. al.* [82, 83] proposed a modeling approach for an underwater eel-like robot using recursive algorithms based on the Newton-Euler equations. The modeling approach was based on three hierarchical levels: 1) a Navier-Stokes code modeling the fluid/structure interaction, 2) a "micro – continuous" modeling based on a beam-like approach, and 3) a serial structure with revolute joints. Moreover, a simplified model of the fluid structure contact was proposed in [82]. The model of the contact between the fluid and the body of the eel is that of Morison [111].

This proposed dynamic model is easy to implement and simulate using numerical calculations. Moreover, in [40] a 3D-Hybrid dynamic modeling of underwater eel-like robots using recursive algorithms based on the Newton-Euler equations was presented. Also, in [15], a continuum 3D model of a swimming eel-like robot was formulated based on beam theory. Finally, [81] summarizes the inverse and direct dynamic modeling, using the recursive Newton-Euler formalism of different robotic systems.

In [135], Wiens *et. al.* applied a semi-empirical resistive-reactive model, proposed by Jordan [58], in order to produce a low-cost simulation of an underwater hyper-redundant mechanism. This modeling approach was used to derive an efficient swimming method of a robotic device. A low-cost gait optimization scheme was applied to generate efficient swimming kinematics. In this modeling both the drag and added mass effects were considered. McIsaac and Ostrowski [106] present a dynamic model of anguilliform swimming for eel-like robots and Boyer et al. [15] present the dynamic modeling of a continuous three-dimensional swimming eel-like robot. Chen et al. [22] demonstrate a model for the body-fluid interaction in undulatory swimming of leeches, where the body is represented by a chain of rigid links and the hydrodynamic force model is based on resistive and reactive force theories. [11] presents the equations of motion for a general multibody rectifier system taking into account the currents by assuming that the environmental force is a (possibly nonlinear) function of the relative velocity (i.e. the velocity of the link in water in the presence of current). However, the added mass and the fluid torque effects are not taken into account. Furthermore, in [144], a simplified model of [11] is used to develop a feedback controller that achieves the desired body oscillation, orientation, and locomotion velocity. [20] presents the modeling of the reactive force and moment acting on an elongated body moving in a weakly non-uniform potential flow. This model has been used to investigate the passive and the active swimming of a fish in a vortex street. In [16], a solution to the fast dynamics of eel-like robots has been proposed and tested in comparison with a Navier-Stokes solver. In [120], the dynamic model of a fish-like robot named AmphiBot III is presented. This modeling approach is based on the adaptation of Lighthill's large amplitude elongated body theory to a serial mobile multibody system and the results are compared to the planar motion of the real robot for forward swimming gaits and turning maneuvers. Furthermore, a number of research groups have developed computational fluid dynamics solutions capable of modeling undulatory swimmers [21, 94, 95], but the computation time required by such methods makes them not suitable for real time control approaches.

However, the majority of swimming robots modeling omit fluid moments which are supposed to have a negligible effect on the overall motion of the system [33, 106]. It should be noted that fluid moments are directly related to the power consumption of the system (see e.g. [135]) but they are neglected in these modeling approaches in order to simplify the hydrodynamic effects. It is also worth noting that in [135], [15] and [83] fluid moments are modeled, but the drag force and moment are integrated numerically at each sample time of the algorithm and evaluated numerically, which results in the lack of a closed-form solution. For control design purposes, it is a main advantage that the hydrodynamic modeling concludes in a closed-form, without the need of an algorithmic way to compute the drag force and torque. [20] presents the

modeling of the reactive force and moment acting on an elongated body, moving in a weakly non-uniform potential flow. This model has been used to investigate passive and active swimming of a fish in a vortex street, while no viscous effects have been taken into account. Furthermore, a number of research groups are currently working to develop accurate low-cost swimming models required for such problems [135].

Remark 1.1: *To our best knowledge, a closed-form solution for modeling of underwater snake robots that takes into account both the resistive and reactive effects while at the same time models the current effects is not considered in previous literature.*

1.3.2 Development of Physical Underwater Snake Robots

This subsection gives an overview of previous research efforts related to implementation of underwater snake robots (also referred to as eel-like robots). A review of ground snake-like robots can be found in [100, 127]. In [100], the snake-like robots have been separated into two categories: snake robots without contact force sensors and snake robot with contact force sensors. The work of Hirose [51], one of the first approaches to develop a snake robot, is essential. While a variety of different snake-like robots have been constructed since then, only a few working examples of swimming snake robots currently exist. This includes the eel robots REEL I [108] and II [105], the lamprey robot built at Northeastern University [136], AmphiBot I [31], AmphiBot II [27] and AmphiBot III [120] from the EPFL lab, Perambulator III [93], the amphibious snake robot ACM 5 [138, 139], the HELIX-I [125], a biorobotic platform inspired by the lamprey [124] and the underwater snake robot Mamba that is implemented at NTNU in Norway [102].

AmphiBot I, shown in Fig. 1.3(a), is an amphibious snake robot capable of crawling and swimming, that was implemented by the EPFL. The robot was designed to be capable of anguilliform swimming in water, and lateral undulatory locomotion on the ground [31]. AmphiBot I is a novel type of robot with dexterous locomotion abilities. Its design was inspired by snakes and elongated fishes such as lampreys. This amphibious snake robot is modular and constructed out of several identical segments, named elements (Fig. 1.3(a)). Each element has a single DOF and consists of four structure parts: a body, two covers and a connection piece. The locomotion of the robot is controlled by a CPG. AmphiBot II (Fig. 1.3(b)) is an updated version of AmphiBot I with a significant number of improvements in mechanical design and CPG [27, 28, 30]. AmphiBot II is one of the first amphibious snake robots controlled online by an on-board CPG. The swimming robot AmphiBot III (Fig. 1.4) consists of eight segments, with the first being the head segment, while in the last segment (tail segment) a caudal fin is attached. The total length of the robot is 0.88 m [120]. The caudal fin has a length of 10.3 cm and a cross-section of 0.3 cm $\times$ 5.7 cm. The AmphiBot III is designed to be modular similar to AmphiBot I and II while in addition a caudal fin is attached to the last segment to study the efficiency of underwater snake robots with and without the attached tail.

McIsaac and Ostrowski built the REEL I robot, a simple waterproof RC-controlled four-link robot with actuated servomotor joints. REEL I consists of four

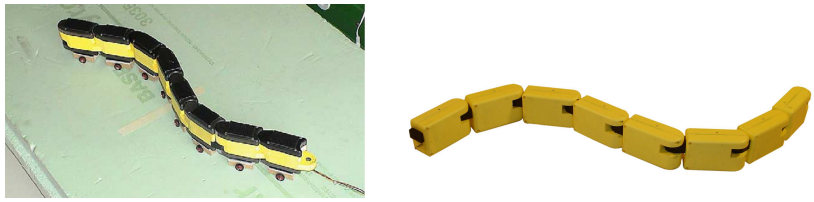

(a) AmphiBot I (b) AmphiBot II

Figure 1.3: The amphibious snake-like robots AmphiBot I [31] and AmphiBot II [27].

Figure 1.4: The amphibious snake-like robots AmphiBot III [120].

rigid identical links (aluminium plates), and a rubber tube is used as its waterproof skin. Due to what the developers call some poor design choices, the REEL I was never suitable for qualitative experiments [108]. REEL II is a second generation version of REEL I, in which the number of the links was increased, from four to five, improving the symmetry of the robot [105]. The new design of the waterproof eel-like robot (Fig. 1.5) approximate the actual shape of an eel, and the plastic shells provide a means of buoyancy for the robot in water. In order to maintain the proper upright attitude during swimming, small weights were attached to the bottom of the robot links, and inflatable air sacs were used to provide the buoyancy to float the robot near the surface of the water. In order to achieve a streamlined hydrodynamic profile, the head and tail links were rounded cones. The robot shape is controlled by a PC ground station calculating the shape variables, which are transmitted using an off-the-shelf radio controller to a receiver in the nose of the robot. This new design increases the robot's robustness in terms of modularity, efficiency and reproducibility [106].

Helix I [125], shown in Fig. 1.6, is a hermetic 3D active cord mechanism that moves both on the ground and in the water. Helix I has a length of 180 cm, the diameter of the body is 8 cm, and the total density is near to the density of water. It consists of 10 joints and 11 body segments. Each body segment is equipped with 4 paddles. All joints have 2 degrees of freedom which can create distortion motions. All joints are covered with bellows to keep the electronics from the water and to generate buoyancy. Helix I can perform helical distortion motion and the paddles create torques, so that the whole body revolves around itself and it progresses. In addition, the active cord mechanism does not require rotational parts such as wheels or propellers that are driven by actuators, so it is easy to construct a hermetical

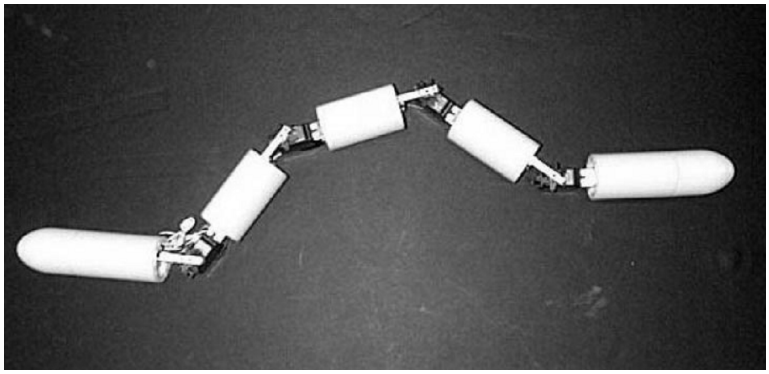

Figure 1.5: The REEL II [106].

(a) Moving on the ground

(b) Swimming in the water

Figure 1.6: The amphibious snake-like robot HELIX-I [52, 125].

robot that can be used in any kind of environment.

Typical studies of the propulsion of the active cord mechanism focus on the winding movement, like a snake, on the ground Fig. (1.6(a)), and this same propulsion principle can be applied to movements in water. In the water, the whole body surface of the robot is in contact with the water (Fig. 1.6(b)), so all articulated body segments produce the same power by this motion, in an apparently more efficient way than the two-dimensional motion. The principle that the whole body is under water was considered, but the density of the HELIX is less than that of water, and part of the body is above the water surface. So, HELIX deviated slightly sideways [52, 125].

Hirose et. al. [138] developed another amphibious snake-like robot, the ACM-R5 (Fig. 1.7). The general mechanical design of ACM-R5 is the same as in the amphibious snake-like robot HELIX. The body of this robot is composed of a series of several joints. In order to make the body waterlight, each joint is covered with bellows and the connections between joints are sealed with O-rings. Compared with HELIX, in the new version of the amphibious snake robot the driving system

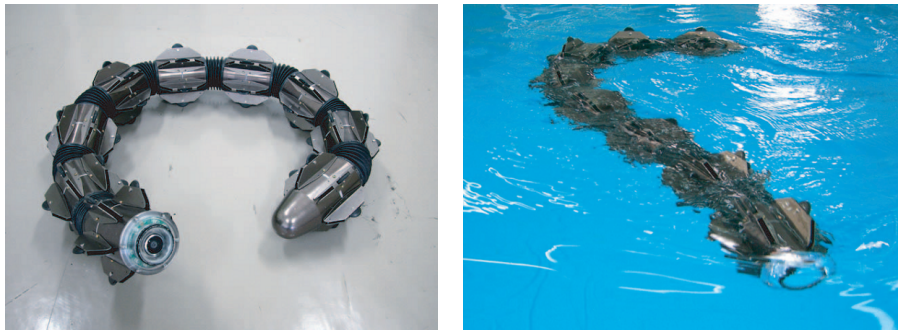

(a) Moving on the ground (b) Swimming in the water

Figure 1.7: The amphibious snake-like robot ACM – R5 [138].

was reinforced in order to work on the ground. ACM-R5 has special propulsive devices in order to work both on ground and in the water. Each of these devices is composed of a passive wheel and a paddle. In this robot, by attaching paddles along the body of the snake-like robot the difference of resistance and thus the efficiency were increased. Experiments show that the ACM-R5 has the ability to swim in water by serpentine motion. Also, this robot was able to carry out sharp turns and go up and down freely in the water [138].

The Biomimetic Intelligent Mechatronics Lab in Japan developed the amphibious snake-like robot Perambulator III (Fig. 1.8). This amphibious snake-like robot has novel design in its joints and water-proof accessories [93, 141, 146]. The robot has 10 modules in total. Each diameter of the module is 11 cm and its length is 17 cm, giving a total length of 174 cm. Each module has 4 passive wheels in order to reduce the friction of the robot when it moves on ground, and create the difference in friction in longitudinal versus lateral direction that is necessary for propulsion. Each module consist of three servos, with servos 1 and 2 coupled to form a universal joint capable of rotating in tree dimensions. Servo 3 gives the snake-like robot the ability to reverse itself. To enhance the robot's motion abilities on the ground and in the water, eight oars with passive wheels are installed around each trunk module. Between joints are water-proof rubber bellows, two O-rings and a set of sleeves. Perambulator III displays high performance in its motion ability, by realizing common two– and three – dimensional gaits. Additionally, in the water, the robot has the ability to go forward and backward, turn, and dive into the water. It is observed that, under serpentine gait, the robot behaves smoothly and exhibits rapid motion on the floor and in the pool [146]. This amphibious snake-like robot can not only perform serpentine locomotion, concertina locomotion, sidewinding locomotion and arc-shape rolling, but also displays several previously unheard-of gaits in the experiments: like S-shape rolling and helical rolling. The robot in the pool displays a helical rolling under the same motion pattern, apparently without changing its position [93, 141, 146].

A lamprey-inspired robot was implemented based on biomimetic neurotechnology (Fig. 1.9) by Knutsen *et. al.* [86]. This robot is functionally a three component

Figure 1.8: The amphibious snake-like robot Perambulator III [93, 141, 146].

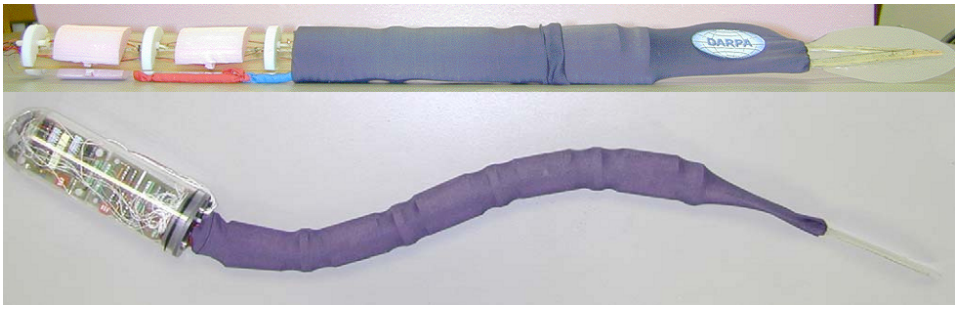

Figure 1.9: The Undulatory Robot [9, 136].

system consisting of a rigid hull/electronics bay, a flexible body axis supporting the nitinol actuator and a thin, passive tail. The watertight plexiglas cylindrical hull houses the electronics. The polyurethane body axis supports six Teflon vertebrae that attach and pin the shape memory alloys (SMA) actuators along the midline. Lycra covers the body axis acting as a skin attached posteriorly to the hull, continuing the length of the notochord, and terminating between the fins of the tail. The vehicle is propelled by ten nitinol actuators, which are controlled by neural-based circuit software that activates the actuators in a characteristic bursting pattern and control the amplitude of contractions via pulse width modulation. Finally, a serial I/O interface links the processor to the sensors and actuator interfaces. These interfaces consist of three boards: a serial/sensor interface, a current-driver interface to control the nitinol actuators and an analog sensor board that supports a compass and pitch and roll inclinometers and quantizes these signals to bit representations [9, 136].

The aim of the French national research project ROBEA-ANGUILLE was to design, construct and control the 3D motion of an eel-like robot (Fig. 1.10(b)). The

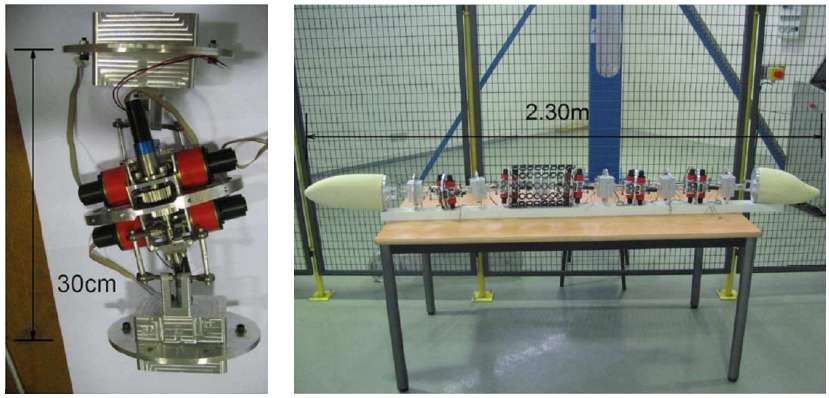

(a) Vertebrae (b) Serial assemblage of vertebrae

Figure 1.10: The eel-like robot of the ROBEA-ANGUILLE project [17].

study was based on the analysis of eel swimming and resulted in the realization of a prototype with 12 vertebrae (Fig. 1.10(a)), skin and a head with two fins. The main purpose of this project was to enhance biomimetics by producing a prototype eel-like robot that was "more continuous" than its existing counterparts. The vertebrae have three rotational degrees of freedom (focal lengths of 18 cm and 13 cm, height of 15 cm), a rigid head and a passive and flexible tail. The head is equipped with side wings mimicking the pectoral fins used to control roll and pitch. In this robot, a parallel architecture, with spherical wrist, was chosen. The body of the robot was constructed by mounting the vertebrae in series. Each section consists of the actuators, an on-board computer and power supply. The skin of the robot was made with tree types of material: plastic rings for reinforcements, chains of rubber to ensure continuity in curvature, and a latex skin to seal between the fluid and the eel-like robot and provide lift. Additionally, in order to achieve the deformation of the body of the eel, each joint is powered by three motors located in adjacent vertebrae. The motors are distributed over the whole length of the eel. The head of the eel-like robot houses several sensors (tilt sensor, accelerometers, a measure of relative speed, camera, etc.), and a computer to manage sensors, communication with the operator and which acts as the supervisor of the whole robot. In addition the head is equipped with two fins to ensure stability. Initial results validated the watertightness of the skin and showed that the prototype is very dependent on the differential of the pressure between the inside and the outside parts of the robot [17].

A new biorobotic platform inspired by the lamprey is developed in project Lampetra [124]. The overall objective of the European Research Project Lampetra was to develop lamprey/salamander bioinspired robots, which design, fabrication and implemented control are all based on biomechanical and neuroscientific findings on the eel-like fish (Fig. 1.11). The overall structure of the robot is shown in Fig. 1.11(a). The robot consist of 21 segments with the total length 99 cm and it has a muscle-like actuation system based on the use of direct magnet interaction. The

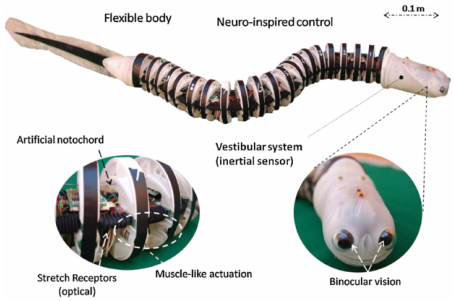

(a) Overall architecture of the robot

(b) Swimming in water

Figure 1.11: The underwater snake robot developed at the European research project Lampetra [124].

(a) Moving on ground

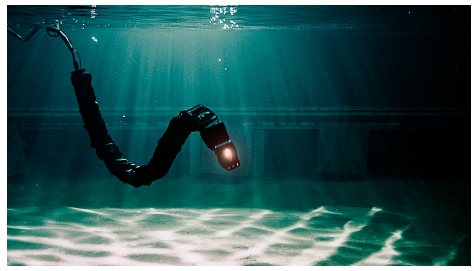

(b) Swimming in water

Figure 1.12: The underwater snake robot Mamba developed at NTNU [102].

control system of the robot is based in CPG locomotion, while the head of the robot contains a binocular vision system that can be used for object tracking or obstacle avoidance purposes. An artificial skin covers the robot making it waterproof and compliant. At the last segment of the robot a multi-layer fibreglass tail is attached in order to ensure a good fluid dynamic behaviour and propulsion at the robotic platform [124].

The underwater snake robot Mamba (Fig. 1.12) is built at NTNU in Norway. The robot is waterproof and consists of different types of modules that can be interconnected in arbitrary configurations (cf. [102]). Mamba is a mechanically robust and easily reconfigurable experimental platform developed to support the ongoing research on ground and underwater snake robot locomotion at the snake robotics group at NTNU.

Remark 1.2: *The underwater snake robot Mamba will be used in order to obtain the experimental results presented in this thesis.*

1.3.3 Control of Underwater Snake Robots

Many challenges on control design need to be addressed, in order to incorporate the resulting control strategies on underwater snake robots and make them operational at all. Several control approaches for underwater snake robots have been proposed in the literature. However, the emphasis so far has mainly been on achieving forward and turning locomotion [104, 120]. The next step would be not only to achieve forward locomotion, but also to make the snake robot follow a desired path, i.e. solving the path following control problem. The works of [106, 130] and [110] synthesize gaits for translational and rotational motion of various fish-like mechanisms and propose controllers for tracking straight and curved trajectories. The work of [27] studies the evolution from fish to amphibian by use of central pattern generators (CPG). Eel-like motion is considered in [106] and [107], where controllers for tracking straight and curved trajectories are proposed.

Motion planning, i.e. designing a path covering a certain area or moving the robot towards a desired location-goal taking into account energy consumption [38], is a challenging task for underwater snake robot locomotion. One important feature of motion planning is obstacle avoidance. Algorithms for obstacle avoidance for robots appeared as early as mid-1980s [24, 92]. [13] proposes the use of vector field histograms to steer the robot towards the direction of low obstacle density areas. In [84], the idea for potentials creation from obstacles that repel the robot and potentials from the target that attracts it, is presented. [118] presents a solution for collision and obstacle free formation flight and reconfiguration of groups of autonomous helicopters. Artificial Potential Fields (APF) have since been utilised in various applications as they offer a fast and simple method for obstacle avoidance [54]. Also, this method is used by [119] in the case of a fish robot. Moreover, a waypoint guidance strategy, where the waypoints are defined a priori, is proposed for a Carangiform swimmer in [49].

In [7], results of a feedback control scheme for 3D movement of the robot continuous model in [15] are presented. The stabilization of the rolling angle is achieved with two pectoral fins that are attached to the head of the robot. In [35], motion control of a three-dimensional eel-like robot without pectoral fins is presented. This controller enables the tracking of a desired 3D position of the eel head as well as the stabilization of the rolling angle without pectoral fins. A multi-variable constrained feedback control scheme is proposed in [34] based on a reduced model of an eel robot. [90] presents a solution for path following of eel-like robots where a type of autonomous gait generation is developed by explicitly controlling the local system curvature. The proposed path following controller is inspired by a control method for marine vehicles and the heading control is combined with the *virtual target* principle. Experimental validation of open-loop motion planning for eel-like robots is presented in [104, 106, 120]. In addition, [106] presents closed-loop experiments for straight-line tracking and disturbance rejection in the plane, using image-based position feedback. These preliminary closed-loop experiments with eel-like robot proved the concept, but were not satisfactory for closed-loop control, as mentioned by the authors [106]. Note that all these previous approaches for path following control are based on dynamic models of the swimming robots where ocean current effects are neglected.

Biological swimming animals as well as underwater swimming robots operate under the influence of highly nonlinear hydrodynamic effects, e.g. turbulent fluid, current and wave effects [88]. The key to successfully manoeuvring under complex hydrodynamic effects for aquatic animals lies in the ability to sense, process and react to environmental disturbances. Fish and aquatic organisms may actively orient either positively (upstream/positive rheotaxis) to minimize the drag or negatively (downstream/negative rheotaxis) to water flows [10]. Rheotaxis, i.e. orientation to currents, is a robust, multisensory behavior found in many aquatic organisms. Biological fish have a lateral line sensing organ in order to detect movement and vibration in the surrounding water, providing spatial awareness and the ability to navigate in space [10]. Biological studies of aquatic animals show that the lateral line is important in many behaviors, including rheotaxis, prey detection, predator avoidance, station holding, spawning behavior and schooling behavior [60, 88]. Flow sensing is used in [88] to control a fish robot. In particular, a flow-aided path following control strategy for fish robots is presented in [59, 88]. From experimental results, it is shown that the fish robot manages to follow the desired trajectory in the flow by adjusting its flow-relative speed and using the side-slipping effect.

Remark 1.3: *To our best knowledge, previous literature has not presented and experimentally validated a path following control approach that is able to steer an underwater snake robot along a straight line path in the presence of ocean currents of unknown direction and magnitude.*

1.3.4 Energy Efficiency of Underwater Snake Robots

The use of underwater vehicles has rapidly increased the last decades since these systems are able to operate in deep and high risk areas which humans cannot reach. Nowadays, autonomous underwater vehicles (AUVs) and remotely operated vehicles (ROVs) are widely used in the subsea environment for different challenging tasks [38]. These vehicles are suitable for various work assignments such as inspection, surveillance, maintenance, repairing equipment, building structures, and data collection, and they are extensively used in the subsea oil and gas industry and by the science community. For the long term autonomy of these systems, energy efficiency is one of the main challenges.

An interesting control problem concerns the ability to achieve efficient motion with preferably a minimum amount of consumed energy in order to be able to undertake longer missions. Hence, for the long term autonomy of underwater vehicles, energy efficiency is one of the main challenges. Few solutions in this direction are proposed in the literature. In [89], a genetic algorithm (GA) is applied to a three link swimmer in order to optimize the swimming gait. Furthermore, a notable study regarding the optimization of swimming gaits is performed in [79], where optimized patterns of anguilliform swimming are investigated using 3D simulations. In particular, a custom evolutionary optimization algorithm combined with a three-dimensional numerical solution is obtained for the swimmer. By using Navier-Stokes equations an optimization problem with two distinct optimization objectives, efficiency and velocity, is solved. Note that the computational cost of solving the Navier-Stokes equations of their model restricts the results to only one

optimization run for each fitness goal. In [135], optimization is used to generate efficient hyper-redundant mechanism swimming gaits. In particular, they investigated how the energy recovery influence the efficiency of the robot by optimizing the economy cost for multiple swimming velocities. Consequently, as also mentioned in [135], derivative free and stochastic methods are an appropriate choice for the motion optimization. Derivative free algorithms are adopted from researchers in the fields of swimming robots to investigate the efficiency of undulatory locomotion.

Remark 1.4: *Note that the efficiency of underwater swimming robots remains an open question and many aspects should be investigated to realize operational snake robots for underwater applications. For instance the relationships between the gait parameters, the consumed energy and the forward velocity for the different motion patterns for underwater snake robots should be investigated through simulation and experimental studies. In addition, it is essential to find a method for maximizing the achieved forward velocity of the robot and minimizing the corresponding average power consumption of underwater snake robots. To our best knowledge, investigation of efficient motion patterns by solving a multi-objective optimization problem has not been considered in previous literature. Furthermore, as fas as we know experimental investigation of the power consumption of underwater snake robots has not been addressed in previous literature.*

1.4 Scope of the Thesis

In the following subsections, we describe the general scope of the research carried out in this thesis.

1.4.1 Analytical Closed-form Approach

This thesis is mainly motivated by the attribute of the snake robots that they are able to move over land as well underwater while the physiology of the robot remains the same. This adaptability to different motion demands depending on the environment is one of the main characteristics of the snake robots. Even though several results have been reported in the related fields of design, modeling and control of underwater robots that that are inspired by fish locomotion, there are several interesting aspects regarding the modeling, control and energy efficiency of the underwater snake robots that have not been investigated yet. Research presented in the previous literature is based on either simplified models of hydrodynamic effects or employ numerical evaluations of the drag effects which results in a lack of an analytical closed-form solution for the dynamic model of underwater snake robots. To this end, in this thesis, we address the problem of modeling the hydrodynamic effects with an analytical perspective and a primary objective to conclude in a closed-form solution for the dynamic model of an underwater snake robot. The objective is that this analytical approach will eventually contribute to further improving our understanding of underwater snake robot locomotion since it is well-suited for control design and stability analysis purposes.

1.4.2 Locomotion of Underwater Snake Robots in 2D plane

This thesis presents results for locomotion of underwater snake robots in both a horizontal and a vertical plane. Even though the locomotion of underwater snake robots is purely three-dimensional, the fundamental properties of locomotion can be captured during the modeling and analysis of 2D motion of these systems. To this end, the thesis considers modeling and locomotion of fully immersed underwater snake robots which are constrained to swim in any 2D plane of 3D. These initial studies, will provide interesting inputs regarding the essential principles of locomotion control of biologically inspired swimming robots. Furthermore, the locomotion of an underwater snake moving in three-dimensional space can be realized by a combination of horizontal and vertical waves propagating from head to tail of the robot. Therefore, we can assume that the outcomes from the analysis and the control design approaches investigated in 2D can be extended to be applicable for motion in three-dimensional space. Furthermore, it is better to get familiar with simpler problems regarding the motion of swimming robots with highly nonlinear and complex models before we address more complicated problems. Consequently, in the research reported in this thesis, at first, we decided to fully understand the fundamental principles of locomotion of underwater snake robots in 2D space before we target solutions in the three-dimensional space.

1.4.3 Control Strategies Compensating the Current Effects

As already stated, one of the objectives of this thesis is to contribute to the development of control strategies for underwater snake robots locomotion. Generally, control design for underwater snake robots is challenging mainly because these mechanisms are underactuated and because the model of the hydrodynamic effects is highly nonlinear. In this thesis, based on the derived model of the underwater snake robot locomotion, we propose straight line path following control strategies that are able to steer the robot towards and along the desired path. In addition, we investigate the ability of an underwater snake robot to follow a path compensating the environmental disturbances. In particular, we propose solutions to path following control problem enabling the robot to track a straight path in both the absence and presence of ocean currents. The proposed control approaches are both verified through simulations and through experiments with a physical underwater snake robot.

1.4.4 Motion based on General Sinusoidal Motion Pattern

The mathematical expression for the gait of the snake robot in locomotion studies depends on its construction and model. Previous studies on swimming snake robots have focused on two motion patterns: lateral undulation and eel-like motion. In this thesis, both the motion analysis and control strategies are conducted based on a general sinusoidal motion pattern which can be used for a broad class of motion patterns including lateral undulation and eel-like motion. Therefore, the motion analysis results and the control approaches proposed in this thesis are general

because they are based on a more general sinusoidal motion pattern than what has been analysed in previous literature.

1.4.5 Energy Efficiency

As we have already mention, an important control problem for underwater snake robots locomotion concerns the ability to achieve efficient motion with preferably a minimum amount of consumed energy, in order to be able to undertake longer missions. To this end, this thesis targets also this really interesting problem for underwater snake robots. We believe that the results regarding energy efficiency of underwater snake robots will give interesting inputs, in order to realize operational snake robots for underwater applications in the future.

1.5 Contributions of the Thesis

The title of this thesis *Modeling, Control and Energy Efficiency of Underwater Snake Robots* describes the results presented in the following chapters in this dissertation. As the title describes, the first part of the thesis targets the modeling of underwater snake robots, while the second part contributes to the path following control problem for biologically inspired swimming snake robots. Finally, the last part addresses the energy efficiency of underwater robots by investigating the different gait patterns for underwater snake robots. In the following, the topic and the contributions of each chapter are presented.

Chapter 2

Topic: We present two mathematical models of the kinematics and dynamics of underwater snake robots swimming in virtual horizontal and vertical planes aimed at control design. The proposed models are derived in a closed-form and can be utilized in modern model-based control schemes.

Contributions: The main contribution of this chapter is a modeling approach for underwater snake robots that results in a closed-form solution, avoiding the numerical evaluation of drag effects. In particular, in this chapter we present models of the kinematics and dynamics of planar underwater snake robots aimed at control design. The proposed hydrodynamic model considers both the linear and nonlinear drag forces (resistive fluid forces), the added mass effect (reactive fluid forces), the fluid moments and current effect. Fluid contact forces and torques are modeled using analytical fluid dynamics. To our best knowledge, this model is the first modeling approach that takes into account both the current effect and the combination of linear and nonlinear drag effect. Furthermore, the ground snake robot model [101] falls out as a special case of the developed snake robot model, by replacing the fluid friction model with the ground friction model and setting the fluid parameters to zero. The presented model is thus an extension of the land based snake robot model, and comprises snake robots moving both on land and in water. In addition to providing completeness, this also makes the model applicable for

unified control methods for amphibious snake robots moving both on land and in water.

Another contribution of this chapter is modeling of underwater snake robots moving in the vertical plane that also results in a closed-form solution. This model considers hydrodynamic and hydrostatic forces (gravitational and buoyancy forces) and torques and avoids the numerical evaluation of drag effects. To our best knowledge, this modeling approach is the first one that combines the hydrodynamic effects, in analytical-closed-form with the hydrostatic forces. It is important to notice that this model provides a complete closed-form solution, which makes it possible to apply advanced control methods for underwater snake robots. Furthermore, the proposed model is valid for a neutrally buoyant underwater snake robot, moving in any tilted virtual 2D plane of 3D. Hence, the model of an underwater snake robot moving in the horizontal plane is a special case of the developed underwater snake robot model, achieved by setting the hydrostatic forces to zero. The presented model is thus an extension of the underwater snake robot model moving in a virtual horizontal plane, and comprises underwater snake robots moving both in horizontal and vertical planes.

Chapter 3

Topic: We conduct an extensive analysis of the model of a fully immersed underwater snake robot moving in a virtual horizontal plane. Based on this analysis, we derive a set of essential properties that characterize the overall motion of underwater snake robots.

Contributions: The first contribution of this chapter is a general sinusoidal motion pattern which is introduced, and can be used to describe a broad class of motion patterns for underwater snake robot locomotion including lateral undulation and eel-like motion. The second contribution of the chapter is to develop fundamental properties of underwater snake robot locomotion. It is well-known that the hydrodynamic forces (fluid forces) induced by the motion of a rigid body in an underwater environment are very complex and highly nonlinear. Therefore, in this chapter we are conducting an extensive analysis of the complex model of a fully immersed underwater snake robot moving in a virtual horizontal plane, and from this analysis a set of essential properties that characterize the overall motion of underwater snake robots is derived. Based on this analysis the hydrodynamic effects which are essential for the overall behavior of the swimming snake robot are identified. In addition, propositions regarding the turning motion of an underwater snake robot and the relative displacement of the links during both lateral undulation and eel-like motion patterns are addressed.

Chapter 4

Topic: We present a control-oriented model of an underwater snake robot moving in a virtual horizontal plane that is well-suited for control design and stability analysis.

Contributions: The main contribution of this chapter is a control-oriented model of an underwater snake robot moving in a virtual horizontal plane. The idea behind the control-oriented model of underwater snake robot locomotion is based on the simplified modeling approach presented for ground snake robots [101]. In particular, the idea is to describe the body shape changes of an underwater snake robot as linear displacements of the links with respect to each other instead of rotational displacements. The proposed model is notably less complex than the existing models, while significant parameters such as added mass effects, linear drag forces, torques due to the added mass and linear drag forces, are all taken into account in the modeling. Hence, this model is well-suited for control design and stability analysis purposes, and at the same time has the same essential properties as the complex model.

Chapter 5

Topic: We use the averaging theory to reveal new fundamental properties of underwater snake robot locomotion that are useful from a motion planning perspective.

Contributions: The fist contribution of this chapter is an averaged model of the velocity dynamics of an underwater snake robot following general sinusoidal motion gait patterns, which is well-suited for stability analysis and motion planning purposes. Averaging theory is applied in order to derive a model of the average velocity for a control-oriented model of an underwater snake robot that is influenced by added mass effects (reactive fluid forces) and linear drag forces (resistive fluid forces). A similar study was presented in [97] for ground robots. The results in this chapter extend this by taking into account the hydrodynamic effects that underwater snake robots experience, i.e. the reactive and resistive fluid forces, including added mass and drag forces. The results in this chapter thus extend [97] to amphibious snake robots and general sinusoidal motion patterns, and the results in [97] fall out as a special case when the motion pattern is lateral undulation and when the drag forces are replaced by viscous friction forces. Hence, this model can be used for stability analysis and control design for a broad class of motion patterns including lateral undulation and eel-like motion.

As a second contribution, based on the model presented in Chapter 4, we show that the average velocity of an underwater snake robot following sinusoidal motion gait patterns converges exponentially to a steady-state velocity, while an explicit analytical relation is given between the steady state velocity and the amplitude, the frequency, the phase shift and the offset of the joint motion. Note that previous studies for ground snake robots [97, 101] and eel-like robots, where the added mass effects and fluid torques are neglected [106], show that the average forward velocity of the robot during lateral undulation is: 1) proportional to the square of the amplitude of the sinusoidal motion pattern, 2) proportional to the gait frequency and 3) depends also on the weighted sum of the constant phase shift between the joints. In this chapter, we show that the average forward velocity of an underwater snake robot,

influenced both by added mass and linear drag effects, and under any sinusoidal gait pattern, is: 1) a function of the amplitude of the sinusoidal motion pattern, 2) depends on a linear and a nonlinear term of the gait frequency and 3) depends on the phase shift between the joints. The results of this paper are thus more general and constitute a powerful tool for achieving faster forward motion by selecting the most appropriate motion pattern and the best combination of the gait parameters. Furthermore, the derived relationship for the averaged velocity dynamics can be used to select the most appropriate motion pattern to achieve the desired velocity requirements, while also taking into account the power consumption requirements. Results in this direction will be shown in Chapter 7.

Another contribution of this chapter is the experimental investigation of a set of fundamental properties of the velocity dynamics of an underwater snake robot that are essential for motion planning purposes and the efficiency of these systems. Initially, we present simulation results to investigate the validity of these properties for both the complex model presented in Chapter 2 and the control-oriented model presented in Chapter 4. The simulation results show that the derived properties, which are based on a control-oriented model of the underwater snake robot hold also for the complex model where complex hydrodynamic effects are considered. Subsequently, we present experimental results using a physical underwater snake robot, Mamba, and we show that the experimental results support the derived properties of the velocity dynamics. Both the simulation and experimental results are obtained for the two most common swimming patterns for underwater snake robot locomotion: lateral undulation and eel-like motion patterns. To the authors' best knowledge, an experimental investigation of efficient motion patterns by investigating the relationship between the gait parameters and the forward velocity has not been considered in previous literature.

Chapter 6

Topic: We propose and experimentally validate solutions to the path following control problem for biologically inspired swimming snake robots. We present line-of-sight (LOS) and integral line-of-sight (I-LOS) guidance laws, which are combined with a sinusoidal gait pattern and a directional controller that steers the robot towards and along the desired path.

Contributions: The first and the main contribution of this chapter is the straight line path following control strategies for underwater snake robots. We have proposed two approaches for the path following problem of underwater snake robots. Initially, we present a LOS guidance law which is applied to underwater snake robots to achieve straight line path following both for lateral undulation and eel-like motion patterns. Secondly, we propose a controller that is able to compensate for the ocean current effects in the absence of sensing the surrounding flow effects. In particular, we propose an I-LOS path following controller for steering an underwater snake robot along a straight line path in the presence of ocean currents of unknown direction and mag-

nitude. The integral LOS guidance strategy is widely used for directional control of marine surface vessels for ocean current compensation but has not been employed previously for directional control of underwater snake robots in the presence of ocean currents. The second contribution of this chapter is comparative studies between the experimental results and the corresponding simulation results for the path following control of underwater snake robots. In particular, the efficacy of the LOS and the I-LOS path following control strategies are investigated through experiments with the underwater snake robot Mamba. The experimental results show that the integral LOS guidance law can be applied to underwater snake robots to compensate for the ocean drift effects, including the current effects, and achieve path following of straight lines. As fas as we know, experimental results for path following control of underwater snake robots compensating for the current effects have not been investigated in previous literature.

To our best knowledge, stability of the locomotion of an underwater snake robot along a straight line path in the presence of ocean currents has never been studied before. In this chapter, we analyse the stability using Poincaré maps, and this is considered as a contribution of this chapter. Another contribution of this chapter is the experimental validation of a complex fluid model, which allow an accurate back-to-back comparison of real experimental and simulated data, by giving us the opportunity to obtain a qualitative and quantitative comparison between the motion of the simulated and the physical snake robot. The last contribution of this chapter is the combined use of an artificial potential fields-based path planner with a new waypoint guidance strategy for steering an underwater snake robot along a path defined by waypoints interconnected by straight lines. The waypoints are derived by using a path planner based on the artificial potential field method in order to also address the obstacle avoidance problems.

Chapter 7

Topic: We consider the energy efficiency of underwater snake robots. In particular, we investigate the relationship between the parameters of the gait patterns, the forward velocity and the energy consumption for the different motion patterns for underwater snake robots.

Contributions: The first contribution of this chapter is the investigation of the issues that influence the performance of underwater snake robots, both when it comes to the achieved forward velocity and the energy efficiency. We present in this chapter simulation results in order to investigate the relationships between the parameters of the gait patterns, the consumed energy and the forward velocity. We initially present simulation result by investigating the power consumption of different motion patterns for underwater snake robots. Based on the results of this investigation, we present empirical rules to choose the values for the parameters of the motion gait pattern of underwater snake robots.

The second contribution of this chapter is the investigation of the power

consumption of different underwater robotic systems and pointing out the most efficient vehicle depending on the desired motion. In particular, we present simulation results in order to compare the power consumption of swimming snake robots with that of today's benchmark solution for subsea inspection, maintenance and repair, which are ROVs, and comparison results are thus obtained for the power consumption of underwater snake robots and ROVs. Comparison results are obtained for the total energy consumption and the cost of transportation of underwater snake robots and ROVs. To our best knowledge, a comparison of the consumed energy between underwater swimming snake robots and remotely operated vehicles have not been investigated in previous literature.

The third contribution of this chapter is the experimental investigation of properties regarding the relationship between the gait parameters and the power consumption for underwater snake robots. In particular, this chapter investigates the validity of the properties through experiments using the underwater snake robot Mamba. The experimental results support the derived properties regarding the relationship between the gait parameters and the power consumption both for lateral undulation and eel-like motion patterns. To our knowledge, no research has been published investigating experimentally the power consumption of underwater snake robots.

Finally, in this chapter a multi-objective optimization problem is developed with the aim of maximizing the achieved forward velocity of the robot and minimizing the corresponding average power consumption of the system. As far as we know, investigation of efficient motion patterns by solving a multi-objective optimization problem has not been considered in previous literature. We therefore also consider the methodology of this chapter to be a contribution within the underwater snake robot literature. In particular, results are obtained for the two most common swimming patterns for underwater snake robot locomotion: the lateral undulation and eel-like motion patterns. Furthermore, the proposed optimization framework is applied to obtain the parameters giving the most efficient motion pattern, which can be used in the future for control and design of underwater snake robots.

Chapter 2

Modeling of Underwater Snake Robot Locomotion

As it is already noted in the Introduction, an accurate dynamic model for underwater snake robots is important both for controller design and efficient locomotion methods. In this chapter, we develop two mathematical models of the kinematics and dynamics of underwater snake robots swimming in a virtual horizontal and a vertical plane, respectively. The proposed models are derived in a closed-form and can be utilized in modern model-based control schemes. The links of the robot are influenced by hydrodynamic and hydrostatic forces. It is well-known that the hydrodynamic forces (fluid forces) induced by the motion of a rigid body in an underwater environment are very complex and highly nonlinear and therefore several of these effects are often not taken into account when modeling the system in previous works. Generally the modeling for control design purposes poses different challenges than hydrodynamic modeling for simulations. In this chapter, the fluid contact forces (hydrodynamic forces) and torques (fluid moments) are modeled using analytical fluid dynamics. Hydrodynamic forces and torques, i.e. linear and nonlinear drag forces, current effects, added mass and fluid torque effects, are considered. In addition, the developed model for an underwater snake robot swimming in a vertical plane also takes into account the hydrostatic forces (gravitational forces and buoyancy). The proposed models are easily implemented and simulated, regardless of the number of robot links. Note that although the proposed hydrodynamic model considers only the significant hydrodynamic effects well-suited for analytical analysis, due to the many degrees of freedom of the robot and dynamic coupling between the links, we will refer to the models developed in this chapter as the complex model of the underwater snake robot, when comparing it to the control-oriented model that is to be developed in Chapter 4.

In Chapter 3, the complex model will be analyzed in order to deduce several fundamental properties of underwater snake robot dynamics. Some of the derived properties will be used for the development of a control-oriented model of the underwater snake robot in Chapter 4. In Chapter 4, we develop a model that captures only the essential part of the dynamics of the complex model.

Contributions of this Chapter: The main contribution of this chapter is to de-

rive the equations of motion of an underwater snake robot that results in a closed-form solution, avoiding the numerical evaluation of drag effects. In particular, in this chapter we present models of the kinematics and dynamics of planar underwater snake robots aimed at control design. It is a main advantage that the hydrodynamic modeling concludes in a closed-form, without the need of an algorithmic way to compute the drag force and torque and thus it is well-suited for model-based control design of underwater snake robots locomotion. The developed hydrodynamic model considers both the linear and nonlinear drag forces (resistive fluid forces), the added mass effect (reactive fluid forces), the fluid moments and current effect. Fluid contact forces and torques are modeled using analytical fluid dynamics. Eventually, the model is derived in a closed-form and can be utilized in modern model-based control schemes. To our best knowledge, this model is the first modeling approach that takes into account both the current effect and the combination of the linear and nonlinear drag effect. In addition, the ground snake robot model [101] falls out as a special case of the developed snake robot model, by replacing the fluid friction model with the ground friction model and setting the fluid parameters to zero. The presented model is thus an extension of the land based snake robot model [101], and comprises snake robots moving both on land and in water. In addition, this also makes the model applicable for unified control methods for amphibious snake robots moving both on land and in water.

Another contribution of this chapter is a model of underwater snake robots moving in the vertical plane that also results in a closed-form solution. This model considers hydrodynamic and hydrostatic forces (gravitational and buoyancy forces) and torques and avoids the numerical evaluation of drag effects. To our best knowledge, this modeling approach is the first one that combines the hydrodynamic effects (i.e the current effect, the combination of linear and nonlinear drag effect), in analytical-closed-form with the hydrostatic forces. It is important to notice that this model provides a complete closed-form solution, which makes it possible to apply advanced control methods for underwater snake robots. This model can be used by biologists to study creatures, such as leeches that swim by undulating the body like eels or snakes, except that the body oscillation occurs in a vertical (rather than horizontal) plane [22]. Note that this model is valid for a neutrally buoyant underwater snake robot, moving in any tilted virtual 2D plane of 3D. Hence, an underwater snake robot model moving in the horizontal plane is a special case of the developed underwater snake robot model, achieved by setting the hydrostatic forces to zero. The presented model is thus an extension of the underwater snake robot model moving in a virtual horizontal plane, and comprises underwater snake robots moving both in horizontal and vertical planes.

Organization of this Chapter: This chapter is organized as follows. In Section 2.1, we introduce some basic notations, matrices and vectors that will be used throughout the thesis. In Section 2.2, we derive a model of an underwater snake robot swimming in a virtual horizontal plane, explaining in detail

the hydrodynamic effects. The dynamic model of an underwater snake robot swimming in a virtual vertical plane considering both the hydrodynamic and the hydrostatic effects is presented in Section 2.3. Finally, the chapter is summarized in Section 2.4.

Publications: The material in this chapter is based on the journal papers [64], [73], [72] and the conference papers [65], [69] and [70].

2.1 Basic Notations

The following vectors and matrices are used in this thesis for the derivation of the kinematics and dynamics of the underwater snake robot.

$$\mathbf{A} = \begin{bmatrix} 1 & 1 & & \\ & \ddots & \ddots & \\ & & 1 & 1 \end{bmatrix}, \mathbf{D} = \begin{bmatrix} 1 & -1 & & \\ & \ddots & \ddots & \\ & & 1 & -1 \end{bmatrix},$$

$$\mathbf{e} = \begin{bmatrix} 1 & \cdots & 1 \end{bmatrix}^T \in \mathbb{R}^n, \mathbf{E} = \begin{bmatrix} \mathbf{e} & \mathbf{0}_{n\times 1} \\ \mathbf{0}_{n\times 1} & \mathbf{e} \end{bmatrix} \in \mathbb{R}^{2n\times 2},$$

$$\begin{aligned} \sin\boldsymbol{\theta} &= \begin{bmatrix} \sin\theta_1 & \cdots & \sin\theta_n \end{bmatrix}^T \in \mathbb{R}^n, \mathbf{S}_\theta = \operatorname{diag}(\sin\boldsymbol{\theta}) \in \mathbb{R}^{n\times n}, \\ \cos\boldsymbol{\theta} &= \begin{bmatrix} \cos\theta_1 & \cdots & \cos\theta_n \end{bmatrix}^T \in \mathbb{R}^n, \mathbf{C}_\theta = \operatorname{diag}(\cos\boldsymbol{\theta}) \in \mathbb{R}^{n\times n}, \\ \operatorname{sgn}\boldsymbol{\theta} &= \begin{bmatrix} \operatorname{sgn}\theta_1 & \cdots & \operatorname{sgn}\theta_n \end{bmatrix}^T \in \mathbb{R}^n, \\ \dot{\boldsymbol{\theta}}^2 &= \begin{bmatrix} \dot{\theta}_1^{\,2} & \cdots & \dot{\theta}_n^{\,2} \end{bmatrix}^T \in \mathbb{R}^n, \mathbf{J} = J\mathbf{I}_n, \mathbf{L} = l\mathbf{I}_n, \mathbf{M} = m\mathbf{I}_n, \end{aligned}$$

$$\mathbf{K} = \mathbf{A}^T\left(\mathbf{D}\mathbf{D}^T\right)^{-1}\mathbf{D}, \mathbf{V} = \mathbf{A}^T\left(\mathbf{D}\mathbf{D}^T\right)^{-1}\mathbf{A}.$$

The matrices $\mathbf{A} \in \mathbb{R}^{(n-1)\times n}$ and $\mathbf{D} \in \mathbb{R}^{(n-1)\times n}$ represent, respectively, an addition and a difference matrix, which will be used for adding and subtracting pairs of adjacent elements of a vector. Furthermore, the vector $\mathbf{e}$ represents a summation vector, which will be used for adding all elements of a n-dimensional vector.

In this thesis, vectors are either expressed in the global coordinate system or in the local link coordinate system of link i. This is indicated by superscript *global* or *link,i*, respectively. If is not specified otherwise, a vector with no superscript is expressed in the global coordinate system.

2.2 Virtual Horizontal Plane

This section presents a continuous model of an underwater snake robot moving in the horizontal plane, i.e. moving at a constant depth as shown in Fig. 2.1. The snake robot is assumed to be neutrally buoyant, such that its depth remains constant unless active depth control (using rotation of the links around the body-fixed y-axis) is utilized. The model is derived with objective being the analysis and the design of motion control for the position and heading of the snake robot in this

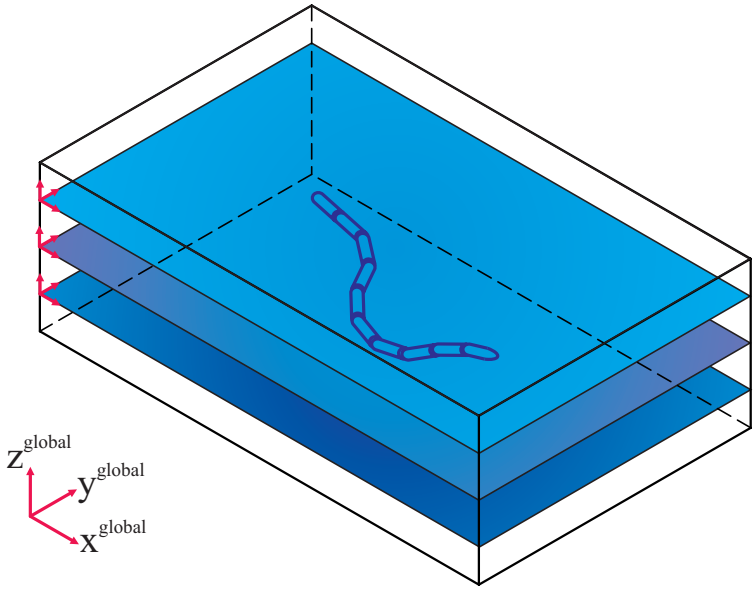

Figure 2.1: Visualization of a ten link underwater snake robot motion in a virtual horizontal plane.

horizontal plane. Following, the kinematics and dynamics of the robot taking into account the hydrodynamic effects will be presented.

2.2.1 The Parameters of the Underwater Snake Robot

The snake robot consists of n rigid links of equal length $2l$ interconnected by $n-1$ joints. The links are assumed to have the same mass m and moment of inertia $J = \frac{1}{3}ml^2$. The mass of each link is uniformly distributed so that the link center of mass (CM) is located at its center point (at length l from the joint at each side). The total mass of the snake robot is therefore nm. In the following subsections, the kinematics and dynamics of the underwater snake robot will be modeled in terms of the mathematical symbols described in Table 2.1 and illustrated in Fig. 2.2 and Fig. 2.3. The coordinates of the center of gravity of ith link and the angle between the link and the x–axis are defined as $p_i = (x_i, y_i)$ and θ_i, respectively.

2.2.2 The Kinematics of the Underwater Snake Robot

The snake robot is assumed to move in a virtual horizontal plane, fully immersed in water, and has $n+2$ degrees of freedom (n link angles and the x-y position of the robot). The *link angle* of each link $i \in \{1, \cdots, n\}$of the snake robot is denoted by $\theta_i \in \mathbb{R}$ and is defined as the angle that the link forms with the global x axis with counterclockwise positive direction, while the *joint angle* of joint $i \in \{1, \cdots, n-1\}$

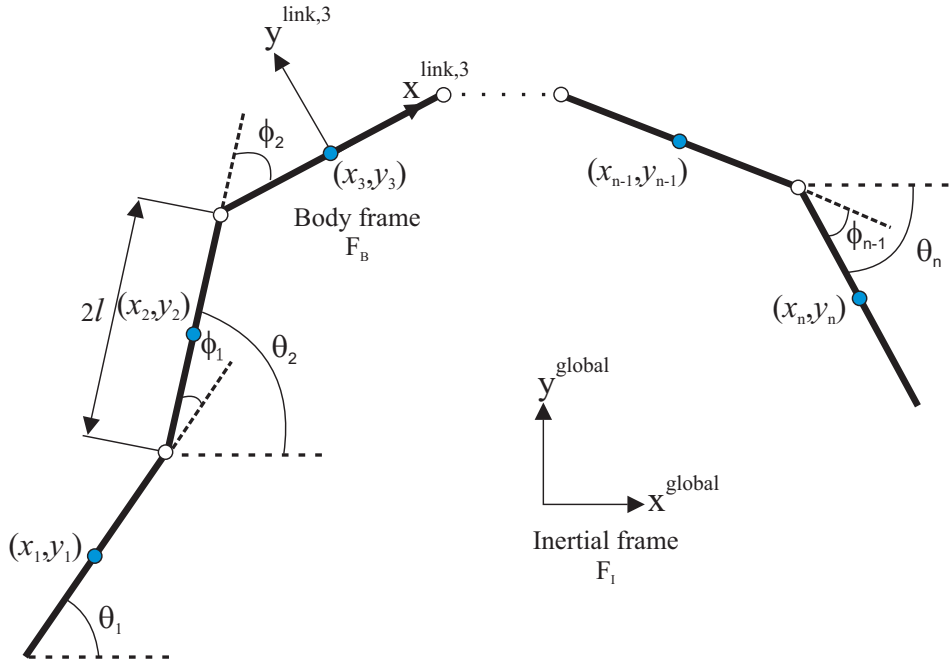

Figure 2.2: Kinematic parameters of the underwater snake robot moving in horizontal plane.

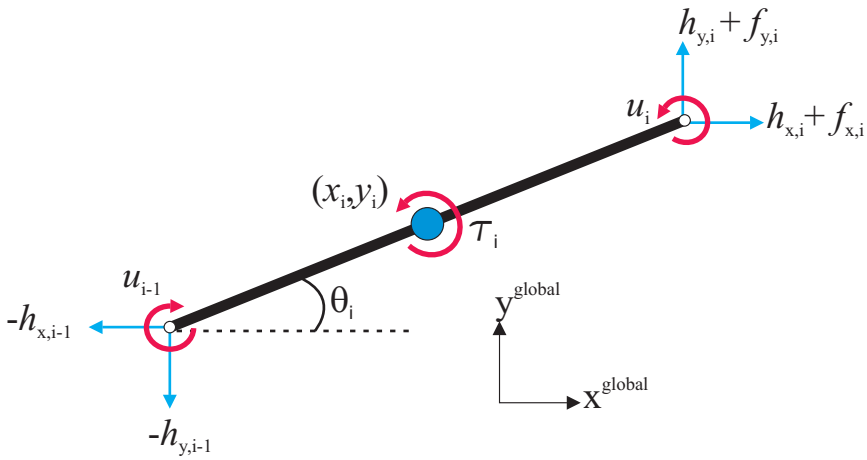

Figure 2.3: Forces and torques acting on each link of the underwater snake robot moving in horizontal plane.

Table 2.1: Definition of mathematical terms for underwater snake robot moving in a virtual horizontal plane.

Symbol	Description	Vector
n	The number of links	
l	The half length of a link	
m	Mass of each link	
J	Moment of inertia of each link	
θ_i	Angle between link i and the global x axis	$\boldsymbol{\theta} \in \mathbb{R}^n$
ϕ_i	Angle of joint i	$\boldsymbol{\phi} \in \mathbb{R}^{n-1}$
(x_i, y_i)	Global coordinates of the CM of link i	$\mathbf{X}, \mathbf{Y} \in \mathbb{R}^n$
(p_x, p_y)	Global coordinates of the CM of the robot	$\mathbf{p}_{\text{CM}} \in \mathbb{R}^2$
u_i	Actuator torque of joint between link i and link $i+1$	$\mathbf{u} \in \mathbb{R}^{n-1}$
u_{i-1}	Actuator torque of joint between link i and link $i-1$	$\mathbf{u} \in \mathbb{R}^{n-1}$
$f_{x,i}$	Fluid force on link i in x direction	$\mathbf{f}_{\mathbf{x}} \in \mathbb{R}^n$
$f_{y,i}$	Fluid force on link i in y direction	$\mathbf{f}_{\mathbf{y}} \in \mathbb{R}^n$
τ_i	Fluid torque on link i	$\boldsymbol{\tau} \in \mathbb{R}^n$
$h_{x,i}$	Joint constraint force in x direction on link i from link $i+1$	$\mathbf{h}_{\mathbf{x}} \in \mathbb{R}^{n-1}$
$h_{y,i}$	Joint constraint force in y direction on link i from link $i+1$	$\mathbf{h}_{\mathbf{y}} \in \mathbb{R}^{n-1}$
$h_{x,i-1}$	Joint constraint force in x direction on link i from link $i-1$	$\mathbf{h}_{\mathbf{x}} \in \mathbb{R}^{n-1}$
$h_{y,i-1}$	Joint constraint force in y direction on link i from link $i-1$	$\mathbf{h}_{\mathbf{y}} \in \mathbb{R}^{n-1}$

is denoted by $\phi_i \in \mathbb{R}$ and defined as

$$\phi_i = \theta_i - \theta_{i-1}. \tag{2.1}$$

The link angles and the joint angles are assembled in the vectors $\boldsymbol{\theta} = [\theta_1, \cdots, \theta_n]^T \in \mathbb{R}^n$ and $\boldsymbol{\phi} = [\phi_1, \cdots, \phi_{n-1}]^T \in \mathbb{R}^{n-1}$, respectively.

The *heading* (or *orientation*) $\bar{\theta} \in \mathbb{R}$ of the snake is defined as the average of the link angles similar as for land-based snake robots in [101]

$$\bar{\theta} = \frac{1}{n} \sum_{i=1}^{n} \theta_i. \tag{2.2}$$

The model of the snake robot will be derived using link angles to simplify the mathematical expressions. The local coordinate system of each link is fixed in the CM of the link with x (tangential) and y (normal) axes oriented such that they are aligned with the global x and y axis, respectively, when all the link angles are zero. The rotation matrix from the global frame to the frame of link i is

$$\mathbf{R}_{\text{link},i}^{\text{global}} = \begin{bmatrix} \cos\theta_i & -\sin\theta_i \\ \sin\theta_i & \cos\theta_i \end{bmatrix}. \tag{2.3}$$

The global frame position $\mathbf{p}_{\text{CM}} \in \mathbb{R}^2$ of the center of mass (CM) of the robot is given by

$$\mathbf{p}_{\text{CM}} = \begin{bmatrix} p_x \\ p_y \end{bmatrix} = \begin{bmatrix} \frac{1}{nm}\sum_{i=1}^{n} mx_i \\ \frac{1}{nm}\sum_{i=1}^{n} my_i \end{bmatrix} = \frac{1}{n}\begin{bmatrix} \mathbf{e}^T\mathbf{X} \\ \mathbf{e}^T\mathbf{Y} \end{bmatrix}, \tag{2.4}$$

where (x_i, y_i) are the global frame coordinates of the CM of link i, $\mathbf{X}= [x_1, \cdots, x_n]^T \in \mathbb{R}^n$ and $\mathbf{Y}= [y_1, \cdots, y_n]^T \in \mathbb{R}^n$.

The forward velocity of the robot is denoted by $\bar{v}_t \in \mathbb{R}$ and is defined as the component of the CM velocity along the current heading of the snake, i.e.

$$\bar{v}_t = \dot{p}_x \cos\bar{\theta} + \dot{p}_y \sin\bar{\theta}. \tag{2.5}$$

The links are constrained by the joints according to

$$\begin{aligned} \mathbf{DX} + l\mathbf{A}\cos\boldsymbol{\theta} &= \mathbf{0}, \\ \mathbf{DY} + l\mathbf{A}\sin\boldsymbol{\theta} &= \mathbf{0}. \end{aligned} \tag{2.6}$$

The position of the individual links as a function of the CM position and the link angles of the robot can be expressed as

$$\mathbf{X} = -l\mathbf{K}^T\cos\boldsymbol{\theta} + \mathbf{e}p_x, \tag{2.7}$$

$$\mathbf{Y} = -l\mathbf{K}^T\sin\boldsymbol{\theta} + \mathbf{e}p_y, \tag{2.8}$$

where $\mathbf{K} = \mathbf{A}^T\left(\mathbf{D}\mathbf{D}^T\right)^{-1}\mathbf{D} \in \mathbb{R}^{n\times n}$, with $\mathbf{D}\mathbf{D}^T$ being nonsingular and thereby invertible [101]. The linear velocities of the links are found by differentiating the position of the individual links (2.7) and (2.8) with respect to time, which gives

$$\begin{aligned} \dot{\mathbf{X}} &= l\mathbf{K}^T\mathbf{S}_\theta\dot{\boldsymbol{\theta}} + \mathbf{e}\dot{p}_x, \\ \dot{\mathbf{Y}} &= -l\mathbf{K}^T\mathbf{C}_\theta\dot{\boldsymbol{\theta}} + \mathbf{e}\dot{p}_y. \end{aligned} \tag{2.9}$$

The kinematics of an underwater snake robot is similar to that of a snake robot moving on land. An extensive presentation of the snake robot kinematics can be found in [101]. Additionally, it is necessary to derive the equation of linear accelerations of the links in order to express the fluid forces. The linear accelerations of the links are found by differentiating the velocity of the individual links (2.9) with respect to time, which gives

$$\begin{aligned} \ddot{\mathbf{X}} &= l\mathbf{K}^T\left(\mathbf{C}_\theta\dot{\boldsymbol{\theta}}^2 + \mathbf{S}_\theta\ddot{\boldsymbol{\theta}}\right) + \mathbf{e}\ddot{p}_x, \\ \ddot{\mathbf{Y}} &= l\mathbf{K}^T\left(\mathbf{S}_\theta\dot{\boldsymbol{\theta}}^2 - \mathbf{C}_\theta\ddot{\boldsymbol{\theta}}\right) + \mathbf{e}\ddot{p}_y. \end{aligned} \tag{2.10}$$

2.2.3 The Hydrodynamic Model of Underwater Snake Robot

As we have already mentioned in Introduction, for the swimming robots, the dynamic modeling of the contact forces is more complicated compared to the modeling of the overall rigid motion. Hence, the hydrodynamic modeling task presents a major challenge. The underwater snake robotic system that is the subject of

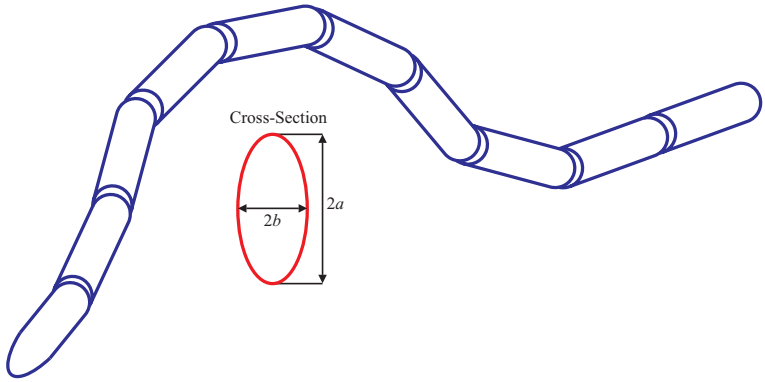

Figure 2.4: Visualization of a ten link underwater snake robot.

this thesis, swims at a Reynolds number of approximately 10^4 to 10^5, thus, both the resistive forces (drag forces) and reactive ones (added mass affects) need to be modeled, since both play a critical role in underwater swimming robotic systems propulsion [135].

The force and moment balance equations require that the fluid terms have to be defined. However, it should be noted that the hydrodynamic forces (fluid forces) induced by the motion of a rigid body in an underwater environment are very complex and highly nonlinear. Consequently, we decided to solve the hydrodynamic modeling problem using an analytical simplified form suited for the design of online control for underwater snake robots. The Navier-Stokes equations are very difficult to solve and quite unsuited for robotics control design purposes. Hence, as far as the fluid effects are considered, for control design purposes, we need to model the hydrodynamic phenomena in a sufficiently simple manner while taking into account all the hydrodynamic effects that are significant for the control design. In particular, the modeling approach presented in this thesis is based on the Morison's equations, assuming that the robot is a slender body. To quantify the fluid forces, each link of the underwater snake robot is considered as an isolated segment. Each segment of the robot is approximated as an elliptical cylinder, as it is shown in Fig. 2.4. The fluid forces are modeled in each cross section of the links and depends only on the transverse motion of the link. Note that, in this modeling approach, the fluid effects that induced by the corners of the joints are neglected.

We now present the assumptions underlying the modeling approach.

Assumption 2.1: The fluid is viscid, incompressible, and irrotational in the inertia frame.

Assumption 2.2: The robot is neutrally buoyant, i.e, we assume that the mass per unit of volume of the robot is equal to that of the water, such that gravity and buoyancy cancel each other out.

Assumption 2.3: The current in the inertial frame, $v_c = [V_{x,i}, V_{y,i}]^T$, is constant and irrotational.

Remark 2.1: *Assumptions 2.1 and 2.2 are common assumptions in hydrodynamic modeling of slender body swimming robots [15, 82, 135], while Assumption 2.3 is a reasonable simplification of the real-world situation [37, 38].*

Remark 2.2: *Neutral buoyancy, ensuring that Assumption 2.2 is satisfied, is achieved by proper ballasting of the snake robot. The ballast will furthermore be positioned at the bottom of each snake robot link, in order to prevent it from rolling, making it self-stabilized in roll.*

Assumption 2.4: The relative velocity at each section of the link in body-fixed frame (F_B) is equal to the relative velocity of the respective center of mass of each link. With this assumption we avoid the complexity of deriving the drag forces in analytical form, due to the nonlinear terms.

Remark 2.3: *This approximation is valid in our case because the link's length is small compared to the total robot's length, which means that the velocities will not vary much from one section to the other. Furthermore, Assumption 2.4 let us avoid the numerical calculation of the drag forces due to the nonlinear terms. Note that due to Assumption 2.4 it is not necessary to evaluate numerically the drag force and use an algorithmic approach of modeling, and thus we are able to derive a compact and closed-form model of the underwater swimming robotic system.*

The fluid forces are functions of the current and it is a generally accepted practice to vectorially superpose the current velocity on the link velocity before calculating the fluid forces. This vector can be added vectorially to the link speed before calculating the fluid forces. In many works in ship control, in the presence of ocean currents, the current is assumed to be constant in the body frame, i.e. it is assumed that $\dot{\mathbf{v}}_c = 0$. This assumption is easily violated during turning [38], and the current velocity should thus be assumed constant in the inertial frame, as given in Assumption 2.3.

The fluid forces are expressed as functions of relative velocity, and thus the relative velocity of link i is defined as $v_{r,i}^{\text{link},i} = \dot{p}_i^{\text{link},i} - \nu_{c,i}^{\text{link},i}$, where $\nu_{c,i}^{\text{link},i} = (\mathbf{R}_{\text{link},i}^{\text{global}})^T v_c = [\nu_{x,i}, \nu_{y,i}]^T$ is the current velocity expressed in body frame coordinates (F_B) and $v_c = [V_{x,i}, V_{y,i}]^T$ is the current velocity expressed in inertial frame coordinates (F_I). Due to Assumption 2.3, $\dot{v}_c = 0$ and thus

$$\dot{\nu}_{c,i}^{\text{link},i} = \frac{d}{dt}\left((\mathbf{R}_{\text{link},i}^{\text{global}})^T v_c\right) = \begin{bmatrix} -\sin\theta_i\dot{\theta}_i & \cos\theta_i\dot{\theta}_i \\ -\cos\theta_i\dot{\theta}_i & -\sin\theta_i\dot{\theta}_i \end{bmatrix} \begin{bmatrix} V_{x,i} \\ V_{y,i} \end{bmatrix} \tag{2.11}$$

Each link of the robot is subject to a force from the fluid acting on the CM of the link and also a fluid torque acting on the CM. In the following, we will derive the fluid forces and torques acting on the snake robot. In particular, we present how the force exerted by the fluid on a cylindrical object is made up of two components: the virtual mass force (added mass effect) and the drag force. The drag model that is employed in this thesis is in a form which takes into account the generalized case of anisotropic friction acting on each link. In particular, this means that each link has two drag coefficients, c_t and c_n, describing the drag force in the tangential (along link x axis) and normal (along link y axis) direction of the link, respectively.

The fluid forces exerted on link i by the fluid are expressed as

$$f_i^{\text{link},i} = -\hat{\mathbf{C}}_A \dot{v}_{r,i}^{\text{link},i} - \hat{\mathbf{C}}_D \, v_{r,i}^{\text{link},i} - \hat{\mathbf{C}}_D \, \text{sgn}\left(v_{r,i}^{\text{link},i}\right)\left(v_{r,i}^{\text{link},i}\right)^2, \tag{2.12}$$

where $\dot{v}_{r,i}^{\text{link},i} = \dot{p}_i^{\text{link},i} - \dot{\nu}_{c,i}^{\text{link},i}$ is the relative acceleration of link i, $\dot{p}_i^{\text{link},i}$ and $\ddot{p}_i^{\text{link},i}$ are the velocity and the acceleration of link i, respectively, expressed in the body frame, and $\hat{\mathbf{C}}_A$ and $\hat{\mathbf{C}}_D$ are constant diagonal (2×2) matrices depending on the shape of the body and the fluid characteristics. Moreover, it is worth to mention that the force expressions are formulated as functions of link x-coordinates, $df_i^{\text{link},i}(x)$, and then integrated over each body section to get the total force as:

$$f_i^{\text{link},i} = \int_{-l}^{l} df_i^{\text{link},i}(x). \tag{2.13}$$

For the cylindrical links with major diameter $2a$ and minor diameter $2b$ and taking into account that the length of each link is $2l$, the matrices $\hat{\mathbf{C}}_D$, $\hat{\mathbf{C}}_A$ in this modeling approach are expressed as

$$\hat{\mathbf{C}}_D = \begin{bmatrix} c_t & 0 \\ 0 & c_n \end{bmatrix} = \begin{bmatrix} \frac{1}{2}\rho\pi C_f \frac{(b+a)}{2} 2l & 0 \\ 0 & \frac{1}{2}\rho C_D 2a 2l \end{bmatrix}, \tag{2.14}$$

$$\hat{\mathbf{C}}_A = \begin{bmatrix} \mu_t & 0 \\ 0 & \mu_n \end{bmatrix} = \begin{bmatrix} 0 & 0 \\ 0 & \rho\pi C_A a^2 2l \end{bmatrix}, \tag{2.15}$$

where C_f and C_D are the drag coefficients in x and y direction of motion, while C_A denotes the added mass coefficient and ρ is the density of the fluid. The added mass parameter in the x direction is considered equal to zero ($\mu_t = 0$), because the added mass of a slender body in longitudinal direction can be neglected compared to the body mass [113].

After modeling the fluid forces acting on the snake robot, we will now model the fluid moment τ_i. In this thesis, we decide to include the fluid moments in the model because, first of all, this implies a more accurate modeling approach from a hydrodynamic perspective and, secondly, due to the fact that the fluid moments are directly related to the power consumption of the system. The fluid torque is a result of the link rotation only and thus the fluid torque on the CM of link i is a result of fluid forces acting normal to the link during link rotation. This approach is based on the common approach for a plate undergoing forced angular oscillation [85]. Each link of the robot is oscillating similarly to a flat plate oscillating in rotational motion. In [85] it is shown that under this assumption, the torque applied on link i by the fluid can be modeled through the relation

$$\tau_i = -\lambda_1 \ddot{\theta}_i - \lambda_2 \dot{\theta}_i - \lambda_3 \dot{\theta}_i |\dot{\theta}_i|, \tag{2.16}$$

where the λ_1, λ_2 and λ_3 parameters depend on the shape of the body and the fluid characteristics. It is worth mentioning that [85] shows that the parameter λ_2 can be set to zero, neglecting the torques due to the linear drag forces. Nevertheless, in this following modeling approach we decide to consider, for completeness, the

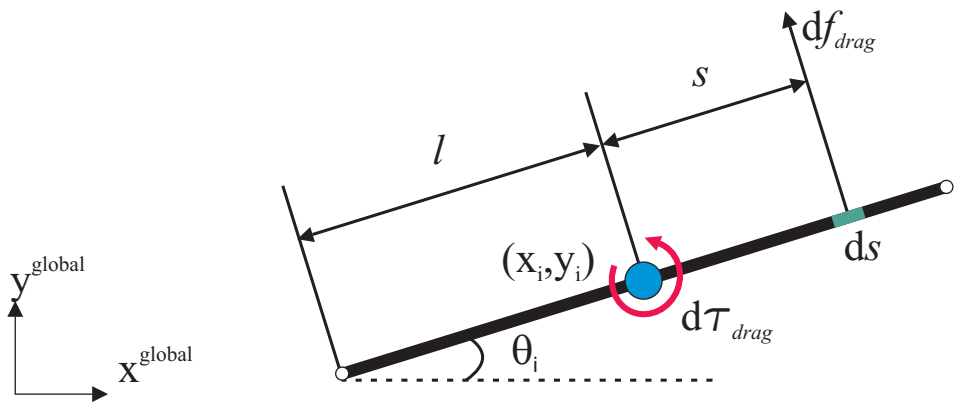

Figure 2.5: The drag fluid torque about the CM of each link.

fluid torques due to the linear drag forces, since, these torques are dominant for slow swimming velocities.

For a cylinder, the added mass torque reduces to a simple analytical form with the parameter λ_1 expressed for a link with length $2l$ as

$$\lambda_1 = \frac{1}{12}\rho\pi C_M (a^2 - b^2)^2 l^3, \tag{2.17}$$

where C_M is the added inertia coefficient. Additionally, in order to derive the parameters λ_2 and λ_3 we need to integrate the drag torque. As illustrated in Fig. 2.5, the drag force on an infinitesimal length of link i due to the link rotation, produces a drag torque about the CM of the link, which is given by

$$d\tau_{drag} = s df_{drag} = -sC_{Ld_x}\, s\dot{\theta}_i ds - sC_{Ld_x}\, \mathrm{sgn}\left(s\dot{\theta}_i\right)\left(s\dot{\theta}_i\right)^2 ds, \tag{2.18}$$

where s is the distance from the CM of link i to the element ds and $C_{Ld_x} = (1/2)\rho\pi C_f (b+a)/2$. Integrating (2.18), we can calculate the total drag torque on link i as

$$\tau_{drag} = -\int_{-l}^{l} \left(sC_{Ld_x}\, s\dot{\theta}_i + sC_{Ld_x}\, \mathrm{sgn}\left(s\dot{\theta}_i\right)\left(s\dot{\theta}_i\right)^2 \right) ds = -\lambda_2 \dot{\theta}_i - \lambda_3 \dot{\theta}_i |\dot{\theta}_i|, \tag{2.19}$$

where λ_2 and λ_3 are given by

$$\lambda_2 = \frac{1}{6}\rho\pi C_f (a+b) l^3 \text{ and } \lambda_3 = \frac{1}{8}\rho\pi C_f (a+b) l^4. \tag{2.20}$$

The matrix $\hat{\mathbf{C}}_D$ and the parameters λ_2, λ_3 represent the drag forces parameters due to the pressure difference between the two sides of the body, while $\hat{\mathbf{C}}_A$ and λ_1 stand for the added mass of fluid carried by the moving body.

Using the transformation matrix, we can express the global frame fluid forces on link i as:

$$\begin{aligned} f_i^{\text{global}} &= \mathbf{R}_{\text{link},i}^{\text{global}} f_i^{\text{link},i} = \begin{bmatrix} \cos\theta_i & -\sin\theta_i \\ \sin\theta_i & \cos\theta_i \end{bmatrix} \begin{bmatrix} f_{x,i}^{\text{link},i} \\ f_{y,i}^{\text{link},i} \end{bmatrix} \\ &= -\mathbf{R}_{\text{link},i}^{\text{global}} \hat{\mathbf{C}}_A \left((\mathbf{R}_{\text{link},i}^{\text{global}})^T \begin{bmatrix} \ddot{x}_i \\ \ddot{y}_i \end{bmatrix} - \begin{bmatrix} -\sin\theta_i \dot{\theta}_i & \cos\theta_i \dot{\theta}_i \\ -\cos\theta_i \dot{\theta}_i & -\sin\theta_i \dot{\theta}_i \end{bmatrix} \begin{bmatrix} V_{x,i} \\ V_{y,i} \end{bmatrix} \right) \\ &\quad - \mathbf{R}_{\text{link},i}^{\text{global}} \hat{\mathbf{C}}_D \begin{bmatrix} V_{r_x,i} \\ V_{r_y,i} \end{bmatrix} - \mathbf{R}_{\text{link},i}^{\text{global}} \hat{\mathbf{C}}_D \text{sgn}\left(\begin{bmatrix} V_{r_x,i} \\ V_{r_y,i} \end{bmatrix} \right) \begin{bmatrix} V_{r_x,i}^2 \\ V_{r_y,i}^2 \end{bmatrix}, \end{aligned} \tag{2.21}$$

where

$$\begin{bmatrix} V_{r_x,i} \\ V_{r_y,i} \end{bmatrix} = (\mathbf{R}_{\text{link},i}^{\text{global}})^T \begin{bmatrix} \dot{x}_i - V_{x,i} \\ \dot{y}_i - V_{y,i} \end{bmatrix}. \tag{2.22}$$

By performing the matrix multiplications and assembling the forces on all links in vector form, we can rewrite the global frame fluid forces on the links as

$$\mathbf{f} = \begin{bmatrix} \mathbf{f_x} \\ \mathbf{f_y} \end{bmatrix} = \begin{bmatrix} \mathbf{f_{A_x}} \\ \mathbf{f_{A_y}} \end{bmatrix} + \begin{bmatrix} \mathbf{f}_{\mathbf{D_x}}^{\text{I}} \\ \mathbf{f}_{\mathbf{D_y}}^{\text{I}} \end{bmatrix} + \begin{bmatrix} \mathbf{f}_{\mathbf{D_x}}^{\text{II}} \\ \mathbf{f}_{\mathbf{D_y}}^{\text{II}} \end{bmatrix}, \tag{2.23}$$

where $\mathbf{f_{A_x}}$ and $\mathbf{f_{A_y}}$ represent the effects from added mass forces and are expressed as

$$\begin{aligned} \begin{bmatrix} \mathbf{f_{A_x}} \\ \mathbf{f_{A_y}} \end{bmatrix} &= -\begin{bmatrix} \mu_n (\mathbf{S}_\theta)^2 & -\mu_n \mathbf{S}_\theta \mathbf{C}_\theta \\ -\mu_n \mathbf{S}_\theta \mathbf{C}_\theta & \mu_n (\mathbf{C}_\theta)^2 \end{bmatrix} \begin{bmatrix} \ddot{\mathbf{X}} \\ \ddot{\mathbf{Y}} \end{bmatrix} \\ &\quad - \begin{bmatrix} -\mu_n \mathbf{S}_\theta \mathbf{C}_\theta & -\mu_n (\mathbf{S}_\theta)^2 \\ \mu_n (\mathbf{C}_\theta)^2 & \mu_n \mathbf{S}_\theta \mathbf{C}_\theta \end{bmatrix} \begin{bmatrix} \mathbf{V}_x^a \\ \mathbf{V}_y^a \end{bmatrix} \dot{\boldsymbol{\theta}}, \end{aligned} \tag{2.24}$$

where $\mathbf{V}_x^a = \text{diag}(V_{x,1}, \cdots, V_{x,n}) \in \mathbb{R}^{n \times n}$ and $\mathbf{V}_y^a = \text{diag}(V_{y,1}, \cdots, V_{y,n}) \in \mathbb{R}^{n \times n}$. The vectors $\mathbf{f}_{\mathbf{D_x}}^{\text{I}}$, $\mathbf{f}_{\mathbf{D_y}}^{\text{I}}$ and $\mathbf{f}_{\mathbf{D_x}}^{\text{II}}$, $\mathbf{f}_{\mathbf{D_y}}^{\text{II}}$ represent the effects from the linear (2.25) and nonlinear drag forces (2.26), respectively, where the relative velocities are given from (2.27).

$$\begin{bmatrix} \mathbf{f}_{\mathbf{D_x}}^{\text{I}} \\ \mathbf{f}_{\mathbf{D_y}}^{\text{I}} \end{bmatrix} = -\begin{bmatrix} c_t (\mathbf{C}_\theta)^2 + c_n (\mathbf{S}_\theta)^2 & (c_t - c_n) \mathbf{S}_\theta \mathbf{C}_\theta \\ (c_t - c_n) \mathbf{S}_\theta \mathbf{C}_\theta & c_t (\mathbf{S}_\theta)^2 + c_n (\mathbf{C}_\theta)^2 \end{bmatrix} \begin{bmatrix} \dot{\mathbf{X}} - \mathbf{V}_x \\ \dot{\mathbf{Y}} - \mathbf{V}_y \end{bmatrix} \tag{2.25}$$

$$\begin{bmatrix} \mathbf{f}_{\mathbf{D_x}}^{\text{II}} \\ \mathbf{f}_{\mathbf{D_y}}^{\text{II}} \end{bmatrix} = -\begin{bmatrix} c_t \mathbf{C}_\theta & -c_n \mathbf{S}_\theta \\ c_t \mathbf{S}_\theta & c_n \mathbf{C}_\theta \end{bmatrix} \text{sgn}\left(\begin{bmatrix} \mathbf{V_{r_x}} \\ \mathbf{V_{r_y}} \end{bmatrix} \right) \begin{bmatrix} \mathbf{V_{r_x}}^2 \\ \mathbf{V_{r_y}}^2 \end{bmatrix} \tag{2.26}$$

$$\begin{bmatrix} \mathbf{V_{r_x}} \\ \mathbf{V_{r_y}} \end{bmatrix} = \begin{bmatrix} \mathbf{C}_\theta & \mathbf{S}_\theta \\ -\mathbf{S}_\theta & \mathbf{C}_\theta \end{bmatrix} \begin{bmatrix} \dot{\mathbf{X}} - \mathbf{V}_x \\ \dot{\mathbf{Y}} - \mathbf{V}_y \end{bmatrix} \tag{2.27}$$

In addition, the fluid torques on all links in matrix form are

$$\boldsymbol{\tau} = -\boldsymbol{\Lambda}_1 \ddot{\boldsymbol{\theta}} - \boldsymbol{\Lambda}_2 \dot{\boldsymbol{\theta}} - \boldsymbol{\Lambda}_3 \dot{\boldsymbol{\theta}} |\dot{\boldsymbol{\theta}}|, \tag{2.28}$$

where $\boldsymbol{\Lambda}_1 = \lambda_1 \mathbf{I}_n$, $\boldsymbol{\Lambda}_2 = \lambda_2 \mathbf{I}_n$ and $\boldsymbol{\Lambda}_3 = \lambda_3 \mathbf{I}_n$.

2.2.4 The Dynamics of the Underwater Snake Robot

The $n+2$ degrees of freedom of the underwater snake robot are defined by the link angles $\boldsymbol{\theta} \in \mathbb{R}^n$ and the CM position $\mathbf{p}_{\text{CM}} \in \mathbb{R}^2$. We now present the equations of motion of the robot in terms of the acceleration of the link angles, $\ddot{\boldsymbol{\theta}}$, and the acceleration of the CM position, $\ddot{\mathbf{p}}_{\text{CM}}$.

As illustrated in Fig. 2.3, link $i \in \{1, \cdots, n\}$ is influenced by hydrodynamic forces $f_{x,i}$, $f_{y,i}$ and also the joint constraint forces, $h_{x,i-1}$, $h_{y,i-1}$, $h_{x,i}$ and $h_{y,i}$ which keep the link connected to link $i-1$ and link $i+1$. The joint constraint forces are described in Table 2.1. Using the first principle, the forces and torques acting on link i are visualized in Fig. 2.3 and the force balance for link i in global frame coordinates is given by

$$\begin{aligned} m\ddot{x}_i &= h_{x,i} - h_{x,i-1} + f_{x,i}, \\ m\ddot{y}_i &= h_{y,i} - h_{y,i-1} + f_{y,i}. \end{aligned} \tag{2.29}$$

The force balance equations for all links may be expressed in matrix form as

$$\begin{aligned} m\ddot{\mathbf{X}} &= \mathbf{D}^T\mathbf{h}_x + \mathbf{f}_{\mathbf{x}}, \\ m\ddot{\mathbf{Y}} &= \mathbf{D}^T\mathbf{h}_y + \mathbf{f}_{\mathbf{y}}. \end{aligned} \tag{2.30}$$

Note that the link accelerations may also be expressed by differentiating (2.6) twice with respect to time. This gives

$$\begin{aligned} \mathbf{D}\ddot{\mathbf{X}} &= l\mathbf{A}\left(\mathbf{C}_\theta\dot{\boldsymbol{\theta}}^2 + \mathbf{S}_\theta\ddot{\boldsymbol{\theta}}\right), \\ \mathbf{D}\ddot{\mathbf{Y}} &= l\mathbf{A}\left(\mathbf{S}_\theta\dot{\boldsymbol{\theta}}^2 - \mathbf{C}_\theta\ddot{\boldsymbol{\theta}}\right), \end{aligned} \tag{2.31}$$

where the square operator of $\dot{\boldsymbol{\theta}}^2$ means that each element of $\dot{\boldsymbol{\theta}}$ is squared ($\dot{\boldsymbol{\theta}}^2 = \text{diag}(\dot{\boldsymbol{\theta}})\dot{\boldsymbol{\theta}}$). We obtain the acceleration of the CM by differentiating (2.4) twice with respect to time, inserting (2.30), and noting that the constraint forces $\mathbf{h}_x$ and $\mathbf{h}_y$, are cancelled out when the link accelerations are summed. This gives

$$\begin{bmatrix} \ddot{p}_x \\ \ddot{p}_y \end{bmatrix} = \frac{1}{n}\begin{bmatrix} \mathbf{e}^T\ddot{\mathbf{X}} \\ \mathbf{e}^T\ddot{\mathbf{Y}} \end{bmatrix} = \frac{1}{nm}\begin{bmatrix} \mathbf{e}^T & \mathbf{0}_{1\times n} \\ \mathbf{0}_{1\times n} & \mathbf{e}^T \end{bmatrix}\mathbf{f} \tag{2.32}$$

By inserting (2.10), (2.23) and (2.24) into (2.32) the acceleration of the CM may be expressed as

$$\begin{aligned} \begin{bmatrix} \ddot{p}_x \\ \ddot{p}_y \end{bmatrix} &= -\mathbf{M}_p\begin{bmatrix} \mathbf{e}^T\mu_n\mathbf{S}_\theta^2 & -\mathbf{e}^T\mu_n\mathbf{S}_\theta\mathbf{C}_\theta \\ -\mathbf{e}^T\mu_n\mathbf{S}_\theta\mathbf{C}_\theta & \mathbf{e}^T\mu_n\mathbf{C}_\theta^2 \end{bmatrix}\begin{bmatrix} l\mathbf{K}^T(\mathbf{C}_\theta\dot{\boldsymbol{\theta}}^2 + \mathbf{S}_\theta\ddot{\boldsymbol{\theta}}) \\ l\mathbf{K}^T(\mathbf{S}_\theta\dot{\boldsymbol{\theta}}^2 - \mathbf{C}_\theta\ddot{\boldsymbol{\theta}}) \end{bmatrix} \\ &- \mathbf{M}_p\begin{bmatrix} -\mathbf{e}^T\mu_n\mathbf{S}_\theta\mathbf{C}_\theta & -\mathbf{e}^T\mu_n\mathbf{S}_\theta^2 \\ \mathbf{e}^T\mu_n\mathbf{C}_\theta^2 & \mathbf{e}^T\mu_n\mathbf{S}_\theta\mathbf{C}_\theta \end{bmatrix}\begin{bmatrix} \mathbf{V}_x^a \\ \mathbf{V}_y^a \end{bmatrix}\dot{\boldsymbol{\theta}} + \mathbf{M}_p\begin{bmatrix} \mathbf{e}^T\mathbf{f}_{\mathbf{Dx}} \\ \mathbf{e}^T\mathbf{f}_{\mathbf{Dy}} \end{bmatrix} \end{aligned} \tag{2.33}$$

where

$$\mathbf{M}_p = \begin{bmatrix} m_{11} & m_{12} \\ m_{21} & m_{22} \end{bmatrix} = \begin{bmatrix} nm + \mathbf{e}^T\mu_n\mathbf{S}_\theta^2\mathbf{e} & -\mathbf{e}^T\mu_n\mathbf{S}_\theta\mathbf{C}_\theta\mathbf{e} \\ -\mathbf{e}^T\mu_n\mathbf{S}_\theta\mathbf{C}_\theta\mathbf{e} & nm + \mathbf{e}^T\mu_n\mathbf{C}_\theta^2\mathbf{e} \end{bmatrix}^{-1}, \tag{2.34}$$

and $\mathbf{f_{Dx}} = \mathbf{f}^{\,\mathrm{I}}_{\mathbf{D_x}} + \mathbf{f}^{\,\mathrm{II}}_{\mathbf{D_x}}$ and $\mathbf{f_{Dy}} = \mathbf{f}^{\,\mathrm{I}}_{\mathbf{D_y}} + \mathbf{f}^{\,\mathrm{II}}_{\mathbf{D_y}}$ are the drag forces in x and y directions. Additionally, it is easily verifiable that the determinant $n^2m^2 + nm\mu_n + \mu_n^2 \sum_{i=1}^{n-1} \sum_{j=i+1}^{n} (\sin(\theta_i - \theta_j))^2$ is nonzero for $n \neq 0$ and $m \neq 0$.

The torque balance for link i is given by

$$J\ddot{\theta}_i = u_i - u_{i-1} - l \sin\theta_i \left(h_{x,i} + h_{x,i-1}\right) + l \cos\theta_i \left(h_{y,i} + h_{y,i-1}\right) + \tau_i, \tag{2.35}$$

where u_i and u_{i-1} are the actuator torques exerted on link i from link $i+1$ and link $i-1$, respectively. In addition, τ_i is the torque applied on link i by the fluid. Hence, the torque balance equations for all links may be expressed in matrix form as

$$\mathbf{J}\ddot{\boldsymbol{\theta}} = \mathbf{D}^T\mathbf{u} - l\mathbf{S}_\theta\mathbf{A}^T\mathbf{h}_x + l\mathbf{C}_\theta\mathbf{A}^T\mathbf{h}_y + \boldsymbol{\tau}, \tag{2.36}$$

where $\boldsymbol{\tau}$ is given from (2.28). Now remains to remove the constraint forces from (2.36). Premultiplying (2.30) by $\mathbf{D}$ and solving for $\mathbf{h}_x$ and $\mathbf{h}_y$, we can write the expression for the joint constraint forces as

$$\begin{aligned}
\mathbf{h}_x &= (\mathbf{D}\mathbf{D}^T)^{-1}\mathbf{D}(m\ddot{\mathbf{X}} + \mu_n \left(\mathbf{S}_\theta\right)^2 \ddot{\mathbf{X}} - \mu_n\mathbf{S}_\theta\mathbf{C}_\theta\ddot{\mathbf{Y}} \\
&\quad - \mu_n\mathbf{S}_\theta\mathbf{C}_\theta\mathbf{V}_x^a\dot{\boldsymbol{\theta}} - \mu_n \left(\mathbf{S}_\theta\right)^2 \mathbf{V}_y^a\dot{\boldsymbol{\theta}} - \mathbf{f}^{\,\mathrm{I}}_{\mathbf{D_x}} - \mathbf{f}^{\,\mathrm{II}}_{\mathbf{D_x}}) \\
\mathbf{h}_y &= (\mathbf{D}\mathbf{D}^T)^{-1}\mathbf{D}(m\ddot{\mathbf{Y}} - \mu_n\mathbf{S}_\theta\mathbf{C}_\theta\ddot{\mathbf{X}} + \mu_n \left(\mathbf{C}_\theta\right)^2 \ddot{\mathbf{Y}} \\
&\quad + \mu_n \left(\mathbf{C}_\theta\right)^2 \mathbf{V}_x^a\dot{\boldsymbol{\theta}} + \mu_n\mathbf{S}_\theta\mathbf{C}_\theta\mathbf{V}_y^a\dot{\boldsymbol{\theta}} - \mathbf{f}^{\,\mathrm{I}}_{\mathbf{D_y}} - \mathbf{f}^{\,\mathrm{II}}_{\mathbf{D_y}}).
\end{aligned} \tag{2.37}$$

Inserting in (2.36) the joint constraints forces (2.37) and also replacing $\mathbf{D}\ddot{\mathbf{X}}$, $\mathbf{D}\ddot{\mathbf{Y}}$ with (2.31), $\ddot{\mathbf{X}}$,$\ddot{\mathbf{Y}}$ with (2.10) and $\ddot{p}_x$, $\ddot{p}_y$ with (2.33), and solving for $\ddot{\boldsymbol{\theta}}$, we express the model of an underwater snake robot as

$$\mathbf{M}_{\boldsymbol{\theta}}\ddot{\boldsymbol{\theta}} + \mathbf{W}_{\boldsymbol{\theta}}\dot{\boldsymbol{\theta}}^2 + \mathbf{V}_\theta\dot{\boldsymbol{\theta}} + \boldsymbol{\Lambda}_3|\dot{\boldsymbol{\theta}}|\dot{\boldsymbol{\theta}} + \mathbf{K_{Dx}}\mathbf{f_{Dx}} + \mathbf{K_{Dy}}\mathbf{f_{Dy}} = \mathbf{D}^T\mathbf{u}, \tag{2.38}$$

where $\mathbf{M}_\theta$, $\mathbf{W}_\theta$, $\mathbf{V}_\theta$, $\mathbf{K_{Dx}}$ and $\mathbf{K_{Dy}}$ are defined as

$$\mathbf{M}_\theta = \mathbf{J} + ml^2\mathbf{S}_\theta\mathbf{V}\mathbf{S}_\theta + ml^2\mathbf{C}_\theta\mathbf{V}\mathbf{C}_\theta + \boldsymbol{\Lambda}_1 + l^2\mu_n\mathbf{K}_1\mathbf{K}^T\mathbf{S}_\theta + l^2\mu_n\mathbf{K}_2\mathbf{K}^T\mathbf{C}_\theta \tag{2.39}$$

$$\mathbf{W}_\theta = ml^2\mathbf{S}_\theta\mathbf{V}\mathbf{C}_\theta - ml^2\mathbf{C}_\theta\mathbf{V}\mathbf{S}_\theta + l^2\mu_n\mathbf{K}_1\mathbf{K}^T\mathbf{C}_\theta - l^2\mu_n\mathbf{K}_2\mathbf{K}^T\mathbf{S}_\theta \tag{2.40}$$

$$\mathbf{V}_\theta = \boldsymbol{\Lambda}_2 - l\mu_n\mathbf{K}_2\mathbf{V}_x^a - l\mu_n\mathbf{K}_1\mathbf{V}_y^a \tag{2.41}$$

$$\mathbf{K_{Dx}} = l\mu_n m_{11}\mathbf{A}_1\mathbf{e}\mathbf{e}^T - l\mu_n m_{21}\mathbf{A}_2\mathbf{e}\mathbf{e}^T - l\mathbf{S}_\theta\mathbf{K} \tag{2.42}$$

$$\mathbf{K_{Dy}} = l\mu_n m_{12}\mathbf{A}_1\mathbf{e}\mathbf{e}^T - l\mu_n m_{22}\mathbf{A}_2\mathbf{e}\mathbf{e}^T + l\mathbf{C}_\theta\mathbf{K} \tag{2.43}$$

where

$$\begin{aligned}
\mathbf{K}_1 &= \mathbf{A}_1 + \mu_n\mathbf{A}_1\mathbf{e}\mathbf{e}^T(m_{12}\mathbf{S}_\theta\mathbf{C}_\theta - m_{11}\mathbf{S}_\theta^2) - \mu_n\mathbf{A}_2\mathbf{e}\mathbf{e}^T(m_{22}\mathbf{S}_\theta\mathbf{C}_\theta - m_{21}\mathbf{S}_\theta^2), \\
\mathbf{K}_2 &= \mathbf{A}_2 - \mu_n\mathbf{A}_1\mathbf{e}\mathbf{e}^T(m_{11}\mathbf{S}_\theta\mathbf{C}_\theta - m_{12}\mathbf{C}_\theta^2) + \mu_n\mathbf{A}_2\mathbf{e}\mathbf{e}^T(m_{21}\mathbf{S}_\theta\mathbf{C}_\theta - m_{22}\mathbf{C}_\theta^2), \\
\mathbf{A}_1 &= \mathbf{S}_\theta\mathbf{K}\mathbf{S}_\theta^2 + \mathbf{C}_\theta\mathbf{K}\mathbf{S}_\theta\mathbf{C}_\theta, \\
\mathbf{A}_2 &= \mathbf{S}_\theta\mathbf{K}\mathbf{S}_\theta\mathbf{C}_\theta + \mathbf{C}_\theta\mathbf{K}\mathbf{C}_\theta^2.
\end{aligned}$$

In summary, the equations of motion for the underwater snake robot are given by (2.33) and (2.38). By introducing the state variable $\mathbf{x} = \left[\boldsymbol{\theta}^T, \mathbf{p}_{\text{CM}}^T, \dot{\boldsymbol{\theta}}^T, \dot{\mathbf{p}}_{\text{CM}}^T\right]^T \in \mathbb{R}^{2n+4}$, we can rewrite the model of the robot compactly in state space form as

$$\dot{\mathbf{x}} = \left[\dot{\boldsymbol{\theta}}^T, \dot{\mathbf{p}}_{\text{CM}}^T, \ddot{\boldsymbol{\theta}}^T, \ddot{\mathbf{p}}_{\text{CM}}^T\right]^T = \mathbf{F}(\mathbf{x}, \mathbf{u}) \tag{2.44}$$

where the elements of $\mathbf{F}(\mathbf{x}, \mathbf{u})$ are found by solving (2.33) and (2.38) for $\ddot{\mathbf{p}}_{\text{CM}}$ and $\ddot{\boldsymbol{\theta}}$, respectively.

Remark 2.4: *It is interesting to note that if, in the dynamic model (2.33,2.38), we set the fluid parameters to zero and replace the drag forces in x and y direction with ground friction models [101], then the model reduces to an identical dynamic model of a ground snake robot, described in [101]. The underwater snake robot model is thus an extension of the land-based snake robot model, and may be used for amphibious snake robots moving both on land and in water.*

2.2.5 Fluid parameters

Another important question that should be addressed during the modeling of underwater snake robot, is the proper choice of the hydrodynamic related coefficients. As already mentioned, in our modelling approach, we decide to use Morison's equation assuming that each link of the robot is an elliptical cylinder. Hence, it is important to investigate the influence of the current effects on cylindrical objects. Even though the force coefficients vary very much in the presence of current, Sarpkaya and Storm [122] found a modified Morison equation to represent the measured force in a coexisting flow field as well as the original equation in a no-current field.

It must be noted that, ideally, the drag and added mass coefficients of the system should be determined experimentally. When this information is not available, the coefficients are chosen under the assumption of a steady-state flow [58, 83]. Generally, the added mass coefficients are simply set to their theoretical values, $C_A = 1$ and $C_M = 1$ [135]. In [50], Guskova et al. investigate the C_D and C_A of laterally oscillating elliptical cylinders under conditions dimensionally equivalent to those of our underwater snake robot. The parameter C_D is found to vary from approximately 2 to 3 and C_A varies between 0.93 and 1. In [50], it is mentioned that the lateral coefficients of the simulated robot may not deviate significantly from their steady-state values. The axial viscous force's coefficient is selected as $C_f = 0.03$ from a review of experimental data presented in [114]. In addition, for a cylindrical obstacle immerged in a flow with a Reynolds number of approximately $R_e \simeq 10^5$, the fluid parameters can be set as $C_D = 1$, $C_A = 1$, $C_f = 0.01$, $C_M = 1$ [83]. In this thesis, we will consider the following fluid coefficients for the simulated motion of the underwater snake robots in the next Chapters: $C_D = 1 - 2$, $C_A = 1$, $C_f = 0.03$, $C_M = 1$.

2.2.6 Simulation Study

We will now present simulation results for three different modeling approaches:

- **case 1** – Added mass and nonlinear drag effects,
- **case 2** – Added mass, linear and nonlinear drag effects and
- **case 3** – Added mass, linear and nonlinear drag effects and current effects.

Simulation results are presented for the two most common motion patterns for underwater snake robots: lateral undulation and eel-like motion. For the simulation results presented in this chapter, it is sufficient to state that both motion patterns are sinusoidal waves propagating backwards from the head to the tail of the robot, while the mathematical expressions for lateral undulation, the eel-like motion and the joint controller are presented and explained in detail in Chapter 3. The models were implemented in *Matlab R2013b*. The dynamics was calculated using the *ode23tb* solver with a relative and absolute error tolerance of 10^{-4}.

Simulation parameters

A snake robot was considered with $n = 10$ links, each one having length $2l = 2\times0.14$ m. The mass of each link is $m = 0.6597$ kg and is chosen so to fulfil the neutrally buoyant assumption. The initial values of the states of the snake robot were set to zero, i.e. the snake robot is initially at rest at the origin, with its heading along the inertial x axis. The hydrodynamic related parameters for the elliptic section with half small and great axis' length 0.03 m and 0.05 m, respectively, $\rho = 1000$ kg/m^3, $C_f = 0.03$, $C_D = 2$, $C_A = 1$ and $C_M = 1$ were chosen as: $\hat{\mathbf{C}}_D = \text{diag}[0.2639 \quad 8.4]$, $\hat{\mathbf{C}}_A = \text{diag}[0 \quad 0.3958]$, $\lambda_1 = 4.3103\times10^{-4}$, $\lambda_2 = 2.2629\times10^{-5}$, $\lambda_3 = 2.2988\times10^{-7}$. It should be noted that the anisotropic friction property is achieved by a low drag coefficient in the tangential direction and a higher one in the perpendicular. The values of a constant current in inertial frame are set to $[0.1, 0.1]$ m/sec. In these simulations a joint PD-controller (3.5) is used with parameters $k_p = 200, k_d = 50$, while lateral undulation or eel-like motion are achieved by moving the joints according to the (3.1) or (3.2), respectively, with gait parameters $\alpha = 30^o$, $\delta = 30^o$, $\omega = 70^o$/sec and $\phi_0 = 0^o$.

Simulation Results

The simulation results for lateral undulation and eel-like motion of the underwater snake robot are presented for the three different cases. In particular, the motion of the center of mass is presented in Fig. 2.6 and Fig. 2.8 for lateral undulation and eel-like motion pattern, respectively. In addition, the achieved forward velocity (2.5) is presented in Fig. 2.7 and Fig. 2.9, respectively, for lateral undulation and eel-like motion patterns. From the simulation results for both motion patterns, we can see that when a more precise hydrodynamic model is considered the robot achieves higher velocities.

2.3 Virtual Vertical Plane

This section presents a continuous model of an underwater snake robot constrained to move within a vertical plane, as visualized in Fig. 2.10. Following, the kinematics

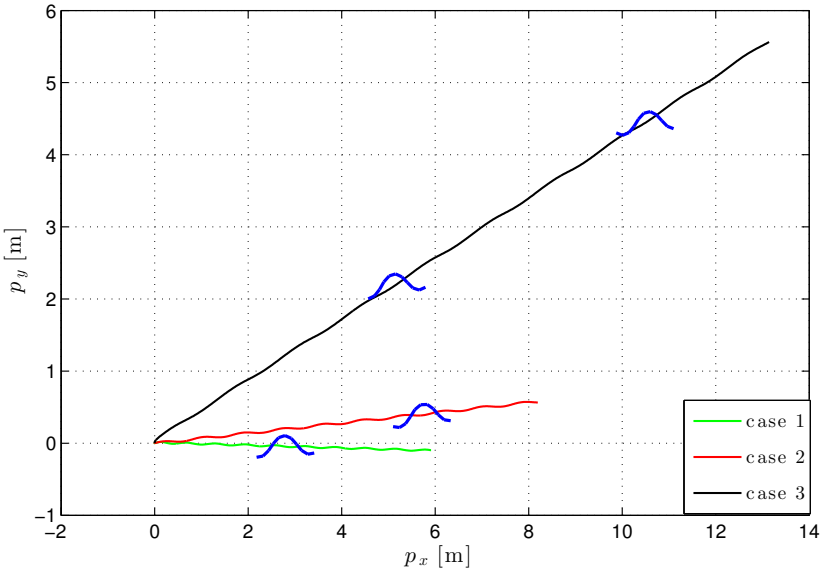

Figure 2.6: The position of the CM of the robot moving in a horizontal plane during lateral undulation motion pattern.

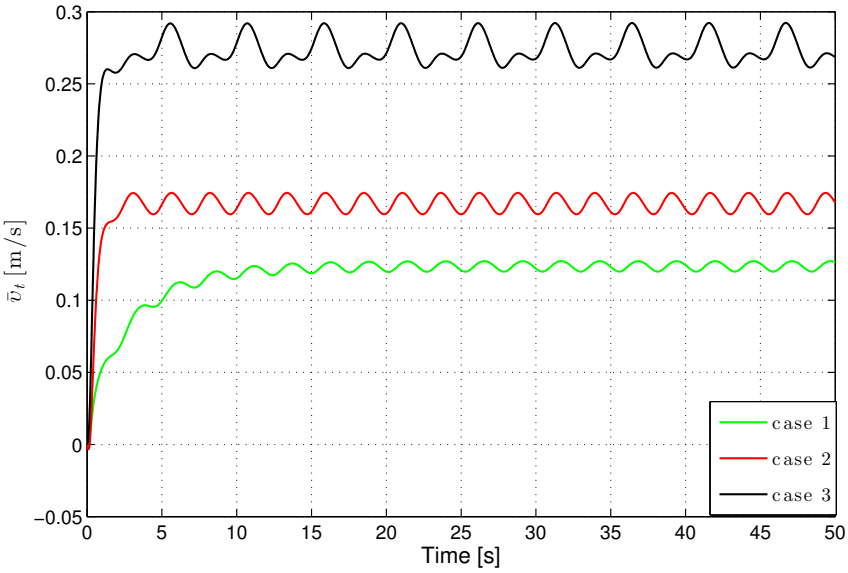

Figure 2.7: The forward velocity of the CM of the robot moving in a horizontal plane during lateral undulation motion pattern.

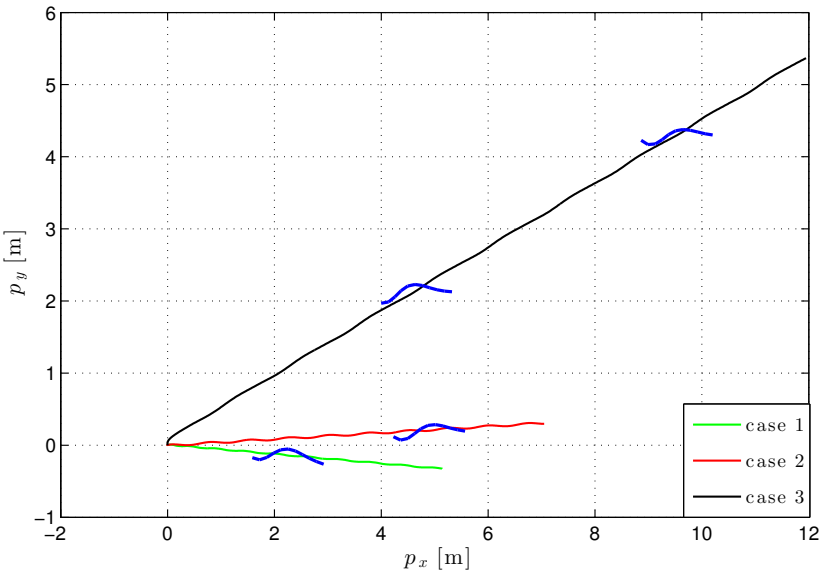

Figure 2.8: The position of the CM of the robot moving in a horizontal plane during eel-like motion pattern.

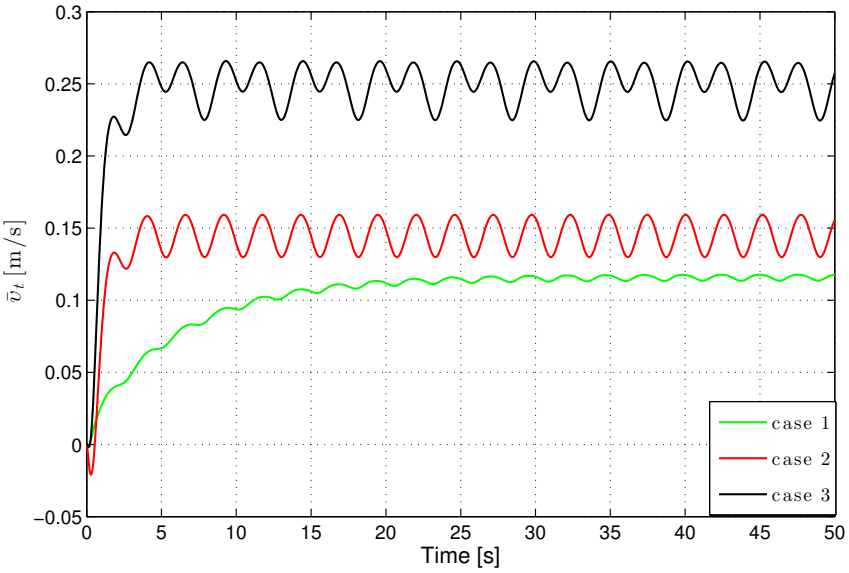

Figure 2.9: The forward velocity of the CM of the robot moving in a horizontal plane during eel-like motion pattern.

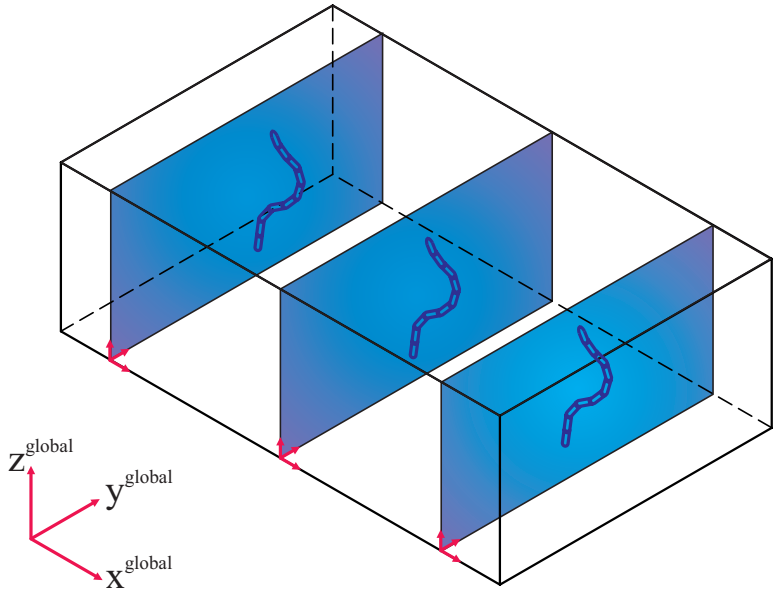

Figure 2.10: Visualization of a ten link underwater snake robot motion in virtual vertical plane.

and dynamics of the robot will be presented taking into account the hydrodynamic and hydrostatic effects.

2.3.1 The Parameters of the Underwater Snake Robot

Similarly to approach presented in Subsection 2.2.1, we assume that the snake robot consists of n rigid links of equal length $2l$ interconnected by $n-1$ joints. The links are assumed to have the same mass m and moment of inertia $J = \frac{1}{3}ml^2$. The mass of each link is uniformly distributed so that the link center of mass (CM) is located at its center point. The total mass of the snake robot is therefore nm. The kinematics and dynamics of the robot moving in vertical plane will be modeled in terms of the mathematical symbols described in Table 2.2 and illustrated in Fig. 2.11 and Fig. 2.12.

2.3.2 The Kinematics of the Underwater Snake Robot

The kinematics of an underwater snake robot moving in a virtual vertical plane is similar to that of an underwater snake robot moving in a virtual horizontal plane. The snake robot is assumed to move in a virtual vertical plane, fully immersed in water, and has $n+2$ degrees of freedom (n link angles and the y-z position of the robot). For a robot swimming in vertical plane, the *link angle* of each link $i \in \{1, \cdots, n\}$ of the robot, $\theta_i \in \mathbb{R}$, is defined as the angle that the link forms with the global z axis with counterclockwise positive direction, while the *joint angle* of joint $i \in \{1, \cdots, n-1\}$ are given by (2.1). The local coordinate system of each

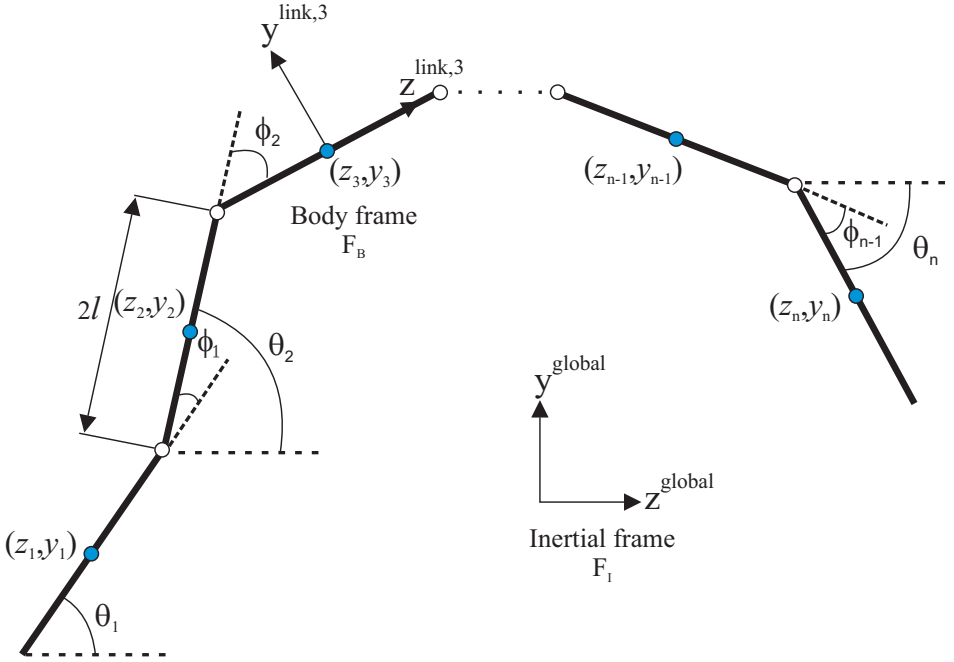

Figure 2.11: Kinematic parameters of the underwater snake robot moving in virtual vertical plane.

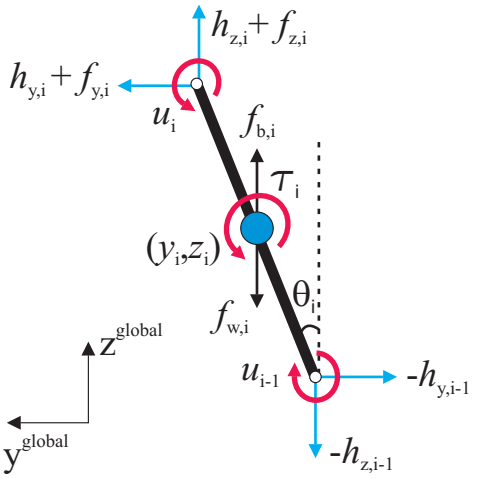

Figure 2.12: Forces and torques acting on each link of the underwater snake robot moving in vertical plane.

Table 2.2: Definition of mathematical terms for underwater snake robot moving in vertical plane.

Symbol	Description	Vector
n	The number of links	
l	The half length of a link	
m	Mass of each link	
J	Moment of inertia of each link	
θ_i	Angle between link i and the global z axis	$\boldsymbol{\theta} \in \mathbb{R}^n$
ϕ_i	Angle of joint i	$\boldsymbol{\phi} \in \mathbb{R}^{n-1}$
(y_i, z_i)	Global coordinates of the CM of link i	$\mathbf{Y}, \mathbf{Z} \in \mathbb{R}^n$
(p_y, p_z)	Global coordinates of the CM of the robot	$\mathbf{p}_{\text{CM}} \in \mathbb{R}^2$
u_i	Actuator torque of joint between link i and link $i+1$	$\mathbf{u} \in \mathbb{R}^{n-1}$
u_{i-1}	Actuator torque of joint between link i and link $i-1$	$\mathbf{u} \in \mathbb{R}^{n-1}$
$f_{y,i}$	Fluid force on link i in y direction	$\mathbf{f_y} \in \mathbb{R}^n$
$f_{z,i}$	Fluid force on link i in z direction	$\mathbf{f_z} \in \mathbb{R}^n$
$f_{w,i}$	Gravitational force on link i	$\mathbf{f}_w \in \mathbb{R}^n$
$f_{b,i}$	Buoyancy force on link i	$\mathbf{f}_b \in \mathbb{R}^n$
τ_i	Fluid torque on link i	$\boldsymbol{\tau} \in \mathbb{R}^n$
$h_{y,i}$	Joint constraint force in y direction on link i from link $i+1$	$\mathbf{h_y} \in \mathbb{R}^{n-1}$
$h_{z,i}$	Joint constraint force in z direction on link i from link $i+1$	$\mathbf{h_z} \in \mathbb{R}^{n-1}$
$h_{y,i-1}$	Joint constraint force in y direction on link i from link $i-1$	$\mathbf{h_y} \in \mathbb{R}^{n-1}$
$h_{z,i-1}$	Joint constraint force in z direction on link i from link $i-1$	$\mathbf{h_z} \in \mathbb{R}^{n-1}$

link is fixed in the CM of the link with y (normal) and z (tangential) axes oriented such that they are aligned with the global y and z axis, respectively, when all the link angles are zero.

The global frame position $\mathbf{p}_{\text{CM}} \in \mathbb{R}^2$ of the CM of the robot is given by

$$\mathbf{p}_{\text{CM}} = \begin{bmatrix} p_y \\ p_z \end{bmatrix} = \begin{bmatrix} \frac{1}{nm}\sum_{i=1}^{n} m y_i \\ \frac{1}{nm}\sum_{i=1}^{n} m z_i \end{bmatrix} = \frac{1}{n}\begin{bmatrix} \mathbf{e}^T\mathbf{Y} \\ \mathbf{e}^T\mathbf{Z} \end{bmatrix}, \tag{2.45}$$

where (y_i, z_i) are the global frame coordinates of the CM of link i, $\mathbf{Y} = [y_1, \cdots, y_n]^T \in \mathbb{R}^n$ and $\mathbf{Z} = [z_1, \cdots, z_n]^T \in \mathbb{R}^n$.

The links are constrained by the joints according to

$$\begin{aligned} \mathbf{D}\mathbf{Y} + l\mathbf{A}\sin\boldsymbol{\theta} &= \mathbf{0}, \\ \mathbf{D}\mathbf{Z} + l\mathbf{A}\cos\boldsymbol{\theta} &= \mathbf{0}. \end{aligned} \tag{2.46}$$

Following similar approach presented in Subsection 2.2.2, the position, the linear velocities and the linear accelerations of the individual links of an underwater snake

robot moving in a virtual vertical plane are given by (2.47), (2.48) and (2.49), respectively.

$$\begin{aligned} \mathbf{Y} &= -l\mathbf{K}^T \sin\boldsymbol{\theta} + \mathbf{e}p_y, \\ \mathbf{Z} &= -l\mathbf{K}^T \cos\boldsymbol{\theta} + \mathbf{e}p_z, \end{aligned} \tag{2.47}$$

$$\begin{aligned} \dot{\mathbf{Y}} &= -l\mathbf{K}^T \mathbf{C}_\theta \dot{\boldsymbol{\theta}} + \mathbf{e}\dot{p}_y, \\ \dot{\mathbf{Z}} &= l\mathbf{K}^T \mathbf{S}_\theta \dot{\boldsymbol{\theta}} + \mathbf{e}\dot{p}_z. \end{aligned} \tag{2.48}$$

$$\begin{aligned} \ddot{\mathbf{Y}} &= l\mathbf{K}^T \left(\mathbf{S}_\theta \dot{\boldsymbol{\theta}}^2 - \mathbf{C}_\theta \ddot{\boldsymbol{\theta}} \right) + \mathbf{e}\ddot{p}_y, \\ \ddot{\mathbf{Z}} &= l\mathbf{K}^T \left(\mathbf{C}_\theta \dot{\boldsymbol{\theta}}^2 + \mathbf{S}_\theta \ddot{\boldsymbol{\theta}} \right) + \mathbf{e}\ddot{p}_z. \end{aligned} \tag{2.49}$$

2.3.3 The Hydrodynamic Model of Underwater Snake Robot

The hydrodynamics of an underwater snake robot moving in virtual vertical plane is similar to that of an underwater snake robot moving in a virtual horizontal plane, except that the motion is performed in the $y-z$ plane instead of the $x-y$ plane. The hydrodynamic model presented in this subsection is valid under the Assumptions 2.1, 2.3 and 2.4 presented in Subsection 2.2.3, while Assumption 2.2 is modified in the following subsection in order to take into account the hydrostatic forces for a not neutrally buoyant robot.

The relative velocity of link i is defined as $v_{r,i}^{\text{link},i} = \dot{p}_i^{\text{link},i} - \nu_{c,i}^{\text{link},i}$, where $\nu_{c,i}^{\text{link},i} = (\mathbf{R}_{\text{link},i}^{\text{global}})^T v_c = [\nu_{y,i}, \nu_{z,i}]^T$ is the current velocity expressed in body frame coordinates (F_B) and $v_c = [V_{y,i}, V_{z,i}]^T$ is the current velocity expressed in inertial frame coordinates (F_I). Due to Assumption 2.3 $\dot{v}_c = 0$ and thus

$$\dot{\nu}_{c,i}^{\text{link},i} = \frac{d}{dt}\left((\mathbf{R}_{\text{link},i}^{\text{global}})^T v_c \right) = \begin{bmatrix} -\sin\theta_i\dot{\theta}_i & -\cos\theta_i\dot{\theta}_i \\ \cos\theta_i\dot{\theta}_i & -\sin\theta_i\dot{\theta}_i \end{bmatrix} \begin{bmatrix} V_{y,i} \\ V_{z,i} \end{bmatrix} \tag{2.50}$$

For a robot swimming in vertical plane the global frame fluid forces on link i are expressed as:

$$\begin{aligned} f_i^{\text{global}} &= \mathbf{R}_{\text{link},i}^{\text{global}} f_i^{\text{link},i} = \begin{bmatrix} \cos\theta_i & \sin\theta_i \\ -\sin\theta_i & \cos\theta_i \end{bmatrix} \begin{bmatrix} f_{y,i}^{\text{link},i} \\ f_{z,i}^{\text{link},i} \end{bmatrix} \\ &= -\mathbf{R}_{\text{link},i}^{\text{global}} \hat{\mathbf{C}}_A \left((\mathbf{R}_{\text{link},i}^{\text{global}})^T \begin{bmatrix} \ddot{y}_i \\ \ddot{z}_i \end{bmatrix} - \begin{bmatrix} -\sin\theta_i\dot{\theta}_i & -\cos\theta_i\dot{\theta}_i \\ \cos\theta_i\dot{\theta}_i & -\sin\theta_i\dot{\theta}_i \end{bmatrix} \begin{bmatrix} V_{y,i} \\ V_{z,i} \end{bmatrix} \right) \\ &- \mathbf{R}_{\text{link},i}^{\text{global}} \hat{\mathbf{C}}_D \begin{bmatrix} V_{r_y,i} \\ V_{r_z,i} \end{bmatrix} - \mathbf{R}_{\text{link},i}^{\text{global}} \hat{\mathbf{C}}_D \text{sgn}\left(\begin{bmatrix} V_{r_y,i} \\ V_{r_z,i} \end{bmatrix} \right) \begin{bmatrix} V_{r_y,i}^2 \\ V_{r_z,i}^2 \end{bmatrix} \end{aligned} \tag{2.51}$$

where

$$\begin{bmatrix} V_{r_y,i} \\ V_{r_z,i} \end{bmatrix} = (\mathbf{R}_{\text{link},i}^{\text{global}})^T \begin{bmatrix} \dot{y}_i - V_{y,i} \\ \dot{z}_i - V_{z,i} \end{bmatrix}. \tag{2.52}$$

By performing the matrix multiplications and assembling the forces on all links in vector form, we can rewrite the global frame fluid forces on the links as

$$\mathbf{f} = \begin{bmatrix} \mathbf{f_y} \\ \mathbf{f_z} \end{bmatrix} = \begin{bmatrix} \mathbf{f_{A_y}} \\ \mathbf{f_{A_z}} \end{bmatrix} + \begin{bmatrix} \mathbf{f}_{\mathbf{D_y}}^{\text{I}} \\ \mathbf{f}_{\mathbf{D_z}}^{\text{I}} \end{bmatrix} + \begin{bmatrix} \mathbf{f}_{\mathbf{D_y}}^{\text{II}} \\ \mathbf{f}_{\mathbf{D_z}}^{\text{II}} \end{bmatrix}, \tag{2.53}$$

where $\mathbf{f_{A_y}}$ and $\mathbf{f_{A_z}}$ represent the effects from added mass forces and are expressed as

$$\begin{aligned}\begin{bmatrix} \mathbf{f_{A_y}} \\ \mathbf{f_{A_z}} \end{bmatrix} = &- \begin{bmatrix} \mu_n \left(\mathbf{C}_\theta\right)^2 & -\mu_n \mathbf{S}_\theta \mathbf{C}_\theta \\ -\mu_n \mathbf{S}_\theta \mathbf{C}_\theta & \mu_n \left(\mathbf{S}_\theta\right)^2 \end{bmatrix} \begin{bmatrix} \ddot{\mathbf{Y}} \\ \ddot{\mathbf{Z}} \end{bmatrix} \\ &- \begin{bmatrix} \mu_n \mathbf{S}_\theta \mathbf{C}_\theta & \mu_n \left(\mathbf{C}_\theta\right)^2 \\ -\mu_n \left(\mathbf{S}_\theta\right)^2 & -\mu_n \mathbf{S}_\theta \mathbf{C}_\theta \end{bmatrix} \begin{bmatrix} \mathbf{V}_y^a \\ \mathbf{V}_z^a \end{bmatrix} \dot{\boldsymbol{\theta}},\end{aligned} \tag{2.54}$$

where $\mathbf{V}_y^a = \mathrm{diag}\left(V_{y,1}, \cdots, V_{y,n}\right) \in \mathbb{R}^{n\times n}$ and $\mathbf{V}_z^a = \mathrm{diag}\left(V_{z,1}, \cdots, V_{z,n}\right) \in \mathbb{R}^{n\times n}$. The vectors $\mathbf{f}^{\,\mathrm{I}}_{\mathbf{D_y}}$, $\mathbf{f}^{\,\mathrm{I}}_{\mathbf{D_z}}$ and $\mathbf{f}^{\,\mathrm{II}}_{\mathbf{D_y}}$, $\mathbf{f}^{\,\mathrm{II}}_{\mathbf{D_z}}$ represent the effects from the linear (2.55) and nonlinear drag forces (2.56), respectively, where the relative velocities are given from (2.57). Furthermore, the fluid torques on all links are given by (2.28).

$$\begin{bmatrix} \mathbf{f}^{\,\mathrm{I}}_{\mathbf{D_y}} \\ \mathbf{f}^{\,\mathrm{I}}_{\mathbf{D_z}} \end{bmatrix} = - \begin{bmatrix} c_t \left(\mathbf{S}_\theta\right)^2 + c_n \left(\mathbf{C}_\theta\right)^2 & \left(c_t - c_n\right) \mathbf{S}_\theta \mathbf{C}_\theta \\ \left(c_t - c_n\right) \mathbf{S}_\theta \mathbf{C}_\theta & c_t \left(\mathbf{C}_\theta\right)^2 + c_n \left(\mathbf{S}_\theta\right)^2 \end{bmatrix} \begin{bmatrix} \dot{\mathbf{Y}} - \mathbf{V}_y \\ \dot{\mathbf{Z}} - \mathbf{V}_z \end{bmatrix} \tag{2.55}$$

$$\begin{bmatrix} \mathbf{f}^{\,\mathrm{II}}_{\mathbf{D_y}} \\ \mathbf{f}^{\,\mathrm{II}}_{\mathbf{D_z}} \end{bmatrix} = - \begin{bmatrix} c_n \mathbf{C}_\theta & c_t \mathbf{S}_\theta \\ -c_n \mathbf{S}_\theta & c_t \mathbf{C}_\theta \end{bmatrix} \mathrm{sgn}\left(\begin{bmatrix} \mathbf{V_{r_y}} \\ \mathbf{V_{r_z}} \end{bmatrix} \right) \begin{bmatrix} \mathbf{V_{r_y}}^2 \\ \mathbf{V_{r_z}}^2 \end{bmatrix} \tag{2.56}$$

$$\begin{bmatrix} \mathbf{V_{r_y}} \\ \mathbf{V_{r_z}} \end{bmatrix} = \begin{bmatrix} \mathbf{C}_\theta & -\mathbf{S}_\theta \\ \mathbf{S}_\theta & \mathbf{C}_\theta \end{bmatrix} \begin{bmatrix} \dot{\mathbf{Y}} - \mathbf{V}_y \\ \dot{\mathbf{Z}} - \mathbf{V}_z \end{bmatrix} \tag{2.57}$$

2.3.4 The Hydrostatic Model of Underwater Snake Robot

It is well-known that for an elliptical cylinder with uniformly mass distribution the center of gravity is the geometrical center of the cylinder. Furthermore, the center of buoyancy is located at the center of the volume of an object, which means that for the cylindrical joint the center of buoyancy is coincident with the center of gravity. Thus, we consider the following assumption in our modeling approach.

Assumption 2.5: The snake robot is considered not neutrally buoyant, while the center of gravity and the center of buoyancy are coincident. Since the center of gravity and buoyancy are coincident, the total moment due to the hydrostatic forces vanishes.

Remark 2.5: *Assumption 2.5 is a reasonable assumption for any symmetric object with uniformly mass distribution, i.e for a homogeneous symmetric body, the center of buoyancy and center of mass are equivalent [134].*

As pointed out in Assumption 2.5, the center of gravity, (y_{g_i}, z_{g_i}) and center of buoyancy, (y_{b_i}, z_{b_i}) coincide in each link of the robot, i.e $(y_i, z_i) = (y_{g_i}, z_{g_i}) = (y_{b_i}, z_{b_i})$. Using (2.45), it is obvious that the center of gravity and buoyancy of the snake also coincide, even if the center of the robot oscillates during the locomotion of the snake robot.

The hydrostatic forces are illustrated in Fig. 2.14 for the case of a tilted (inclined) plane (Fig. 2.13). Since the forces due to the gravity and buoyancy are neither parallel nor perpendicular to the inclined plane, it is imperative that it could be resolved into two components of force which are directed parallel and

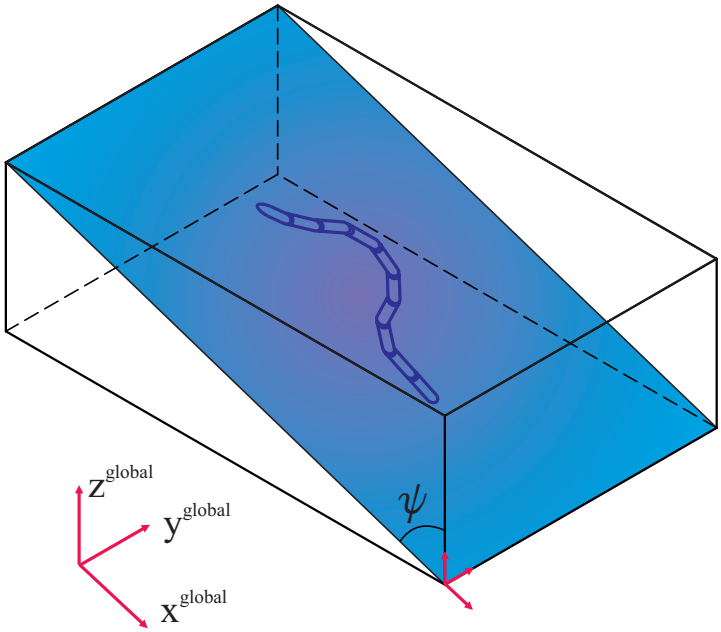

Figure 2.13: Visualization of a ten link underwater snake robot motion in any 2D tilted plane.

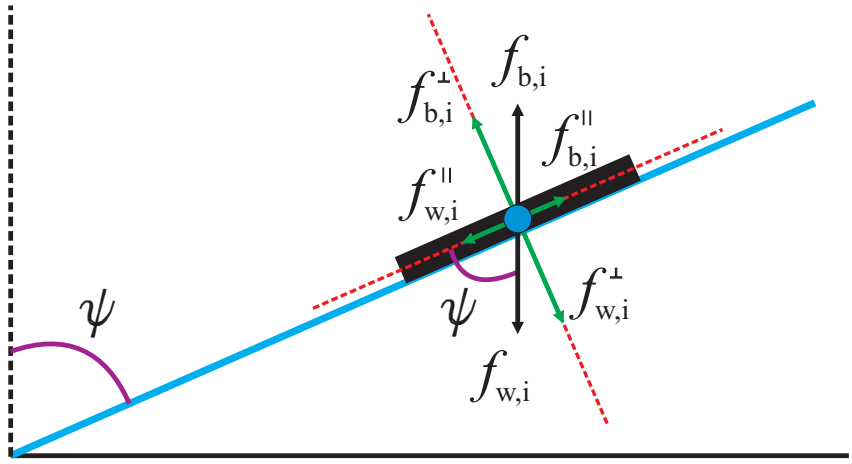

Figure 2.14: Hydrostatic forces.

perpendicular to the incline plane, shown in Fig. 2.13. Without loss of generality, in this paper we consider the case where the tilted plane angle is $\psi = 0$ (i.e. locomotion in vertical 2D plane of 3D).

Remark 2.6: *The hydrostatic forces and torques vanish for a neutrally buoyant un-*

derwater snake robot, leading to the conclusion that the proposed modeling approach is valid for underwater motion in any 2D-tilted plane of 3D. However, in this subsection the hydrostatic forces are analyzed for the tilted plane angle $\psi = 0$ under the Assumption 2.5, in order to investigate the results in locomotion of a not neutrally buoyant snake robot.

Gravity forces act at the center of gravity of each link in the system. The force due to gravity acting on an arbitrary link i is given by

$$f_{w,i} = -mg = -\rho_b V g, \tag{2.58}$$

where, ρ_b is the density of the joint, g is the acceleration of gravity and V is the volume of fluid displaced by link i. By assembling the forces on all links in vector form, we can rewrite the global frame gravity forces on the links as

$$\mathbf{f_w} = [f_{w,1}, f_{w,2}, \cdots, f_{w,n}]^T, \tag{2.59}$$

The buoyancy force is proportional to the mass of the fluid displaced by the link, it acts through the center of gravity of the link and is given by the expression

$$f_{b,i} = \rho V g, \tag{2.60}$$

where, ρ is the density of the fluid and (2.61) gives the sum of the hydrostatic forces in each joint.

$$f_{b,i} + f_{w,i} = \rho V g - \rho_b V g = m(\frac{\rho}{\rho_b} - 1)g. \tag{2.61}$$

By assembling the forces on all links in vector form, we can rewrite the global frame buoyancy forces on the links as

$$\mathbf{f_b} = [f_{b,1}, f_{b,2}, \cdots, f_{b,n}]^T, \tag{2.62}$$

Remark 2.7: *Note that if $\rho = \rho_b$ then the robot is neutrally buoyant, if $\rho > \rho_b$ the robot will float and if $\rho < \rho_b$ the robot will sink [112, 134].*

2.3.5 The Dynamics of the Underwater Snake Robot

The equations of motion for the underwater snake robot moving in vertical plane will be presented in this subsection. The $n+2$ degrees of freedom of the underwater snake robot are defined by the link angles $\boldsymbol{\theta} \in \mathbb{R}^n$ and the CM position $\mathbf{p}_{\text{CM}} \in \mathbb{R}^2$. We now present the equations of motion of the robot in terms of the acceleration of the link angles, $\ddot{\boldsymbol{\theta}}$, and the acceleration of the CM position, $\ddot{\mathbf{p}}_{\text{CM}}$.

The forces and torques acting on link i are visualized in Fig. 2.12. Each link $i \in \{1, \cdots, n\}$ is influenced by hydrodynamic forces $f_{y,i}$, $f_{z,i}$, the hydrostatic forces, $f_{b,i}$ and $f_{w,i}$, and also the joint constraint forces, $h_{y,i-1}$, $h_{z,i-1}$, $h_{y,i}$ and $h_{z,i}$ which keep the link connected to link $i-1$ and link $i+1$. The joint constraint forces are described in Table 2.2. Using the first principle, the forces and torques acting on link i are visualized in Fig. 2.12 and the force balance for link i in global frame coordinates is given by

$$\begin{aligned} m\ddot{y}_i &= h_{y,i} - h_{y,i-1} + f_{y,i}, \\ m\ddot{z}_i &= h_{z,i} - h_{z,i-1} + f_{z,i} + f_{b,i} + f_{w,i} \end{aligned} \tag{2.63}$$

The force balance equations for all links may be expressed in matrix form as

$$\begin{aligned} m\ddot{\mathbf{Y}} &= \mathbf{D}^T\mathbf{h}_y + \mathbf{f_y}, \\ m\ddot{\mathbf{Z}} &= \mathbf{D}^T\mathbf{h}_z + \mathbf{f_z} + \mathbf{f_b} + \mathbf{f_w}. \end{aligned} \tag{2.64}$$

Note that the link accelerations may also be expressed by differentiating (2.46) twice with respect to time. This gives

$$\begin{aligned} \mathbf{D}\ddot{\mathbf{Y}} &= l\mathbf{A}\left(\mathbf{S}_\theta\dot{\theta}^2 - \mathbf{C}_\theta\ddot{\theta}\right), \\ \mathbf{D}\ddot{\mathbf{Z}} &= l\mathbf{A}\left(\mathbf{C}_\theta\dot{\theta}^2 + \mathbf{S}_\theta\ddot{\theta}\right). \end{aligned} \tag{2.65}$$

We obtain the acceleration of the CM by differentiating (2.45) twice with respect to time, inserting (2.64), and noting that the constraint forces $\mathbf{h}_y$ and $\mathbf{h}_z$, are cancelled out when the link accelerations are summed. This gives

$$\begin{bmatrix} \ddot{p}_y \\ \ddot{p}_z \end{bmatrix} = \frac{1}{n}\begin{bmatrix} \mathbf{e}^T\ddot{\mathbf{Y}} \\ \mathbf{e}^T\ddot{\mathbf{Z}} \end{bmatrix} = \frac{1}{nm}\begin{bmatrix} \mathbf{e}^T & \mathbf{0}_{1\times n} \\ \mathbf{0}_{1\times n} & \mathbf{e}^T \end{bmatrix}\mathbf{f} + \frac{1}{nm}\begin{bmatrix} 0 \\ \mathbf{e}^T(\mathbf{f_b} + \mathbf{f_w}) \end{bmatrix}. \tag{2.66}$$

By inserting (2.49), (2.53) and (2.54) into (2.66) the acceleration of the CM may be expressed as

$$\begin{aligned} \begin{bmatrix} \ddot{p}_y \\ \ddot{p}_z \end{bmatrix} = &- \mathbf{M}_p\begin{bmatrix} \mathbf{e}^T\mu_n\mathbf{C}_\theta^2 & -\mathbf{e}^T\mu_n\mathbf{S}_\theta\mathbf{C}_\theta \\ -\mathbf{e}^T\mu_n\mathbf{S}_\theta\mathbf{C}_\theta & \mathbf{e}^T\mu_n\mathbf{S}_\theta^2 \end{bmatrix}\begin{bmatrix} l\mathbf{K}^T(\mathbf{S}_\theta\dot{\boldsymbol{\theta}}^2 - \mathbf{C}_\theta\ddot{\boldsymbol{\theta}}) \\ l\mathbf{K}^T(\mathbf{C}_\theta\dot{\boldsymbol{\theta}}^2 + \mathbf{S}_\theta\ddot{\boldsymbol{\theta}}) \end{bmatrix} \\ &- \mathbf{M}_p\begin{bmatrix} \mathbf{e}^T\mu_n\mathbf{S}_\theta\mathbf{C}_\theta & \mathbf{e}^T\mu_n\mathbf{C}_\theta^2 \\ -\mathbf{e}^T\mu_n\mathbf{S}_\theta^2 & -\mathbf{e}^T\mu_n\mathbf{S}_\theta\mathbf{C}_\theta \end{bmatrix}\begin{bmatrix} \mathbf{V}_y^a \\ \mathbf{V}_z^a \end{bmatrix}\dot{\boldsymbol{\theta}} \\ &+ \mathbf{M}_p\begin{bmatrix} \mathbf{e}^T\mathbf{f_{Dy}} \\ \mathbf{e}^T\mathbf{f_{Dz}} \end{bmatrix} + \mathbf{M}_p\begin{bmatrix} 0 \\ \mathbf{e}^T(\mathbf{f_b} + \mathbf{f_w}) \end{bmatrix}, \end{aligned} \tag{2.67}$$

where

$$\mathbf{M}_p = \begin{bmatrix} m_{11} & m_{12} \\ m_{21} & m_{22} \end{bmatrix} = \begin{bmatrix} nm + \mathbf{e}^T\mu_n\mathbf{C}_\theta^2\mathbf{e} & -\mathbf{e}^T\mu_n\mathbf{S}_\theta\mathbf{C}_\theta\mathbf{e} \\ -\mathbf{e}^T\mu_n\mathbf{S}_\theta\mathbf{C}_\theta\mathbf{e} & nm + \mathbf{e}^T\mu_n\mathbf{S}_\theta^2\mathbf{e} \end{bmatrix}^{-1}. \tag{2.68}$$

and $\mathbf{f_{Dy}} = \mathbf{f}^{\,\mathrm{I}}_{\mathbf{D_y}} + \mathbf{f}^{\,\mathrm{II}}_{\mathbf{D_y}}$ and $\mathbf{f_{Dz}} = \mathbf{f}^{\,\mathrm{I}}_{\mathbf{D_z}} + \mathbf{f}^{\,\mathrm{II}}_{\mathbf{D_z}}$ are the drag forces in y and z directions.

The torque balance for link i is given by

$$J\ddot{\theta}_i = u_i - u_{i-1} - l\sin\theta_i\left(h'_{z,i} + h'_{z,i-1}\right) + l\cos\theta_i\left(h_{y,i} + h_{y,i-1}\right) + \tau_i, \tag{2.69}$$

where $h'_{z,i} + h'_{z,i-1}$ is the joint constraint forces which contribute in the torque balance equation (the hydrostatic forces act in the center of gravity and thus the torques due to the gravity and buoyancy are removed). u_i and u_{i-1} are the actuator

torques exerted on link i from link $i+1$ and link $i-1$, respectively, and τ_i is the torque applied on link i by the fluid. Hence, the torque balance equations for all links are expressed in matrix form as

$$\mathbf{J}\ddot{\boldsymbol{\theta}} = \mathbf{D}^T\mathbf{u} - l\mathbf{S}_\theta\mathbf{A}^T\mathbf{h}_z^{'} + l\mathbf{C}_\theta\mathbf{A}^T\mathbf{h}_y + \boldsymbol{\tau}, \tag{2.70}$$

where $\boldsymbol{\tau}$ is given from (2.28).

Premultiplying (2.64) by $\mathbf{D}$ and solving for $\mathbf{h}_y$ and $\mathbf{h}_z^{'}$, we can write the expression for the joint constraint forces as

$$\begin{aligned}\mathbf{h}_y = (\mathbf{D}\mathbf{D}^T)^{-1}\mathbf{D}(&m\ddot{\mathbf{Y}} - \mu_n\mathbf{S}_\theta\mathbf{C}_\theta\ddot{\mathbf{Z}} + \mu_n(\mathbf{C}_\theta)^2\ddot{\mathbf{Y}} \\ &+ \mu_n(\mathbf{C}_\theta)^2\mathbf{V}_z^a\dot{\boldsymbol{\theta}} + \mu_n\mathbf{S}_\theta\mathbf{C}_\theta\mathbf{V}_y^a\dot{\boldsymbol{\theta}} - \mathbf{f}_{\mathbf{D_y}}^{\mathrm{I}} - \mathbf{f}_{\mathbf{D_y}}^{\mathrm{II}}).\end{aligned} \tag{2.71}$$

$$\begin{aligned}\mathbf{h}_z^{'} = (\mathbf{D}\mathbf{D}^T)^{-1}\mathbf{D}(&m\ddot{\mathbf{Z}} + \mu_n(\mathbf{S}_\theta)^2\ddot{\mathbf{Z}} - \mu_n\mathbf{S}_\theta\mathbf{C}_\theta\ddot{\mathbf{Y}} \\ &- \mu_n\mathbf{S}_\theta\mathbf{C}_\theta\mathbf{V}_z^a\dot{\boldsymbol{\theta}} - \mu_n(\mathbf{S}_\theta)^2\mathbf{V}_y^a\dot{\boldsymbol{\theta}} - \mathbf{f}_{\mathbf{D_z}}^{\mathrm{I}} - \mathbf{f}_{\mathbf{D_z}}^{\mathrm{II}})\end{aligned} \tag{2.72}$$

Inserting in (2.70) the joint constraints forces (2.71, 2.72) and also replacing $\mathbf{D}\ddot{\mathbf{Y}}$, $\mathbf{D}\ddot{\mathbf{Z}}$ with (2.65), $\ddot{\mathbf{Y}}$,$\ddot{\mathbf{Z}}$ with (2.49) and $\ddot{p}_y$, $\ddot{p}_z$ with (2.67), we can finally express the model of the robot as

$$\mathbf{M}_{\boldsymbol{\theta}}\ddot{\boldsymbol{\theta}} + \mathbf{W}_{\boldsymbol{\theta}}\dot{\boldsymbol{\theta}}^2 + \mathbf{V}_\theta\dot{\boldsymbol{\theta}} + \boldsymbol{\Lambda}_3|\dot{\boldsymbol{\theta}}|\dot{\boldsymbol{\theta}} + \mathbf{K}_{\mathbf{Dz}}\mathbf{f}_{\mathbf{Dz}} + \mathbf{K}_{\mathbf{Dy}}\mathbf{f}_{\mathbf{Dy}} = \mathbf{D}^T\mathbf{u}, \tag{2.73}$$

where $\mathbf{M}_\theta$, $\mathbf{W}_\theta$, $\mathbf{V}_\theta$, $\mathbf{K}_{\mathbf{Dz}}$ and $\mathbf{K}_{\mathbf{Dy}}$ are defined as

$$\mathbf{M}_\theta = \mathbf{J} + ml^2\mathbf{S}_\theta\mathbf{V}\mathbf{S}_\theta + ml^2\mathbf{C}_\theta\mathbf{V}\mathbf{C}_\theta + \boldsymbol{\Lambda}_1 + l^2\mu_n\mathbf{K}_1\mathbf{K}^T\mathbf{S}_\theta + l^2\mu_n\mathbf{K}_2\mathbf{K}^T\mathbf{C}_\theta \tag{2.74}$$

$$\mathbf{W}_\theta = ml^2\mathbf{S}_\theta\mathbf{V}\mathbf{C}_\theta - ml^2\mathbf{C}_\theta\mathbf{V}\mathbf{S}_\theta + l^2\mu_n\mathbf{K}_1\mathbf{K}^T\mathbf{C}_\theta - l^2\mu_n\mathbf{K}_2\mathbf{K}^T\mathbf{S}_\theta \tag{2.75}$$

$$\mathbf{V}_\theta = \boldsymbol{\Lambda}_2 - l\mu_n\mathbf{K}_2\mathbf{V}_z^a - l\mu_n\mathbf{K}_1\mathbf{V}_y^a \tag{2.76}$$

$$\mathbf{K}_{\mathbf{Dz}} = l\mu_n m_{22}\mathbf{A}_1\mathbf{e}\mathbf{e}^T - l\mu_n m_{12}\mathbf{A}_2\mathbf{e}\mathbf{e}^T - l\mathbf{S}_\theta\mathbf{K} \tag{2.77}$$

$$\mathbf{K}_{\mathbf{Dy}} = l\mu_n m_{21}\mathbf{A}_1\mathbf{e}\mathbf{e}^T - l\mu_n m_{11}\mathbf{A}_2\mathbf{e}\mathbf{e}^T + l\mathbf{C}_\theta\mathbf{K} \tag{2.78}$$

where

$$\begin{aligned}\mathbf{K}_1 &= \mathbf{A}_1 + \mu_n\mathbf{A}_1\mathbf{e}\mathbf{e}^T(m_{21}\mathbf{S}_\theta\mathbf{C}_\theta - m_{22}\mathbf{S}_\theta^2) - \mu_n\mathbf{A}_2\mathbf{e}\mathbf{e}^T(m_{11}\mathbf{S}_\theta\mathbf{C}_\theta - m_{12}\mathbf{S}_\theta^2),\\ \mathbf{K}_2 &= \mathbf{A}_2 - \mu_n\mathbf{A}_1\mathbf{e}\mathbf{e}^T(m_{22}\mathbf{S}_\theta\mathbf{C}_\theta - m_{21}\mathbf{C}_\theta^2) + \mu_n\mathbf{A}_2\mathbf{e}\mathbf{e}^T(m_{12}\mathbf{S}_\theta\mathbf{C}_\theta - m_{11}\mathbf{C}_\theta^2),\\ \mathbf{A}_1 &= \mathbf{S}_\theta\mathbf{K}\mathbf{S}_\theta^2 + \mathbf{C}_\theta\mathbf{K}\mathbf{S}_\theta\mathbf{C}_\theta,\\ \mathbf{A}_2 &= \mathbf{S}_\theta\mathbf{K}\mathbf{S}_\theta\mathbf{C}_\theta + \mathbf{C}_\theta\mathbf{K}\mathbf{C}_\theta^2.\end{aligned}$$

The equations of motion for the underwater snake robot are given by (2.67) and (2.73). By introducing the state variable $\mathbf{x} = \left[\boldsymbol{\theta}^T, \mathbf{p}_{\mathrm{CM}}^T, \dot{\boldsymbol{\theta}}^T, \dot{\mathbf{p}}_{\mathrm{CM}}^T\right]^T \in \mathbb{R}^{2n+4}$, we can rewrite the model of the underwater snake like robot compactly in state space form as

$$\dot{\mathbf{x}} = \left[\dot{\boldsymbol{\theta}}^T, \dot{\mathbf{p}}_{\mathrm{CM}}^T, \ddot{\boldsymbol{\theta}}^T, \ddot{\mathbf{p}}_{\mathrm{CM}}^T\right]^T = \mathbf{F}(\mathbf{x}, \mathbf{u}) \tag{2.79}$$

where the elements of $\mathbf{F}(\mathbf{x}, \mathbf{u})$ are easily found by solving (2.67) and (2.73) for $\ddot{\mathbf{p}}_{\mathrm{CM}}$ and $\ddot{\boldsymbol{\theta}}$, respectively.

Remark 2.8: *Note that the modeling approach presented in this subsection is valid for motion in any tilted plane of 3D for a neutrally buoyant underwater snake robot. Furthermore, it is interesting to note that if, in the dynamic model (2.67) and (2.73), we change the axis z with x and set the hydrostatic forces to zero, then the model reduces to an identical hydrodynamic model of an underwater snake robot moving in a virtual horizontal plane, described in previous Section 2.2. Hence, the underwater snake robot moving in any 2D plane of 3D presented in this section is thus an extension of the underwater snake robot moving in a virtual horizontal plane shown in Section 2.2.*

2.3.6 Simulation Study

We now will present simulation results for three different modeling approaches:

- **case 1**–Added mass and nonlinear drag effect,
- **case 2**–Added mass, linear and nonlinear drag effect and
- **case 3**–Added mass, linear, nonlinear drag and current effects.

Simulation results are presented for the two most common motion patterns: lateral undulation and eel-like motion. The models were implemented in *Matlab R2013b*. The dynamics was calculated using the *ode23tb* solver with a relative and absolute error tolerance of 10^{-4}.

Simulation parameters

A snake robot was considered with $n = 10$ links, each one having length $2l = 0.14$ m and mass $m = \rho_b V$ kg. Three different values for the density of the snake robot are examined, $\rho_b = (1000, 998, 1002)\text{kg/m}^3$. The initial values of the states of the underwater snake robot were set to zero, i.e. the snake robot is initially at rest at the origin, with its heading along the inertial z axis. The hydrodynamic related parameters, $\hat{\mathbf{C}}_D$, $\hat{\mathbf{C}}_A$, λ_1, λ_2, λ_3, for the elliptic section with half small and great axis' length 0.03 m and 0.05 m, respectively, $\rho = 1000$ kg/m^3, $C_f = 0.03$, $C_D = 2$, $C_A = 1$ and $C_M = 1$ were calculated using (2.14), (2.15), (2.17) and (2.20), respectively. Additionally, the anisotropic friction property is achieved by a low drag coefficient in the tangential direction and a higher one in the perpendicular. The values of a constant irrotational current in the inertial frame are set to $[0.1, 0.1]$ m/sec. In these simulations a joint PD controller (3.5) is used with parameters $k_p = 200, k_d = 50$, while lateral undulation or eel-like motion are achieved by moving the joints according to (3.1) or (3.2), respectively, with gait parameters $\alpha = 30^o$, $\delta = 50^o$, $\omega = 70^o$/sec and $\phi_0 = 0^o$.

Simulation Results

Simulation results for lateral undulation and eel-like motion of the underwater snake robot will be presented for the three different cases. In particular, the motion of the center of mass is presented in Fig. 2.15-2.17 and Fig. 2.21-2.23 for lateral undulation and eel-like motion, respectively. The forward velocity (2.5) is presented in Fig. 2.18-2.20 and Fig. 2.24-2.26, respectively, for lateral undulation and eel-like motion patterns. All the simulation results are presented in case that a) the density of the robot is less than the density of the water, b) for neutrally

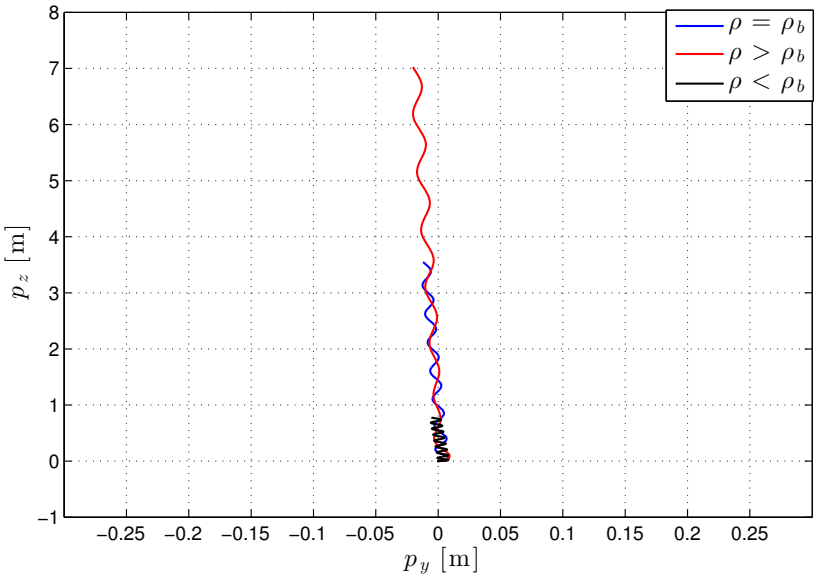

Figure 2.15: Case 1: The position of the CM of the robot for lateral undulation motion pattern.

buoyant robot and c) for the case where the density of the body is greater than the density of the water. These cases are examined in order to investigate the total motion response of a not neutrally buoyant underwater snake robot considering three different modeling approaches. From the simulation results, we can argue that small variations between ρ_b and ρ have a negligible effect in the total motion response of the underwater snake robot, in the case where the detailed modeling of the hydrodynamic effects is considered (Fig.2.17,2.26). This indicates that the modeling with detailed modeling of the hydrodynamic effects is less sensitive in variation between the density of the water and the density of the body. However, in case 1, where only the added mass and linear drag effects are considered, it is shown that even small variation between the densities has significant effects in the overall motion (Fig. (2.15,2.18,2.21,2.24)). In particular, for eel-like motion pattern when $\rho < \rho_b$, the robot moves backwards (Fig. (2.21,2.24)) and this happens because the robot did not manage to achieve positive forward propulsion for the chosen parameters of eel-like motion. However, it can be easily seen that the effects of error between the ρ and ρ_b vanish in Fig. (2.23,2.26).

2.4 Chapter Summary

This chapter is summarized as follows:

- We have presented mathematical models of an underwater snake robot with n rigid links interconnected by $n-1$ motorized joints moving either in a

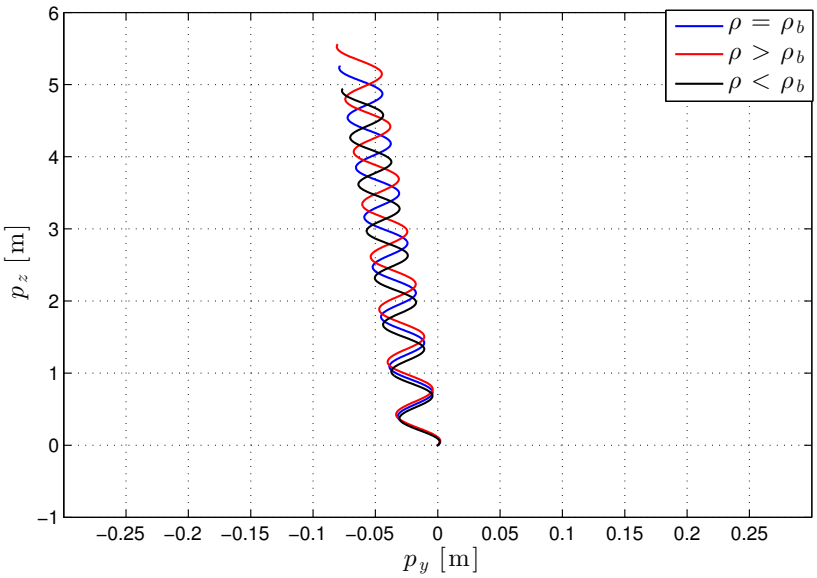

Figure 2.16: Case 2: The position of the CM of the robot for lateral undulation motion pattern.

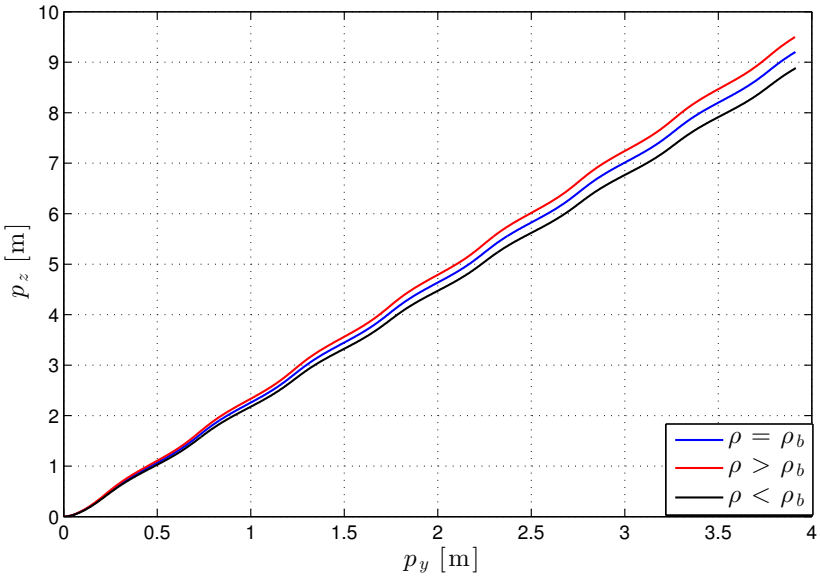

Figure 2.17: Case 3: The position of the CM of the robot for lateral undulation motion pattern.

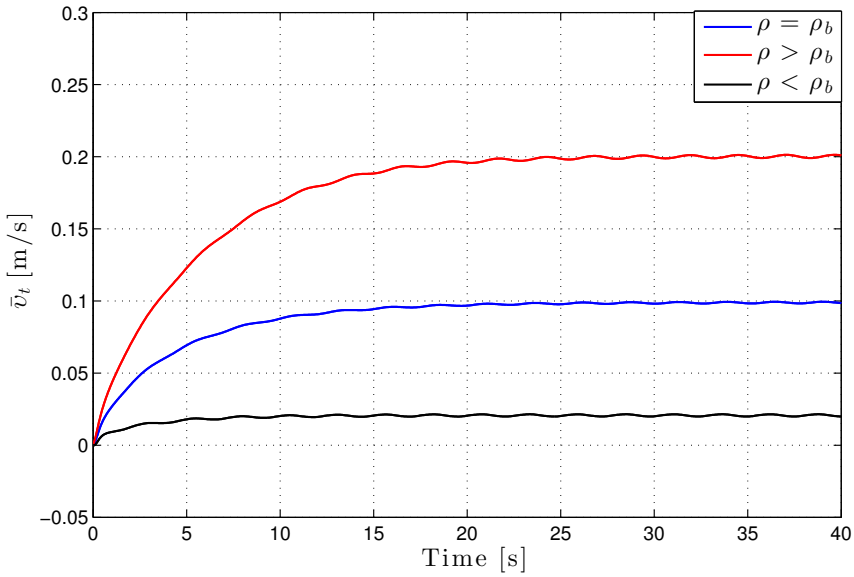

Figure 2.18: Case 1: The forward velocity of the robot for lateral undulation motion pattern.

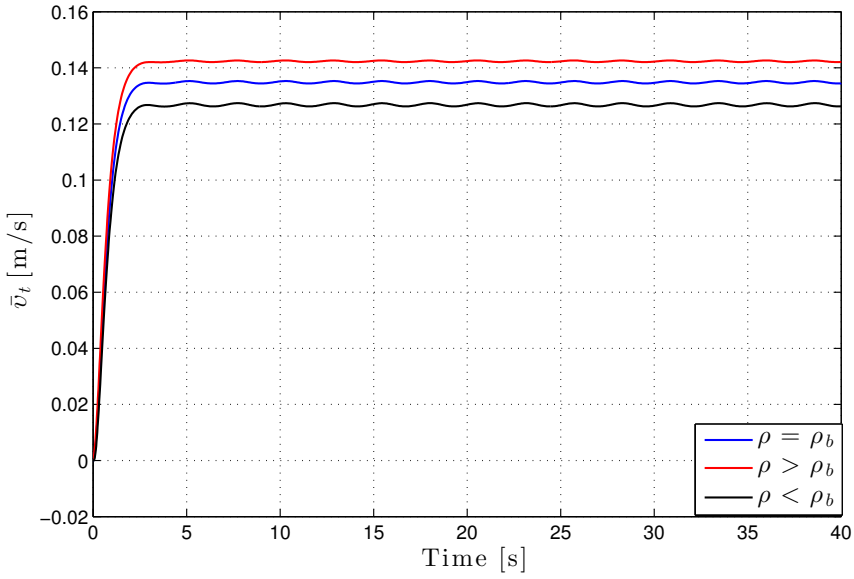

Figure 2.19: Case 2: The forward velocity of the robot for lateral undulation motion pattern.

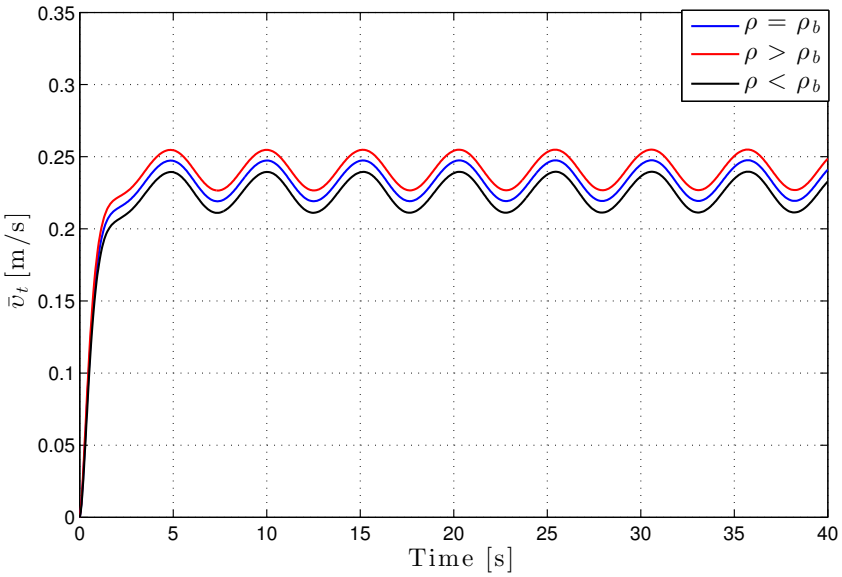

Figure 2.20: Case 3: The forward velocity of the robot for lateral undulation motion pattern.

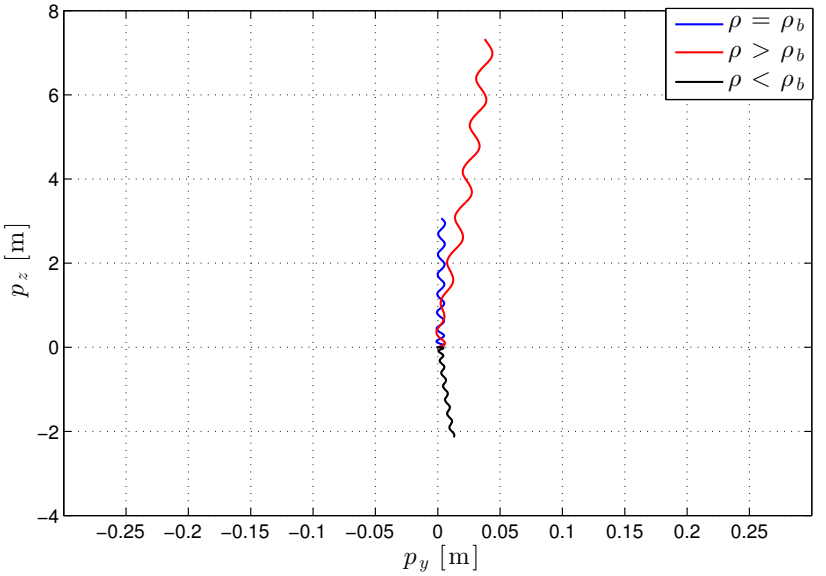

Figure 2.21: Case 1: The position of the CM of the robot for eel-like motion pattern.

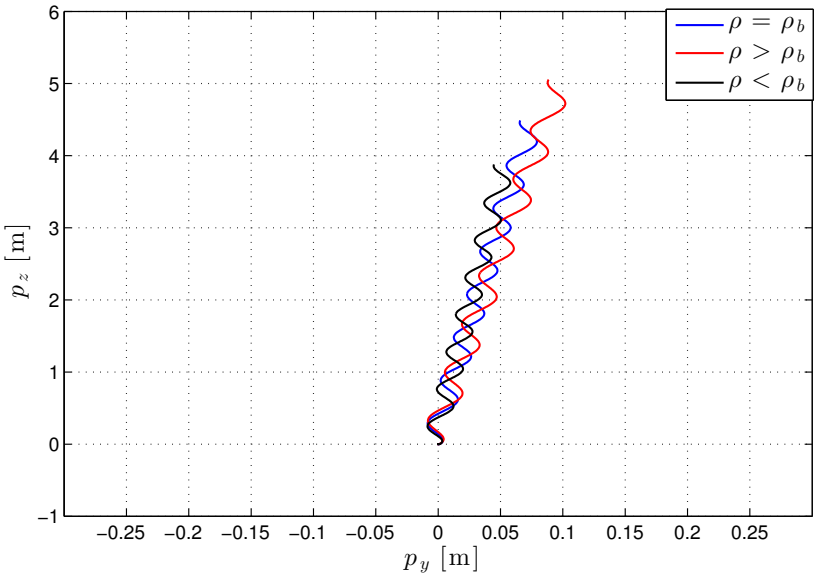

Figure 2.22: Case 2: The position of the CM of the robot for eel-like motion pattern.

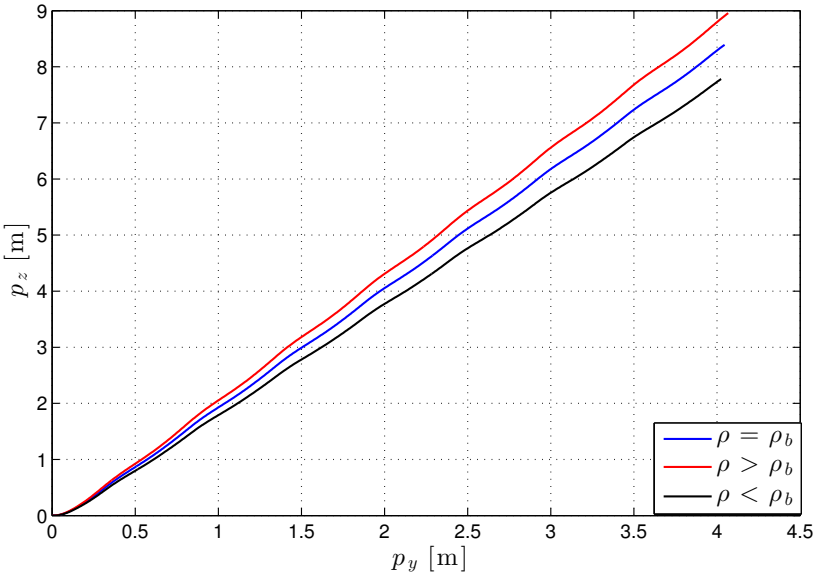

Figure 2.23: Case 3: The position of the CM of the robot for eel-like motion pattern.

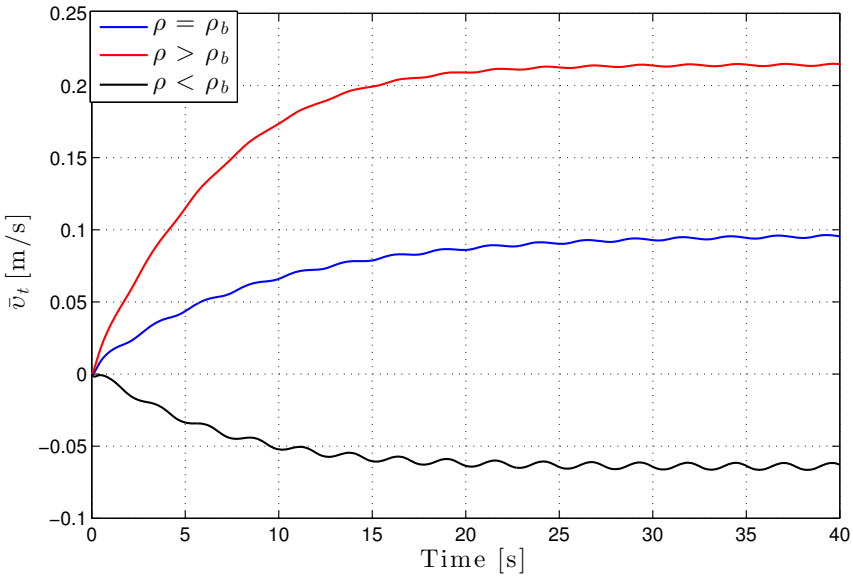

Figure 2.24: Case 1: The forward velocity of the robot for eel-like motion pattern.

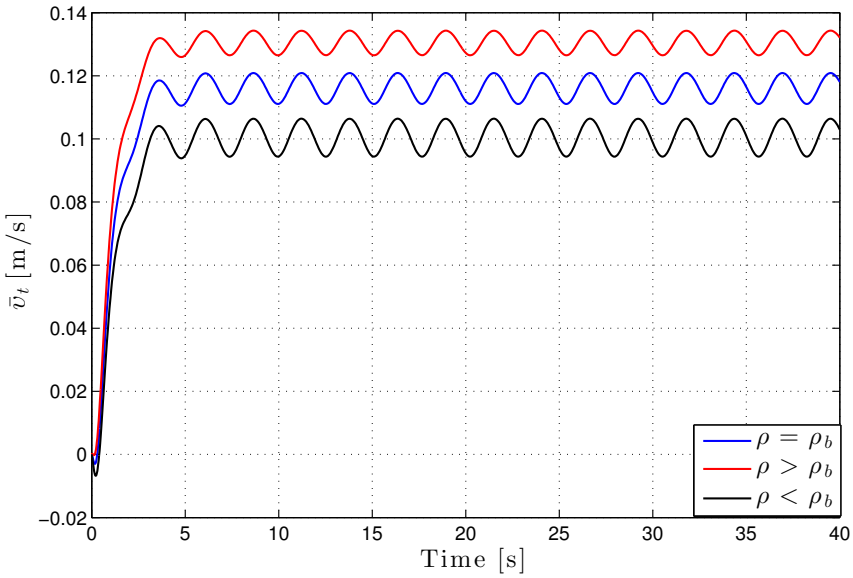

Figure 2.25: Case 2: The forward velocity of the robot for eel-like motion pattern.

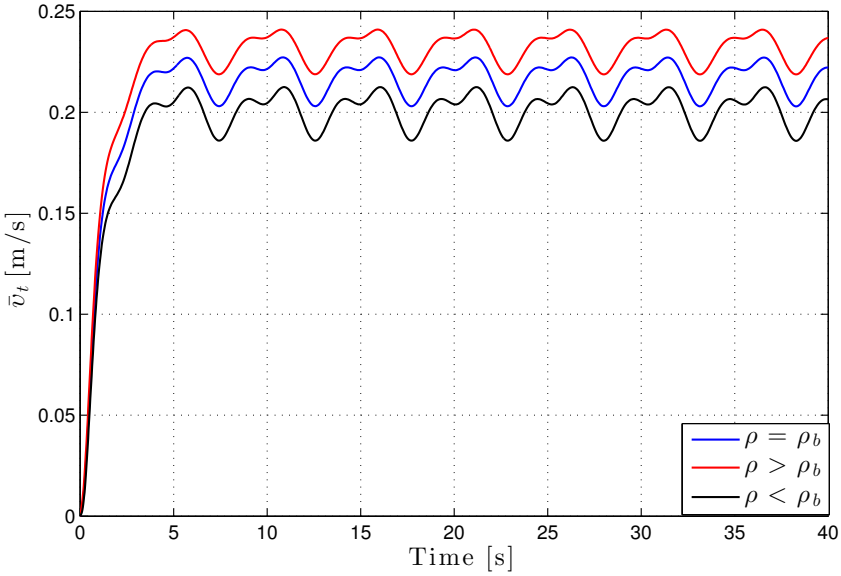

Figure 2.26: Case 3: The forward velocity of the robot for eel-like motion pattern.

virtual horizontal plane or a virtual vertical plane.

- We have developed a hydrodynamic model of the underwater snake robot considering the combination of linear and nonlinear drag forces, the added mass effect, the fluid moments and current effects. The hydrodynamic models given in (2.23) and (2.53) are in closed-form avoiding the numerical evaluations of drag effects.
- We have developed a hydrostatic model for underwater snake robots fully submerged swimming in a virtual vertical plane. In this case, the proposed modeling approach takes into account the hydrostatic forces due to the buoyancy and gravity.
- The equation of motion of the underwater snake robot in terms of acceleration of the link angles, $\ddot{\boldsymbol{\theta}}$, and the acceleration of the CM position, $\ddot{\mathbf{p}}_{\mathrm{CM}}$, are given by (2.33,2.38) and by (2.67,2.73) for motion in the horizontal and vertical plane, respectively.
- The model of underwater snake robots in (2.67,2.73) is valid for motion in any 2D tilted plane of 3D for a neutrally buoyant underwater snake robot.
- The developed models (2.33,2.38) and (2.67,2.73) for underwater snake robots are in closed-form and are thus particularly well-suited for model-based control design schemes.

Chapter 3

Analysis and Synthesis of Underwater Snake Robot Locomotion

Inspired by biological swimming creatures, underwater snake robots robots are intended to meet the growing need for robotic mobility in underwater environments. Thus, they bring a promising perspective on improving the efficiency and maneuverability of modernday underwater vehicles. Generally, studies of hyper-redundant mechanisms (HRMs), also known as snake robots, have largely restricted themselves to land-based studies [101]. However, the amphibious snake robots have the advantage to adapt to aquatic environments while the physiology of the robot remains the same. In Chapter 2, we have presented a modeling approach for underwater snake robots that results in a closed-form solution. This modeling approach takes into account both the linear and nonlinear drag forces (resistive fluid forces), the added mass effect (reactive fluid forces), the fluid moments and current effect. As it is already noted, the hydrodynamic forces (fluid forces) induced by the motion of a rigid body in an underwater environment are very complex and highly nonlinear. Therefore, in this chapter we are conducting an extensive analysis of the complex model of a fully immersed underwater snake robot moving in a virtual horizontal plane, and from this analysis a set of essential properties that characterize the overall motion of underwater snake robots is derived. These essential properties form the basis of the model developed in Chapter 4, which is a control-oriented model of underwater snake robot locomotion aimed at control design and stability analysis purposes.

In this chapter, we investigate the two most common motion patterns for underwater snake robot locomotion: lateral undulation and eel-like motion patterns. Generally, in order to achieve lateral undulation, the robot is commanded to follow the serpenoid curve as proposed in [51], while eel-like motion can be achieved by propagating lateral axial undulations with increasing amplitude from nose to tail [26]. Furthermore, in this chapter we introduce a general sinusoidal motion pattern, which can be used for a broad class of motion patterns including lateral undulation and eel-like motion.

Contributions of this Chapter: The first contribution of this chapter is a general sinusoidal motion pattern which is introduced, and it can be used to describe a broad class of motion patterns for underwater snake robot locomotion including lateral undulation and eel-like motion. The second contribution of the chapter is to develop fundamental properties of underwater snake robot locomotion. In particular, we are conducting an extensive analysis of the complex model presented in Chapter 2.2, and from this analysis a set of essential properties that characterize the overall motion of underwater snake robots is derived (see Property 3.1-3.3). Based on this analysis the hydrodynamic effects which are essential for the overall behavior of the swimming snake robot are identified. In addition, propositions regarding the turning motion of an underwater snake robot (see Proposition 3.1) and the relative displacement of the links during both lateral undulation and eel-like motion patterns (see Proposition 3.2) are addressed. The Properties 3.1-3.3 and Propositions 3.1-3.2 form the basis of the control-oriented model developed in Chapter 4.

Organization of this Chapter: This chapter is organized as follows. In Section 3.1, a general sinusoidal motion pattern for underwater snake robot locomotion is introduced, followed by the presentation of different control laws for the joints of the underwater snake robot in Section 3.2. Section 3.3 presents fundamental properties that characterize the overall motion of underwater snake robots. The properties regarding the turning motion and the relative displacements of the links both for lateral undulation and eel-like motion patterns are presented in Section 3.4 and Section 3.5, respectively. Finally, the chapter is summarized in Section 3.6.

Publications: The material in this chapter is based on the journal papers [72] and the conference papers [68], [69] and [70].

3.1 The General Sinusoidal Motion Pattern

The mathematical expression for the gait of the snake robot in locomotion studies depends on its construction and model. Previous studies of swimming snake robots have been focused on two motion patterns: lateral undulation and eel-like motion. Lateral undulation [101], which is the fastest and the most common form of ground snake locomotion, can be achieved by creating continuous body waves, with constant amplitude, that are propagated backwards from head to tail. In order to achieve lateral undulation, the snake is commanded to follow the serpenoid curve as proposed in [51]. The gait pattern lateral undulation can be achieved by controlling each joint of the underwater snake robot according to the sinusoidal reference

$$\phi_i^* = \alpha \sin(\omega t + (i-1)\delta) + \phi_0, \quad i \in \{1, \cdots, n-1\} \ , \tag{3.1}$$

where the parameter α corresponds to the amplitude of the serpentine wave that propagates along the body of the snake robot, ω is the angular frequency of the sinusoidal joint motion, δ determines the phase shift between the sequential joints, and ϕ_0 is the joint offset that is used to control the direction of the motion.

From the other hand, eel-like motion can be achieved by propagating lateral axial undulations with increasing amplitude from nose to tail [26]. This type of

swimming is called anguilliform swimming among elongate fish, such as eels and lampreys. A simple equation is derived for the eel-like motion by controlling each joint of the snake robot according to the reference signal

$$\phi_i^* = \alpha \left(\frac{n-i}{n+1} \right) \sin(\omega t + (i-1)\delta) + \phi_0, \quad i \in \{1, \cdots, n-1\} \ , \tag{3.2}$$

where the parameter $\alpha(n-i)/(n+1)$ corresponds to the increasing amplitude, from nose to tail, of the wave that propagates along the body of the snake robot, ω is the angular frequency of the sinusoidal joint motion, δ determines the phase shift between the joints, and ϕ_0 is the joint offset.

We now summarize the above discussion by presenting a general sinusoidal motion pattern which can be used for a broad class of motion patterns including lateral undulation and eel-like motion.

Definition 3.1: A general sinusoidal motion pattern is achieved by moving the joints of an underwater snake robot according to

$$\phi_i^* = \alpha \mathrm{g}(i, n) \sin(\omega t + (i-1)\delta) + \phi_0, \tag{3.3}$$

where $i \in \{1, \cdots, n-1\}$, α and ω are the maximum amplitude and frequency, respectively, of the sinusoidal joint motion, δ determines the phase shift between the joints, while the function $\mathrm{g}(i, n)$ is a scaling function for the amplitude of joint i.

Remark 3.1: *The scaling function for the amplitude of joint i, $\mathrm{g}(i, n)$, allows (3.3) to describe a quite general class of sinusoidal functions and corresponding snake motion patterns. For instance, $\mathrm{g}(i, n) = 1$ gives lateral undulation, while $\mathrm{g}(i, n) = (n-i)/(n+1)$ gives eel-like motion.*

Remark 3.2: *The parameter ϕ_0 is a joint offset coordinate that can be used to control the direction of the locomotion [49, 101]. In particular in [101] and [49], ϕ_0 affects the direction locomotion in the case of land-based snake robots and fish robots, respectively.*

Remark 3.3: *Note that for amphibious robots, the lateral undulation is the most common mode of locomotion in order to traverse any uneven terrain or confined spaces, like tunnels or pipes, whereas for locomotion in three-dimensional dynamic aquatic environments the eel-like motions are considered as the most appropriate. To this end, in this thesis we consider both lateral undulation and eel-like motion patterns in the following chapters.*

3.2 The Control System of the Joints

In this thesis, we consider two different control laws to calculate the actuator torques of the joints from their reference angles. The joint controller is responsible for making the joint angles $\boldsymbol{\phi} = [\phi_1, \cdots, \phi_{n-1}]$ track the joint reference angles, $\boldsymbol{\phi}^* = [\phi_1^*, \cdots, \phi_{n-1}^*]$. In particular, we assume that the control input $\mathbf{u} \in \mathbb{R}^{n-1} =$

$[u_1, \cdots, u_{n-1}]$ of the models presented in this thesis is set according to either a simple PD joint controller given by

$$\mathbf{u} = k_p(\boldsymbol{\phi}^* - \boldsymbol{\phi}) - k_d\dot{\boldsymbol{\phi}}, \tag{3.4}$$

or a standard PD-controller given by

$$\mathbf{u} = \ddot{\boldsymbol{\phi}}^* + k_d(\dot{\boldsymbol{\phi}}^* - \dot{\boldsymbol{\phi}}) + k_p(\boldsymbol{\phi}^* - \boldsymbol{\phi}), \tag{3.5}$$

where $k_p > 0$ and $k_d > 0$ are the gains of the controller. Note that for a general sinusoidal motion pattern according to (3.3), we can easily calculate $\ddot{\boldsymbol{\phi}}^*$ and $\dot{\boldsymbol{\phi}}^*$, if ϕ_0 is assumed to be a constant offset [101]. This gives

$$\dot{\phi}_i^* = \alpha \mathrm{g}(i,n)\omega\cos(\omega t + (i-1)\delta), \qquad i \in \{1, \cdots, n-1\}, \tag{3.6}$$

$$\ddot{\phi}_i^* = -\alpha \mathrm{g}(i,n)\omega^2\sin(\omega t + (i-1)\delta), \qquad i \in \{1, \cdots, n-1\}. \tag{3.7}$$

In case that the joint offset in not constant but instead is a complex function of time and it is not easy to obtain analytical expressions for $\ddot{\phi}_i^*$ and $\dot{\phi}_i^*$, then $\ddot{\phi}_i^*$ and $\dot{\phi}_i^*$ can be obtained by using the 3rd order low pass filtering reference model, as presented in [101].

Remark 3.4: *In this thesis, we will use the simple PD controller (3.4) when we do not require to calculate the derivative of ϕ_i^* with respect to time. In this simple controller a velocity reference is not included in (3.4) since the purpose of the derivative part is simply to damp the joint motion, if the joint velocities become large. However, the disadvantage of this simpler joint controller is that it is unable to track time-varying joint reference angles perfectly. In all the other cases, we will use the standard PD controller as defined in (3.5) and when it is necessary the derivatives of the joint reference signal will be obtained using 3rd low pass filtering reference model [101].*

3.3 Analysis of Propulsive Forces

In this section, the complex model presented in Section 2.2 will be analyzed in order to identify a set of properties that characterize the motion of an underwater snake robot. These properties will be used as a basis for the development of a control-oriented model of an underwater snake robot moving in a virtual horizontal plane in Chapter 4. In particular, for simplicity, we choose to consider a fluid dynamic model where only the added mass effect (reactive fluid forces), linear drag forces (resistive fluid forces) and the fluid torques due to the added mass and drag forces are considered. This leads to simpler equation of motion compared to the full hydrodynamic modeling approach described in Section 2.2. Note that the analysis of the full hydrodynamic model that includes the nonlinear drag term and the currents effects can be considered as future work.

Under anisotropic drag forces, a link has two drag fluid coefficients, c_t and c_n, describing the resistive fluid force in the tangential (along link x axis) and the normal (along link y axis) direction of the link, respectively. The added mass fluid coefficient in the normal direction of the link is denoted by μ_n. As shown in

Subsection 2.2.3, the fluid forces on the link i, denoted by $\mathbf{f}_i \in \mathbb{R}^2$, can be written in terms of the link velocity, $\dot{x}_i$ and $\dot{y}_i$, and the link acceleration, $\ddot{x}_i$ and $\ddot{y}_i$, as

$$\mathbf{f}_i = \begin{bmatrix} f_{x,i} \\ f_{y,i} \end{bmatrix} = -\begin{bmatrix} F^a_x(\theta_i) & F^a_{xy}(\theta_i) \\ F^a_{xy}(\theta_i) & F^a_y(\theta_i) \end{bmatrix} \begin{bmatrix} \ddot{x}_i \\ \ddot{y}_i \end{bmatrix} - \begin{bmatrix} F^d_x(\theta_i) & F^d_{xy}(\theta_i) \\ F^d_{xy}(\theta_i) & F^d_y(\theta_i) \end{bmatrix} \begin{bmatrix} \dot{x}_i \\ \dot{y}_i \end{bmatrix}, \tag{3.8}$$

where

$$F^a_x(\theta_i) = \mu_n \sin^2(\theta_i), \tag{3.9a}$$
$$F^a_{xy}(\theta_i) = -\mu_n \sin\theta_i \cos\theta_i, \tag{3.9b}$$
$$F^a_y(\theta_i) = \mu_n \cos^2(\theta_i), \tag{3.9c}$$
$$F^d_x(\theta_i) = c_t \cos^2(\theta_i) + c_n \sin^2(\theta_i), \tag{3.9d}$$
$$F^d_{xy}(\theta_i) = (c_t - c_n) \sin\theta_i \cos\theta_i, \tag{3.9e}$$
$$F^d_y(\theta_i) = c_t \sin^2(\theta_i) + c_n \cos^2(\theta_i). \tag{3.9f}$$

By taking into account the added mass and linear drag effects the equation of the motion of the underwater snake robot presented in Section 2.2 can be written as

$$\mathbf{M}_{\boldsymbol{\theta}}\ddot{\boldsymbol{\theta}} + \mathbf{W}_{\boldsymbol{\theta}}\dot{\boldsymbol{\theta}}^2 + \mathbf{V}_{\theta}\dot{\boldsymbol{\theta}} + \mathbf{K}_{\mathbf{Dx}}\mathbf{f}^{\mathbf{I}}_{\mathbf{Dx}} + \mathbf{K}_{\mathbf{Dy}}\mathbf{f}^{\mathbf{I}}_{\mathbf{Dy}} = \mathbf{D}^T\mathbf{u}, \tag{3.10a}$$
$$nm\ddot{p}_x = \sum_{i=1}^{n} f_{x,i}, \tag{3.10b}$$
$$nm\ddot{p}_y = \sum_{i=1}^{n} f_{y,i}. \tag{3.10c}$$

We begin by deriving an expression for the total force propelling the CM of the underwater snake forward. We choose the inertial coordinate system such that the forward direction of the motion of the underwater snake robot is along the global positive x axis, which means that the propulsive force is simply the sum of all external forces on the robot in the global x direction. Hence, the total force propelling the CM of the robot forward is given as

$$\begin{aligned} nm\ddot{p}_x = \sum_{i=1}^{n} f_{x,i} = &-\sum_{i=1}^{n} F^a_x(\theta_i)\ddot{x}_i - \sum_{i=1}^{n} F^a_{xy}(\theta_i)\ddot{y}_i \\ &- \sum_{i=1}^{n} F^d_x(\theta_i)\dot{x}_i - \sum_{i=1}^{n} F^d_{xy}(\theta_i)\dot{y}_i. \end{aligned} \tag{3.11}$$

From (3.11), we can see that the total propulsive force consists of four components: a) first one involving the linear acceleration of the link in the forward direction of motion, $F^a_x(\theta_i)\ddot{x}_i$, b) the second one involving the linear acceleration normal to the direction of motion, $F^a_{xy}(\theta_i)\ddot{y}_i$, c) the third one involving the linear velocity of the link in the forward direction of the motion, $F^d_x(\theta_i)\dot{x}_i$, and d) the last one involving the linear velocity of the link normal to the direction of motion, $F^d_{xy}(\theta_i)\dot{y}_i$. It is easily seen that, due to the minus signs in (3.11), all the components (3.9a)-(3.9f) provide a positive contribution to the propulsive force only if they are negative.

Considering that the fluid coefficients due to the drag and the added mass effects are positive, c_t, c_n and μ_n, are always positive, the expressions $F_x^a(\theta_i)$ (3.9a) and $F_x^d(\theta_i)$ (3.9d) are also positive. Initially, we consider the case that when the robot is moving in the forward direction with $\dot{p}_x > 0$ and $\ddot{p}_x > 0$, which means that $\dot{x}_i > 0$ and $\ddot{x}_i > 0$, and therefore the products $F_x^a(\theta_i)\ddot{x}_i$ and $F_x^d(\theta_i)\dot{x}_i$ are always positive. Hence, we can conclude that in this case these products are not contributing to the forward propulsion of the robot. In addition, it is easily seen that when the robot is moving forward with $\dot{p}_x > 0$ and $\ddot{p}_x < 0$, which means that $\dot{x}_i > 0$ and $\ddot{x}_i < 0$, the product $F_x^a(\theta_i)\ddot{x}_i$ is contributing to the forward propulsion of the robot. Note that the magnitude of the propulsive force increases by decreasing the linear acceleration of the link in the forward direction, $\ddot{x}_i$.

Now, what remains is to analyze the effects of the products $F_{xy}^a(\theta_i)\ddot{y}_i$ and $F_{xy}^d(\theta_i)\dot{y}_i$. A plot of $F_{xy}^a(\theta_i)$ for different values of μ_n is shown in Fig. 3.1, while a plot of $F_{xy}^d(\theta_i)$ for different values of c_n and $c_t = 1$ is shown in Fig. 3.2. In each plot, the angle between the link and the forward direction, θ_i, is varied from -90° to 90°. We see that when $c_n = c_t$, i.e. the drag coefficients are equal, there is no effect on the propulsive force of the underwater snake robot due to the drag effect, since this gives $F_{xy}^d(\theta_i) = 0$. It is easily seen (Fig. 3.2) that when the $c_n > c_t$ the component $F_{xy}^d(\theta_i)$ is negative as long as θ_i is positive, and vice versa. This means that the product $F_{xy}^d(\theta_i)\dot{y}_i$ is negative as long as $\text{sgn}(\theta_i) = \text{sgn}(\dot{y}_i)$. In addition, from Fig. 3.1 it is seen that for any positive value of μ_n the component $F_{xy}^a(\theta_i)$ is negative as long as θ_i is positive, and vice versa. It should be noted that the only case that $F_{xy}^a(\theta_i) = 0$ is the case where the parameter $\mu_n = 0$, i.e. the case where the added mass effects are neglectable. Hence, we can conclude that for any positive values of parameters μ_n the product $F_{xy}^a(\theta_i)\ddot{y}_i$ is negative as long as $\text{sgn}(\theta_i) = \text{sgn}(\ddot{y}_i)$.

Additionally, we see that for a given $\ddot{y}_i$ and $\dot{y}_i$, a link produces its highest propulsive force when it forms an angle of $\pm 45^\circ$ with the forward direction of motion. It should be noted that the magnitude of the propulsive force becomes greater by increasing c_n with respect to c_t, or by increasing the magnitude of the sideways link velocity, $\dot{y}_i$, by increasing the parameter μ_n, or by increasing the magnitude of the sideways link acceleration, $\ddot{y}_i$ and by increasing the parameter μ_n, or by decreasing the linear acceleration of the link in the forward direction, $\ddot{x}_i$.

Remark 3.5: *In Fig. 3.1-3.2 we present the mapping from the sideways link motion to the forward propulsion for some fluid coefficients values without missing the generality of the analysis [101].*

Now, we can summarize the properties of an underwater snake robot locomotion based on the previous analysis.

Property 3.1: For an underwater snake robot described by (3.10) with $c_n > c_t$, $\mu_n > 0$, $\dot{x}_i > 0$ and $\ddot{x}_i > 0$, forward propulsion is produced by link velocity and link acceleration components that are normal to the forward direction.

Property 3.2: For an underwater snake robot described by (3.10) with $c_n > c_t$, $\mu_n > 0$, $\dot{x}_i > 0$ and $\ddot{x}_i > 0$, the propulsive force generated by the transversal motion of link i is positive as long as $\text{sgn}(\theta_i) = \text{sgn}(\dot{y}_i)$ and $\text{sgn}(\theta_i) = \text{sgn}(\ddot{y}_i)$.

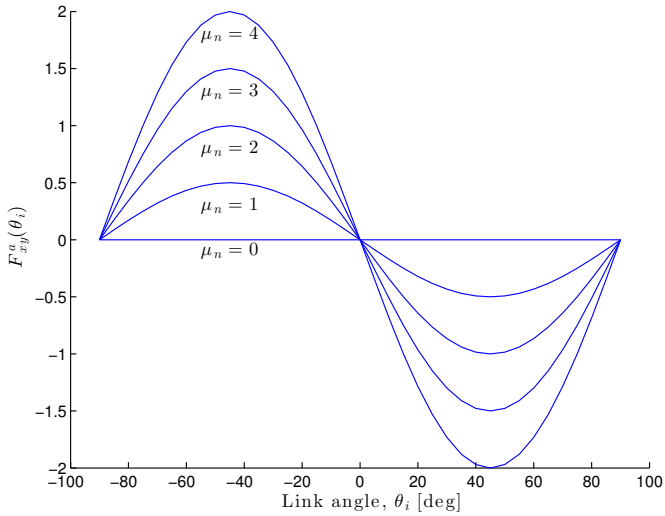

Figure 3.1: The mapping from the sideways link motion to the forward propulsion for the added mass component of the fluid forces.

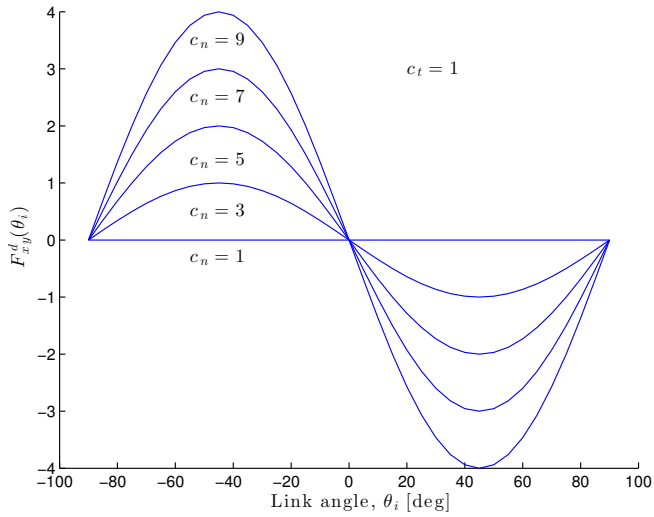

Figure 3.2: The mapping from the sideways link motion to the forward propulsion for the drag component of the fluid forces.

Property 3.3: For an underwater snake robot described by (3.10) with $c_n > c_t$, $\mu_n > 0$, $\dot{x}_i > 0$ and $\ddot{x}_i > 0$, the magnitude of the propulsive force produced by link i increases when $|\theta_i|$ increases as long as $|\theta_i| < 45°$.

Property 3.4: For an underwater snake robot described by (3.10) with $c_n > c_t$, $\mu_n > 0$, $\dot{x}_i > 0$ and $\ddot{x}_i < 0$, forward propulsion is produced by link velocity and link acceleration components that are normal to the forward direction and also by the linear acceleration of the links in the forward direction.

Remark 3.6: *It is worth mentioning that the results presented in this section are general, because they are based on a more general sinusoidal motion pattern than what has been analysed in previous literature.*

3.4 Analysis of Turning Motion

In the previous section, we determined how propulsion is generally achieved with an underwater snake robot, while in this section we will investigate how turning motion is achieved through simulations. In particular, we investigate the turning motion for the two most common locomotion patterns for swimming snakes: In the first case the underwater snake robot moves by lateral undulation and in the second case the robot moves by eel-like motion pattern. Both gait patterns, lateral undulation and eel-like motion, consist of horizontal waves that are propagated backward along the underwater snake body from head to tail, with the difference that in the latter the amplitude of the wave increases from the head to tail. The lateral undulation and eel-like motion are realized by controlling each joint of the robot according to (3.1) and (3.2), respectively.

The effect of changing the turning parameter is illustrated in Fig. 3.3-3.6 for lateral undulation and eel-like motion. These present the results of a simulation of an underwater snake robot described by (3.10) with $n = 10$ links of length $l = 0.14$ m and mass $m = 0.6597$ kg. Furthermore, the hydrodynamic related parameters for the elliptic section with half small and great axis' length 0.03 m and 0.05 m, respectively, $\rho = 1000$ kg/m^3, $C_f = 0.03$, $C_D = 1$, $C_A = 1$ and $C_M = 1$ were calculated as: $c_t = 0.2639$, $c_n = 4.2$, $\mu_n = 0.3957$, $\lambda_1 = 2.2988 \times 10^{-7}$, $\lambda_2 = 4.3103 \times 10^{-4}$, for the simulated model. The model is implemented and simulated in *Matlab R2013b*. The dynamics was calculated using the *ode23tb* solver with a relative and absolute error tolerance of 10^{-4}. The trace of the head is shown in Fig. 3.3-3.4, while the average joint angle, defined as $\bar{\phi} = \sum_{i=1}^{n-1} \phi_i/(n-1)$, is shown in Fig. 3.5-3.6. The underwater snake robot is controlled according to lateral undulation, (3.1), and eel-like motion, (3.2), with $\alpha = 30°$, $\omega = 120°/\text{s}$ and $\delta = 40°$. In addition, the offset angle is set to $\phi_0 = 5°$ in the time interval $t \in [20, 30]$ and $\phi_0 = -10°$ in the time interval $t \in [50, 60]$, while the offset angle is set to $\phi_0 = 0°$ outside these two time intervals.

From Fig. 3.3-3.6, we can see that the robot swims forward without turning as long as the average joint angle, $\bar{\phi}$, oscillates around zero, while the direction of the motion changes when the average joint angle is non-zero. It is seen (Fig. 3.5-3.6) that in the case of eel-like motion the average joint angle oscillates with larger amplitude compared to lateral undulation around the expected direction.

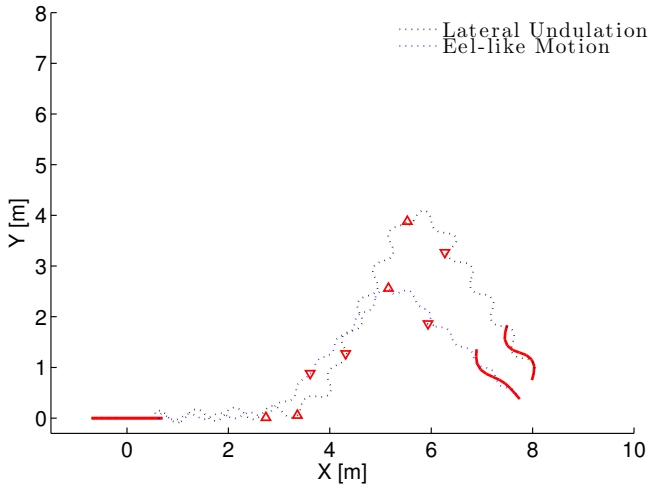

Figure 3.3: Turning locomotion analysis for an underwater snake robot with $n = 10$ links both for lateral undulation and eel-like motion patterns: Trace of the head for $\omega = 70^{\circ}/\text{s}$.

The positive (resp. negative) average joint angle produces a counterclockwise (resp. clockwise) rotation of the underwater snake robot. In addition, we can see that the speed of the directional change is correlated with the amplitude of the average joint angle. Moreover, Fig. 3.3-3.4 show that the rate of directional change is larger when the robot moves with larger forward velocity (for $\omega = 120^{\circ}/\text{s}$). This indicates that the speed of the directional change, for some fixed joint angle offset, becomes greater by increasing the forward velocity of the underwater snake robot. Through the simulation study based on the complex model we observe a set of qualitative properties and similar formulations as the ones that observed for the ground snake robot locomotion presented in [98, 101]. We will now summarize the observations of this simulation study of the turning locomotion of an underwater snake robot.

Proposition 3.1: During both lateral undulation and eel-like motion for an underwater snake robot described by (3.10) with $c_n > c_t$ and $\mu_n > 0$, the overall direction of the locomotion remains constant as long as the average joint angle is zero. However, this will change in the counterclockwise (resp. clockwise) direction when the average joint angle is positive (resp. negative). The speed of directional change of the locomotion becomes greater by increasing the amplitude of the average joint angle and/or by increasing the forward velocity (assuming that the average joint angle is non-zero).

3.5 Analysis of Relative Link Motion

From the analysis in Section 3.3, it is clear that underwater snake locomotion consists of periodic body shape changes that generate external forces that propel the

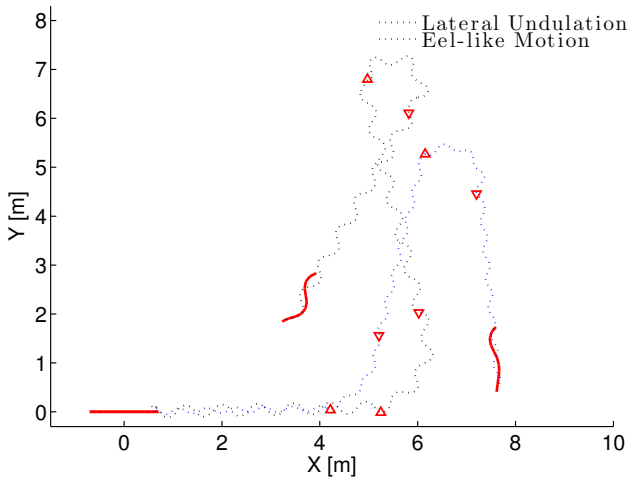

Figure 3.4: Turning locomotion analysis for an underwater snake robot with $n = 10$ links both for lateral undulation and eel-like motion patterns: Trace of the head for $\omega = 120^{\circ}/\text{s}$.

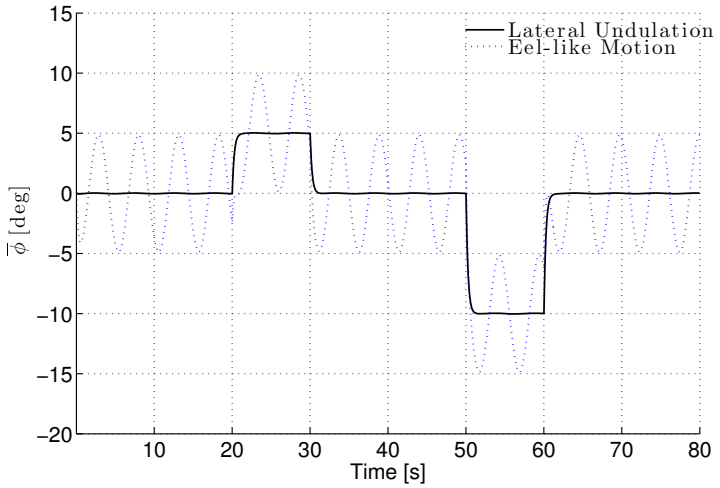

Figure 3.5: Turning locomotion analysis for an underwater snake robot with $n = 10$ links both for lateral undulation and eel-like motion patterns: The averaged ϕ for $\omega = 70^{\circ}/\text{s}$.

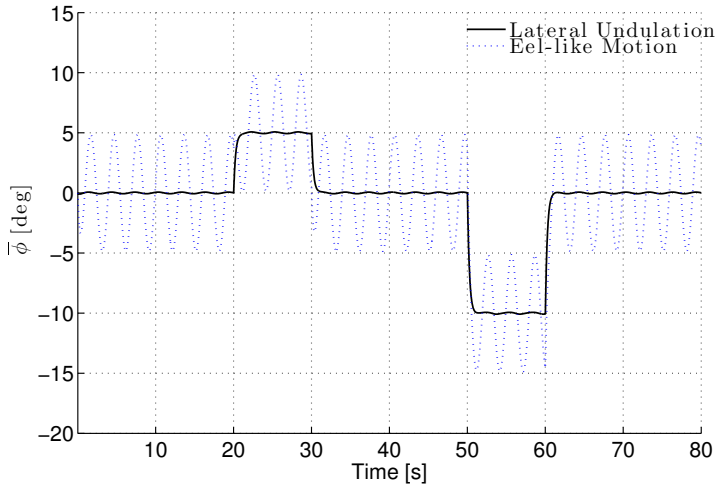

Figure 3.6: Turning locomotion analysis for an underwater snake robot with $n = 10$ links both for lateral undulation and eel-like motion patterns: The averaged ϕ for $\omega = 120^{\circ}/\text{s}$.

robot forward. According to the Property 3.1, the forward motion is inducted by the motion of the links normal to the forward direction. The above result led us to wonder if the body shape changes can be characterized in terms of the translational displacements of the links instead of the rotational joints motion. This would be similar to the approach presented for the ground snake robot in [98, 101]. Generally, the model given by (3.10), which describes the rotational link motion of an underwater snake robot, is quite complex.

In order to support this idea, we consider an underwater snake robot described by (3.10) forced to move with lateral undulation, (3.1), and eel-like motion, (3.2), along the global x axis with $\phi_0 = 0^{\circ}$. The parameters of the underwater snake robot are kept the same as described in Section 3.4. Fig. 3.7 shows the relative displacement between the CM of two arbitrarily chosen links (link 3 and link 4) in the global x and y directions. These plots indicate that, during both lateral undulation and eel-like motion, the relative displacements between the CM of two adjacent links along the forward direction of motion are approximately constant, while the relative displacements normal to the direction of motion oscillate around zero. Hence, based on these simulation results we can compose the following proposition.

Proposition 3.2: During both lateral undulation and eel-like motion, the change in body shape consists mainly of relative displacement of the CM of the links normal to the direction of motion. In addition, the relative displacement of the CM of the links along the forward direction can be approximated as constant.

Remark 3.7: *Property 3.1, which is supported by Proposition 3.2, constitutes the*

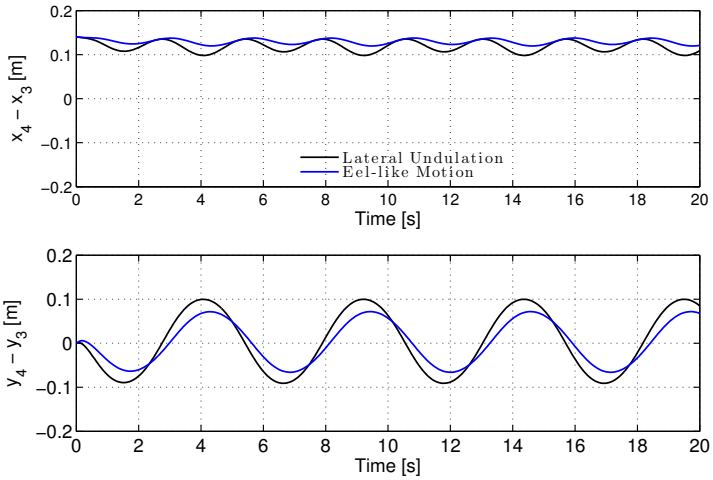

Figure 3.7: Relative displacement of the CM of link 3 and 4 in the global x direction (Top) and y direction (Bottom) both for lateral undulation and eel-like motion patterns.

basis for the development of the control-oriented model of the underwater snake robot presented in Chapter 4. Particularly, these results indicate that (1) lateral undulation and eel-like motion mainly consist of link displacements that are transversal to the direction of the motion and (2) the transversal link displacements propel the robot forward. Hence, these contentions are important in the sense as they point out that the underwater snake robot locomotion can be described in terms of the transversal displacement of the links, instead of the more complex rotational links motion.

Remark 3.8: *The analysis of the underwater snake robot locomotion gives the Properties 3.1-3.4 and the Propositions 3.1-3.2, which are similar to the ones presented in [98, 101] for a ground snake robot. However, in this section, the properties are developed under the assumption that the snake robot moves according to lateral undulation and eel-like motion, and also the hydrodynamic effects are analyzed.*

3.6 Chapter Summary

This chapter is summarized as follows:

- We have presented a general sinusoidal motion pattern which can be used for a broad class of motion patterns for underwater snake robot locomotion including lateral undulation and eel-like motion.
- We have employed an extensive analysis of the complex model (3.10) of a fully immersed underwater snake robot moving in a virtual horizontal plane and a set of essential properties that characterize the overall motion of an underwater snake robot has been derived (see Properties 3.1-3.4).

- The results presented in Section 3.3 are general, because they are based on a more general sinusoidal motion pattern than what has been analysed in previous literature. Based on the analysis in this chapter, the hydrodynamic effects which are essential for the overall behavior of the swimming snake robot have been identified.
- Propositions regarding the turning motion of an underwater snake robot (see Proposition 3.1) and the relative displacement of the links during both lateral undulation and eel-like motion patterns (see Proposition 3.2) have been addressed.
- The Properties 3.1-3.3 and Propositions 3.1-3.2 form the basis of the control-oriented model of underwater snake robot locomotion aimed at control design and stability analysis purposes derived in Chapter 4.

Chapter 4

Control-Oriented Model of Underwater Snake Robots

A number of researchers have developed analytical models for the forces generated during the motion of biologically inspired swimming robots. However, the existing models for underwater snake robots are quite complex from a stability analysis and control design perspective. The modeling for control design purposes poses different challenges than modeling for simulations. In the latter, high accuracy and modeling of all the effects are important, while the model does not need to be in a form suited for analytical analysis. When modeling for model-based control design purposes, however, the model needs to be well-suited for analytical analysis while only the significant effects need to be included. The complexity of the model of underwater snake robot locomotion given by (3.10) is the main motivation behind the control-oriented model developed in this chapter.

In this chapter, we propose a model that is well-suited for control design and stability analysis for swimming snake robots. The development of the control-oriented model is inspired by the modeling approach that was presented in [98, 101] for a land-based snake robot. In these references the authors developed a simplified modeling approach for a planar snake robot describing the body shape dynamics in terms of the translational motion of the links, something which is seen to significantly simplify the equations of motion. Motivated by this work, we model the underwater snake robot locomotion by the translational motion of each link, in order to exploit that translational motion is generally less complex to model than rotational one, at the same time as it captures the essential features of the locomotion. In particular, by using the results from Chapter 3, we develop a control-oriented model of an underwater snake robot moving in a virtual horizontal plane. Simulation results for lateral undulation and eel-like motion patterns are presented to show that the proposed control-oriented model in (4.32) and the complex model in (3.10) have similar qualitative and quantitative behavior.

Contributions of this Chapter: The main contribution of this chapter is a control oriented model of an underwater snake robot moving in a virtual horizontal plane. The idea is to describe the body shape changes of an underwater snake robot as linear displacements of the links. The proposed model is no-

tably less complex than the existing models, while significant parameters such as added mass effects, linear drag forces, and the torques due to the added mass and linear drag forces, are all taken into account in the modeling. Hence, this model is well-suited for control design and stability analysis purposes, and at the same time has the same essential properties as the complex model (3.10).

Organization of this Chapter: This chapter is organized as follows. In Section 4.1, we present an overview of the control-oriented model. In Section 4.2, the kinematic model of the underwater snake robot is presented, followed by the hydrodynamic and dynamic model of the robot in Sections 4.3 and 4.4, respectively. The complete control-oriented model is outlined in Section 4.5. In Section 4.6, simulation results are presented, comparing the behavior of the complex and the control-oriented models, to validate that the control-oriented model captures the essential properties of swimming snake robot locomotion. Finally, the chapter is summarized in Section 4.7.

Publications: The material in this chapter is based on the journal paper [72] and the conference papers [67] and [68].

4.1 Overview of the Modeling Approach

Using the results from Chapter 3, we now develop a control-oriented model of an underwater snake robot moving in a virtual horizontal plane. As it is already mentioned, the model is derived for control design and stability analysis purposes. Based on the observation that the rotation of each link in essence creates a linear displacements of the CM of each link, the idea is to describe the body shape changes of an underwater snake robot as linear displacements of the links with respect to each other instead of rotational displacements [98, 101]. Proposition 3.2 indicates that these linear displacements should be normal to the forward direction of the motion, while Property 3.1 points out that these transversal displacements of the links are that which propel the underwater snake robot forward. This suggests that we can model the revolute joints of an underwater snake robot as prismatic (translational) joints.

In the following subsections, the kinematics and dynamics of the underwater snake robot will be modeled in terms of the mathematical symbols described in Table 4.1 and illustrated in Fig. 4.1-4.2. The following vectors and matrices are used in order to derive the model

$$\mathbf{A} = \begin{bmatrix} 1 & 1 & & \\ & \ddots & \ddots & \\ & & 1 & 1 \end{bmatrix}, \mathbf{D} = \begin{bmatrix} 1 & -1 & & \\ & \ddots & \ddots & \\ & & 1 & -1 \end{bmatrix},$$

$$\mathbf{e} = \begin{bmatrix} 1 & \cdots & 1 \end{bmatrix}^T \in \mathbb{R}^N, \bar{\mathbf{e}} = \begin{bmatrix} 1 & \cdots & 1 \end{bmatrix}^T \in \mathbb{R}^{N-1},$$

$$\bar{\mathbf{D}} = \mathbf{D}^T \left(\mathbf{D}\mathbf{D}^T\right)^{-1} \in \mathbb{R}^{N \times N-1},$$

where $\mathbf{A}, \mathbf{D} \in \mathbb{R}^{(N-1)\times N}$.

Table 4.1: Definition of mathematical terms for the control-oriented model.

Symbol	Description	Vector
N	The number of links	
l	The length of a link	
m	Mass of each link	
ϕ_i	Normal direction distance between links i and $i+1$	$\boldsymbol{\phi} \in \mathbb{R}^{N-1}$
$\upsilon_{\phi,i}$	Relative velocity between links i and $i+1$	$\boldsymbol{\upsilon}_\phi \in \mathbb{R}^{N-1}$
θ	Orientation of the underwater snake robot	$\theta \in \mathbb{R}$
υ_θ	Angular velocity of the underwater snake robot	$\upsilon_\theta \in \mathbb{R}$
(t_i, n_i)	Coordinates of the CM of link i in the $t-n$ frame	$(\mathbf{t}, \mathbf{n}) \in \mathbb{R}^{2N}$
(p_t, p_n)	Coordinates of the CM of the robot in the $t-n$ frame	$(p_t, p_n) \in \mathbb{R}^2$
(p_x, p_y)	Coordinates of the CM of the robot in the global frame	$(p_x, p_y) \in \mathbb{R}^2$
(υ_t, υ_n)	Forward and normal direction velocity of the robot	$(\upsilon_t, \upsilon_n) \in \mathbb{R}^2$
u_i	Actuator force at joint i	$\mathbf{u} \in \mathbb{R}^{N-1}$
$(f_{x,i}, f_{y,i})$	Fluid force on link i in the global frame	$(\mathbf{f_x}, \mathbf{f_y}) \in \mathbb{R}^{2N}$
$(f_{t,i}, f_{n,i})$	Fluid force on link i in the $t-n$ frame	$(\mathbf{f_t}, \mathbf{f_n}) \in \mathbb{R}^{2N}$

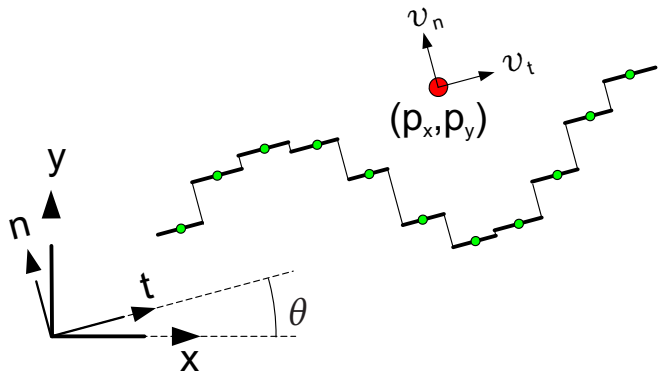

Figure 4.1: Illustration of the coordinates employed in the control-oriented model.

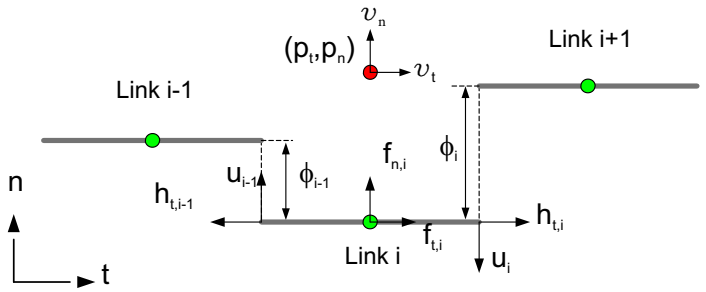

Figure 4.2: Kinematics and dynamics of the underwater snake robot.

Remark 4.1: *In this chapter, we choose to define the parameter for the link numbers of the underwater snake robots as N in contrast with the complex model presented in Chapter 2, where the link numbers is described by the parameter n. This is done mainly in order to avoid the confusion between the link numbers parameter definition and the convention of the normal direction axis, n, that is used for the derivation of the control-oriented model. Generally in this thesis, we use N to describe the link numbers of the control-oriented model and with n the link numbers of the complex model.*

4.2 The Kinematics of the Underwater Snake Robot

The underwater snake robot is assumed to move in a horizontal plane, fully immersed in water, and has $N+2$ degrees of freedom. The motion of the robot is defined with respect to the fixed global frame, $x-y$, and the $t-n$ frame that is always aligned with the robot (Fig. 4.1). The origin of both frames are fixed and coincide. The direction of the t axis is denoted as the tangential or forward direction of the robot, and the direction of the n axis as the normal direction. As shown in Fig. 4.1, the position of the CM of the underwater snake robot in the global frame is denoted by $(p_x, p_y) \in \mathbb{R}^2$, while $(p_t, p_n) \in \mathbb{R}^2$ is the position in the $t-n$ frame. $\theta \in \mathbb{R}$ represents the orientation of the snake robot with respect to the global x axis with counterclockwise positive direction. The angle between the global x axis and the t axis is also θ since the $t-n$ frame is always aligned with the snake robot. The relationship between the $t-n$ frame position and the global frame position is thus given by

$$\begin{aligned} p_t &= p_x \cos\theta + p_y \sin\theta, \\ p_n &= -p_x \sin\theta + p_y \cos\theta. \end{aligned} \tag{4.1}$$

The relationship between the global frame velocities of the robot and the $t-n$ frame velocities is given by

$$\begin{aligned} \dot{p}_x &= \upsilon_t \cos\theta - \upsilon_n \sin\theta, \\ \dot{p}_y &= \upsilon_t \sin\theta + \upsilon_n \cos\theta, \end{aligned} \tag{4.2}$$

and the inverse relationship is given by

$$\begin{aligned} \upsilon_t &= \dot{p}_x \cos\theta + \dot{p}_y \sin\theta, \\ \upsilon_n &= -\dot{p}_x \sin\theta + \dot{p}_y \cos\theta. \end{aligned} \tag{4.3}$$

Differentiating (4.1) with respect to time and inserting (4.3) gives

$$\begin{aligned} \dot{p}_t &= \upsilon_t + p_n\dot{\theta}, \\ \dot{p}_n &= \upsilon_n - p_t\dot{\theta}. \end{aligned} \tag{4.4}$$

We denote the $t-n$ frame position of the CM of the link i by $(t_i, n_i) \in \mathbb{R}^2$. The $N-1$ prismatic joints of the underwater snake robot control the normal direction distance between the links. As seen in Fig. 4.2, the normal direction distance between the link i and link $i+1$ is given by

$$\phi_i = n_{i+1} - n_i, \tag{4.5}$$

and represents the coordinate of joint i. In the control-oriented approach, we refer to ϕ_i as a joint coordinate instead of a joint angle. The holonomic constraints are expressed in matrix form for all links as

$$\begin{aligned} \mathbf{D}\mathbf{t} + l\bar{\mathbf{e}} &= \mathbf{0}, \\ \mathbf{D}\mathbf{n} + \boldsymbol{\phi} &= \mathbf{0}, \end{aligned} \tag{4.6}$$

where $\mathbf{t} = [t_1, \cdots, t_N] \in \mathbb{R}^N$, $\mathbf{n} = [n_1, \cdots, n_N] \in \mathbb{R}^N$, and $\boldsymbol{\phi} = [\phi_1, \cdots, \phi_{N-1}] \in \mathbb{R}^{N-1}$. The $t-n$ frame position of the CM of the underwater snake robot can be written in terms of the link positions as

$$\begin{aligned} p_t &= \mathbf{e}^T\mathbf{t}/N, \\ p_n &= \mathbf{e}^T\mathbf{n}/N. \end{aligned} \tag{4.7}$$

The link positions can be expressed as

$$\begin{aligned} \mathbf{t} &= p_t\mathbf{e} - l\bar{\mathbf{D}}\bar{\mathbf{e}}, \\ \mathbf{n} &= p_n\mathbf{e} - \bar{\mathbf{D}}\boldsymbol{\phi}. \end{aligned} \tag{4.8}$$

By differentiating (4.8) with respect to time and inserting (4.4), the individual link velocities are given as

$$\begin{aligned} \dot{\mathbf{t}} &= (\upsilon_t + p_n\dot{\theta})\mathbf{e}, \\ \dot{\mathbf{n}} &= (\upsilon_n - p_t\dot{\theta})\mathbf{e} - \bar{\mathbf{D}}\dot{\boldsymbol{\phi}}. \end{aligned} \tag{4.9}$$

The linear accelerations of the links are found by differentiating the velocity of the individual links (4.9) with respect to time, which gives

$$\begin{aligned} \ddot{\mathbf{t}} &= (\dot{\upsilon}_t + \dot{p}_n\dot{\theta} + p_n\ddot{\theta})\mathbf{e}, \\ \ddot{\mathbf{n}} &= (\dot{\upsilon}_n - \dot{p}_t\dot{\theta} - p_t\ddot{\theta})\mathbf{e} - \bar{\mathbf{D}}\ddot{\boldsymbol{\phi}}. \end{aligned} \tag{4.10}$$

Remark 4.2: *The kinematics of an underwater snake robot, described in this subsection, is similar to that of a snake robot moving on land [101]. In this section we provide a brief presentation of the kinematics for completeness. An extensive presentation of the snake robot kinematics can be found in [98, 101]. Additionally, it is necessary to derive the equations of linear accelerations of the links (4.10) in order to express the fluid forces below.*

4.3 The Fluid Friction Model

In this section, we employ a fluid model that takes into account the added mass effects and linear drag forces, similar to the hydrodynamic model described in Section 3.3. The hydrodynamic forces, which act on the CM of each link, must be defined so that Properties 3.1-3.3 from Section 3.3 being also applicable for the control-oriented model of the robot.

By assembling the forces in (3.8) on all links in vector form, we can rewrite the global frame fluid forces on the links as

$$\mathbf{f} = \begin{bmatrix} \mathbf{f_x} \\ \mathbf{f_y} \end{bmatrix} = \begin{bmatrix} \mathbf{f_{A_x}} \\ \mathbf{f_{A_y}} \end{bmatrix} + \begin{bmatrix} \mathbf{f}^{\,\mathrm{I}}_{\mathbf{D_x}} \\ \mathbf{f}^{\,\mathrm{I}}_{\mathbf{D_y}} \end{bmatrix}, \tag{4.11}$$

where $\mathbf{f_{A_x}}$ and $\mathbf{f_{A_y}}$ represent the effects from added mass forces and are expressed as defined in (2.24). The vectors $\mathbf{f}^{\,\mathrm{I}}_{\mathbf{D_x}}$, $\mathbf{f}^{\,\mathrm{I}}_{\mathbf{D_y}}$ represent the effects from the linear drag forces (2.25).

Assumption 4.1: When θ_i is small, the following approximations hold $\sin^2\theta_i \approx 0$, $\cos^2\theta_i \approx 1$ and $\sin\theta_i \cos\theta_i \approx \theta_i$ (see e.g. [98]).

Remark 4.3: *Assumption 4.1 is valid for* ($\mid \theta_i \mid < 20^o$) *as it is shown in [98, 101]. We will therefore approximate the added mass and drag forces based on this assumption.*

Note that in (3.8), the velocities $\dot{x}_i$ and $\dot{y}_i$ correspond to the velocity of link i in the tangential and normal directions of the underwater snake robot, respectively, while the accelerations $\ddot{x}_i$ and $\ddot{y}_i$ correspond to the acceleration of link i in the tangential and normal directions of the underwater snake robot, respectively. In addition, the forces $f_{x,i}$ and $f_{y,i}$ correspond to the fluid forces on link i in the tangential and normal directions, respectively. Now, by denoting the fluid force components on link i in the $t-n$ frame of the control-oriented model by $f_{t,i}$ and $f_{n,i}$, respectively and letting the $t-n$ frame velocity and acceleration components of link i be given by $(\dot{t}_i, \dot{n}_i)$ and $(\ddot{t}_i, \ddot{n}_i)$, we then have that

$$\begin{aligned} \dot{x}_i &= \dot{t}_i, & \dot{y}_i &= \dot{n}_i, \\ \ddot{x}_i &= \ddot{t}_i, & \ddot{y}_i &= \ddot{n}_i, \\ f_{x,i} &= f_{t,i}, & f_{y,i} &= f_{n,i}. \end{aligned} \tag{4.12}$$

Using Assumption 4.1 and $\theta_i \approx (\phi_{i-1} + \phi_i)/2l$ (see e.g. [98, 101]), the fluid forces in the tangential, $\mathbf{f_t} \in \mathbb{R}^N$, and normal, $\mathbf{f_n} \in \mathbb{R}^N$, directions can be written as

$$\begin{bmatrix} \mathbf{f_t} \\ \mathbf{f_n} \end{bmatrix} = \begin{bmatrix} \mathbf{f_{A_t}} \\ \mathbf{f_{A_n}} \end{bmatrix} + \begin{bmatrix} \mathbf{f_{D_t}} \\ \mathbf{f_{D_n}} \end{bmatrix}, \tag{4.13}$$

where

$$\begin{bmatrix} \mathbf{f_{A_t}} \\ \mathbf{f_{A_n}} \end{bmatrix} = -\begin{bmatrix} \mathbf{0}_{N\times N} & -\frac{\mu_n}{2l}\text{diag}(\mathbf{A}^T\boldsymbol{\phi}) \\ -\frac{\mu_n}{2l}\text{diag}(\mathbf{A}^T\boldsymbol{\phi}) & \mu_n\mathbf{I}_N \end{bmatrix} \begin{bmatrix} \ddot{\mathbf{t}} \\ \ddot{\mathbf{n}} \end{bmatrix}_{\dot{\theta}=0,\ddot{\theta}=0}, \tag{4.14}$$

and

$$\begin{bmatrix} \mathbf{f_{D_t}} \\ \mathbf{f_{D_n}} \end{bmatrix} = \begin{bmatrix} -c_t\mathbf{I}_N & c_p\text{diag}(\mathbf{A}^T\boldsymbol{\phi}) \\ c_p\text{diag}(\mathbf{A}^T\boldsymbol{\phi}) & -c_n\mathbf{I}_N \end{bmatrix} \begin{bmatrix} \dot{\mathbf{t}} \\ \dot{\mathbf{n}} \end{bmatrix}_{\dot{\theta}=0}. \tag{4.15}$$

The parameter $c_p = (c_n - c_t)/2l$ is a propulsion coefficient which maps the normal direction link velocities and the joint coordinates into propulsive fluid forces in the forward (tangential) direction of the underwater snake robot.

Remark 4.4: *From (4.14) and (4.15), we can see that the propulsive force on link i that propels the robot forward is produced by the normal direction link velocity, $\dot{n}_i$, and by the normal direction link acceleration, $\ddot{n}_i$, which is in agreement with Property 3.1. Furthermore, we see from (4.14) and (4.15) that the magnitude of the propulsive forces produced by link i is increased by increasing $\mid \phi_{i-1} + \phi_i \mid$, which from $\theta_i \approx (\phi_{i-1}+\phi_i)/2l$, corresponds to increasing $\mid \theta_i \mid$. This is in agreement with Property 3.3. Finally, we can see from (4.14) and (4.15) that the forward direction force components produced by $\dot{n}_i$ and $\ddot{n}_i$ is positive when sgn$(\phi_{i-1} + \phi_i)$ = sgn$(\dot{n}_i)$ and sgn$(\phi_{i-1} + \phi_i)$ = sgn$(\ddot{n}_i)$, which are in agreement with Property 3.2. Hence, we conclude that the simplified/control-oriented fluid model directly captures the Properties 3.1-3.3 from Section 3.3, which means that we can argue that the simplified fluid model in (4.14), (4.15) is qualitatively similar to the complex fluid model in (4.11).*

Remark 4.5: *In this control-oriented modeling approach, we choose to disregard the link velocity components due to the angular velocity $\dot{\theta}$ of the underwater snake robot and the link acceleration components $\ddot{\theta}$, due to the angular velocity. These are reasonable assumptions since the dynamics of the angular motion of the underwater snake robot will generally be much slower than the body shape dynamics. Furthermore, these assumptions simplify the fluid model significantly.*

Inserting (4.10) into (4.14) and (4.9) into (4.15) with $\dot{\theta} = 0$, and $\ddot{\theta} = 0$ the final expressions for the added mass effects and linear drag forces can be written as

$$\begin{aligned} \begin{bmatrix} \mathbf{f_{A_t}} \\ \mathbf{f_{A_n}} \end{bmatrix} = &-\begin{bmatrix} \mathbf{0}_{N\times N} & -\frac{\mu_n}{2l}\text{diag}(\mathbf{A}^T\boldsymbol{\phi})\mathbf{e} \\ -\frac{\mu_n}{2l}\text{diag}(\mathbf{A}^T\boldsymbol{\phi})\mathbf{e} & \mu_n\mathbf{I}_N\mathbf{e} \end{bmatrix} \begin{bmatrix} \dot{\upsilon}_t \\ \dot{\upsilon}_n \end{bmatrix} \\ &-\begin{bmatrix} \mathbf{0}_{N\times N} & -\frac{\mu_n}{2l}\text{diag}(\mathbf{A}^T\boldsymbol{\phi}) \\ -\frac{\mu_n}{2l}\text{diag}(\mathbf{A}^T\boldsymbol{\phi}) & \mu_n\mathbf{I}_N \end{bmatrix} \begin{bmatrix} \mathbf{0}_N \\ -\bar{\mathbf{D}}\ddot{\boldsymbol{\phi}} \end{bmatrix}, \end{aligned} \tag{4.16}$$

and

$$\begin{bmatrix} \mathbf{f_{D_t}} \\ \mathbf{f_{D_n}} \end{bmatrix} = \begin{bmatrix} -c_t\upsilon_t\mathbf{e} + c_p\text{diag}(\mathbf{A}^T\boldsymbol{\phi})(\upsilon_n\mathbf{e} - \bar{\mathbf{D}}\dot{\boldsymbol{\phi}}) \\ -c_n\upsilon_n\mathbf{e} + c_n\bar{\mathbf{D}}\dot{\boldsymbol{\phi}} + c_p\upsilon_t\text{diag}(\mathbf{A}^T\boldsymbol{\phi})\mathbf{e} \end{bmatrix}. \tag{4.17}$$

4.4 The Dynamics of the Underwater Snake Robot

This section presents the equations of motion for the underwater snake robot. The forces and torques acting on link i are visualized in Fig. 4.2 and the force balance for link i in global frame coordinates is given by

$$\begin{aligned} m\ddot{t}_i &= f_{t,i} + h_{t,i} - h_{t,i-1}, \\ m\ddot{n}_i &= f_{n,i} - u_i + u_{i-1}, \end{aligned} \tag{4.18}$$

where $f_{t,i}$ and $f_{n,i}$ are the fluid forces, $h_{t,i}$ and $h_{t,i-1}$ are the joint constraint forces on link i from link $i+1$ and link $i-1$, respectively, and u_i and u_{i-1}, produce relative motion between the links in the normal direction. The force balance equations for all links may be expressed in matrix form as

$$m\ddot{\mathbf{t}} = \mathbf{f_t} + \mathbf{D}^T\mathbf{h}_t, \tag{4.19}$$

$$m\ddot{\mathbf{n}} = \mathbf{f_n} - \mathbf{D}^T\mathbf{u}, \tag{4.20}$$

where $\mathbf{h}_t = [h_{t,1}, \cdots, h_{t,N-1}]^T \in \mathbb{R}^{N-1}$ and $\mathbf{u} = [u_1, \cdots, u_{N-1}]^T \in \mathbb{R}^{N-1}$. Premultiplying (4.20) by $\mathbf{D}/m$ gives

$$\mathbf{D}\ddot{\mathbf{n}} = \frac{1}{m}\mathbf{D}\mathbf{f_n} - \frac{1}{m}\mathbf{D}\mathbf{D}^T\mathbf{u}. \tag{4.21}$$

By differentiating (4.6) twice with respect to time, it is seen that $\mathbf{D}\ddot{\mathbf{n}} = -\ddot{\boldsymbol{\phi}}$. We can therefore write the body shape dynamics of the underwater snake robot as

$$\ddot{\boldsymbol{\phi}} = -\frac{1}{m}\mathbf{D}\mathbf{f_n} + \frac{1}{m}\mathbf{D}\mathbf{D}^T\mathbf{u}. \tag{4.22}$$

Inserting (4.13) into (4.22) and using the easily verifiable relations $\mathbf{D}\mathbf{e} = 0$, $\mathbf{D}\bar{\mathbf{D}} = \mathbf{I}_{N-1}$, $\mathbf{D}\mathrm{diag}(\mathbf{A}^T\boldsymbol{\phi})\mathbf{e} = -\mathbf{A}\mathbf{D}^T\boldsymbol{\phi}$, we get

$$\ddot{\boldsymbol{\phi}} = -\frac{c_n}{m+\mu_n}\dot{\boldsymbol{\phi}} + \frac{1}{m+\mu_n}\left(\frac{\mu_n}{2l}\mathbf{A}\mathbf{D}^T\dot{v}_t + c_p\mathbf{A}\mathbf{D}^T v_t\right)\boldsymbol{\phi} + \frac{1}{m+\mu_n}\mathbf{D}\mathbf{D}^T\mathbf{u}. \tag{4.23}$$

The tangential and normal direction accelerations of the CM of the underwater snake robot, denoted by $\dot{v}_t$ and $\dot{v}_n$, respectively, are given as the sum of all tangential and normal direction forces on the links divided by its mass. This gives

$$\begin{bmatrix} \dot{v}_t \\ \dot{v}_n \end{bmatrix} = \frac{1}{Nm}\begin{bmatrix} \mathbf{e}^T & \mathbf{0}_{N\times N} \\ \mathbf{0}_{N\times N} & \mathbf{e}^T \end{bmatrix}\begin{bmatrix} \mathbf{f_t} \\ \mathbf{f_n} \end{bmatrix}, \tag{4.24}$$

where we can see that the joint constraint forces, $\mathbf{h}_t$, and the actuator forces, $\mathbf{u}$, are cancelled out when the link accelerations are summed. Now, inserting (4.13) into (4.24) and using easily verifiable relations, $\mathbf{e}^T\mathrm{diag}(\mathbf{A}^T\boldsymbol{\phi})\mathbf{e} = 2\bar{\mathbf{e}}^T\boldsymbol{\phi}$, $\mathbf{e}^T\bar{\mathbf{D}} = 0$, and $\mathbf{e}^T\mathrm{diag}(\mathbf{A}^T\boldsymbol{\phi})\bar{\mathbf{D}} = \boldsymbol{\phi}^T\mathbf{A}\bar{\mathbf{D}}$, we get

$$\begin{aligned} \dot{v}_t = {} & k_3\left(k_1 2c_p(\bar{\mathbf{e}}^T\boldsymbol{\phi})^2 - k_2 c_t N\right)v_t + k_3\left(k_2 2c_p\bar{\mathbf{e}}^T\boldsymbol{\phi} - k_1 c_n N\bar{\mathbf{e}}^T\boldsymbol{\phi}\right)v_n \\ & - k_3(k_2\frac{k_1}{2}\boldsymbol{\phi}^T\mathbf{A}\bar{\mathbf{D}}\ddot{\phi} + k_2 c_p\boldsymbol{\phi}^T\mathbf{A}\bar{\mathbf{D}}\dot{\phi}), \end{aligned} \tag{4.25}$$

$$\begin{aligned}\dot{\upsilon}_n = k_3 \left(Nm2c_p\bar{\mathbf{e}}^T\boldsymbol{\phi} - k_1c_tN\bar{\mathbf{e}}^T\boldsymbol{\phi}\right)\upsilon_t + k_3\left(k_12c_p(\bar{\mathbf{e}}^T\boldsymbol{\phi})^2 - N^2mc_n\right)\upsilon_n \\ - \bar{\mathbf{e}}^T\boldsymbol{\phi}k_3(k_1c_p\boldsymbol{\phi}^T\mathbf{A}\bar{\mathbf{D}}\dot{\phi} + \frac{{k_1}^2}{2}\boldsymbol{\phi}^T\mathbf{A}\bar{\mathbf{D}}\ddot{\phi}),\end{aligned} \tag{4.26}$$

where $k_1 = \dfrac{\mu_n}{l}$, $k_2 = Nm + N\mu_n$ and $k_3 = \dfrac{1}{Nmk_2 - (k_1\bar{\mathbf{e}}^T\boldsymbol{\phi})^2}$.

We also need to model the dynamics of the snake robot orientation. As mentioned in previous sections, the idea behind the control-oriented modeling approach of the underwater snake robot locomotion is to disregard the rotational motion of the links and instead only consider the translational displacements of the links. The orientation of the robot with prismatic joints is defined as θ, which is also the angle of all the links.

Proposition 3.1 states that the direction of the forward motion changes when the average of the joint angles oscillates around a non-zero value and that the speed of direction changes increases by increasing the average of the joint angles and/or by increasing the forward velocity. This observation should also hold for the control-oriented model. The direction of the forward motion in the control-oriented model is given by the orientation θ, the forward velocity is given by υ_t, and the average of the joint angles corresponds to the average of the joint coordinates $\bar{\mathbf{e}}^T\boldsymbol{\phi}/(N-1)$. Hence, using Proposition 3.1, the overall torque that induces the rotational motion of a snake robot should be

$$\ddot{\theta}_{rotation} = \lambda_2\upsilon_t\frac{\bar{\mathbf{e}}^T\boldsymbol{\phi}}{N-1}, \tag{4.27}$$

where λ_2 is a constant parameter which gives the scaling of the mapping from the average of the joint coordinates and forward velocity to rotational acceleration. The induced torque is multiplied by υ_t since the snake robot otherwise would experience a constant angular velocity, even in the case of a nonzero average joint coordinate in the rest mode, similarly to the ground robot presented in [101]. Furthermore, fluid forces act on the underwater snake robot in order to induce fluid torques that oppose to the rotational motion. Since the fluid forces are the linear drag forces and added mass effects, we can assume that the rotational fluid torques are obtained due to the added mass and the linear drag forces. We choose to model the torque due to the added mass effect as

$$\ddot{\theta}_{am} = -\lambda_3\ddot{\theta}, \tag{4.28}$$

where λ_3 is a constant parameter which represents the torque coefficient due to the added mass effect. In addition, we model the torque due to the linear drag forces as

$$\ddot{\theta}_{drag} = -\lambda_1\dot{\theta}, \tag{4.29}$$

where λ_1 is a constant parameter which determines the drag torque opposing to the rotation of the underwater snake robot. By combining (4.27), (4.28) and (4.29) we can write the control-oriented model of the rotational dynamics of the underwater snake robot as

$$\ddot{\theta} = -\frac{\lambda_1}{1+\lambda_3}\dot{\theta} + \frac{\lambda_2}{(N-1)(1+\lambda_3)}\upsilon_t\bar{\mathbf{e}}^T\boldsymbol{\phi}. \tag{4.30}$$

Remark 4.6: *Although, the model of $\ddot{\theta}$ is not based on first principles of the rotational dynamics (see e.g. [101]) of an underwater snake robot, we can presume that the behavior of this model will be qualitatively similar to the behavior of an underwater snake robot with revolute joints. It will also be quantitatively similar when the rotation parameters λ_1, λ_2 and λ_3 are properly chosen. This claim will be supported by simulation results in Section 4.6.*

4.5 The Complete Control-Oriented Model

We now present the complete control-oriented model of the underwater snake robot. The state vector of the model is chosen as

$$\mathbf{x} = \left[\boldsymbol{\phi}^T, \theta, p_x, p_y, \mathbf{v}_\phi^T, \upsilon_\theta, \upsilon_t, \upsilon_n\right]^T \in \mathbb{R}^{2N+4}, \tag{4.31}$$

where $\boldsymbol{\phi} \in \mathbb{R}^{N-1}$ are the joint coordinates, $\theta \in \mathbb{R}$ is the absolute orientation, $(p_x, p_y) \in \mathbb{R}^2$ is the position of the CM in the the global frame, $\mathbf{v}_\phi = \dot{\boldsymbol{\phi}} \in \mathbb{R}^{N-1}$ are the joint velocities, $\upsilon_\theta = \dot{\theta} \in \mathbb{R}$ is the angular velocity, and $(\upsilon_t, \upsilon_n) \in \mathbb{R}^2$ are the tangential and normal direction velocities of the robot. As illustrated in Fig. 4.2, each link is influenced by fluid forces, linear drag forces and the added mass effects, and constraint forces that hold the joints together. The complete control-oriented model of the robot can be written as

$$\dot{\boldsymbol{\phi}} = \mathbf{v}_\phi \tag{4.32a}$$
$$\dot{\theta} = \upsilon_\theta \tag{4.32b}$$
$$\dot{p}_x = \upsilon_t \cos\theta - \upsilon_n \sin\theta \tag{4.32c}$$
$$\dot{p}_y = \upsilon_t \sin\theta + \upsilon_n \cos\theta \tag{4.32d}$$
$$\dot{\mathbf{v}}_\phi = -\frac{c_n N}{k_2}\mathbf{v}_\phi + \frac{N}{k_2}\left(\frac{k_1}{2}\mathbf{A}\mathbf{D}^T\dot{\upsilon}_t + c_p\mathbf{A}\mathbf{D}^T\upsilon_t\right)\boldsymbol{\phi} + \frac{N}{k_2}\mathbf{D}\mathbf{D}^T\mathbf{u} \tag{4.32e}$$
$$\dot{\upsilon}_\theta = -\frac{\lambda_1}{1+\lambda_3}\upsilon_\theta + \frac{\lambda_2}{(N-1)(1+\lambda_3)}\upsilon_t\bar{\mathbf{e}}^T\boldsymbol{\phi} \tag{4.32f}$$
$$\begin{aligned}\dot{\upsilon}_t = {} & k_3\left(k_1 2c_p(\bar{\mathbf{e}}^T\boldsymbol{\phi})^2 - k_2 c_t N\right)\upsilon_t + k_3\left(k_2 2c_p\bar{\mathbf{e}}^T\boldsymbol{\phi} - k_1 c_n N\bar{\mathbf{e}}^T\boldsymbol{\phi}\right)\upsilon_n \\ & - k_3\left(k_2\frac{k_1}{2}\boldsymbol{\phi}^T\mathbf{A}\bar{\mathbf{D}}\dot{\mathbf{v}}_\phi + k_2 c_p\boldsymbol{\phi}^T\mathbf{A}\bar{\mathbf{D}}\mathbf{v}_\phi\right)\end{aligned} \tag{4.32g}$$
$$\begin{aligned}\dot{\upsilon}_n = {} & k_3\left(Nm2c_p\bar{\mathbf{e}}^T\boldsymbol{\phi} - k_1 c_t N\bar{\mathbf{e}}^T\boldsymbol{\phi}\right)\upsilon_t + k_3\left(k_1 2c_p(\bar{\mathbf{e}}^T\boldsymbol{\phi})^2 - N^2 m c_n\right)\upsilon_n \\ & - \bar{\mathbf{e}}^T\boldsymbol{\phi}k_3\left(k_1 c_p\boldsymbol{\phi}^T\mathbf{A}\bar{\mathbf{D}}\mathbf{v}_\phi + \frac{{k_1}^2}{2}\boldsymbol{\phi}^T\mathbf{A}\bar{\mathbf{D}}\dot{\mathbf{v}}_\phi\right)\end{aligned} \tag{4.32h}$$

where $\mathbf{u} \in \mathbb{R}^{N-1}$ are the transformed actuator forces at the joints which we assume that are chosen according to the feedback linearizing control law

$$\mathbf{u} = \frac{k_2}{N}(\mathbf{D}\mathbf{D}^T)^{-1}\left(\bar{\mathbf{u}} + \frac{c_n N}{k_2}\dot{\boldsymbol{\phi}} - \frac{N}{k_2}\left(\frac{k_1}{2}\mathbf{A}\mathbf{D}^T\dot{\upsilon}_t + c_p\mathbf{A}\mathbf{D}^T\upsilon_t\right)\boldsymbol{\phi}\right), \tag{4.33}$$

where $\bar{\mathbf{u}} \in \mathbb{R}^{N-1}$ denotes the new control inputs. By using this control law the joint dynamics (4.32e) are transformed into

$$\dot{\mathbf{v}}_\phi = \bar{\mathbf{u}} \tag{4.32e*}$$

Remark 4.7: *It should be noted that in this chapter the control-oriented model is derived based on the Properties 3.1-3.3 and the Propositions 3.1-3.2. This modeling approach is not able to capture the results in the case pointed in Property 3.4.*

4.6 Simulation Study

This section presents simulation results for lateral undulation and eel-like motion in order to compare the complex model of the underwater snake robot given by (3.10) and the control-oriented model given by (4.32). Both models were implemented and simulated in *Matlab R2013b*. The dynamics was calculated using *ode23tb* solver in *Matlab* with a relative and absolute error tolerance of 10^{-6}.

4.6.1 Simulation Parameters

We consider an underwater snake robot with $N = 10$ links of length $l = 0.14$ m. The mass of each link is $m = 0.6597$ kg and it chosen to fulfil the neutrally buoyant assumption (see Assumption 2.2). Furthermore, we choose the fluid forces and torque coefficients as $c_t = 0.2639$, $c_n = 4.2$, $\mu_n = 0.3957$, $\lambda_1 = 2.2988 \times 10^{-7}$, $\lambda_2 = 4.3103 \times 10^{-4}$, for the complex model and $c_t = 0.45$, $c_n = 5$, $\mu_n = 0.4$, $\lambda_1 = 0.5$, $\lambda_2 = 20$, $\lambda_3 = 0.01$ for the control-oriented one. Please note that defining a general mapping between the fluid coefficients in the two models remains a topic of future work. The coefficients here are chosen through trial and error. The joint reference coordinates were calculated according to the motion pattern lateral undulation and eel-like motion, defined in (3.1) and (3.2), respectively. The values of the controller parameters are set to $\omega = 120^\text{o}/\text{s}$, $\delta = 40^\text{o}$ in both models, while the values of parameter α are noted in each simulation results. In addition, the joint offset angle was set to $\phi_0 = \alpha/6$ in the time interval $t \in [40, 70]$, $\phi_0 = -\alpha/6$ in the time interval $t \in [130, 160]$ and $\phi_0 = 0$ outside of these two time intervals. Both models are simulated with the initial values set to zero. Furthermore, in order to achieve the desired locomotion patterns given in (3.1) and (3.2) we use the standard PD-controller both for the complex and control-oriented models, as defined in (3.5) with the controller gains $k_p = 200$ and $k_d = 50$.

4.6.2 Simulation Results

Simulation results for lateral undulation and eel-like motion of the underwater snake robot are presented for two different joints angle amplitudes. In particular, the amplitude of (3.1) and (3.2) is set to the values $\alpha = 7.1^\text{o}$, 13.9^o, for the complex model and $\alpha = 2.24$ cm, 4.3 cm, respectively, for the control-oriented model. These amplitudes correspond to the link angles $\theta_i = 10^\text{o}$ and $\theta_i = 20^\text{o}$, respectively (cf. [101] for details about how to transform between angular and translational link motion). The simulation results from the two cases are shown in Fig. 4.3 and Fig.

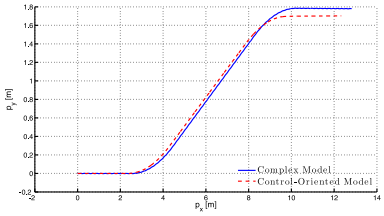

(a) Position of the CM of the robot

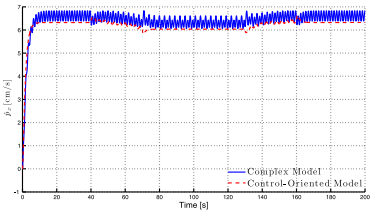

(b) CM velocity in x direction, $\dot{p}_x$

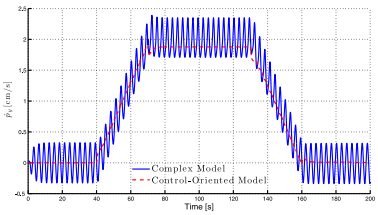

(c) CM velocity in y direction, $\dot{p}_y$

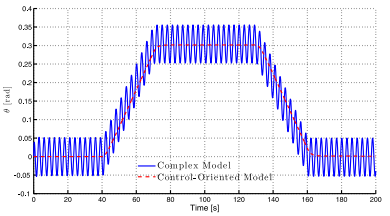

(d) The orientation of the robot

Figure 4.3: Simulation results for lateral undulation (complex model: $\alpha = 7.1^{\circ}$ and control-oriented model: $\alpha = 2.24$ cm).

4.5 for lateral undulation, while simulation results for eel-like motion are shown in Fig. 4.4 and Fig. 4.6. In all figures, the motion of CM for both models is presented in subfigure (a), while subfigures (b) and (c) show the CM velocity of the underwater snake robots in the global x and y direction, respectively. Furthermore, subfigure (d) shows the orientation of the underwater snake robots, which is given by θ in the control-oriented model, and is estimated as the average of the link angles in the complex model, i.e. as is expressed in (2.2).

The simulation results, both for lateral undulation and eel-like motion, indicate that the qualitative behavior of the underwater robot expected by the control-oriented model is similar to the corresponding behavior of the complex model. In addition, choosing the presented values for the fluid coefficients, we also achieved a good quantitative similarity between the two models. The similar behavior of the two models confirms that the control-oriented model can capture the significant effects that determine the overall motion of the underwater snake robot. Hence, the proposed control-oriented modeling approach can be used to develop a general analysis and control design, in order to get results that will also be applicable to the complex model.

4.7 Chapter Summary

This chapter is summarized as follows:

- We have presented a model of the kinematics and dynamics of a planar underwater snake robot, aimed at control design and stability analysis purposes.

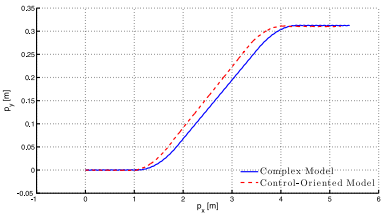

(a) Position of the CM of the robot

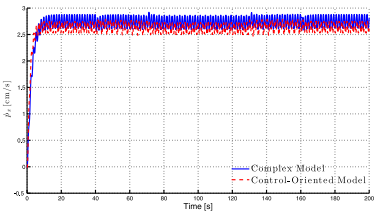

(b) CM velocity in x direction, $\dot{p}_x$

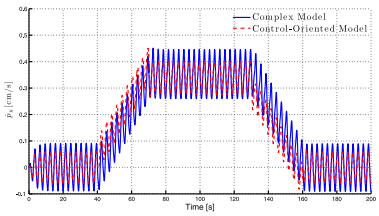

(c) CM velocity in y direction, $\dot{p}_y$

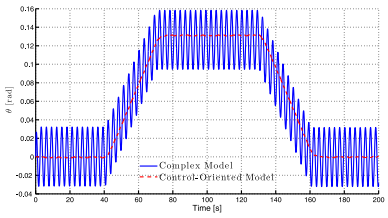

(d) The orientation of the robot

Figure 4.4: Simulation results for eel-like motion (complex model: $\alpha = 7.1^{\circ}$ and control-oriented model: $\alpha = 2.24$ cm).

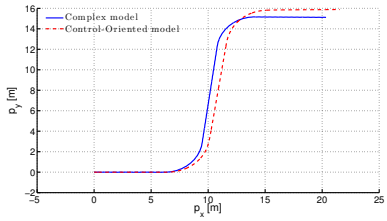

(a) Position of the CM of the robot

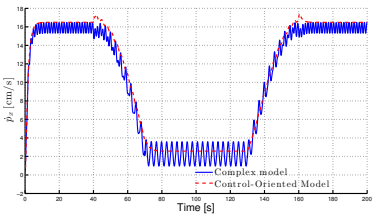

(b) CM velocity in x direction, $\dot{p}_x$

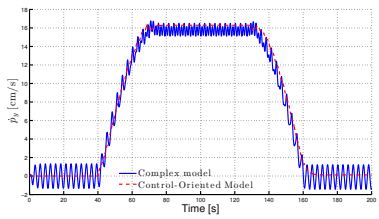

(c) CM velocity in y direction, $\dot{p}_y$

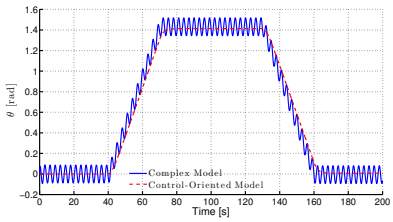

(d) The orientation of the robot

Figure 4.5: Simulation results for lateral undulation (complex model: $\alpha = 13.9^{\circ}$ and control-oriented model: $\alpha = 4.3$ cm).

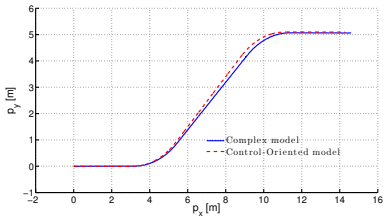

(a) Position of the CM of the robot

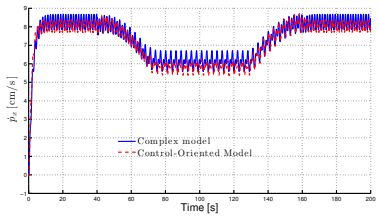

(b) CM velocity in x direction, $\dot{p}_x$

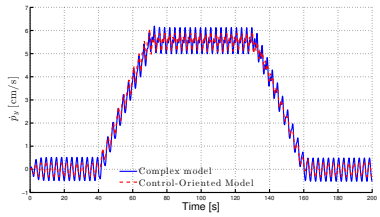

(c) CM velocity in y direction, $\dot{p}_y$

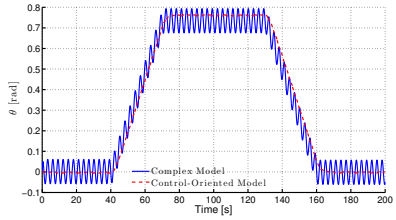

(d) The orientation of the robot

Figure 4.6: Simulation results for eel-like motion (complex model: $\alpha = 13.9^{\circ}$ and control-oriented model: $\alpha = 4.3$ cm).

- We have shown that the developed model in (4.32), which takes into account the added mass effects, the linear drag forces, and the torques due to the added mass and linear drag forces, is significantly less complex than the existing models of underwater snake robots.
- We have presented simulation results for lateral undulation and eel-like motion which indicate that the proposed control-oriented model in (4.32) and the complex model in (3.10) have similar qualitative and quantitative behavior.

Chapter 5

Analysis of Underwater Snake Robots based on Averaging Theory

Averaging theory is extensively used for the analysis of locomotion of biomimetic systems with oscillatory inputs, and it is applied in several works to study the locomotion of snake or fish robots [97, 101, 106, 109, 110, 130–132]. For instance, [109] presents second order averaging methods suited for control purposes of underactuated mechanical systems such as fish robots. Averaging-based control methods for the stabilization of driftless underactuated systems by periodic feedback are introduced in [130]. [131] proposes a control-oriented data-driven averaging approach for robotic fish. In [23], based on the dynamic model derived in [131], a target-tracking control problem for a tail-actuated robotic fish is presented. In this chapter, we will use the averaging theory to reveal new fundamental properties of underwater snake robot locomotion that are useful in a motion planning perspective.

It is well-known that the joint motion of swimming biological snakes is periodic, and snake robots adapt the same motion pattern. The control-oriented model presented in Chapter 4 is specifically designed to capture this motion by capturing the corresponding translational motion during oscillations. The analysis in this chapter is based on the hypothesis that the oscillatory behavior causes some averaged effect that forces the robot to move forward [97, 101]. By converting periodic time-varying systems into time-invariant systems, averaging constitutes a useful tool to simplify complex systems with periodic and oscillatory behavior [130], [80].

Contributions of this Chapter: The first contribution of this chapter is an averaged model of the velocity dynamics of an underwater snake robot under general sinusoidal motion gait patterns, which is well-suited for stability analysis and motion planning purposes. Averaging theory is applied in order to derive a model of the average velocity for the control-oriented model of an underwater snake robot developed in Chapter 4. A similar study was presented in [97] for ground robots. The results in this chapter extend this by taking into account the hydrodynamic effects that underwater snake robots experience, i.e. the reactive and resistive fluid forces, including added mass and drag forces. Moreover, while the results in [97] were derived for the particular motion pattern lateral undulation, the results in this chapter are derived for

any periodic motion pattern. The results in this chapter thus extend [97] to amphibious snake robots and general sinusoidal motion patterns. Hence, the results in [97] fall out as a special case when the motion pattern is lateral undulation and when the drag forces are replaced by viscous friction forces. Therefore, this model can be used for stability analysis and control design for a broad class of motion patterns including lateral undulation and eel-like motion.

As a second contribution, based on the model presented in Chapter 4, we show that the average velocity of an underwater snake robot following sinusoidal motion gait patterns converges exponentially to a steady-state velocity, while an explicit analytical relation is given between the steady state velocity and the amplitude, the frequency, the phase shift and the offset of the joint motion. Note that previous studies for ground snake robots [97, 101] and eel-like robots [106], where the added mass effects and fluid torques are neglected, show that the average forward velocity of the robot during lateral undulation: 1) is proportional to the square of the amplitude of the sinusoidal motion pattern, 2) proportional to the gait frequency and 3) depends also on the weighted sum of the constant phase shift between the joints. In this chapter, we show that the average forward velocity of an underwater snake robot, influenced both by added mass and linear drag effects, and under any sinusoidal gait pattern: 1) is a function of the amplitude of the sinusoidal motion pattern, 2) depends on a linear and a nonlinear term of the gait frequency and 3) depends on the phase shift between the joints. The results of this paper are thus more general and constitute a powerful tool for achieving faster forward motion by selecting the most appropriate motion pattern and an optimal combination of the gait parameters. Furthermore, the derived relationship for the averaged velocity dynamics can be used to select the most appropriate motion pattern to achieve the desired velocity requirements, while also taking into account the power consumption requirements. Results for energy efficiency of underwater snake robots will be shown in Chapter 7.

Another contribution of this chapter is the experimental investigation of a set of fundamental properties of the velocity dynamics for an underwater snake robot that are essential for motion planning purposes and the efficiency of these systems. Initially, we present simulation results to investigate the validity of these properties both for the complex model presented in Chapter 2 and the control-oriented model presented in Chapter 4. The simulation results show that the derived properties, which are based on the control-oriented model of the underwater snake robot hold also for the complex model where complex hydrodynamic effects are considered. In addition, we show that experimental results using the underwater snake robot Mamba, support the derived properties of the velocity dynamics. Note that the simulation and experimental results are obtained for the two most common swimming patterns for underwater snake robot locomotion: lateral undulation and eel-like motion patterns. To the author's best knowledge, experimental investigation of efficient motion patterns for underwater snake robots by investigating the relationship between the gait parameters and the forward velocity has not

been considered in previous literature.

Organization of this Chapter: This chapter is organized as follows. In Section 5.1, the velocity dynamics are presented, followed by the presentation of the averaged velocity dynamics in Section 5.2. Section 5.3 presents the steady state behavior of the velocity dynamics, while the relationship between the gait parameters of a general sinusoidal motion pattern and the forward velocity is presented in Section 5.4. Simulation studies are presented in Section 5.5 and Section 5.6 in order to validate the averaged velocity dynamics and the properties derived in Section 5.3 and Section 5.4, respectively. Section 5.7 presents the experimental setup employed for our experiments with the underwater snake robot Mamba, while Section 5.8 presents experimental results in order to validate the derived properties for the velocity dynamics. Finally, the chapter is summarized in Section 5.9.

Publications: The material in this chapter is based on the journal paper [72] and the conference paper [68].

5.1 The Velocity Dynamics during General Sinusoidal Motion Pattern

In this section, averaging theory is applied to the model of underwater snake robot (4.32) in order to derive the averaged velocity dynamics of the underwater snake robot in the general case when it moves according to the sinusoidal motion patterns described by (3.3). In this chapter, we assume that ϕ_0 is constant so that $\dot{\phi}_i^*$ and $\ddot{\phi}_i^*$ are given by (3.6) and (3.7), respectively. By choosing the control input $\bar{\mathbf{u}}$ as (3.5), the error dynamics of the joints is therefore given by (4.32a), (4.32e*) and (3.5) as

$$(\ddot{\boldsymbol{\phi}}^* - \ddot{\boldsymbol{\phi}}) + k_d(\dot{\boldsymbol{\phi}}^* - \dot{\boldsymbol{\phi}}) + k_p(\boldsymbol{\phi}^* - \boldsymbol{\phi}) = 0, \tag{5.1}$$

which is uniformly globally exponentially stable [80]. Note that (5.1) represents the external dynamics of the underactuated system (4.32), (3.5) [56]. The internal dynamics remains to be analyzed, and we will consider the velocity dynamics below in this section.

We assume in the following analysis that $\boldsymbol{\phi}$, v_ϕ and $\dot{v}_\phi$ are given by (3.3), (3.6) and (3.7). Choosing the state vector $\boldsymbol{v} = (v_t, v_n, v_\theta) \in \mathbb{R}^3$ and taking into account (3.3), (3.6), (3.7), the velocity dynamics can be written as

$$\dot{\boldsymbol{v}} = \begin{bmatrix} \dot{v}_t & \dot{v}_n & \dot{v}_\theta \end{bmatrix}^T = \mathbf{f}(t, \boldsymbol{v}), \tag{5.2}$$

where

$$\mathbf{f}(t, \boldsymbol{v}) = \begin{bmatrix} k_3\left(k_1 2c_p f_1(\omega t)^2 - k_2 c_t N\right) v_t + k_3 f_1(\omega t)(k_2 2c_p \\ k_1 c_n N) v_n - k_3(k_2 k_1 f_3(\omega t)/2 + k_2 c_p f_2(\omega t)) \\ k_3 f_1(\omega t)\left(N m 2c_p - k_1 c_t N\right) v_t + k_3(k_1 2c_p (f_1(\omega t))^2 - \\ N^2 m c_n) v_n - k_3 f_1(\omega t)(k_1 c_p f_2(\omega t) + {k_1}^2 f_3(\omega t)/2) \\ -\lambda_1 v_\theta/(1+\lambda_3) + \lambda_2 v_t f_1(\omega t)/((N-1)(1+\lambda_3)) \end{bmatrix}, \tag{5.3}$$

where

$$f_1(\omega t) = (N-1)\phi_0 + \sum_{i=1}^{N-1} \alpha \mathrm{g}(i,N)\sin(\omega t + (i-1)\delta), \tag{5.4}$$

$$\begin{aligned} f_2(\omega t) = &\sum_{i=1}^{N-1}\sum_{j=1}^{N-1}\Big(\frac{k_{\alpha\omega}}{\alpha}\phi_0 a_{ij}\mathrm{g}(j,N)\cos(\omega t + (j-1)\delta) \\ &+ k_{\alpha\omega}a_{ij}\mathrm{g}(i,N)\sin(\omega t + (i-1)\delta)\mathrm{g}(j,N)\cos(\omega t + (j-1)\delta)\Big), \end{aligned} \tag{5.5}$$

$$\begin{aligned} f_3(\omega t) = &-\sum_{i=1}^{N-1}\sum_{j=1}^{N-1}\Big(\frac{k_{\alpha\omega}^2}{\alpha^3}\phi_0 a_{ij}\mathrm{g}(j,N)\sin(\omega t + (j-1)\delta) \\ &+ \frac{k_{\alpha\omega}^2}{\alpha^2}a_{ij}\mathrm{g}(i,N)\sin(\omega t + (i-1)\delta)\mathrm{g}(j,N)\sin(\omega t + (j-1)\delta)\Big), \end{aligned} \tag{5.6}$$

and a_{ij} denotes the ij element of the matrix $\mathbf{A}\bar{\mathbf{D}}$. Note that in order to be able to write the velocity dynamics in standard form for averaging, we define the parameter $k_{\alpha\omega} = \alpha^2\omega$, similarly to the approach presented in [101].

5.2 The Averaged Velocity Dynamics

As shown in [121], averaging theory is applicable to systems that can be written in the form

$$\dot{\mathbf{x}} = \varepsilon \mathbf{f}(t, \mathbf{x}), \tag{5.7}$$

where ε is a small positive parameter characterizing the magnitude of the perturbations of the systems and $\mathbf{f}(t,\mathbf{x})$ is $T-$periodic, i.e. periodic in time with period T. A system that "in average" has similar behavior to the original system (5.7) can be approximated by

$$\dot{\mathbf{x}} = \varepsilon \mathbf{f}_{av}(\mathbf{x}), \tag{5.8}$$

where

$$\mathbf{f}_{av}(\mathbf{x}) = \frac{1}{T}\int_0^T \mathbf{f}(\tau, \mathbf{x})d\tau. \tag{5.9}$$

We need to rewrite the model of the velocity dynamics of the underwater snake robot (5.2) in the standard form of averaging (5.7). To achieve this, we change the time scale from t to $\tau = \omega t$ and define $\varepsilon = 1/\omega$. Furthermore, using the easily verifiable expression $\frac{d}{dt} = \frac{1}{\varepsilon}\frac{d}{d\tau}$, we can express the model (5.2) in a standard form of averaging, as

$$\frac{d\boldsymbol{\upsilon}}{d\tau} = \varepsilon \mathbf{f}(\tau, \boldsymbol{\upsilon}), \tag{5.10}$$

where

$$\mathbf{f}(\tau,\boldsymbol{\upsilon}) = \begin{bmatrix} k_3\left(k_1 2c_p f_1(\tau)^2 - k_2 c_t N\right)\upsilon_t + k_3 f_1(\tau)(k_2 2c_p - \\ k_1 c_n N)\upsilon_n - k_3(k_2 k_1 f_3(\tau)/2 + k_2 c_p f_2(\tau)) \\ k_3 f_1(\tau)\left(Nm2c_p - k_1 c_t N\right)\upsilon_t + k_3(k_1 2c_p (f_1(\tau))^2 - \\ N^2 m c_n)\upsilon_n - k_3 f_1(\tau)(k_1 c_p f_2(\tau) + {k_1}^2 f_3(\tau)/2) \\ -\lambda_1 \upsilon_\theta(1+\lambda_3) + \lambda_2 \upsilon_t f_1(\tau)/((N-1)(1+\lambda_3)) \end{bmatrix}. \tag{5.11}$$

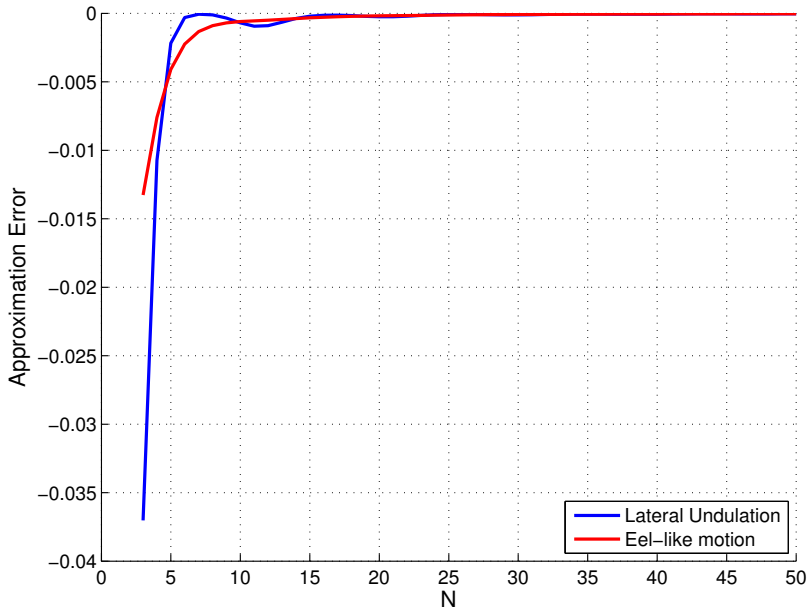

Figure 5.1: Approximation error for parameter k_3.

The smallness requirement of ε [121] can always be achieved by choosing $\omega = 1/\varepsilon$ sufficiently large. Now, using (5.8), we calculate the averaged model of (5.10) for general motion pattern locomotion as

$$\frac{d\boldsymbol{\upsilon}}{d\tau} = \varepsilon \frac{1}{2\pi} \int_0^{2\pi} \mathbf{f}(\tau, \boldsymbol{\upsilon}) d\tau. \tag{5.12}$$

To avoid the complexity of the integral calculation we consider the following assumption.

Assumption 5.1: By assuming that $Nm(Nm + N\mu_n) \ll (\mu_n \bar{\mathbf{e}}^T \boldsymbol{\phi}/l)^2$, the parameter k_3 can be approximated by $k_3 \approx 1/(Nm(Nm + N\mu_n))$.

Remark 5.1: *From Fig. 5.1, we see that the error, i.e.* $\frac{1}{Nm(Nm+N\mu_n)} - \frac{1}{Nm(Nm+N\mu_n) - (\mu_n \bar{\mathbf{e}}^T \boldsymbol{\phi}/l)^2}$, *is small for an underwater snake robot with* $m = 0.6597$, $l = 0.14$, *added mass coefficient* $\mu_n = 0.4$, *the parameters of the motion pattern* $\alpha = 0.2$ *m*, $\omega = 120^o/s$, $\delta = 40^o$, $\phi_0 = l/8$ *m and* N *taking values from 3 to 50, both for lateral undulation and eel-like motion. Additionally, it is easily seen that for a robot with* $N > 10$ *the error is almost zero.*

Remark 5.2: *Note that Assumption 5.1 not only simplifies the integral calculation but also leads us to a solution where the averaged velocity dynamics constitutes a*

good approximation of the original velocity dynamics of the system. If Assumption 5.1 is disregarded, then the averaged velocity dynamics becomes faster than the original one, i.e. the forcing terms in the averaged model and the original one are different [131]. In this study, using Assumption 5.1, we show that the classical averaging method can be applied for swimming robots, avoiding to derive the averaged velocity dynamics by scaling the original forcing terms by functions of motion pattern parameters, as it is presented in [131]. This means that the proposed averaged model can be derived using directly the classical averaging, avoiding a control-oriented data-driven averaging approach; a solution for fish robots based on a simulation comparison of the original model and the averaged model obtained through classical averaging presented in [131].

By taking the trigonometric expansion of the expressions (5.4)-(5.6) and choosing the parameters as in (5.17), the averaged model of the velocity dynamics can be written as

$$\frac{d\boldsymbol{\upsilon}}{d\tau} = \varepsilon(\mathcal{A}\boldsymbol{\upsilon} + \mathbf{b}), \tag{5.13}$$

where $\mathcal{A}$ and $\mathbf{b}$ are given by (5.15) and (5.16), respectively. Since $d/d\tau = \varepsilon d/dt$, by changing the time scale from τ to t, the averaged model can be expressed as

$$\dot{\boldsymbol{\upsilon}} = \mathcal{A}\boldsymbol{\upsilon} + \mathbf{b}, \tag{5.14}$$

where

$$\mathcal{A} = \begin{bmatrix} \frac{k_4}{Nmk_2l} - \frac{c_t}{m} & (N-1)\phi_0(\frac{2c_p}{Nm} - \frac{\mu_n c_n}{mk_2l}) & 0 \\ (N-1)\phi_0(\frac{2c_p}{k_2} - \frac{\mu_n c_t}{mk_2l}) & \frac{k_4}{Nmk_2l} - \frac{Nc_n}{k_2} & 0 \\ \frac{\lambda_2}{1+\lambda_3}\phi_0 & 0 & \frac{-\lambda_1}{1+\lambda_3} \end{bmatrix}, \tag{5.15}$$

$$\mathbf{b} = \begin{bmatrix} B_1 \\ B_2 \\ 0 \end{bmatrix} = \begin{bmatrix} \frac{\mu_n k_{\alpha\omega}^2 \mu_3}{4Nml\alpha^2} - \frac{c_p k_{\alpha\omega}\mu_2}{2Nm} \\ -\frac{k_5}{2Nmk_2l} + \frac{k_6}{2Nmk_2l^2\alpha^2} \\ 0 \end{bmatrix}, \tag{5.16}$$

$$k_4 = \mu_n c_p(2(N-1)^2\phi_0^2 + \alpha^2\mu_1), \qquad k_5 = \mu_n c_p k_{\alpha\omega}\phi_0((N-1)\mu_2 - p_1p_3 + p_2p_4),$$
$$k_6 = \mu_n^2 k_{\alpha\omega}^2\phi_0((N-1)\mu_3 + p_1p_4 + p_2p_3), \qquad k_2 = Nm + N\mu_n,$$
$$p_1 = \sum_{i=1}^{N-1} \mathrm{g}(i,N)\cos((i-1)\delta), \quad p_2 = \sum_{i=1}^{N-1} \mathrm{g}(i,N)\sin((i-1)\delta), \quad \mu_1 = p_1^2 + p_2^2,$$
$$p_3 = \sum_{i=1}^{N-1}\sum_{j=1}^{N-1} a_{ij}\mathrm{g}(j,N)\sin((j-1)\delta), \ \mu_2 = \sum_{i=1}^{N-1}\sum_{j=1}^{N-1} a_{ij}\mathrm{g}(i,N)\mathrm{g}(j,N)\sin((i-j)\delta),$$
$$p_4 = \sum_{i=1}^{N-1}\sum_{j=1}^{N-1} a_{ij}\mathrm{g}(j,N)\cos((j-1)\delta), \ \mu_3 = \sum_{i=1}^{N-1}\sum_{j=1}^{N-1} a_{ij}\mathrm{g}(i,N)\mathrm{g}(j,N)\cos((i-j)\delta). \tag{5.17}$$

From (5.14), we see that the averaged model of the velocity dynamics of an underwater snake robot following the sinusoidal motion given by (3.3) is a linear system

and depends on the parameters of the motion pattern, α ω, δ, ϕ_0, the physical parameters of the robot and the parameters of the external forces (i.e. fluid forces and torques).

Remark 5.3: *Note that the averaged model of the velocity dynamics is general in the sense that it comprises a general class of sinusoidal motion patterns given by (3.3), instead of one specific motion pattern like lateral undulation as in previous works [97, 101]. Hence the proposed averaged model can be used for analysis and control design for a broader class of motion patterns, including lateral undulation and eel-like motion. In addition, the averaged model presented in [97, 101] for lateral undulation of ground snake robots falls out as a special case by setting the fluid coefficients due to the added mass effects to zero (i.e. $\mu_n = 0$ and $\lambda_3 = 0$).*

5.3 The Steady State Behavior of the Velocity Dynamics

In this section, we analyze the stability properties of the averaged model (5.14). Initially, we need to remove the constant offset term $\mathbf{b}$. We do so by employing the coordinate transformation $\mathbf{z} = \boldsymbol{\upsilon} + \mathcal{A}^{-1}\mathbf{b}$, which transforms (5.14) to

$$\dot{\mathbf{z}} = \dot{\boldsymbol{\upsilon}} = \mathcal{A}(\mathbf{z} - \mathcal{A}^{-1}\mathbf{b} + \mathbf{b}) = \mathcal{A}\mathbf{z}. \tag{5.18}$$

Using Mathematica, the eigenvalues of $\mathcal{A}$ are found as

$$\begin{aligned}
s_1 =& \frac{2c_p l\mu_n(\alpha^2\mu_1 + 2\phi_0^2(N-1)^2) - l^2(c_n m + c_t(m+\mu_n))N^2 - \sqrt{\Delta}}{2l^2 m(m+\mu_n)N^2},\\
s_2 =& \frac{(c_n - c_t)(2\phi_0^2 + \alpha^2\mu_1)\mu_n + 4(c_t - c_n)\phi_0^2\mu_n N}{2l^2 m(m+\mu_n)N^2},\\
&- \frac{((c_n + c_t)l^2 m + (2(c_t - c_n)\phi_0^2 + c_t l^2)\mu_n)N^2 - \sqrt{\Delta}}{2l^2 m(m+\mu_n)N^2},\\
s_3 =& -\lambda_1/(1+\lambda_3),
\end{aligned} \tag{5.19}$$

where $\Delta = l^2(c_n m - c_t(m+\mu_n))^2 N^2(4\phi_0^2(N-1)^2 + l^2N^2)$. In order to show that the equilibrium point $\mathbf{z} = 0$ is globally exponentially stable, we need to show that all eigenvalues of $\mathcal{A}$ are in the negative complex half plane [80]. By employing a symbolic inequality solver in Mathematica, with conditions, $m > 0$, $l > 0$, $\mu_n > 0$, $N > 1$, $0 < c_t < c_n$ and $\alpha > 0$, it can be shown that the eigenvalues of the averaged model are in the left half plane under the following conditions

$$\begin{aligned}
&\mu_1 < \frac{l^2N^2((c_n + c_t)m + c_t\mu_n)}{\alpha^2(c_n - c_t)\mu_n},\\
&|\phi_0| < \sqrt{\frac{(c_n + c_t)l^2 mN^2 + (\alpha^2(c_t - cn)\mu_1 + c_t l^2N^2)\mu_n}{2(c_n - c_t)(N-1)^2\mu_n}},\\
&\mu_1 + \frac{2\phi_0^2(N-1)^2}{\alpha^2} - \frac{l^2(c_n m + c_t(\mu_n - m))N^3 - \sqrt{\Delta}}{\alpha^2(c_n - c_t)\mu_n N} < 0.
\end{aligned} \tag{5.20}$$

Remark 5.4: *The stability conditions (5.20) hold for an underwater snake robot influenced by drag forces with anisotropic properties, $c_t < c_n$, and added mass effects, $\mu_n > 0$.*

The above results are summarized in the following proposition.

Proposition 5.1: Given an underwater snake robot described by (4.32), influenced by drag forces with anisotropic properties, $c_t < c_n$, and added mass effects, $\mu_n > 0$, and with the parameter $k_3 \approx 1/(N^2 m(m+\mu_n))$. If the joint coordinates, $\boldsymbol{\phi}$, the joint velocities, $\mathbf{v}_\phi$, and the joint accelerations, $\dot{\mathbf{v}}_\phi$, are given by (3.3), (3.6) and (3.7), respectively, and the frequency ω is sufficiently large, then the averaged model of the velocity dynamics, $\dot{\boldsymbol{\upsilon}} = \mathcal{A}\boldsymbol{\upsilon} + \mathbf{b}$, approximates the original one (5.2) with the error being of order $1/\omega$.

Remark 5.5: *From (5.20), it is seen that the amplitude of the sinusoidal motion pattern is essential in the stability conditions. Note that the stability conditions presented in [97] for a ground snake robot, are independent of the amplitude of the lateral undulation. This provides a new input for the stability analysis of swimming snake robots, where both added mass and linear drag effects are considered.*

Under the conditions in (5.20), the averaged system (5.18) is exponentially stable. Hence, $\boldsymbol{\upsilon}$ will converge exponentially to $-\mathcal{A}^{-1}\mathbf{b}$, which means that the average velocity will converge exponentially to the steady state velocity

$$\bar{\boldsymbol{\upsilon}} = -\mathcal{A}^{-1}\mathbf{b} = \begin{bmatrix} \bar{\upsilon}_t & \bar{\upsilon}_n & \bar{\upsilon}_\theta \end{bmatrix}^T, \tag{5.21}$$

which is given analytically by

$$\begin{aligned}\bar{\upsilon}_t = &\frac{k_{\alpha\omega} l^2 m(m+\mu_n)\left(k_{\alpha\omega}\mu_3\mu_n - 2c_p l\mu_2\alpha^2\right)\left(\frac{2c_p\mu_n c_1}{lm} - 2c_n N^2\right)}{K_1} \\ &- \frac{k_{\alpha\omega} 2\phi_0^2\mu_n(c_n m - c_t(m+\mu_n))(N-1)\left(k_{\alpha\omega}\mu_n c_2 - \alpha^2 2c_p l c_3\right)}{K_1},\end{aligned} \tag{5.22a}$$

$$\begin{aligned}\bar{\upsilon}_n = &\frac{\phi_0 k_{\alpha\omega}(m+\mu_n)\mu_n\left(\frac{2c_p\mu_n c_1}{l(m+\mu_n)N^2} - 2c_t\right)\left(k_{\alpha\omega}\mu_n c_2 - \alpha^2(c_n - c_t)c_3\right)}{K_1} \\ &- \frac{\phi_0 k_{\alpha\omega} 2(m+\mu_n)\left((c_t - c_n)\mu_2\alpha^2 + k_{\alpha\omega}\mu_3\mu_n\right)(c_n m - c_t(m+\mu_n))(N-1)}{K_1},\end{aligned} \tag{5.22b}$$

$$\begin{aligned}\bar{\upsilon}_\theta = &\frac{\phi_0 k_{\alpha\omega}\lambda_2 l^2 m(m+\mu_n)\left(k_{\alpha\omega}\mu_3\mu_n - 2c_p l\mu_2\alpha^2\right)\left(\frac{2c_p\mu_n c_1}{lm} - 2c_n N^2\right)}{K_1} \\ &- \frac{\phi_0 k_{\alpha\omega}\lambda_2 2\phi_0^2\mu_n(c_n m - c_t(m+\mu_n))(N-1)\left(k_{\alpha\omega}\mu_n c_2 - \alpha^2 2c_p l c_3\right)}{K_1},\end{aligned} \tag{5.22c}$$

where

$$K_1 = 2\alpha^2 l^3 \lambda_1 N m(m+\mu_n)\left(\frac{(c_n-c_t)\mu_n c_1}{l^2(m+\mu_n)N^2} - 2c_t\right)\left(\frac{(c_n-c_t)\mu_n c_1}{l^2 m} - 2c_n N^2\right)$$
$$- 2\alpha^2 l^3 \lambda_1 N \frac{4\phi_0^2(c_n m - c_t(m+\mu_n))^2(N-1)^2}{l^2}, \quad c_1 = \left(\mu_1\alpha^2 + 2\phi_0^2(N-1)^2\right),$$
$$c_2 = \mu_3(N-1) + p_2 p_3 + p_1 p_4, \quad c_3 = \mu_2(N-1) - p_1 p_3 + p_2 p_4$$

According to Theorem 10.4 in [80], the averaged model of the velocity dynamics (5.14) under the conditions (5.20), for sufficiently small ε (i.e. for sufficiently large ω) will approximate the exact velocity dynamics (5.2) for all time, with the error being of order ε.

We now summarize the above discussion in the following proposition.

Proposition 5.2: Given an underwater snake robot described by (4.32), influenced by drag forces with anisotropic properties, $c_t < c_n$, and added mass effects, $\mu_n > 0$. If Assumption 5.1 is satisfied, the joint coordinates, the joint velocities and the joint accelerations are given by, respectively, (3.3), (3.6) and (3.7), and the conditions (5.20) are satisfied, then there exist $k > 0$ and $\omega^* > 0$ such that for all $\omega > \omega^*$,

$$\|\boldsymbol{v}(t) - \boldsymbol{v}_{\alpha v}(t)\| \leq k/\omega, \text{ for all } t \in [0, \infty), \tag{5.23}$$

where $\boldsymbol{v}(t)$ denotes the exact velocity of the underwater snake robot given by (5.2) and $\boldsymbol{v}_{\alpha v}(t)$ is the average velocity given by (5.14). Moreover, the average velocity $\boldsymbol{v}_{\alpha v}(t)$ of the underwater snake robot will converge exponentially fast to the steady state velocity $\bar{\boldsymbol{v}}$ given by (5.21).

5.4 Relationship between Gait Parameters and Velocity

Proposition 5.2 states mathematically that for an underwater snake robot influenced by drag forces with anisotropic properties and added mass effects, forward propulsion is achieved by the general sinusoidal motion pattern given in (3.3). Furthermore, the results give an analytical expression for the steady state velocity as a function of the motion pattern parameters α, ω, δ, and ϕ_0, i.e. the amplitude, the frequency, phase shift and offset of the joint motion during general sinusoidal motion pattern. Note that the results of this study are general and constitute a powerful tool in order to achieve faster motion by choosing the appropriate motion pattern and an optimal combination for the gait parameters.

The resulting steady state velocity of the underwater snake robot in addition to depending on the parameters of the robot (i.e. m, l, N, μ_n, c_n, c_t, λ_1, λ_2, λ_3), also depend on the sinusoidal gait pattern parameters α, ω δ and ϕ_0. Additionally, it is easily verifiable that the steady state velocity of the underwater snake robot with zero joint offset ($\phi_0 = 0$) is given by $\bar{v}_t = \dfrac{k_{\alpha\omega} l(m+\mu_n)(\alpha^2(c_t-c_n)\mu_2 + k_{\alpha\omega}\mu_3\mu_n)N}{2\alpha^4(c_n-c_t)\mu_1\mu_n - 4\alpha^2 c_t l^2(m+\mu_n)N^2}$, $\bar{v}_n = 0$ and $\bar{v}_\theta = 0$.

Note that similar studies are presented for the special case of lateral undulation motion pattern for eel-like robots [106] and ground snake robots [101]. In particular, earlier studies for ground snake robots [101] and eel-like robots, where the added

mass effects and fluid torques are neglected [106], show that the average forward velocity of the robot: 1) is proportional to the square of the amplitude of the sinusoidal motion pattern, 2) is proportional to the gait frequency and 3) depends also on the weighted sum of the constant phase shift between the joints. However, in this section, it is shown that the average forward velocity of an underwater snake robot, influenced both by added mass and linear drag effects, and following a more general sinusoidal gait pattern, has a more complex relationships to the gait pattern parameters α, ω and δ.

The results of this section can be summarised in the following proposition.

Proposition 5.3: Consider an underwater snake robot with N links described by (4.32), influenced both by added mass and linear drag effects, that follows any sinusoidal gait pattern described by (3.3). The average forward velocity of the underwater snake robot will converge exponentially to a steady state velocity which:

- is a function of the amplitude of the sinusoidal motion pattern, α.
- depends on a linear and a nonlinear term of the gait frequency, ω.
- depends on the phase shift between the joints, δ.

Remark 5.6: *It is worth to mention that the derived relationship between the gait pattern parameters and the steady-state velocity presented in Proposition 5.3 provides a useful tool for motion planning and parameter tuning of sinusoidal gait patterns for underwater snake robots. This information is useful since an increase/decrease of the forward velocity can be achieved by increasing/decreasing the gait parameters. The results presented in this section are general and constitute a powerful tool for achieving faster forward motion by selecting the most appropriate motion pattern and an optimal combination for the gait parameters.*

5.5 Simulation Study: Exact and Averaged Velocity

This section presents simulation results, for lateral undulation and eel-like motion, to investigate the validity of the derived properties for the averaged velocity dynamics of an underwater snake robot. The exact model of the underwater snake robot is given by (4.32) under the assumption that $\boldsymbol{\phi}$ is controlled by (3.3), while the averaged model of the underwater snake robot is given by (5.14). Both models are implemented and simulated in *Matlab R2013b*. The dynamics was calculated using *ode45* solver in *Matlab* with a relative and absolute error tolerance of 10^{-6}.

5.5.1 Simulation Parameters

We consider an underwater snake robot having $N = 10$ links of length $l = 0.14$ m and mass $m = 0.6597$ kg. Furthermore, we choose the fluid forces and torque coefficients as $c_t = 0.45$, $c_n = 5$, $\mu_n = 0.4$, $\lambda_1 = 0.5$, $\lambda_2 = 20$ and $\lambda_3 = 0.01$, the initial values as ($\boldsymbol{\phi} = 0$, $\theta = 0$, $p_t = 0$, $p_n = 0$, $\boldsymbol{\upsilon}_\phi = 0$, $\upsilon_\theta = 0$, $\upsilon_t = 0$, $\upsilon_n = 0$). Note that, as it is shown in 4.6, for these coefficients the qualitative and quantitative behavior of the control-oriented model of an underwater snake robot (4.32) is similar to the behavior of the complex model (3.10). The joint reference

coordinates were calculated according to the motion pattern (3.3) with $\alpha = 0.05$ m, $\omega = 120^{\circ}/\text{s}$, $\delta = 40^{\circ}$. The values of the joint offset angle, ϕ_0, will be presented for each simulation result. Furthermore, in order to achieve the desired motion patterns (3.3) the joint PD controller (3.5) is used with the controller gains $k_p = 20$ and $k_d = 5$.

5.5.2 Simulation results for lateral undulation

The motion of the underwater snake robot during lateral undulation is initially simulated with the joint offset angle $\phi_0 = 0$ m, i.e. locomotion along the earth-fixed x axis. For the simulation parameters of the underwater snake robot given in the previous subsection, the eigenvalues of the averaged system, $s_1 = -4.7183$, $s_2 = -0.6821$, $s_3 = -0.4950$, are all in the left half complex plane, which means that the conditions (5.20) hold for the chosen parameters of the underwater snake robot. In addition, in Fig. 5.1 it is shown that Assumption 5.1 holds for the simulated robot. Hence Proposition 5.2 gives that the average velocity will converge exponentially fast to the steady state velocity given in (5.22), which for the given parameters is $\bar{v}_t \approx 0.2338$ m/s, $\bar{v}_n = 0$ m/s and $\bar{v}_\theta = 0^{\circ}/\text{s}$. The simulation results are presented in Fig. 5.2. The top left plot illustrates the global CM position of the underwater snake robot, while the other three plots show the exact and the average velocities of the underwater snake robot. The simulation results shown in Fig. 5.2 verify that the velocities of the averaged model converge to the expected values of the steady state velocities. Furthermore, the error between the exact velocities and the averaged ones of the underwater snake robot is almost zero.

We then performed a simulation to study the averaged velocity dynamics during lateral undulation for the joint offset angle $\phi_0 = l/8$ m, i.e. for lateral undulation along a curve. The eigenvalues of the corresponding averaged model are all negative: $s_1 = -0.4950$, $s_2 = -4.7358$, $s_3 = -0.5987$. By Proposition 5.2 the average velocity of the underwater snake robot should converge to $\bar{v}_t \approx 0.2646$ m/s, $\bar{v}_n \approx 0.0271$ m/s and $\bar{v}_\theta \approx 0.1852^{\circ}/\text{s}$. This agrees with the simulation results shown in Fig. 5.3. In addition, from Fig. 5.3 we can see that the averaged model approximates very well the original model for the case of a nonzero joint offset angle as well.

In order to investigate how well the averaged system approximates the original system for lower frequencies, we performed a simulation with frequency $\omega = 30^{\circ}/\text{s}$, and joint offset angle $\phi_0 = l/8$ m. The simulation results are presented in Fig. 5.4. The averaged model is also here stable, with eigenvalues $s_1 = -0.4950$, $s_2 = -4.7358$, $s_3 = -0.5987$, and the steady state velocities converge to $\bar{v}_t \approx 0.0661$ m/s, $\bar{v}_n \approx 0.0068$ m/s and $\bar{v}_\theta \approx 0.0463^{\circ}/\text{s}$ as predicted by (5.22). The simulation results show that even though the deviation between the averaged and the original model increases, the averaged model is still able to approximate the original velocity dynamics quite well even in the case when the frequency of the sinusoidal motion is reduced significantly. Note that the eigenvalues of the averaged system did not change by changing the frequency of the sinusoidal motion because the eigenvalues of the system (5.19) are independent of the parameter ω.

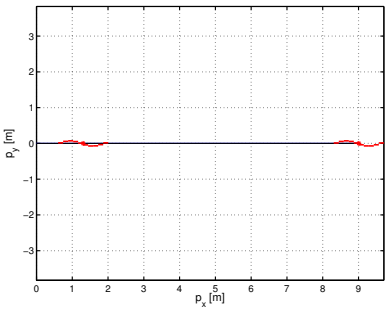

(a) The position of the CM

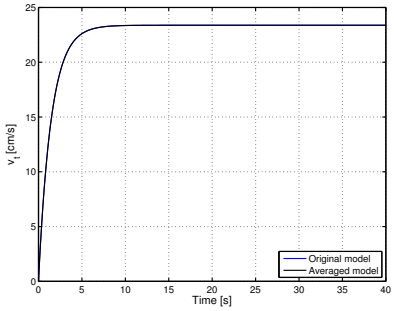

(b) The tangential velocity, v_t

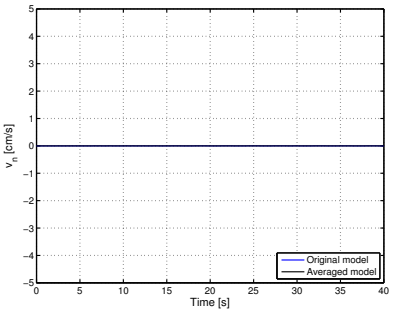

(c) The normal velocity, v_n

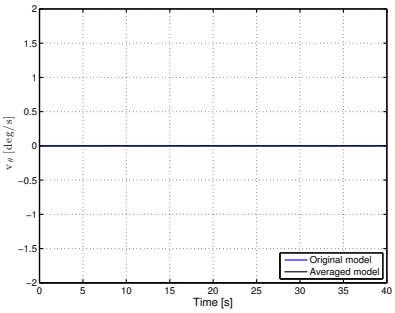

(d) The angular velocity, v_θ

Figure 5.2: Lateral undulation along a straight line ($\phi_0 = 0$ m).

5.5.3 Simulation results for eel-like motion

Eel-like motion is achieved by propagating lateral axial undulations with increasing amplitude from nose to tail. This is achieved by choosing $g(i, N) = (N - i)/(N + 1)$ in (3.3). At first, eel-like motion is examined by setting the joint offset angle $\phi_0 = 0$ m. Simulation results are presented in Fig. 5.5. The eigenvalues of the averaged system, $s_1 = -4.7159$, $s_2 = -0.6798$, $s_3 = -0.4950$, are negative. Thus, by Proposition 5.2 the average velocity will converge exponentially to the steady state velocity $\bar{v}_t \approx 0.0606$ m/s, $\bar{v}_n = 0$ m/s and $\bar{v}_\theta = 0^\text{o}$/s. This is fully in line with the simulation results shown in Fig. 5.5. We then choose the joint offset angle $\phi_0 = l/8$ m. The eigenvalues of the corresponding averaged model are then $s_1 = -0.4950$, $s_2 = -4.7334$ and $s_3 = -0.5964$, which shows that the averaged system is also exponentially stable and by Proposition 5.2 the average velocity of the underwater snake robot should converge to $\bar{v}_t \approx 0.0686$ m/s, $\bar{v}_n \approx 0.0070$ m/s and $\bar{v}_\theta \approx 0.0480^\text{o}$/ s. This is fully in line with the simulation results presented in Fig. 5.6.

Similarly to the lateral undulation case, simulation results during eel-like motion with reduced frequency $\omega = 30^\text{o}$/s and joint offset angle $\phi_0 = l/8$ m are performed.

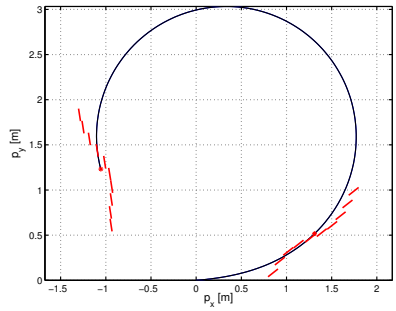

(a) The position of the CM

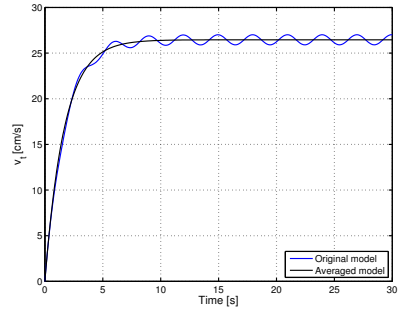

(b) The tangential velocity, v_t

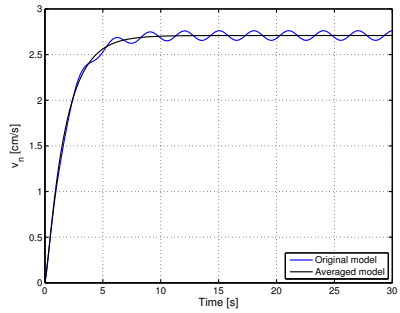

(c) The normal velocity, v_n

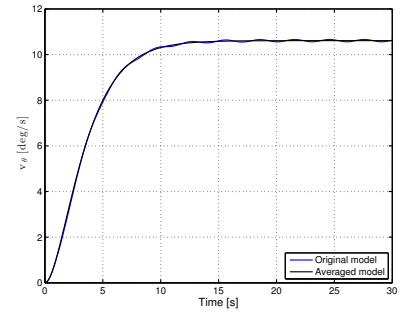

(d) The angular velocity, v_θ

Figure 5.3: Lateral undulation for turning motion with joint offset angle $\phi_0 = l/8$ m and $\omega = 120^o/s$.

These are presented in Fig. 5.7. The steady state velocities are expected to converge to $\bar{v}_t \approx 0.0166$ m/s, $\bar{v}_n \approx 0.0017$ m/s and $\bar{v}_\theta \approx 0.0116^o/s$. Note that the averaged model is able to approximate the original velocity dynamics also when reducing the frequency of the eel-like gait pattern (Fig. 5.7). To conclude, the simulation results for eel-like motion pattern (Fig. 5.5-5.7), show that the velocities of the averaged model converge to the expected values of the steady state velocities. A more efficient way for generating the eel-like motion pattern has to be analyzed, in the future, in order to reduce the higher oscillation behavior.

5.6 Simulation Study: Forward Velocity Relationships

In this section, the validity of Proposition 5.3 will be investigated through a simulation study. In particular, we will present simulation results in order to validate the properties derived for the relationship between the gait pattern parameters and the forward velocity both for lateral undulation and eel-like motion patterns. Simulation results are presented both for the control-oriented model and the complex one. The simulation study will thus investigate the validity of the theoretical

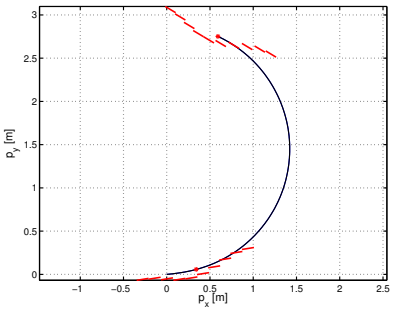

(a) The position of the CM

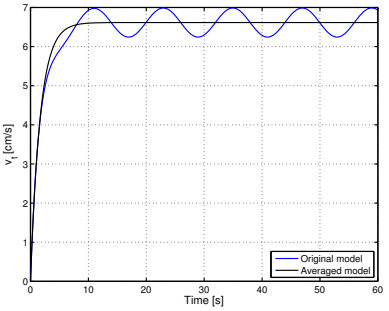

(b) The tangential velocity, v_t

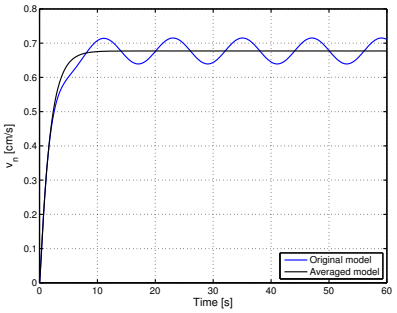

(c) The normal velocity, v_n

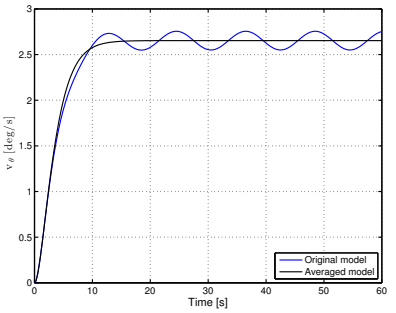

(d) The angular velocity, v_θ

Figure 5.4: Lateral undulation for turning motion with joint offset angle $\phi_0 = l/8$ m and $\omega = 30°/s$.

results in Propositions 5.3, and in addition the study will further investigate the validity of the control-oriented model as an adequate representation of the dynamics of the complex model, by investigating whether the results developed based on the control-oriented model also hold for the original complex model. In this chapter, the current effects have not been considered, since the current effects are not taken into account in the control-oriented model. The models were implemented in *Matlab R2013b*. The dynamics was calculated using the *ode23tb* solver with a relative and absolute error tolerance of 10^{-4}.

5.6.1 Simulation Parameters

We consider snake robots with respectively $N = 5$, $N = 10$, $N = 20$ links, each one having length $l = 0.14$ m. The five links constitute a rather short snake robot, while ten to twenty links constitute a more normal length for snake robots. The mass of each link is $m = 0.6597$ kg and is chosen so to fulfil the neutrally buoyant assumption. The initial values of the states of the snake robot were set to the initial reference values at $t = 0$, since it is not the transient behavior of the controller

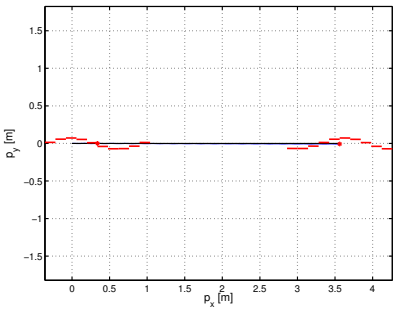

(a) The position of the CM

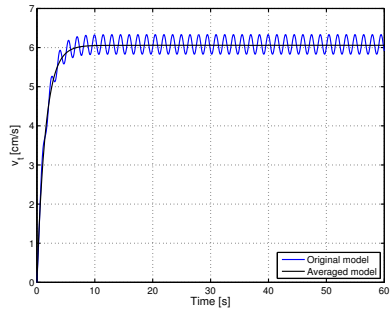

(b) The tangential velocity, υ_t

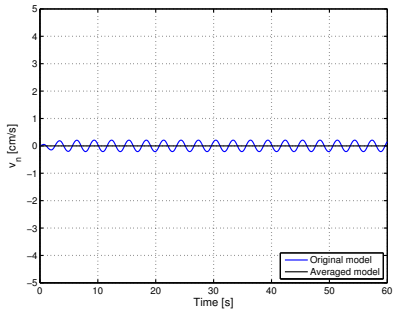

(c) The normal velocity, υ_n

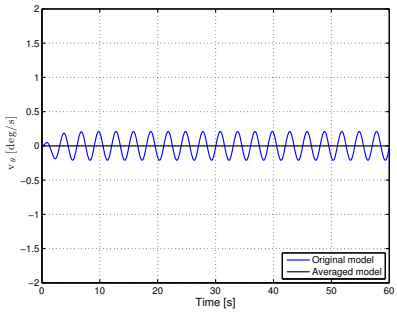

(d) The angular velocity, υ_θ

Figure 5.5: Eel-like motion along a straight line ($\phi_0 = 0$ m).

(4.33) that is to be verified, but rather the relationship between the gait pattern parameters and the forward velocity when the joints follow the sinusoidal reference signal (3.3). The initial heading of the robot is along the inertial x axis. Furthermore, we choose the fluid forces and torque coefficients as $c_t = 0.2639$, $c_n = 4.2$, $\mu_n = 0.3957$, $\lambda_1 = 2.2988 \times 10^{-7}$, $\lambda_2 = 4.3103 \times 10^{-4}$, for the complex model and $c_t = 0.45$, $c_n = 5$, $\mu_n = 0.4$, $\lambda_1 = 0.5$, $\lambda_2 = 20$, $\lambda_3 = 0.01$ for the control-oriented model. The joint PD controller (3.5) is used for each joint with parameters $k_p = 20$, $k_d = 5$, and lateral undulation and eel-like motion are achieved by choosing $\mathrm{g}(i,n) = 1$ and $\mathrm{g}(i,n) = (n-i)/(n+1)$ in (3.3), respectively. The gait pattern parameters are presented in each simulation result. In particular, in the simulation results the forward velocity of the underwater snake robot, denoted as $\bar{v}$, is presented for the different values of the gait parameters. The forward velocity can be calculated based on the initial and final position. In particular, for each simulation trial with simulation time set to 30 sec the average forward velocity is given by

$$\bar{v} = \frac{\sqrt{(p_x(30) - p_x(0))^2 + (p_y(30) - p_y(0))^2}}{30}. \tag{5.24}$$

Remark 5.7: Note that the values of the gait parameter α for the complex does not

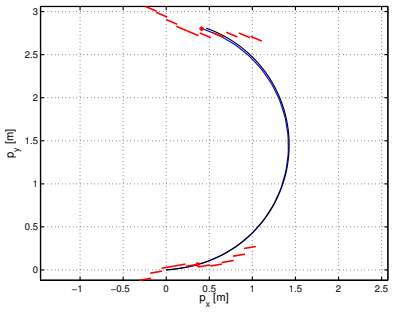

(a) The position of the CM

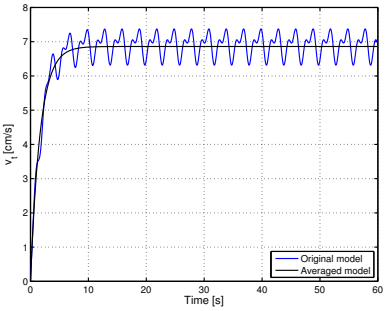

(b) The tangential velocity, v_t

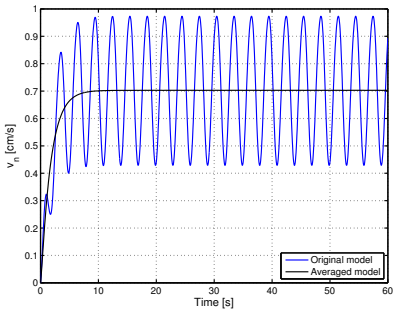

(c) The normal velocity, v_n

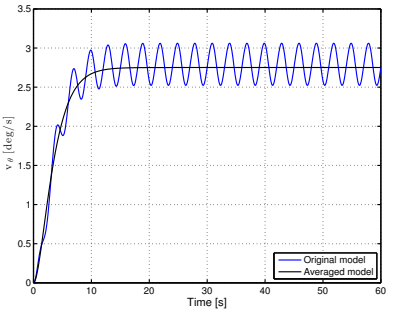

(d) The angular velocity, v_θ

Figure 5.6: Eel-like motion for turning motion with joint offset angle $\phi_0 = l/8$ m and $\omega = 120^\circ/\text{s}$.

correspond directly to α for the control-oriented model, since a general mapping for the amplitudes of the corresponding models remains topic of future work, and thus a quantitative comparison between the results from the complex and the control-oriented model is not relevant. Hence, the simulation results below present only a qualitative comparison between the complex and the control-oriented models.

Remark 5.8: *It is worth to mention that even though the joint coordinates of the control-oriented and the complex model are different, it still makes sense to investigate the validity of the Proposition 5.3 for the complex model (see [101]).*

5.6.2 Relationship between α and the forward velocity

As stated in Proposition 5.3, the average forward velocity is a function of the amplitude of the sinusoidal motion pattern, α. In order to investigate the influence of this parameter on the achieved forward velocity of the underwater snake robot, simulation results are presented for different values of the parameter α both for lateral undulation and eel-like motion patterns. The average forward velocity is

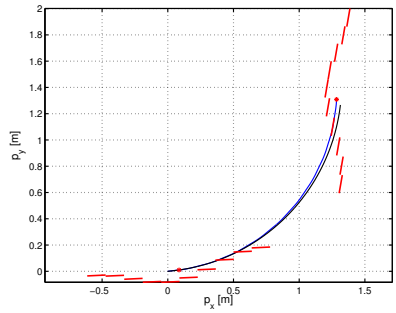

(a) The position of the CM

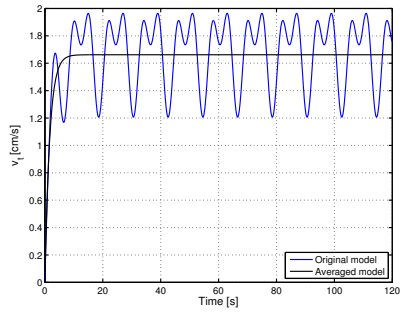

(b) The tangential velocity, v_t

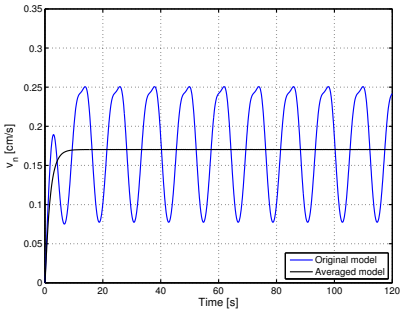

(c) The normal velocity, v_n

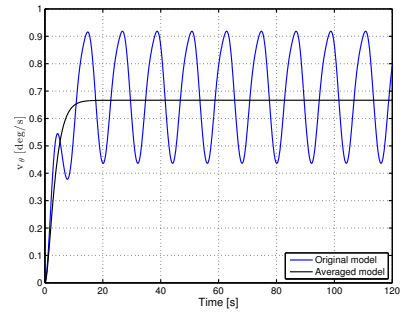

(d) The angular velocity, v_θ

Figure 5.7: Eel-like motion for turning motion with joint offset angle $\phi_0 = l/8$ m and $\omega = 30^o/s$.

calculated according to the (5.24). Simulation results for the control-oriented model taking into account the added mass and linear drag effects are presented in Fig. (5.8(a),5.9(a)) for lateral undulation and eel-like motion patters, respectively. Fig. (5.8(b),5.9(b)) present simulation results for the complex model of underwater snake robot where the added mass, linear and nonlinear drag effects are taken into account, respectively, for lateral undulation and eel-like motion patterns. The number of links N and the values of the gait parameters ω and δ are shown in each simulation result for the different motion patterns.

From Fig. 5.8 and Fig. 5.9, we see that the average forward velocity is increased by increasing the parameter α for constant values of ω and δ both for lateral undulation and eel-like motion. Note that for small values of the parameter $\alpha \leq 20^o$, for which the control-oriented model is valid (see Assumption 4.1), the forward velocity has an exponential increase when increasing the parameter α. Furthermore, we can see that even if the properties in Proposition 5.3 are derived based on the control-oriented model of underwater snake robots, the results for the complex model show a similar influence of the parameter α on the forward velocity. In particular, we see that for constant values of ω and δ, an increase of the parameter

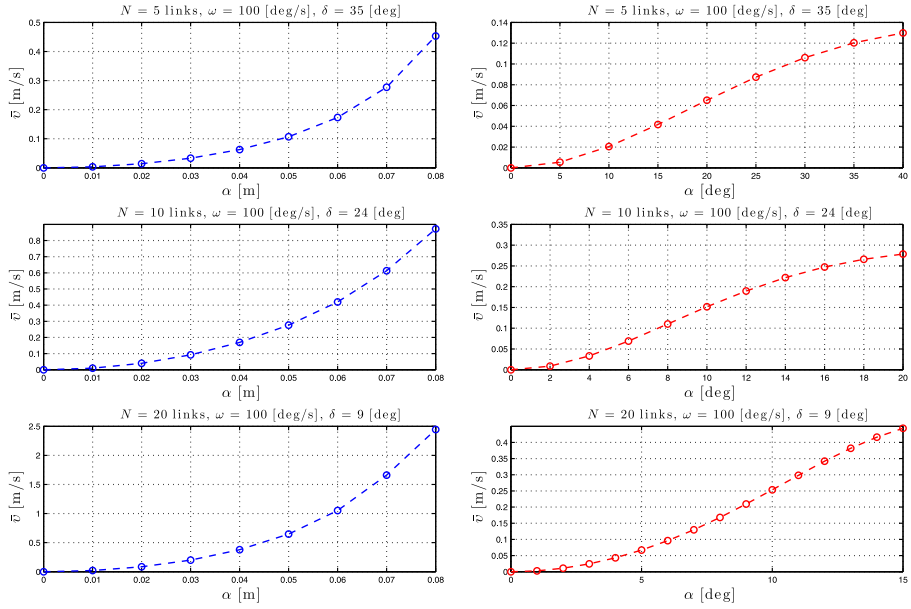

(a) Control-oriented model (b) Complex model

Figure 5.8: Lateral undulation: Simulation results for the forward velocity of the underwater snake robot for different values of α.

α results in an increase of the forward velocity both for the complex and the control-oriented models. These results are in accordance with the properties presented in Proposition 5.3.

5.6.3 Relationship between ω and the forward velocity

Proposition 5.3 states that the average forward velocity depends on a linear and a nonlinear function of the gait frequency, ω. To validate the influence of this parameter, simulation results are presented by calculating the forward velocity of the robot for different values of the gait parameter ω. Simulation results for the control-oriented model are shown in Fig. (5.10(a),5.11(a)), while Fig. (5.10(b),5.11(b)) show simulation results for the complex model presented in Section 2.2. The number of links N and the values of the gait parameters α and δ are shown in each simulation result for the different motion patterns.

From Fig. 5.10 and 5.11, we can see that for constant values of the parameters α and δ, an increase of ω results in an increase of the forward velocity. This is in accordance with Proposition 5.3 which states that the average forward velocity depends on a linear and a nonlinear function of the parameter ω. In addition, from Fig. (5.10(a),5.11(a)), we see that the increase of the forward velocity is almost linear both for lateral undulation and eel-like motion patterns. Hence, the influence of the nonlinear function of the parameter ω on the forward velocity is almost negligible compared to the linear relationship between these given in

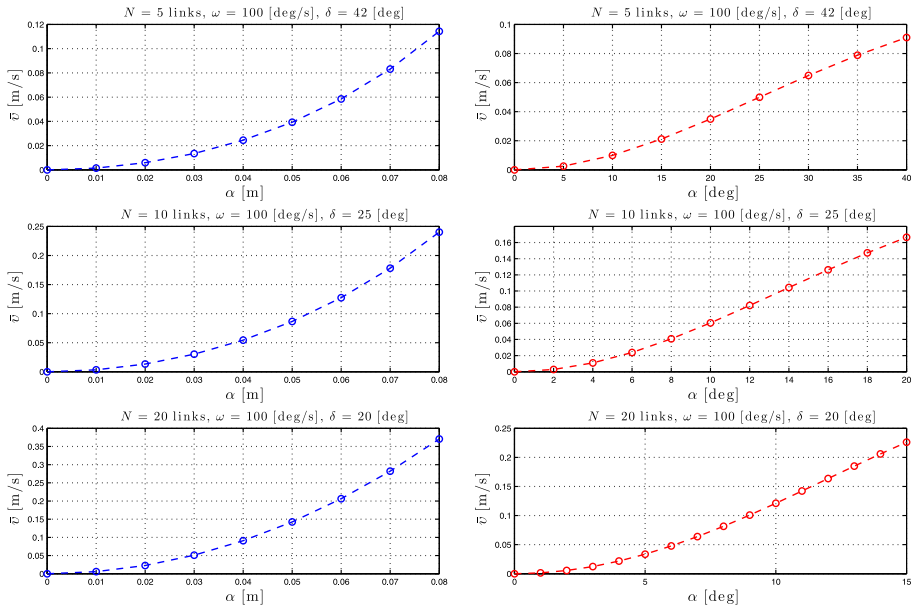

(a) Control-oriented model (b) Complex model

Figure 5.9: Eel-like motion: Simulation results for the forward velocity of the underwater snake robot for different values of α.

Proposition 5.3 for the control-oriented model. However, in Fig. (5.10(b),5.11(b)), we clearly see the influence of the effects of a nonlinear function of ω. Except for the high frequency case there is a good qualitative agreement between the simulation results of the complex and the control-oriented model. This is probably because the control-oriented model is not able to capture the effects of the nonlinear drag since these effects seems to dominate in high frequencies. This is mainly because the nonlinear drag effects that are considered in the complex model and are not taken into account in the control-oriented model. It seems that in high frequencies the nonlinear drag effects that are considered for the complex model has notable influence to the response of the system. The simulation results show that the properties derived based on the control-oriented model hold also for the complex model presented in Section 2.2, something which supports the assumption that the control-oriented model is a valid approximation of the complex model for analysis and control design.

5.6.4 Relationship between δ and the forward velocity

Regarding the influence of the parameter δ, Proposition 5.3 states that the forward velocity depends on the phase shift between the joints, δ. To investigate the influence of the phase shift on the achieved forward velocity, simulation results are presented for different values of δ while keeping the gait parameters α and ω constant. Simulation results for the complex model and the control-oriented model

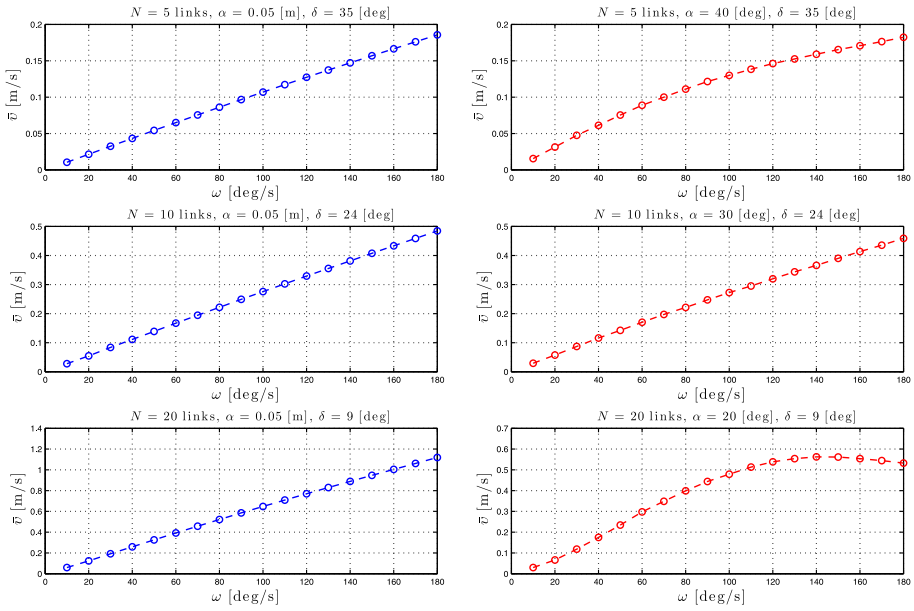

(a) Control-oriented model (b) Complex model

Figure 5.10: Lateral undulation: Simulation results for the forward velocity of the underwater snake robot for different values of ω.

are presented in Fig. (5.12(b),5.13(b)) and Fig. (5.12(a),5.13(a)) respectively, for lateral undulation and eel-like motion patterns. The number of links N and the values of the gait parameters α and ω are shown in each simulation result for the different motion patterns.

From Fig. 5.12 and Fig. 5.13, we see that there is a value of the gait parameter δ which gives the maximum forward velocity when the gait parameters α and ω are kept constant. In addition, we see that the forward velocity depends on the values of the parameter δ, which is in accordance with the properties presented in Proposition 5.3. In particular, we see that we have an increase of the forward velocity until a certain value of the parameter δ, while after this value an additional increase of this parameter for constant values of α and ω results in a decrease in the forward velocity. Note that the results presented in Fig. 5.12 and Fig. 5.13 for the complex and the control-oriented models are only qualitatively comparable. However, the qualitative comparison supports that the control-oriented model is an adequate representation of the complex model, i.e. that the properties stated in Proposition 5.3 hold for both the control-oriented and the complex model.

5.7 Experimental Setup

This section describes the experimental setup employed in order to obtain the experimental results presented in the following chapters of this thesis.

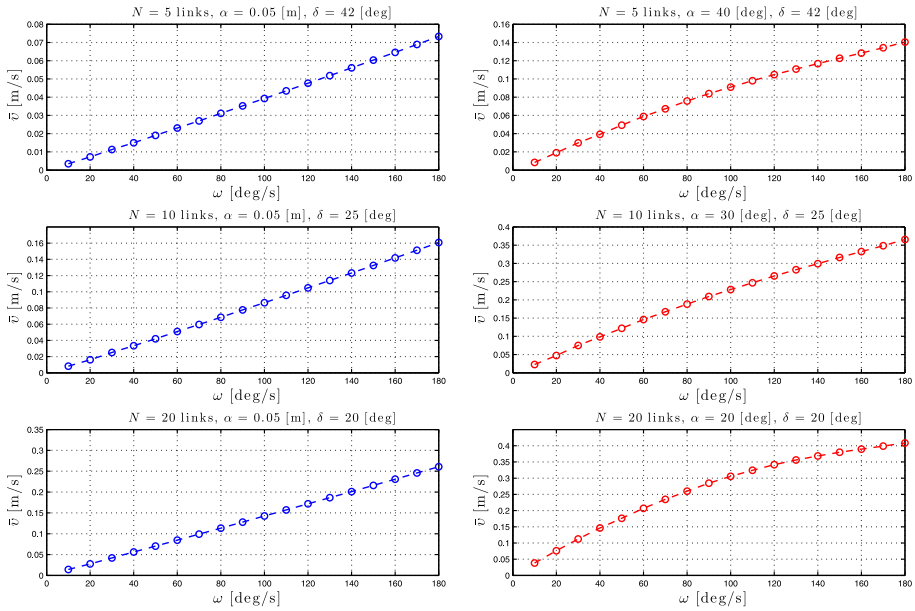

(a) Control-oriented model (b) Complex model

Figure 5.11: Eel-like motion: Simulation results for the forward velocity of the underwater snake robot for different values of ω.

5.7.1 Underwater Snake Robot – Mamba

We now present the underwater snake robot that was used in our experiments. Mamba (Fig. 5.14) is a snake robot that is developed for research on both ground and underwater snake robot locomotion. This flexibility results from its mechanical robustness and reconfigurable nature. The robot is watertight and has a modular design with a common mechanical and electrical interface between the modules. Each joint module is actuated by a Hitec servo motor (HSR 5990TG) and in each joint, a force/torque sensor on the joint shaft, two temperature sensors, a 3-axis accelerometer and a water leakage detector, are included. Furthermore, each joint is controlled by means of a microcontroller card (TITechSH2 Tiny Controller from HiBot), while the total number of microcontrollers inter-communicate over a CAN bus. Power supply cables (35 V) run among the modules along with the CAN bus. A more detailed description of this robot can be found in [102].

During the experiments, Mamba was covered by a watertight skin, despite all the modules of the robot being watertight down to about 5 m, in order to achieve an extra water barrier (Fig. 5.15). The skin is made by Groundsheet, Nylon, PU-coated, 120 g/sqm material and it is attached at the head and the tail parts using rubber bottle wrist seals, which are glued to the skin. This type of cover makes the robot's outer surface smoother and thus reduces the drag effects.

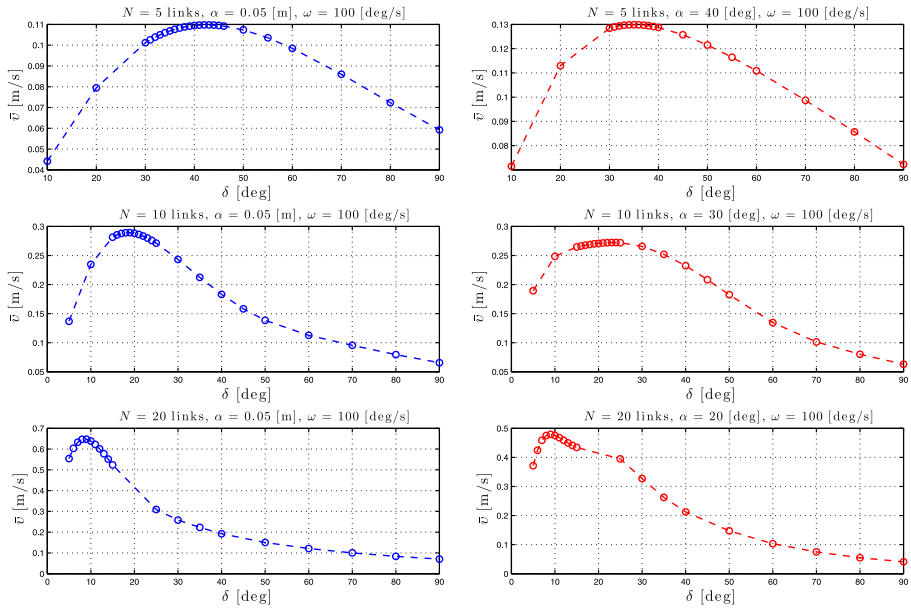

(a) Control-oriented model (b) Complex model

Figure 5.12: Lateral undulation: Simulation results for the forward velocity of the underwater snake robot for different values of δ.

5.7.2 Experimental setup

The experiments were performed in the MC-lab in Marintek, Trondheim, Norway [2], in a tank of dimensions L: 40 m, H: 1.5 m and W: 6.45 m. In order to have accurate real time measurements of the position and orientation of underwater objects the integration of a motion capturing system is essential. Thus, for our experimental process, an underwater motion capture system from Qualisys [4] was installed in the basin, covering an underwater working area of dimensions 10m×1.35m× 5.45m.

The particular configuration of the snake robot Mamba [102], see Fig. 5.15, used in these experiments, consisted of 18 identical joint modules mounted horizontally and vertically in an alternating fashion. In order for the robot to move according to a strictly horizontal motion pattern, the angles for the joints with vertical rotating axis were set to zero degrees. In this case, the kinematics of the snake robot corresponds to a planar snake robot with links of length $2l = 0.18$ m and mass $m \approx 0.8$ kg. The experiments demonstrated that the robot had a slightly positive buoyancy and was swimming near the water surface.

In order to have accurate measurements of the position and orientation of the robot, reflective markers were attached on the tail part of the robot, something that is required by the motion capturing system, as shown in Fig. 5.15. Although the robot was swimming on the surface of the tank, the markers were submerged, approximately 0.15 m under the water surface, due to constraints in the work area

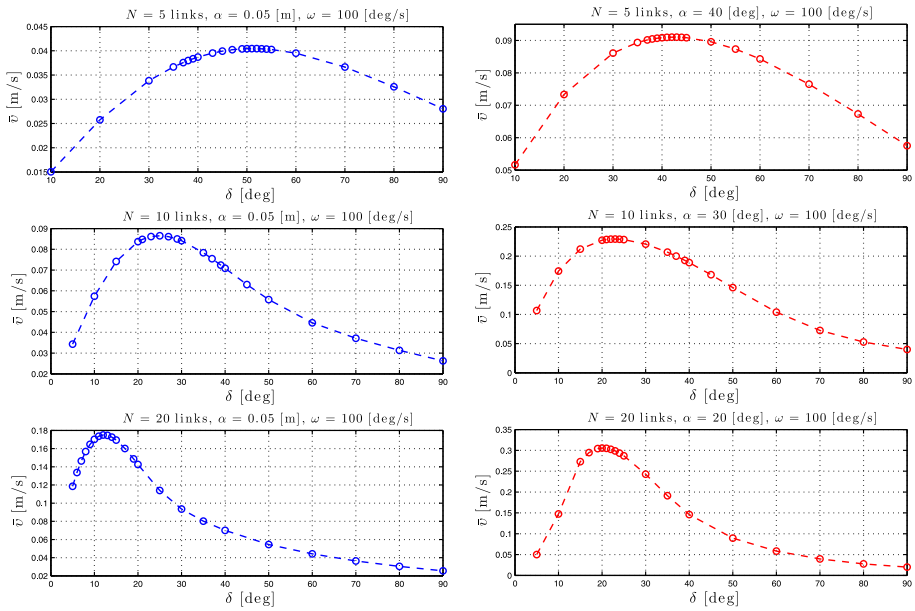

(a) Control-oriented model (b) Complex model

Figure 5.13: Eel-like motion: Simulation results for the forward velocity of the underwater snake robot for different values of δ.

covered by the camera system. The global frame coordinates of the tail link and the absolute angle of the tail were extracted by the camera-based motion capture system. In particular, the camera system consists of six identical cameras, which allow reflective markers to be tracked under the water. The measured position and the absolute angle of the tail were obtained from an external computer where the Qualisys system [4] was connected, and afterwards these measurements were sent through UDP in *LabVIEW 2013* to another computer. Having the measurements of the tail position and orientation, and the individual joint angles, the center of mass position, $\mathbf{p}_{\text{CM}}$, and the absolute link angles, $\boldsymbol{\theta}$, of the underwater snake robot were calculated from the kinematics equations presented in Section 2.2.

5.8 Experimental Study: Forward Velocity Relationships

In this section, experimental results are presented in order to investigate the properties noted in Proposition 5.3. In particular, we will experimentally validate the properties regarding the gait parameters using the underwater snake robot Mamba (Fig. 5.15). The underwater snake robot Mamba and the experimental setup were presented in Section 5.7.

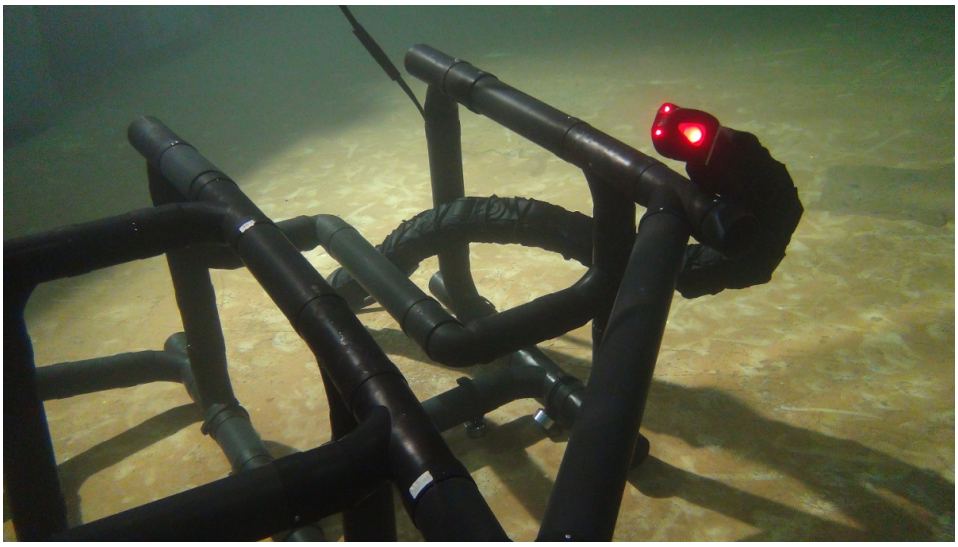

Figure 5.14: The underwater snake robot Mamba developed at NTNU to support the research on both ground and underwater snake robot locomotion.

Figure 5.15: The underwater snake robot Mamba in the pool at MC-lab with the markers attached to the tail for position measurements.

5.8.1 Simulation results

In order to compare the experimental results with ideal simulation results, we simulate the model of the underwater snake robot presented in Section 2.2 with the fluid coefficients set to $C_f = 0.03$, $C_D = 1$, $C_A = 1$, $C_M = 1$, in order to compare the experimental results and the ideal simulation results. We consider an underwater snake robot with $n = 9$ links, each one having length $2l = 0.18$ m and mass $m = 0.8$ kg, i.e. identical to the physical robot, Mamba (Fig. 5.15). The hydrodynamic related parameters c_t, c_n, μ_n λ_1, λ_2 and λ_3 for the elliptic section with major and minor diameters $2a = 2 \cdot 0.055$ m and $2b = 2 \cdot 0.05$ m, respectively, and $\rho = 1000$ kg/m^3 were calculated by using equations for the fluid parameters derived in Section 2.2. In these simulations a joint PD-controller (3.5) was used with parameters $k_p = 20, k_d = 5$, while lateral undulation or eel-like motion were

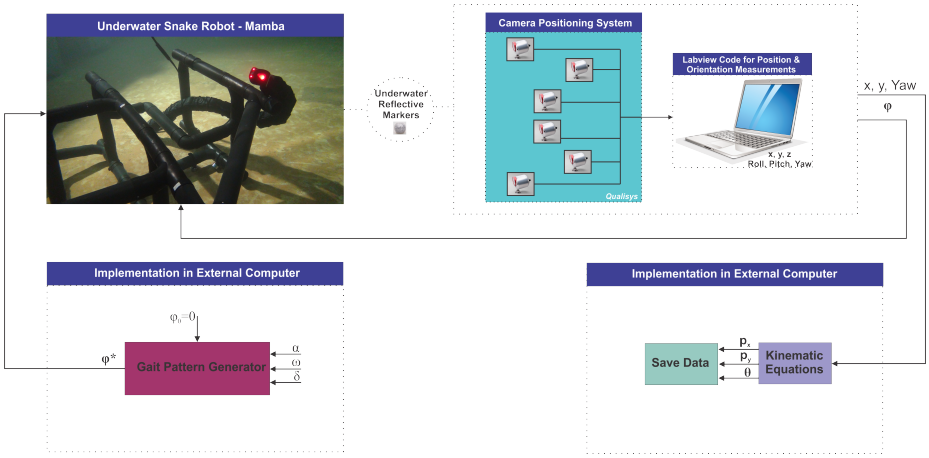

Figure 5.16: Illustration of the experimental process adopted in the experiments.

achieved by moving the joints according to (3.1) and (3.2), respectively, with gait parameters values similar to the ones of the experimental trials.

5.8.2 Experimental results

The essential properties presented in Proposition 5.3 are experimentally investigated using the underwater snake robot Mamba (see Fig. 5.15). As mentioned in Section 5.7 the robot consist of 18 identical joint modules mounted horizontally and vertically in an alternating fashion. The center of mass position, $\mathbf{p}_{\mathrm{CM}}$, and the absolute link angles, $\boldsymbol{\theta}$, of the underwater snake robot were obtained as described in Section 5.7. We applied sinusoidal motion pattern with different gait pattern parameters. In particular, in each trial, the reference joint angles, computed by (3.3) for $n = 9$, choosing $\mathrm{g}(i, n) = 1$ and $\mathrm{g}(i, n) = (n - i)/(n + 1)$ in case of lateral undulation or eel-like motion, were sent to the robot via the CAN. In each trial we measured the position of the center of mass and the steady state values of the achieved velocity for approximately 30 sec of motion. A proportional controller, implemented in the microcontroller of each joint module controls the corresponding joint angle.

The initial values of the link angles were set to zero in each trial. The total experimental process that is adopted is illustrated in Fig. 5.16. In addition, a visualization from a video recording of the robot in Fig. 5.17 shows how lateral undulation and eel-like motion were carried out by Mamba.

The center of mass position of the robot is calculated as described in Section 5.7, while the average forward velocity for each trial was calculated as

$$\bar{v} = \frac{\sqrt{(p_{\mathrm{stop},x} - p_{\mathrm{start},x})^2 + (p_{\mathrm{stop},y} - p_{\mathrm{stop},y})^2}}{t_{\mathrm{stop}} - t_{\mathrm{start}}}, \tag{5.25}$$

where the positions $\mathbf{p}_{\mathrm{start}}$ and $\mathbf{p}_{\mathrm{stop}}$ define the travelled distance of the center of mass between the beginning and near the end of the travelled distance, as shown

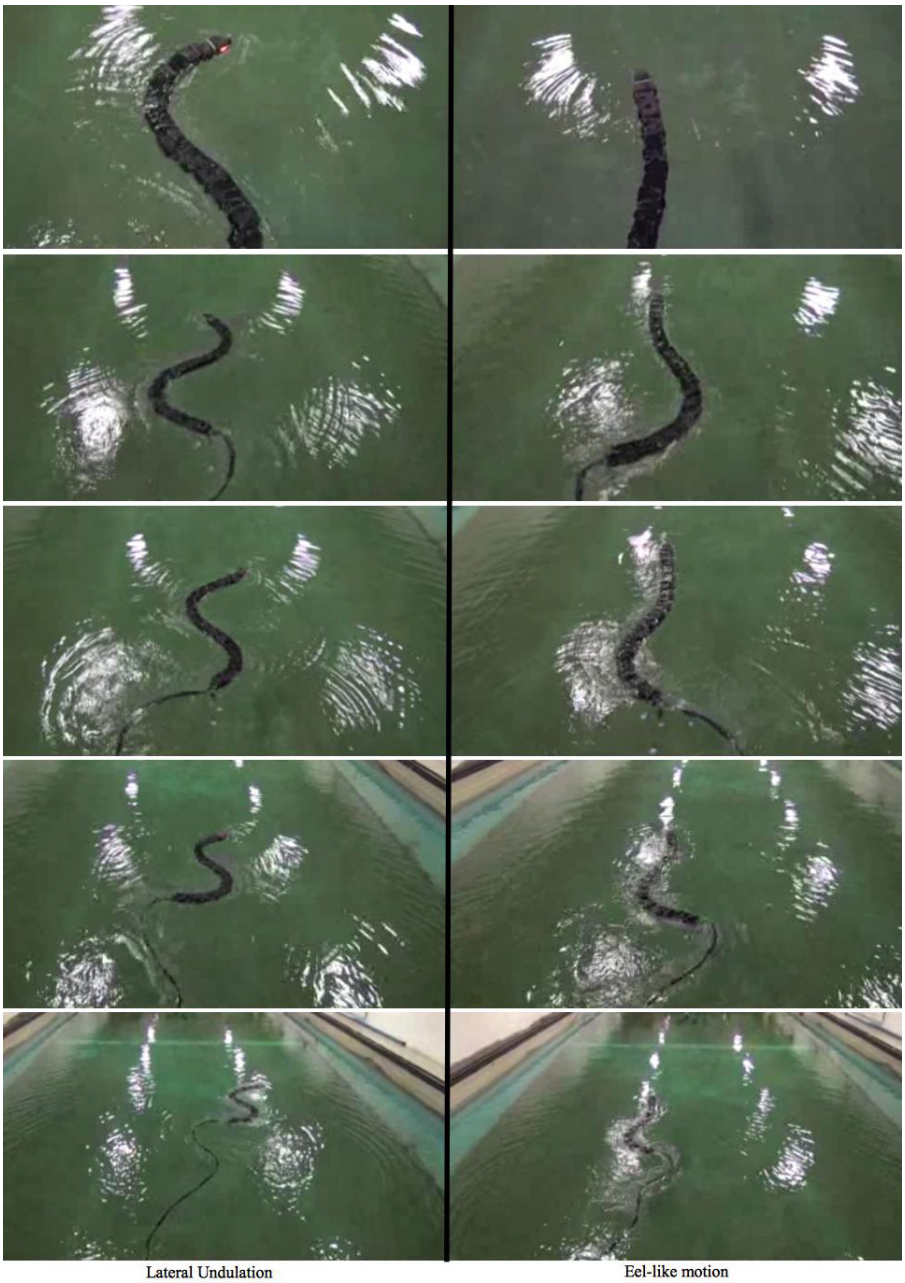

Figure 5.17: The motion of the underwater snake robot during lateral undulation and eel-like motion patterns.

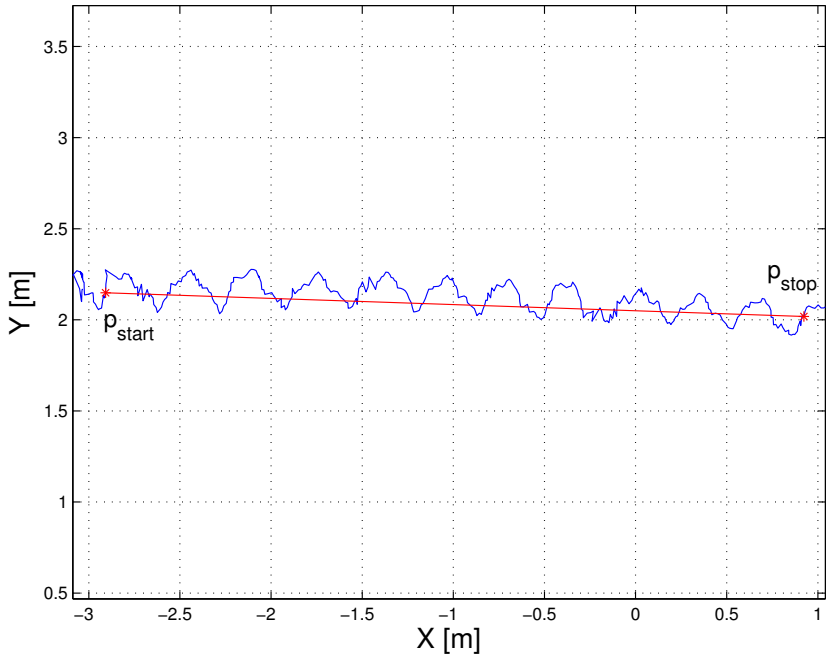

Figure 5.18: Measured position of the underwater snake robot during eel-like motion pattern. The distanced travelled by the robot is shown with red color.

in Fig. 5.18.

In order to investigate the first property stated in Proposition 5.3, that the average forward velocity is a function of the amplitude of the sinusoidal motion pattern, α, we ran experiments with the underwater snake robot Mamba for different values of the gait parameter α and calculate the average forward velocity according to (5.25) both for lateral undulation and eel-like motion patterns. The values of the gait parameters ω and δ are shown in each simulation result for the different motion patterns. From Fig. (5.19(a),5.20(a)) and Fig. (5.19(b),5.20(b)), we can see that the average forward velocity is increased by increasing the parameter α for constant values of ω and δ both for lateral undulation and eel-like motion, until a certain value of the parameter α. After this value, obtained results both for the simulated robot and the physical one show that an additional increase of the amplitude α causes a decrease of the forward velocity. This is also in accordance with the properties in Proposition 5.3.

Furthermore, Proposition 5.3 states that the average forward velocity depends on a linear and a nonlinear term of the gait frequency, ω. To validate the influence of this parameter, experimental trials were performed for different values of the gait parameter ω. The values of the gait parameters α and δ are shown in each simulation result for the different motion patterns. From Fig. (5.19(c),5.19(d)) and

Fig. (5.20(c),5.20(d)), we can clearly see that the increase of the forward velocity is almost linear for lateral undulation and eel-like motion patterns until the value of $\omega = 90^o/\text{s}$. Hence, in this case the influence of the nonlinear term on the forward velocity is almost negligible, similarly to the simulation results presented in previous section. This is also in accordance with the properties in Proposition 5.3. However, we see that the results obtained for the simulated robot and the physical one differs for values of $\omega > 90^o/\text{s}$. This means that the nonlinear term of the frequency is not negligible in results obtained from the experiments. This agrees with the results presented in Fig. (5.10(b),5.11(b)) for the complex model, where we also saw that the nonlinear term of ω has influence on the forward velocity. A probable reason for why there is a discrepancy between the simulation and experimental results may be that the fluid parameters of the simulated model are set to the theoretical values and have not been identified experimentally for the specific physical underwater snake robot. However, it is interesting that this difference in the results appear at high frequencies, which means that in the future further investigation of the hydrodynamic effects should be analysed.

With regard to the influence of the parameter δ, Proposition 5.3 states that the forward velocity depends on the phase shift between the joints, δ. To investigate the influence of the phase shift on the achieved forward velocity, experimental results are presented for different values of δ, keeping the gait parameters α and ω constant. The values of the gait parameters α and ω are shown in each result for the different motion patterns. From Fig. (5.19(e),5.19(f)) and Fig. (5.20(e),5.20(f)), it is clear that there exists a value of the gait parameter δ which gives the highest forward velocity, when the gait parameters α and ω are kept constant, which is in accordance with the simulation results presented in Section 5.6. This is also in accordance with the properties in Proposition 5.3. However, we see that the values of the parameter δ which result on achieving the maximum forward velocity differ for the simulated and the physical robot. This is mainly, because the fluid parameters are not experimentally validated for the specific robot, and thus we can obtain only a qualitative comparison of the results. Note that the qualitative comparison results sufficiently support the properties presented in Proposition 5.3.

Remark 5.9: *It is worth to mention that from the experimental validation of the properties proposed in Proposition 5.3 by using the physical robot Mamba, we can conclude that the control-oriented model, presented in Chapter 4, captures the essential properties of the underwater snake robot locomotion. Hence, this model constitutes a useful tool for control design and analysis for underwater snake robots.*

5.9 Chapter Summary

This chapter is summarized as follows:

- We have presented an averaged model of the velocity dynamics of an underwater snake robot influenced by added mass effects (reactive fluid forces) and linear drag forces (resistive fluid forces) during general sinusoidal motion gait patterns. The model is well-suited for stability analysis and motion planning purposes.

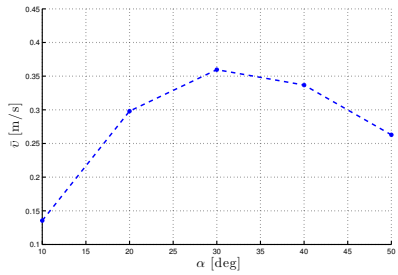

(a) Simulations: $\omega = 120^o$/s and $\delta = 30^o$

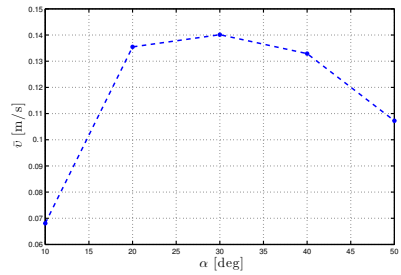

(b) Experiments: $\omega = 120^o$/s and $\delta = 30^o$

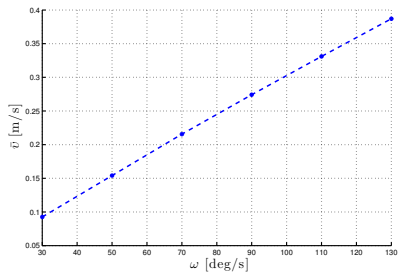

(c) Simulations: $\alpha = 30^o$ and $\delta = 30^o$

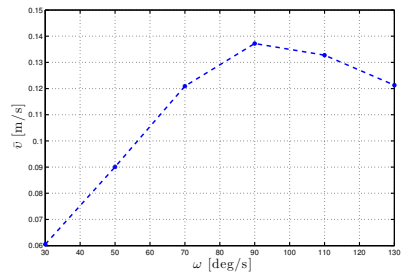

(d) Experiments: $\alpha = 30^o$ and $\delta = 30^o$

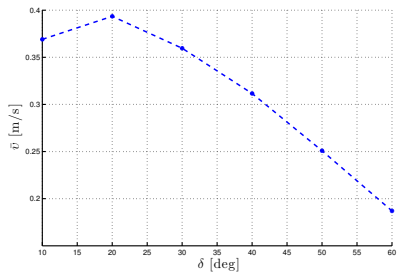

(e) Simulations: $\alpha = 30^o$ and $\omega = 120^o$/s

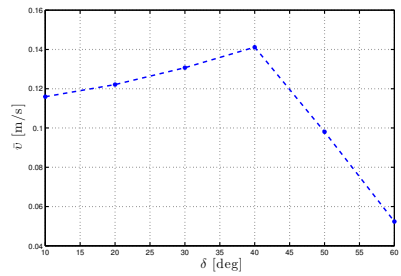

(f) Experiments: $\alpha = 30^o$ and $\omega = 120^o$/s

Figure 5.19: Lateral Undulation: The average forward velocity, $\bar{v}$ [m/s] for different gait parameters.

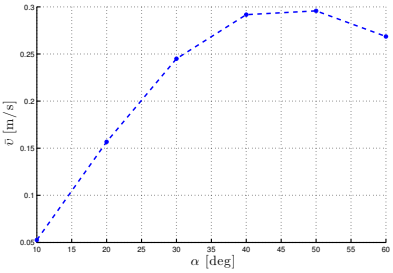

(a) Simulations: $\omega = 120^o/\text{s}$ and $\delta = 30^o$

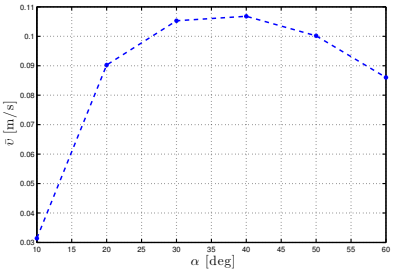

(b) Experiments: $\omega = 120^o/\text{s}$ and $\delta = 30^o$

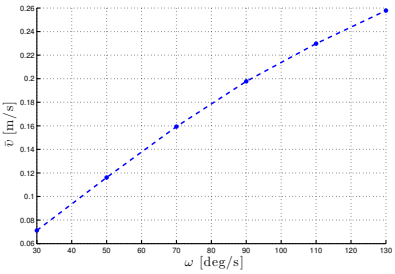

(c) Simulations: $\alpha = 30^o$ and $\delta = 30^o$

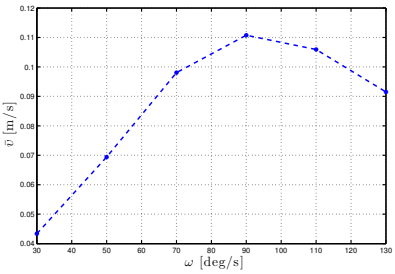

(d) Experiments: $\alpha = 30^o$ and $\delta = 30^o$

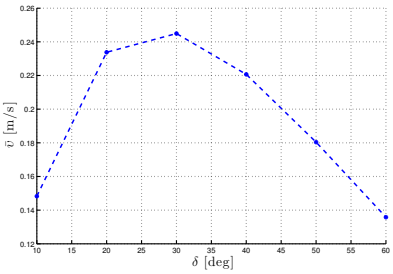

(e) Simulations: $\alpha = 30^o$ and $\omega = 120^o/\text{s}$

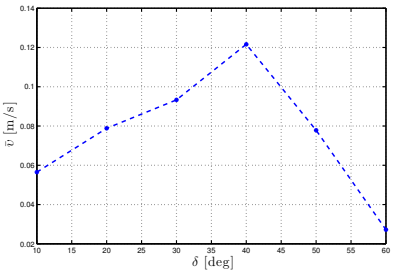

(f) Experiments: $\alpha = 30^o$ and $\omega = 120^o/\text{s}$

Figure 5.20: Eel-like motion: The average forward velocity, $\bar{v}$ [m/s] for different gait parameters.

- We have shown that the average velocity of an underwater snake robot following sinusoidal motion gait patterns converges exponentially to a steady-state velocity given analytically in (5.22) as a function of the gait parameters for the case of general sinusoidal gait patterns.
- We have derived a set of essential properties describing the relationship between the steady state velocity and the amplitude, the frequency, the phase shift and the offset of the joint motion for the case of general sinusoidal motion gait patterns given in (3.3). In particular, it was shown that the average forward velocity of an underwater snake robot, influenced both by added mass and linear drag effects, and under any sinusoidal gait pattern: 1) is a function of the amplitude of the sinusoidal motion pattern, 2) depends on a linear and a nonlinear terms of the gait frequency and 3) depends on the phase shift between the joints. The derived properties are general and provide a useful tool for achieving faster forward motion by selecting the most appropriate motion pattern and the optimal combination of the gait parameters.
- We have presented simulation results both for lateral undulation and eel-like motion in order to illustrate and validate the theoretical outcomes. We have presented simulation results that support the validity of the properties in Proposition 5.3 both for the complex model presented in Chapter 2 and the control-oriented model presented in Chapter 4.
- The derived properties in Proposition 5.3 of the velocity dynamics of an underwater snake robot have been investigated through experiments. We have shown that the experimental results using the physical underwater snake robot Mamba, support the derived properties of the velocity dynamics.

Chapter 6

Path Following Control of Underwater Snake Robots

Regarding control of underwater snake robots, several types of controllers have been proposed in the literature. However, the emphasis so far has mainly been on achieving forward and turning locomotion. The next step would be not only to achieve forward locomotion, but also to make the snake robot follow a desired path, i.e. solving the path following control problem, and this chapter proposes solutions towards this end.

As we have noted in Introduction, increasing efficiency by improving locomotion methods is a key issue for underwater robots, while a number of different control design challenges must be solved in order to realize operational swimming robots for underwater tasks. Generally, control design for underwater snake robots is challenging mainly because these mechanisms are underactuated and because the model of the hydrodynamic effects are highly nonlinear. Motion planning, i.e. designing a path covering a certain area or moving the robot towards a desired location-goal taking into account energy consumption is a challenging task for underwater snake robot locomotion. In this chapter, based on the complex model presented in Section 2.2, we propose and experimentally validate straight line path following controllers for biologically inspired swimming snake robots. In particular, we present a line-of-sight (LOS) and an integral line-of-sight (I-LOS) guidance law, which are combined with a sinusoidal gait pattern and a directional controller that steers the robot towards and along the desired path. Hence, in this chapter, we propose solutions to the path following control problem enabling the robot to follow a straight path both in the absence and the presence of ocean currents. Unlike the biologically inspired flow sensing strategy presented in [88], the integral LOS guidance law proposed in this chapter is inspired by path following control of marine surface vessels in the presence of ocean currents [14], [19]. Note that the I-LOS guidance strategy is widely used for directional control of marine surface vessels for ocean current compensation but has not been employed previously for directional control of underwater snake robots in the presence of ocean currents.

This chapter also investigates the stability analysis of the proposed I-LOS path following controller for an underwater snake robot. In particular, by using

a Poincaré map analysis, we prove that all state variables of an underwater snake robot, except the position along the forward direction, trace out an exponentially stable periodic orbit when the I-LOS path following controller is applied. This chapter also considers path following of more general paths. In particular, we propose a motion algorithm that combines the use of an artificial potential fields-based path planner with a new waypoint guidance strategy for steering an underwater snake robots along a path defined by waypoints interconnected by straight lines. Furthermore, the performance of the LOS and the I-LOS path following controllers are investigated through simulations and through experiments with the underwater snake robot Mamba. The presented experimental results confirm that the proposed integral LOS guidance law can be applied to underwater snake robots to achieve not only tracking of straight lines, but also to compensate for ocean drift effects, including current effects. In addition, experimental results presented in this chapter for the LOS path following controller show that the underwater snake robot is able to follow the reference path both for lateral undulation and eel-like motion. Combining the results of this chapter with the results that we will present in Chapter 7 regarding the power efficiency of the underwater snake robots, we can argue that underwater swimming robots can be considered as good candidates for different challenging tasks in the subsea environment.

Contributions of this Chapter: The first and main contribution of this chapter is the straight line path following control strategies for underwater snake robots. We have proposed two approaches for the path following problem of underwater snake robots. Initially, we present a LOS guidance law which is applied to underwater snake robots to achieve straight line path following both for lateral undulation and eel-like motion patterns. Secondly, we propose a controller that is able to compensate for the current effects in the absence of sensing the surrounding flow effects. In particular, based on the complex model presented in Section 2.2, we propose an integral line-of-sight path following controller for steering an underwater snake robot along a straight line path in the presence of ocean currents of unknown direction and magnitude. The integral LOS guidance strategy is widely used for directional control of marine surface vessels for ocean current compensation but has not been employed previously for directional control of underwater snake robots. The second contribution of this chapter is comparative studies between the experimental results and the corresponding simulation results for the path following control of underwater snake robots. In particular, the efficacy of the LOS and the I-LOS path following control strategies are investigated through experiments with the underwater snake robot Mamba. The experimental results show that the integral LOS guidance law can be applied to underwater snake robots to compensate for the ocean drift effects, including the current effects, and achieve path following of straight lines. As fas as we know, experimental results for path following control of underwater snake robots compensating for the current effects have not been investigated in previous literature.

To our best knowledge, Poincaré maps have never been used to study the stability of the locomotion of an underwater snake robot along a straight line path in the presence of ocean currents, thus it is considered as contribution

of this chapter. As far as we know, no formal stability analysis of an integral LOS path following controller for an underwater snake robot has been presented in previous literature. Another contribution of this chapter is the experimental validation of the complex fluid model presented in Section 2.2. In particular, a back-to-back comparison of real experimental and simulated data, gives us the opportunity to obtain qualitative and quantitative comparison between the motion of the simulated and the physical snake robot. The last contribution of this chapter is the combined use of an artificial potential fields-based path planner with a new waypoint guidance strategy for steering an underwater snake robots along a path defined by waypoints interconnected by straight lines. The waypoints are derived by using a path planner based on the artificial potential field method in order to also address the obstacle avoidance problems.

Organization of this Chapter: This chapter is organized as follows. Section 6.1 presents the line-of-sight (LOS) path following controller along straight lines for underwater snake robots. The integral line-of-sight (I-LOS) path following controller along straight lines is presented in Section 6.2, followed by the stability analysis based on the Poincaré map approach in Section 6.3. Experimental and simulation results for LOS and I-LOS path following control strategies are presented in Section 6.4 and Section 6.5, respectively. The waypoint guidance strategy for an obstacle avoidance scenario for underwater snake robots is proposed in Section 6.6. Finally, the chapter is summarized in Section 6.7.

Publications: The material in this chapter is based on the journal papers [73], [64] and the conference papers [70] and [66]. In addition, the results presented in this chapter resulted in a patent application with the title "Guidance of Underwater Snake Robots" in [63].

6.1 Line-of-Sight (LOS) Path Following Controller

In this section, we present a LOS path following control scheme for underwater snake robots based on the general sinusoidal motion pattern (3.3). The structure of the LOS path following controller, as shown in Fig. 6.1, consists of two parts, the inner-loop PD controller that is used to control the joint angles $\boldsymbol{\phi}$ and the outer-loop controller that is used for generating the reference joint angles, in order to achieve the desired sinusoidal gait pattern and the desired heading $\bar{\theta}_{\text{ref}}$. The latter controller is composed of three separate components, the gait pattern controller which extracts the sinusoidal motion pattern to propel the robot forward, the heading controller, which steers the robot towards and subsequently along the desired path and the LOS guidance law (Fig. 6.2), which generates the desired heading angle, in order to follow the desired path. These three components of the path following controller will be presented in the following subsections.

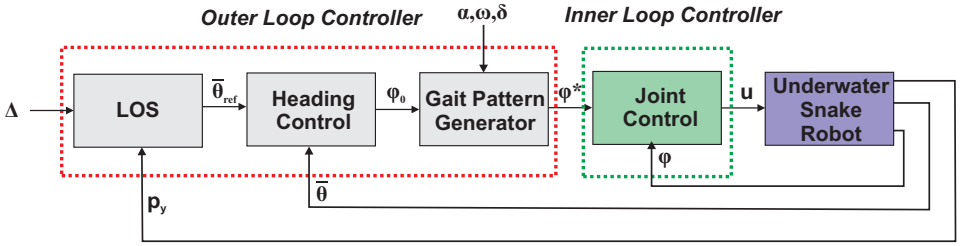

Figure 6.1: The structure of the LOS path following controller.

6.1.1 Control Objectives

The main control objective is the convergence of the robot motion to the desired straight line path. The forward velocity $\bar{v}_t > 0$ of the underwater snake robot, defined in (2.5), does not require accurate control, but only $\bar{v}_t > 0$ to ensure a nonzero forward velocity for the robot. Regarding the position of the robot in the 2D plane, the desired path is aligned with the global x axis, thus the cross track error along the desired path coincides with the robot's position over the global y axis. Furthermore, the heading of the robot (2.2) corresponds to the angle formed between the robot's body and the desired straight line path (Fig. 6.2). Considering these objectives, the control system can be formalized as

$$\lim_{t\to\infty} p_y = 0 \tag{6.1}$$

$$\lim_{t\to\infty} \bar{\theta} = 0 \tag{6.2}$$

$$\lim_{t\to\infty} \bar{v}_t > 0 \tag{6.3}$$

Note that, since underwater snake robots have an oscillatory gait pattern, the control objectives imply that p_y and $\bar{\theta}$ should have steady state oscillations about zero.

6.1.2 The Straight Line Path Following Controller

As noted above, the outer-loop controller generates the reference joint angles, in order to achieve the desired sinusoidal gait pattern and the desired orientation for the robot. Regarding the sinusoidal gait pattern, previous approaches keep the parameters α and δ fixed, while ω, ϕ_0 are used to control the speed and the direction of the snake robot, respectively, [49, 62, 101]. In this thesis, the same approach will be adopted. The orientation $\bar{\theta}$ of the robot is given by (2.2). Moreover, for the desired orientation, motivated by [14], [38], we propose to define the reference orientation using the following LOS guidance law

$$\bar{\theta}_{\text{ref}} = -\arctan\left(\frac{p_y}{\Delta}\right), \qquad \Delta > 0 \tag{6.4}$$

where p_y is the cross-track error (i.e., the position of the underwater snake robot along the global y axis), while Δ is a constant design parameter. In particular,

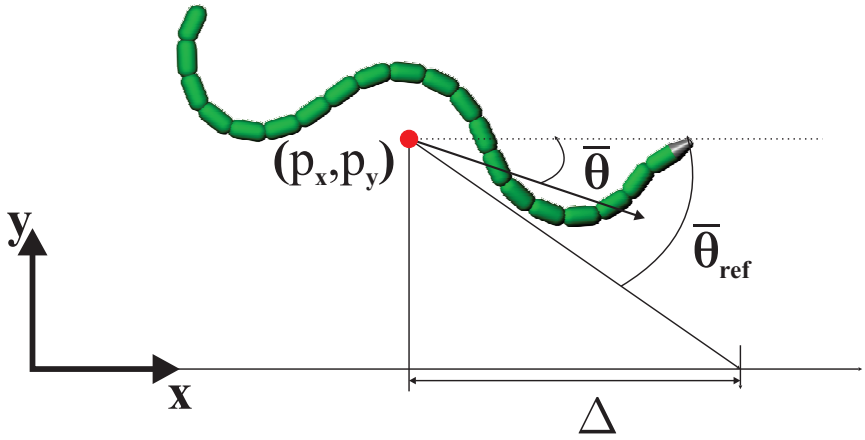

Figure 6.2: Illustration of the LOS guidance law.

Δ denotes the *look-ahead distance* that influences the rate of convergence to the desired path [38]. Note that LOS guidance law is much used in practice for path following control of marine surface vessels [38], [39] and is used for path following control of ground snake robots [101].

Remark 6.1: *The look-ahead distance Δ is an important design parameter that directly influences the transient motion of the underwater snake robot. Choosing Δ large should result in a well-damped transient motion, but the rate of convergence to the path will be slow. On the other hand, choosing Δ too small should result in poor performance or even instability. A rule of thumb is to choose Δ larger than twice the length of the robot (see e.g. [38]).*

Motivated by the effective application of LOS guidance law for path following control of marine surface vessels [38], [39] and especially in the corresponding case of ground snake robots [101], we choose the joint angle offset ϕ_0 as

$$\phi_0 = k_\theta \left(\bar{\theta} - \bar{\theta}_{\text{ref}} \right), \tag{6.5}$$

where $k_\theta > 0$ is a control gain. Furthermore, as we can see from Fig. 6.1, the inner-loop controller is responsible for the joint control. In this section, we will use the PD controller (3.5) to make the joint angle, ϕ_i, follow its reference signal, ϕ_i^*. We have now presented the complete LOS path following controller of the underwater snake robot. The efficacy of the proposed path following controller will be investigated via both simulation and experimental studies in Section 6.4.

6.2 Integral Line-of-Sight (I-LOS) Path Following Controller

In this section, we propose an I-LOS path following control scheme for underwater snake robots. The controller consists of three main components as shown in Fig. 6.3,

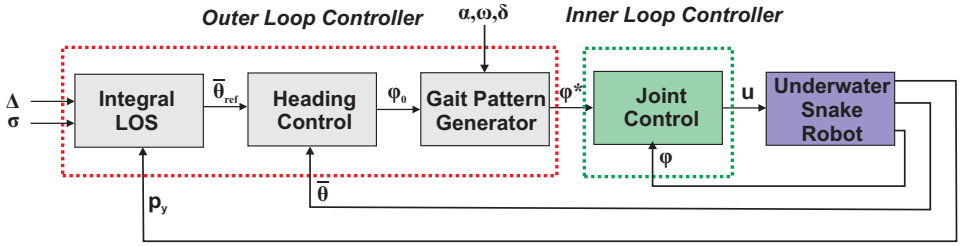

Figure 6.3: The structure of the I-LOS path following controller.

similarly to the control scheme presented in Section 6.1. The first two components are explained in the previous subsection, while the third component is the integral LOS guidance law (Fig. 6.4), which generates the desired heading angle in order to follow the desired path. An inner loop PD controller is used to control the joint angles $\boldsymbol{\phi}$ as defined in (3.5), while an outer loop controller is used for generating the reference joint angles in order to achieve the desired sinusoidal gait pattern and also the desired heading $\bar{\theta}_{\text{ref}}$ (Fig. 6.3). The three components of the path following controller will be presented in the following subsections.

6.2.1 Control Objectives

The path following control objective is to make the robot converge to the desired straight line path and subsequently progress along the path at some nonzero forward velocity $\bar{v}_t > 0$, where $\bar{v}_t$ is defined in (2.5). We consider it as less important to accurately control the forward velocity of the robot. The global x axis is aligned with the desired path, and thus the position of the robot along the global y axis corresponds to the cross track error, and the heading of the robot (2.2) is the angle that the robot forms with the desired path (Fig. 6.5). The objectives of the control system can be formalized as

$$\lim_{t\to\infty} p_y = 0 \tag{6.6}$$

$$\lim_{t\to\infty} \bar{\theta} = \bar{\theta}_{ss} \tag{6.7}$$

$$\lim_{t\to\infty} \bar{v}_t > 0 \tag{6.8}$$

where $\bar{\theta}_{ss}$ is a constant value which will be non-zero when the underwater snake robot is subjected to ocean currents that have a component in the transverse direction of the path. Note that, since underwater snake robots have an oscillatory gait pattern, the control objectives imply that p_y and $\bar{\theta}$ should have steady state oscillations about zero and $\bar{\theta}_{ss}$, respectively.

Remark 6.2: *The heading of the robot is not required to oscillate around zero but rather to oscillate around a steady-state constant value (6.7) in the presence of ocean currents in the transverse direction of the path. This is similar to the results shown in [19] for autonomous surface vessels. In particular, the underwater snake robot then needs to keep a nonzero heading angle in steady state in order to compensate for the*

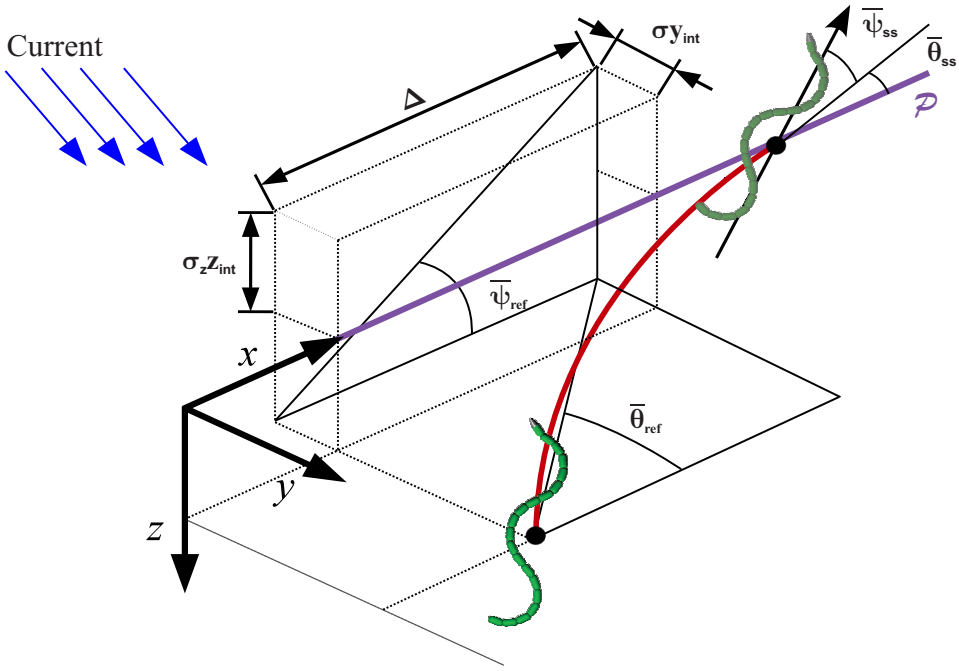

Figure 6.4: Illustration of the integral LOS guidance law for motion in 3D.

current effect. A non-zero angle will allow the underwater snake robot to side-slip in order to compensate for the current effects and thus stay on the desired path, as shown in Fig. 6.6.

We consider the following assumption for the current values in this thesis:

Assumption 6.1: The current has unknown direction and magnitude. It should be bounded by a constant $V_{max} > 0$, i.e. $V_{max} > \sqrt{V_{x,i}^2 + V_{y,i}^2}$, where $[V_{x,i}, V_{y,i}]^T$ is the current velocity expressed in inertial frame coordinates.

Remark 6.3: *The value of V_{max} that the robot is able to compensate is directly connected to the physical limitations of the robot, the actuator forces and the number of the links.*

6.2.2 The Straight Line Path Following Controller

As we have already mentioned, typically, the parameters α and δ are fixed and the parameters ω, ϕ_0 are used to control the speed and the direction of the snake robot [49, 62, 101]. In this section, the same idea will be used in order to steer the underwater snake robot to a desired orientation. The outer-loop controller will be responsible for generating the reference joint angles in order to ensure that the desired orientation is achieved. The orientation $\bar{\theta}$ of the robot is given by (2.2).

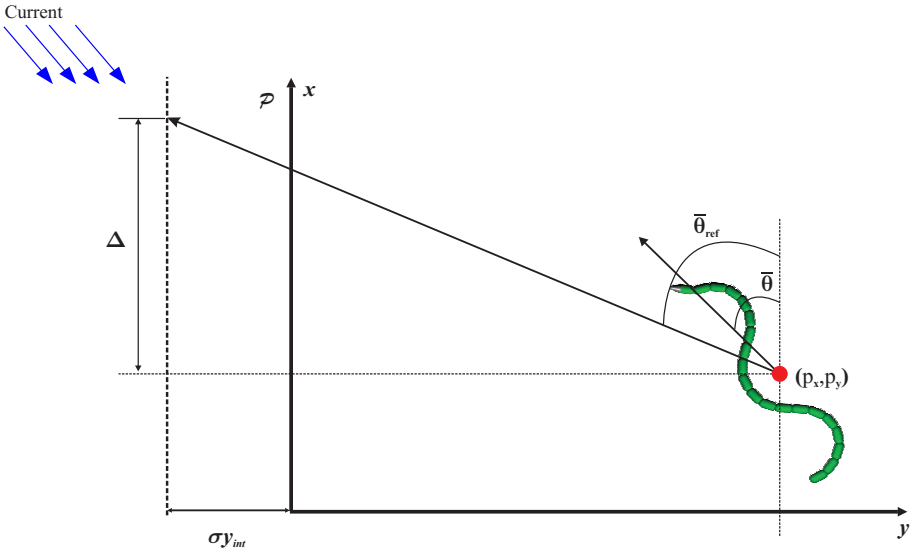

Figure 6.5: Illustration of the integral LOS guidance law for straight line path.

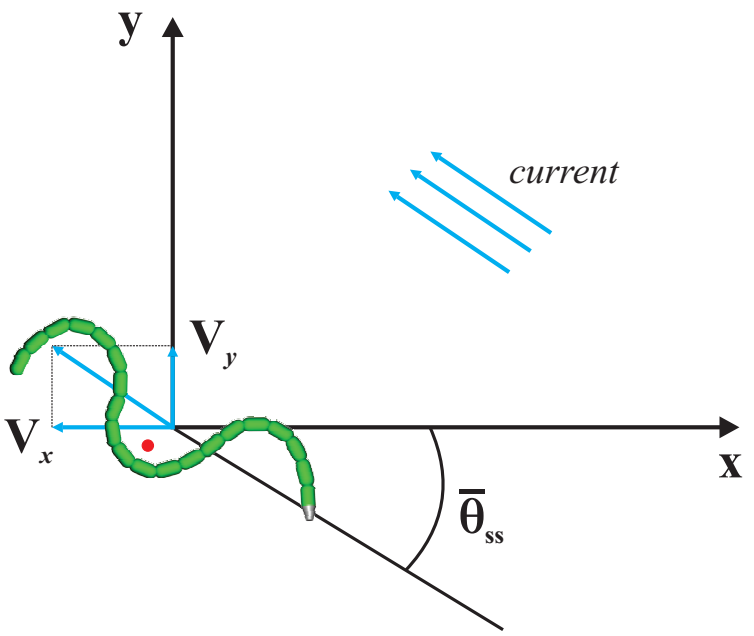

Figure 6.6: Steady state: The underwater snake robot side-slips with a constant $\bar{\theta}_{ss}$ to follow the path.

Moreover, motivated by [14], [19] we propose to define the reference orientation using the following integral LOS guidance law

$$\bar{\theta}_{\text{ref}} = -\arctan\left(\frac{p_y + \sigma y_{int}}{\Delta}\right), \qquad \Delta > 0 \tag{6.9}$$

$$\dot{y}_{int} = \frac{\Delta p_y}{(p_y + \sigma y_{int})^2 + \Delta^2} \tag{6.10}$$

where p_y is the cross-track error (i.e., the position of the underwater snake robot along the global y axis), while Δ and $\sigma > 0$ are both constant design parameters and y_{int} represents the integral action of the guidance law. In particular, Δ denotes the *look-ahead distance* that influences the rate of convergence to the desired path [38] and $\sigma > 0$ is the integral gain. The proposed I-LOS path following controller was recently proposed for path following control of marine surface vessels in presence of unknown constant irrotational ocean current [14], [19]. In particular, the I-LOS path following controller compensates for two environmental disturbances: the drifting effect of the currents, representing a pure kinematic drift, and the heading dependent disturbances caused by currents, winds and waves. This motivated us to believe that the integral LOS guidance law could be well-suited for path following of underwater snake robots in different sea conditions. In particular, the conjecture is that this choice of orientation reference will make the snake robot converge to the path, i.e. make p_y converge to zero, cf. Fig. 6.5. Furthermore, we choose the joint angle offset according to (6.5), similarly to the approach presented in Section 6.1, in order to steer the heading $\bar{\theta}$ according to the integral LOS angle in (6.4). Finally, the PD controller (3.5) will be used for the join control. We have now presented the complete I-LOS path following controller of the underwater snake robot. The efficacy of the I-LOS path following controller approach will be investigated via both simulation and experimental results in Section 6.5.

Remark 6.4: *The integral effect becomes significant when the ocean current effect pushes the underwater snake robot away from its path. Note that (6.10) is designed such that the integral action has less influence when the robot is far from the path, reducing the risk of wind-up effects [19]. In fact, (6.9,6.10) behaves as a traditional LOS law when the underwater snake robot is far away from the path while the integral action takes over when the motion is closer to the desired path.*

6.3 Stability Analysis of the I-LOS Path Following Controller

In this section, the theory of Poincaré maps is employed to prove that the I-LOS path following controller presented in Section 6.2 generates a locally exponentially stable periodic orbit in the state space of the underwater snake robot. This periodic orbit implies that the robot locomotes along the desired straight path in the presence of current.

6.3.1 The Poincaré Map

The Poincaré map is a useful tool for studying the stability of periodic solutions in nonlinear dynamical systems [80]. In particular, the stability of a periodic orbit of a dynamical system is related to the stability of the fixed point of the corresponding Poincaré map of the system. We will thus use a Poincaré map approach as a stability analysis tool for the closed-loop system of the underwater snake robot with the path following controller presented in Section 6.2. In particular, the exponential stability of the system will be investigated by checking if the fixed point is an exponentially stable equilibrium point of the discrete system. The fixed point $\bar{\mathbf{x}}^*$ is locally exponentially stable if the magnitudes of all the eigenvalues of the Jacobian linearization of the Poincaré map $\mathbf{J}_P(\bar{\mathbf{x}}^*)$ about the fixed point are strictly less than one [101].

In order to investigate the stability properties using Poincaré maps, the model of the underwater snake robot should be represented as an autonomous system. Following the approach described in [116], the model (2.44) with the path following controller presented in Section 6.2 can be rewritten as the following autonomous system

$$\begin{aligned} \dot{\mathbf{x}} &= \mathbf{F}\left(\mathbf{x}, \frac{T}{2\pi}\beta\right), \qquad \mathbf{x}(t_0) = \mathbf{x}_0 \\ \dot{\beta} &= \frac{2\pi}{T}, \qquad \beta(t_0) = \frac{2\pi t_0}{T} \end{aligned} \tag{6.11}$$

where $\beta = 2\pi t/T$ is a new state variable and $T = 2\pi/\omega$ is the period of the cyclic locomotion generated by the sinusoidal gait pattern in (3.1). The state variable β is periodic since we force β to be $0 \leq \beta < 2\pi$, i.e. we set β to zero each time $\beta = 2\pi$.

What now remains is to specify the Poincaré section for the underwater snake robot. We choose the global x axis as the Poincaré section S of the system in (6.11) (see e.g. [101]). Furthermore, we exclude p_x from the Poincaré map since the forward position of the robot will not undergo limit cycle behaviour like the other states of the system. As a result, the Poincaré section is given by $S = \{(\boldsymbol{\theta}, p_y, \dot{\boldsymbol{\theta}}, \beta) | p_y = 0\}$, which means that the vector of the independent time-periodic states constrained to S can be expressed as $\bar{\mathbf{x}} = \left[\boldsymbol{\theta}^T, \dot{\boldsymbol{\theta}}^T, \dot{\mathbf{p}}_{\text{CM}}^T, \beta\right]^T \in \mathbb{R}^{2n+3}$.

Remark 6.5: *Note that since p_x is not present on the right hand side in any of the dynamic equations in (2.44), we can exclude p_x from the Poincaré map without affecting the other state variables of the system (2.44).*

Remark 6.6: *In this thesis, we consider a one-sided Poincaré map by assuming that the Poincaré section is crossed when the CM position of the underwater snake robot crosses the x axis from above, similar to the approach presented in [99, 101] for ground snake robots.*

6.3.2 Stability Analysis of the Poincaré map

In order to investigate the stability of the robot with the I-LOS path following controller presented in Section 6.2, we consider an underwater snake robot with $n = 3$ links, each one having length $2l = 0.14$ m and mass $m = 0.6597$ kg. The

hydrodynamic parameters are set to $c_t = 0.2639$, $c_n = 8.4$, $\mu_n = 0.3958$, $\lambda_1 = 2.298810^{-7}$, $\lambda_2 = 4.310310^{-4}$ and $\lambda_3 = 2.262910^{-5}$ (see Section 2.2 for details). The values of a constant ocean current in the inertial frame are $[0.005, 0.01]$ m/sec. The joint PD controller (3.5) is used for each joint with parameters $k_p = 20$, $k_d = 5$, and lateral undulation and eel-like motion are achieved by choosing $\mathrm{g}(i,n) = 1$ and $\mathrm{g}(i,n) = (n-i)/(n+1)$, respectively, with gait parameters $\alpha = 70^{\mathrm{o}}$, $\delta = 70^{\mathrm{o}}$ and $\omega = 120^{\mathrm{o}}$/s in (3.3). Initially, we run simulations with the proposed control strategy until the robot reaches the desired path, and then we choose the initial values of y_{int} as 5.33 and 6.54 for lateral undulation and eel-like motion, respectively. These initial values are used for the stability analysis of the system by using Poincaré map. Furthermore, the control gain in (6.5) is $k_\theta = 0.8$, while the guidance law parameters in (6.9-6.10) are chosen as $\Delta = 2ln$ [38], and $\sigma = 0.01$ [19].

The Poincaré map of the underwater snake robot model in (2.33,2.38) is found using *Matlab R2013b*. The dynamics is calculated using the *ode23tb* solver with a relative and absolute error tolerance of 10^{-4}. Using the Newton-Raphson algorithm, the fixed point, $\bar{\mathbf{x}}^* \in \mathbb{R}^9$, of the Poincaré map for lateral undulation and eel-like motion are given by (6.12) and (6.13), respectively.

$$\begin{aligned}\bar{\mathbf{x}}^* =&[-35.06^{\mathrm{o}},\ -41.79^{\mathrm{o}},\ 17.68^{\mathrm{o}},\ -108.83^{\mathrm{o}}/\mathrm{s},\ 26.49^{\mathrm{o}}/\mathrm{s},\\ &106.96^{\mathrm{o}}/\mathrm{s},\ 10.59\mathrm{cm/s},\ -3.86\mathrm{cm/s},\ 194.04^{\mathrm{o}}]^T\end{aligned} \tag{6.12}$$

$$\begin{aligned}\bar{\mathbf{x}}^* =&[-15.77^{\mathrm{o}},\ -29.99^{\mathrm{o}},\ -2.21^{\mathrm{o}},\ -116.75^{\mathrm{o}}/\mathrm{s},\\ &20.62^{\mathrm{o}}/\mathrm{s},\ 70.89^{\mathrm{o}}/\mathrm{s},\ 9.10\mathrm{cm/s},\ -1.57\mathrm{cm/s},\ 191.88^{\mathrm{o}}]^T\end{aligned} \tag{6.13}$$

The locomotion of the robot over one period is shown in Fig. 6.7 and Fig. 6.8 for lateral undulation and eel-like motion, respectively. The initial values of the states of the robot are given by (6.12) and (6.13), and the initial position is chosen as $\mathbf{p}_{\mathrm{CM}} = 0$. From Fig. 6.7-6.8, we can see that after one period of the motion the state variables have returned to their initial values given by (6.12) and (6.13). In addition, after one period of motion the position of the robot along the x axis has increased. Furthermore, Fig. 6.9(a) and Fig. 6.10(a) illustrate the limit cycle that is traced out by the three link angles of the robot for lateral undulation and eel-like motion. The Jacobian linearization of the Poincaré map about the fixed points (6.12) and (6.13) is calculated, and the magnitudes of the eigenvalues of $\mathbf{J}_P(\bar{\mathbf{x}}^*) \in \mathbb{R}^{9\times 9}$ are found to be given by (6.14) and (6.15) for lateral undulation and eel-like motion, respectively:

$$\begin{aligned}|\ \mathrm{eig}(\mathbf{J}_P(\bar{\mathbf{x}}^*))\ | =&[0.394,\ 0.394,\ 0.041,\ 0.008,\ 0.002,\\ &0.002,\ 2.82\times 10^{-4},\ 2.82\times 10^{-4},\ 4.84\times 10^{-5}]^T\end{aligned} \tag{6.14}$$

$$\begin{aligned}|\ \mathrm{eig}(\mathbf{J}_P(\bar{\mathbf{x}}^*))\ | =&[0.548,\ 0.548,\ 0.059,\ 0.059,\ 0.011,\\ &1.49\times 10^{-3},\ 2.92\times 10^{-4},\ 1.02\times 10^{-4},\ 9.25\times 10^{-5}]^T\end{aligned} \tag{6.15}$$

From (6.14) and (6.15), it is easily seen that all the eigenvalues, both for lateral undulation and eel-like motion cases, are strictly less than one. Therefore we can conclude that the periodic orbit is locally exponentially stable for the given choice of controller parameters both for lateral undulation and eel-like motion. Since the

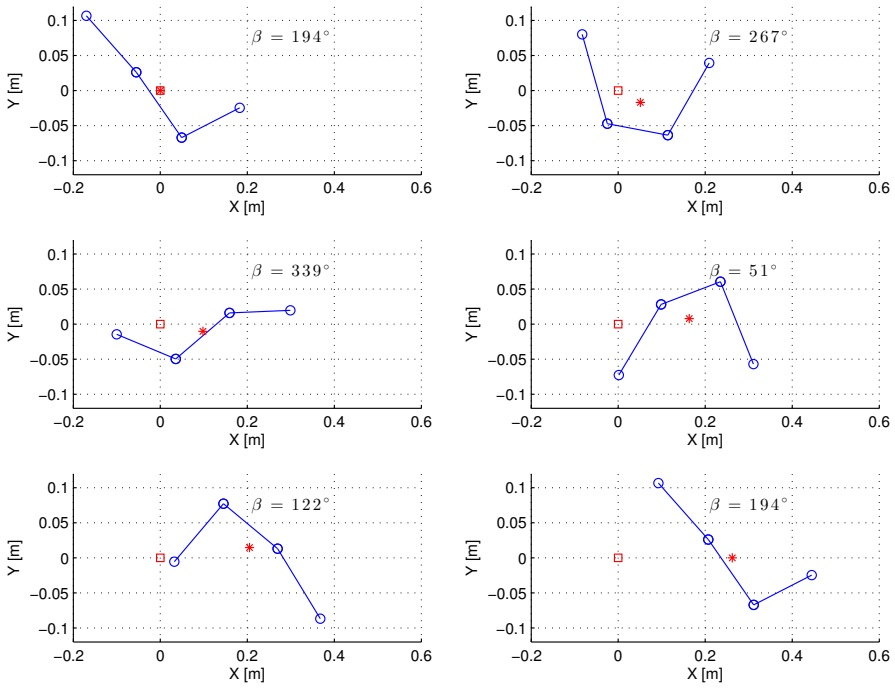

Figure 6.7: Motion of the underwater snake with $n = 3$ links for lateral undulation.

periodic orbit is exponentially stable and the system returns to $p_y = 0$ with time period T, we can conclude that the control objective (6.6) is achieved. Furthermore, in Section 3.3 it is shown that, for an underwater snake robot under anisotropic drag effects, propulsive forces are positive as long as $\text{sgn}(\theta_i) = \text{sgn}(\dot{y}_i)$ and $\text{sgn}(\theta_i) = \text{sgn}(\ddot{y}_i)$. Fig. (6.9(b),6.9(c)) and Fig. (6.10(b),6.10(c)) show that these conditions are valid over the majority of the period both for lateral undulation and eel-like motion. Hence, the robot moves forward and the control objective (6.8) is satisfied. Since the control objectives (6.6) and (6.8) are both satisfied, we can argue that the control objective (6.7) must be satisfied. Note that if the heading did not oscillate around $\bar{\theta}_{ss}$, but rather around zero, then the robot would not be able to compensate the ocean current effects and the robot would drift away from the desired path, which contradicts the fulfilment of control objective (6.6).

Remark 6.7: *A more formal stability analysis of the system in (2.33,2.38) with the proposed controller remains a challenging task, mainly due to the complexity of the dynamic system equations. Thus a numerical approach is adopted in this thesis. Note that by using the Poincaré map approach, we have only proven that the stability of the path following controller presented in Section 6.2 holds for the numerical parameters of the system presented in the beginning of this subsection. However, simulations and*

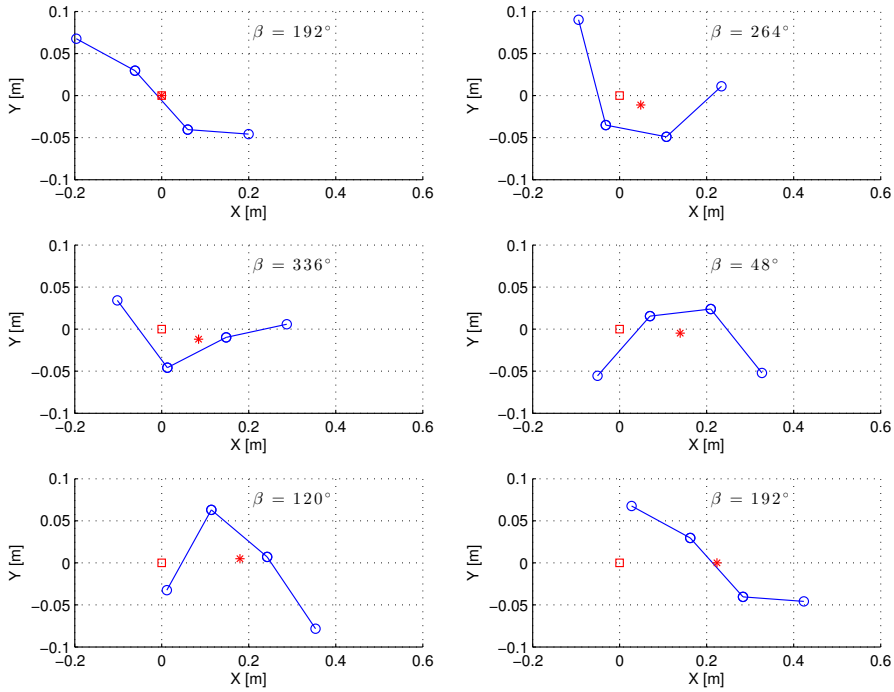

Figure 6.8: Motion of the underwater snake with $n = 3$ links for eel-like motion.

experimental results presented in Section 6.5 indicate that the proposed path following controller can be applied to steer the robot to the desired path in the presence of ocean currents for other parameters of the system and for a wide range of the current values.

6.3.3 Simulation Study: The Performance of the I-LOS Path Following Controller

This section presents simulation results in order to investigate the performance of the integral LOS path following controller described in Section 6.2. The model and controller parameters are the same as in Section 6.3. The initial values of all states of the robot are set to zero except for the initial position of the center of mass, which is selected as $\mathbf{p}_{\mathrm{CM}}(0) = [0, 0.5]$. In Fig. 6.11(a) and Fig. 6.12(a), we can see that (6.5) makes the heading angle converge to and oscillate about the desired heading angle given by (6.4) for lateral undulation and eel-like motion, respectively. Note that the heading of the robot does not converge to oscillations about zero but rather converges to a steady state constant value, $\bar{\theta}_{ss}$, which means that the control objective (6.7) is achieved. Moreover, Fig. 6.11(b) and Fig. 6.12(b) show that control objective (6.6) is verified, i.e. the integral LOS guidance law (6.9)

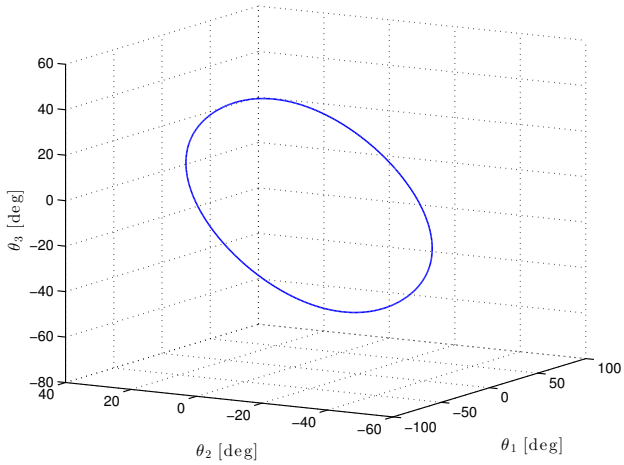

(a) The limit cycle

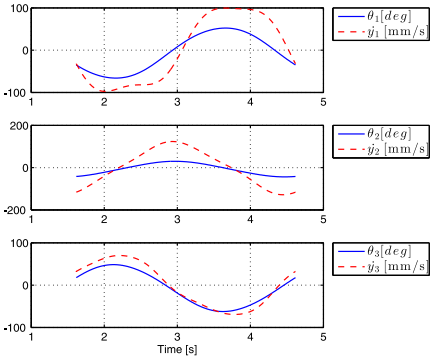

(b) Plot of θ_i and $\dot{y}_i$

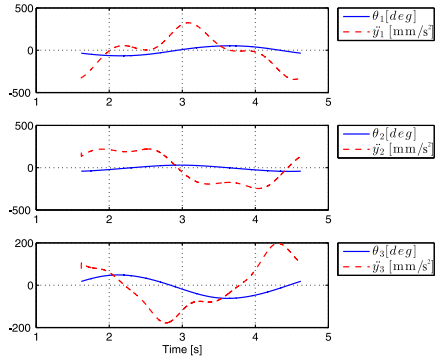

(c) Plot of θ_i and $\ddot{y}_i$

Figure 6.9: Stability analysis of the Poincaré map for lateral undulation.

will make the cross track error converge to zero. Finally, from Fig. 6.11(c) and Fig. 6.12(c) we can see that the CM of the underwater snake robot converges to the desired path both for lateral undulation and eel-like motion. Fig. 6.11-6.12 clearly show that the heading, the cross track error and the position of the robot have a steady state oscillatory behavior when the robot reaches the desired path.

6.4 Experimental Investigation of LOS Path Following Controller

This section describes the experimental setup employed for the fluid parameter identification and the investigation of the performance of the LOS path following controller presented in Section 6.1. In particular, simulation and experimental re-

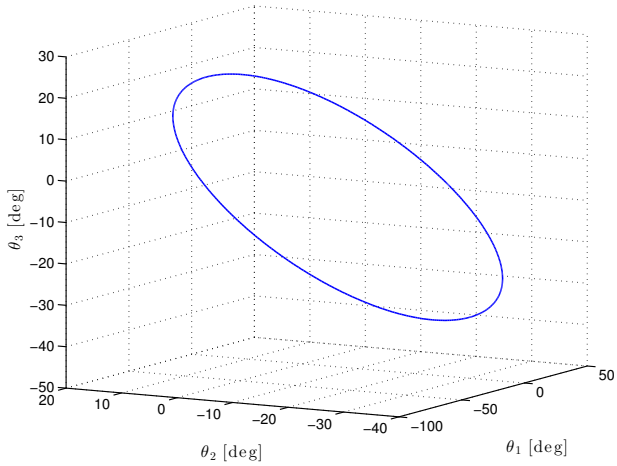

(a) The limit cycle

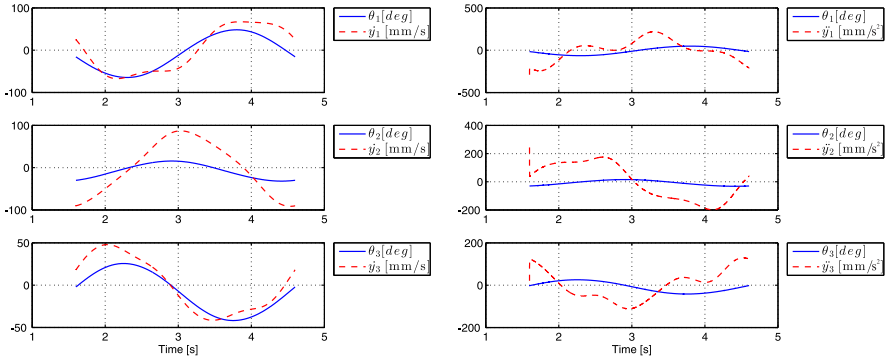

(b) Plot of θ_i and $\dot{y}_i$

(c) Plot of θ_i and $\ddot{y}_i$

Figure 6.10: Stability analysis of the Poincaré map for eel-like motion.

sults will be presented in order to investigate the efficacy of the LOS path following controller presented in Section 6.1. The performance of the guidance strategy will be investigated experimentally for straight line paths both for lateral undulation and eel-like motion patterns.

6.4.1 Fluid Parameter Identification

In this subsection, we present results regarding the fluid parameters identification for the model of the underwater snake robot presented in Section 2.2. We obtained the values of the fluid coefficients by using the method of [120]. Note that the fluid parameters are identified in order to be used in this section for back-to-back comparison of the path following control strategy presented in Section 6.1. The

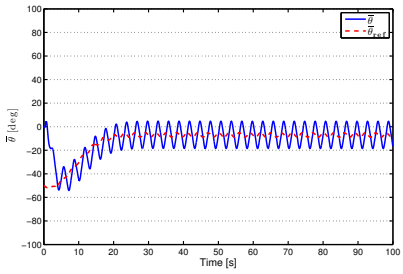

(a) Heading angle, $\bar{\theta}$

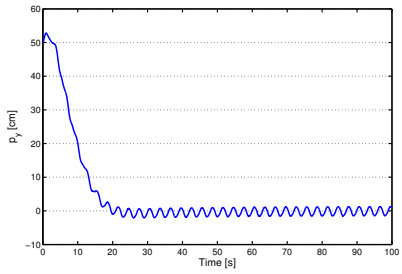

(b) Cross track error, p_y

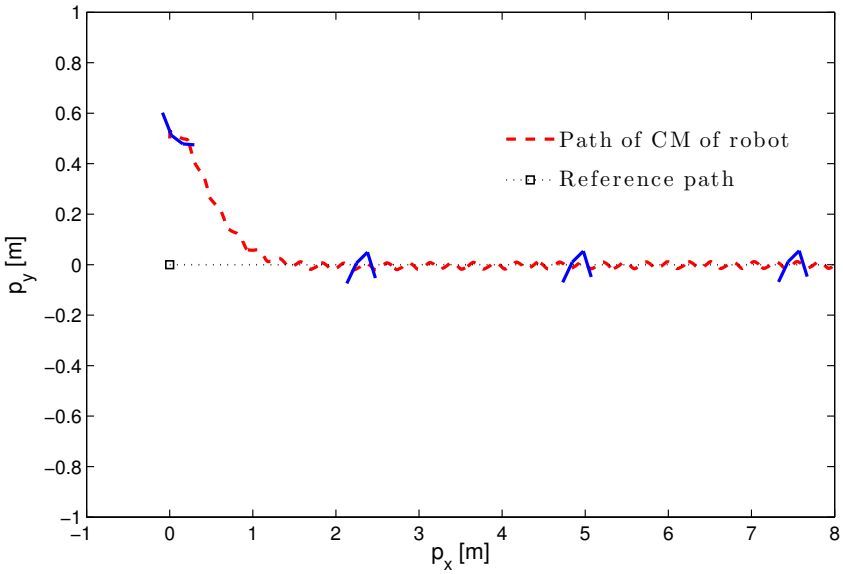

(c) Path of the robot

Figure 6.11: I-LOS path following controller for lateral undulation.

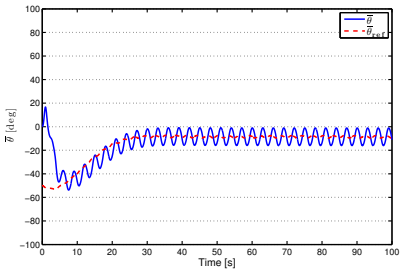

(a) Heading angle, $\bar{\theta}$

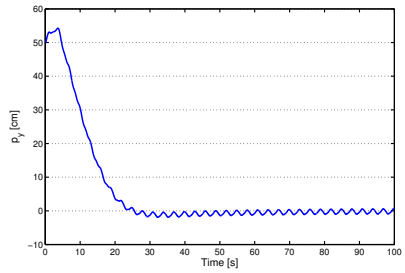

(b) Cross track error, p_y

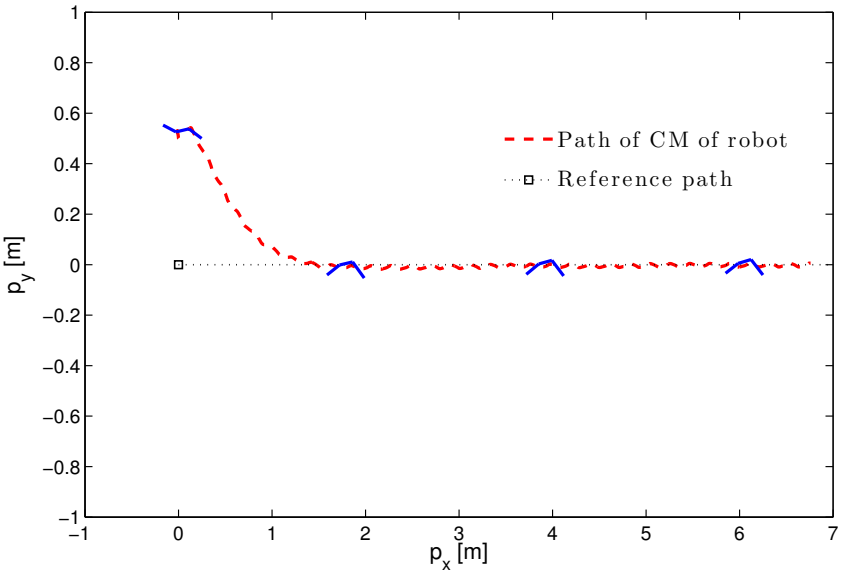

(c) Path of the robot

Figure 6.12: I-LOS path following controller for eel-like motion.

fluid coefficients that will be identified are C_f, C_D and C_A. Note that the added mass inertia coefficient is set to the theoretical value $C_M = 1$ in this study since this parameter does not affect significantly the overall motion of the system [69, 135].

The experimental setup is presented in detail in Section 5.7. In particular, using the underwater snake robot Mamba (Fig. 5.15) with the reflective markers attached on the tail of the robot, we were able to measure the position and the orientation of the tail module by using the camera system described in Section 5.7. Combining these measurements with the measurements of the joint angles and using the kinematic equations presented in Section 2.2, we are able to calculate the position of the center of mass of the robot. We applied sinusoidal motion pattern with different parameters of the gait pattern. In particular, in each trial, the reference joint angles, computed by (3.3) for $n = 9$ choosing $\mathrm{g}(i, n) = 1$ and $\mathrm{g}(i, n) = (n-i)/(n+1)$ in case of lateral undulation or eel-like motion, were sent to the robot via the CAN. In each trial we measured the position of the center of mass and the steady state values of the achieved velocity for approximately 30 sec of motion. Note that a proportional controller, implemented in the microcontroller of each joint module, is present and is responsible for the control of the corresponding joint angle. At this point, it is worth to mentioning that the value of $n = 9$ is resulting from the fact that the robot is commanded to move according to a horizontal motion pattern over a horizontal plane, and thus only the joints with horizontal rotating axis are forced to rotate, while the reference angles corresponding to the vertical joint motion were set to zero. This is because we need only measurements in the 2D horizontal plane for the fluid coefficients identification of the 2D fluid model presented in Section 2.2. Finally, the initial values of the link angles were set to zero in each experiment task.

In order to perform a back-to-back comparison of experimental data and ideal simulation results, we simulate the model of underwater snake robot presented in Section 2.2 with the fluid coefficients set only once via trial and error procedure to $C_f = 0.3$, $C_D = 1.75$, $C_A = 1.5$ for lateral undulation and $C_f = 0.17$, $C_D = 1.75$, $C_A = 1.5$ for eel-like motion. Note that the fluid coefficient C_f is smaller for the eel-like motion compared to the lateral undulation. This is expected since we have oscillations with smaller amplitude at the head of the robot, causing the effect of the drag forces in x direction to be smaller. In particular, we consider an underwater snake robot with $n = 9$ links, each one having length $2l = 0.18$ m and mass $m = 0.8$ kg, i.e. identical to the physical robot presented in Section 5.7. The hydrodynamic related parameters for the elliptic section with major and minor diameters $2a = 2 \cdot 0.055$ m and $2b = 2 \cdot 0.05$ m, respectively, and $\rho = 1000$ kg/m^3 were calculated by (2.14), (2.15), (2.17) and (2.20). In these simulations a joint PD-controller (3.5) was used with parameters $k_p = 20, k_d = 5$, while lateral undulation or eel-like motion were achieved by moving the joints according to the (3.3) by choosing $\mathrm{g}(i, n) = 1$ and $\mathrm{g}(i, n) = (n-i)/(n+1)$, respectively, with gait parameters values similar to ones of the experimental trials.

In Fig. 6.13-6.14, we see simulation and experimental results that are obtained by choosing the fluid coefficients as mentioned earlier and $\alpha = 30^o$, $\omega = 120^o$/s, $\delta = 20^o$ and $\phi_0 = 0$ for lateral undulation and eel-like motion. The simulated and the experimental results are expressed in global frame with the origin being at (0,0) for visualization purposes. This makes the comparison of the simulated

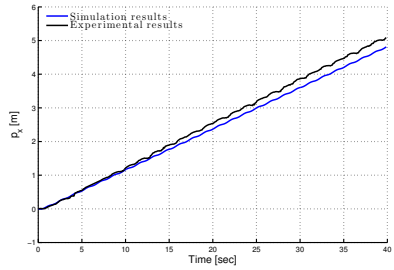

(a) Position along the path, p_x

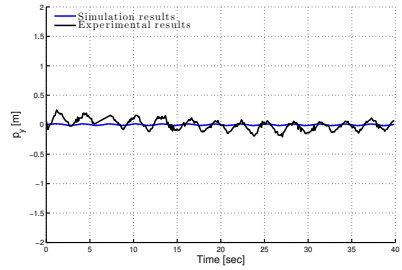

(b) Position along the path, p_y

Figure 6.13: Lateral undulation: Comparison results of the simulated and real robot for the gait parameters $\alpha = 30^o$, $\omega = 120^o/\text{s}$, $\delta = 30^o$ and $\phi_0 = 0$.

and the experimental results more obvious, without changing the response of the system. From Fig. 6.13(a) and Fig. 6.14(a), we see that the robot manage to transverse the same distance in x-direction both in simulations and in experiments. We see that the oscillations in the y-direction (Fig. 6.13(b)-6.14(b)) are bigger in the experimental trial compared to the simulated results. This is mostly due to the inaccuracies on the sensors' measurements involved in the experimental setup. The amplitudes of the achieved forward steady state velocities for the lateral undulation calculated by (6.16), are 0.1275 m/s and 0.1288 m/s for the simulated robot and the real robot, respectively. Note that t_{end} and t_0 indicate the beginning and the end of the time horizon, respectively. The error between these velocities is 1.01 %, which indicates that there is quite good agreement between the simulated dynamics of the robot and the real experiments. In addition, the steady state velocities for the eel-like motion are 0.0897 m/s and 0.0894 m/s for the simulated robot and the real robot, respectively. The error between the velocities for the case of eel-like motion is 0.33 %.

$$V_f = \frac{\sqrt{(p_x(t_{\text{end}}) - p_x(t_0))^2 + (p_y(t_{\text{end}}) - p_y(t_0))^2}}{t_{\text{end}} - t_0} \tag{6.16}$$

Remark 6.8: *Note that another more accurate method for the fluid coefficients identification should be investigated in the future for more precise identified values of the drag and added mass coefficients. In this study, preliminary results are obtained for the complex model presented in Section 2.2, which mainly will be used to investigate the efficacy of the path following controller presented in Section 6.1 by comparing the experimental results with the simulated ones.*

6.4.2 Experimental Setup

The path following controller was experimentally investigated using the underwater snake robot Mamba (see Fig. 5.14). As mentioned in Section 5.7, the robot consist of 18 identical joint modules mounted horizontally and vertically in an alternating

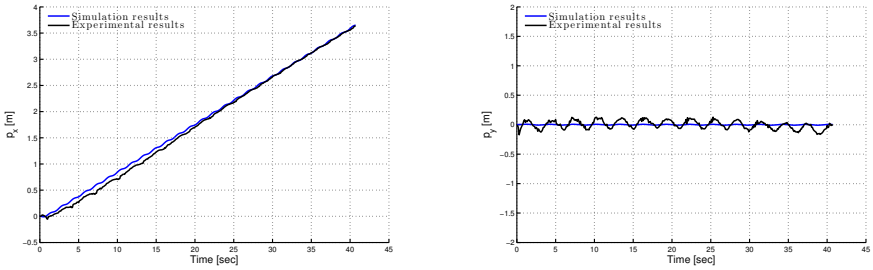

(a) Position along the path, p_x

(b) Position along the path, p_y

Figure 6.14: Eel-like motion: Comparison results of the simulated and real robot for the gait parameters $\alpha = 30^o$, $\omega = 120^o/\text{s}$, $\delta = 30^o$ and $\phi_0 = 0$.

fashion. For our experimental process, the underwater motion capture system from Qualisys [4] was used in order to have accurate measurements of the robot's position and orientation. The total control structure that is adopted in the experimental task is illustrated in Fig. 6.15. The measured position and the absolute angle of the tail were obtained as described in Section 5.7.

Now, the individual computations and the implementation of the path following controller will be described in the sequel steps. Having the measurements of the tail position and orientation, and the individual joint angles, we calculated, using the kinematics equations presented in Section 2.2, the center of mass position, $\mathbf{p}_{\text{CM}}$, and the absolute link angles, $\boldsymbol{\theta}$, of the underwater snake robot. The LOS path following controller of the underwater snake robot was implemented on an external computer according to (3.3), (6.4) and (6.5), i.e. the for the lateral undulation and eel-like motion gait patterns. Specifically, the reference joint angles, computed by (3.3), were sent to each joint module of the robot via the CAN bus running through the robot. A proportional controller implemented in the microcontroller of each joint module controlled the joint angle according to the received reference angle. The joint torque controller given by (3.5) was not implemented, since accurate torque control is not supported by the servo motors installed in the snake robot. The estimation of the robot's orientation was calculated according to (2.2), i.e. as the average of the individual link angles. The LOS guidance law angle given by (6.4) was calculated with a look-ahead distance equal to half the length of the robot, i.e. $\Delta = 0.9$ m [38] for fast convergence, due to the limited working area covered by the camera system. Furthermore, the control gain in (6.5) was $k_\theta = 0.4$ and $k_\theta = 0.6$ for lateral undulation and eel-like motion, respectively. The joint angle offset was saturated according to $\phi_0 = [-20^o, 20^o]$ in order to keep the joint reference angles within reasonable bounds and taking into account the physical robot's joint angle constraints. Moreover, the reference angles were calculated by (3.3) for $n = 9$ choosing $\text{g}(i, n) = 1$ and $\text{g}(i, n) = (n - i)/(n + 1)$ in case of lateral undulation or eel-like motion, respectively, while the rest of the gait parameters were $\alpha = 35^\text{o}$ for lateral undulation and $\alpha = 40^\text{o}$ for eel-like motion, $\delta = 40^\text{o}$ and $\omega = 120^\text{o}/\text{s}$. The initial joint angles were zero in all the trials, while the initial heading and position

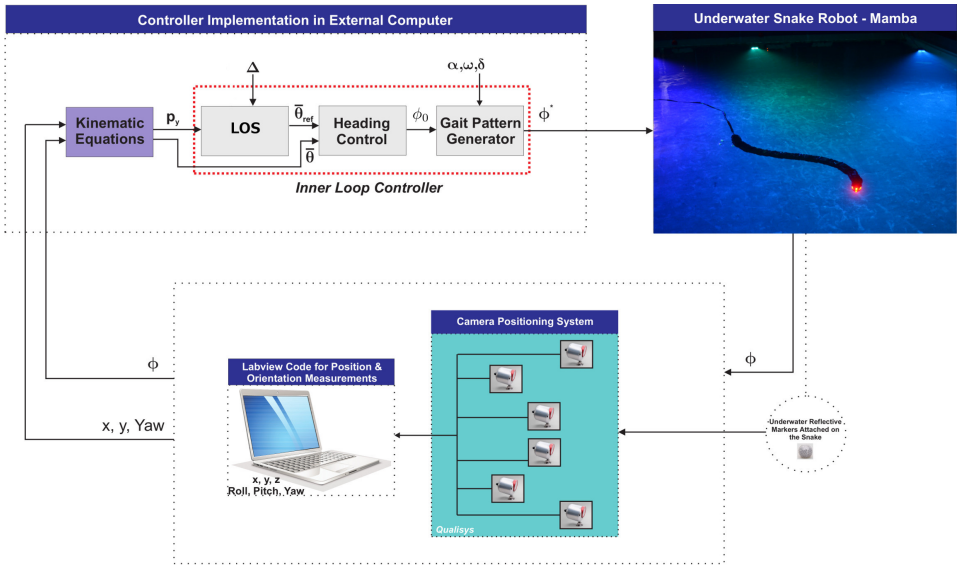

Figure 6.15: Illustration of the controller structure used in the experiments for LOS approach.

of the robot are defined for each trial.

6.4.3 Experimental Results

The straight line path following controller presented in Section 6.1 is experimentally investigated both for lateral undulation and eel-like motion patterns. In particular, experimental results for two different sets of initial conditions are presented both for lateral undulation and eel-like motion patterns. In the first two trials of the experiments, the robot was initially headed along the desired path (the x axis), and the initial distance from the CM to the desired path was 1.89 m and 2.81 m for lateral undulation and 2.75 m and 2.98 m for eel-like motion pattern. In the last two trials, the robot was initially headed towards the desired path (the x axis) with initial heading $\bar{\theta}(0) = -91.3^o$ and $\bar{\theta}(0) = -88.3^o$, for lateral undulation and eel-like motion, and the initial distance from the CM to the desired path was 1.59 m and 1.97 m, respectively. The experimental results for the all the trials are presented in Fig. 6.16(a) - 6.18(a) for lateral undulation and Fig. 6.19(a) - 6.21(a) for eel-like motion pattern, where it is easily seen that the robot converged nicely towards and moved along the desired path during all trials both for lateral undulation and eel-like motion patterns. In particular, we can see that the center of mass of the underwater snake robot converges to the desired path for all the trials.

In Fig. 6.16(d)-6.21(d), we can see that (6.5) makes the heading angle converge to and oscillate around zero both for lateral undulation and eel-like motion patterns. Moreover, Fig. 6.16(c)-6.21(c) show that the cross track error converges to and oscillates around zero. Furthermore, the forward velocity of the robot is shown

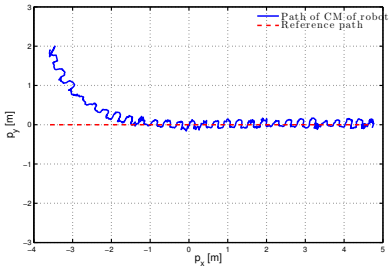

(a) Path of the CM

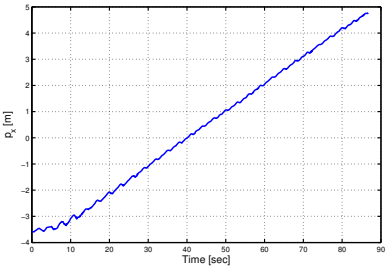

(b) Position along the path, p_x

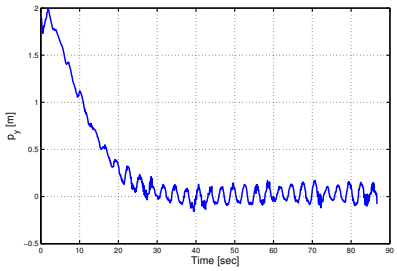

(c) Cross-track error, p_y

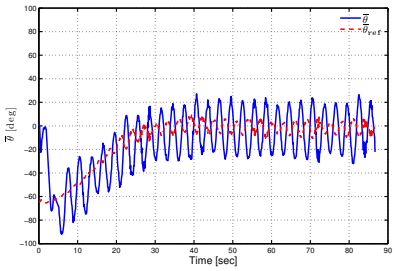

(d) Heading angle, $\overline{\theta}$

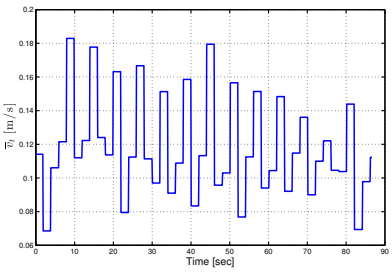

(e) Forward Velocity, $\overline{v}_t$

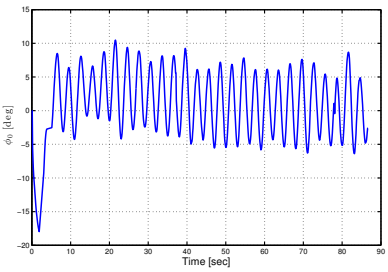

(f) Joint angle offset, ϕ_0

Figure 6.16: Lateral Undulation: Straight line path following with the physical snake with the initial heading along the desired path (First Trial).

in Fig. 6.16(e) -6.21(e) and the joint angle offset is shown in Fig. 6.16(f)-6.21(f). Fig. 6.16-6.21 clearly show that the heading, the cross track error and the position of the robot have a steady state oscillatory behavior when the robot reaches the desired path. Note that this was expected since for an underwater snake robot with revolute joints, it is difficult to achieve a purely non-oscillating motion of the CM. Similar to the oscillatory behaviour of the CM, the orientation of the robot was also expected to oscillate, as it is shown in Fig. 6.16(d)-6.21(d).

The visualisations in Fig. 6.22 and Fig. 6.23 for the results presented in Fig. 6.16 and Fig. 6.19 for lateral undulation and eel-like motion, respectively, illustrate

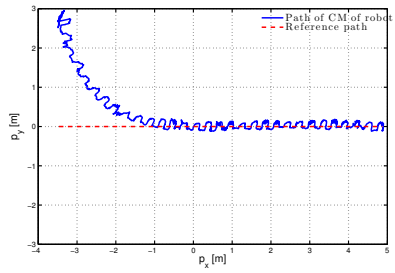

(a) Path of the CM

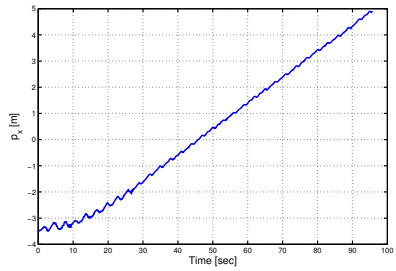

(b) Position along the path, p_x

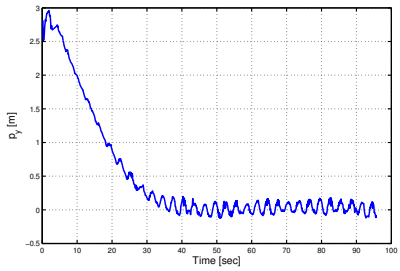

(c) Cross-track error, p_y

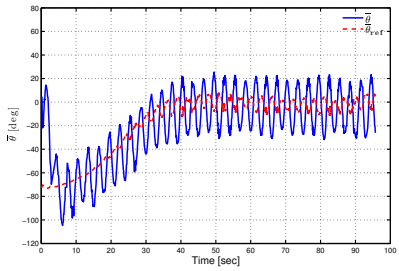

(d) Heading angle, $\overline{\theta}$

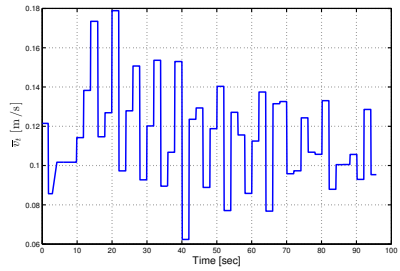

(e) Forward Velocity, $\overline{v}_t$

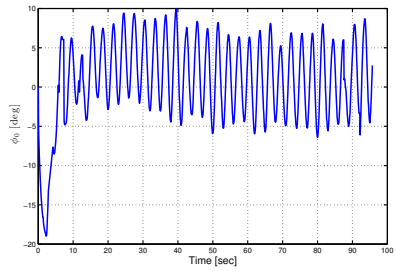

(f) Joint angle offset, ϕ_0

Figure 6.17: Lateral Undulation: Straight line path following with the physical snake with the initial heading along the desired path (Second Trial).

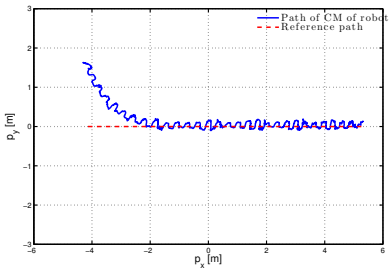

(a) Path of the CM

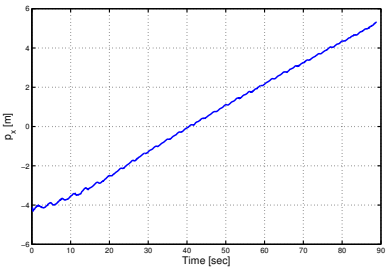

(b) Position along the path, p_x

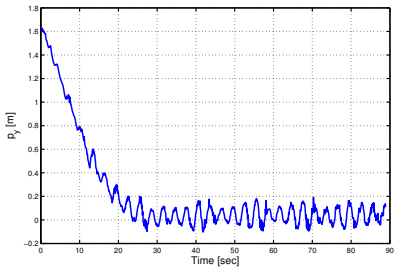

(c) Cross-track error, p_y

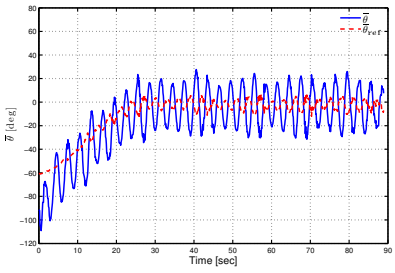

(d) Heading angle, $\overline{\theta}$

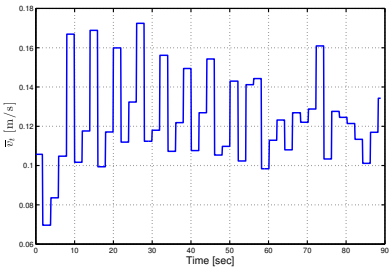

(e) Forward Velocity, $\overline{v}_t$

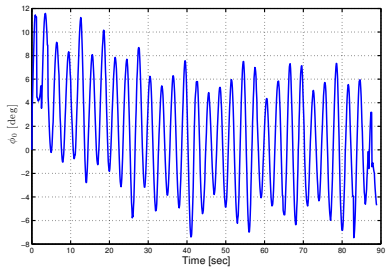

(f) Joint angle offset, ϕ_0

Figure 6.18: Lateral Undulation: Straight line path following with the physical snake with initial heading towards the desired path (Third Trial).

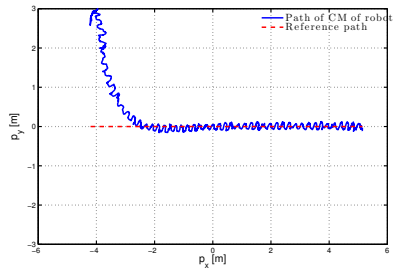

(a) Path of the CM

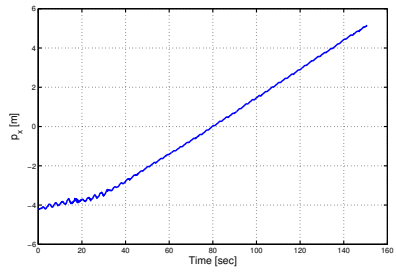

(b) Position along the path, p_x

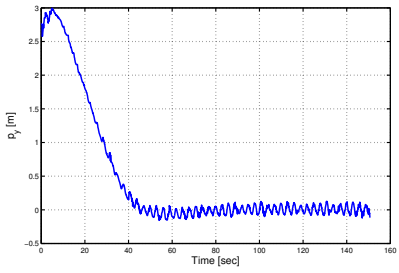

(c) Cross-track error, p_y

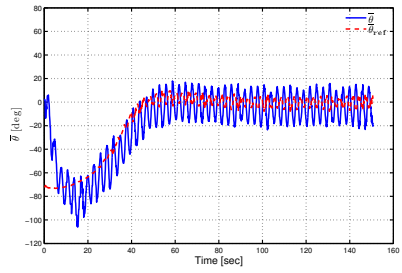

(d) Heading angle, $\overline{\theta}$

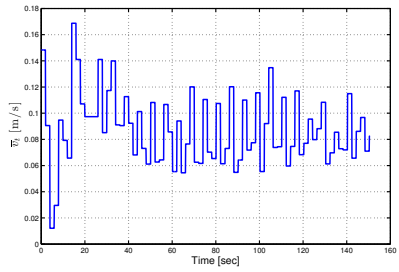

(e) Forward Velocity, $\overline{v}_t$

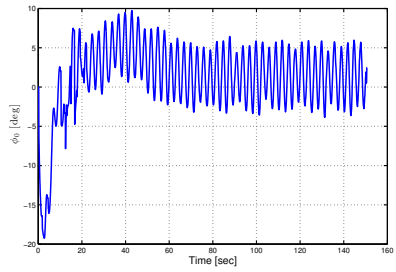

(f) Joint angle offset, ϕ_0

Figure 6.19: Eel-like motion: Straight line path following with the physical snake with the initial heading along the desired path (First Trial).

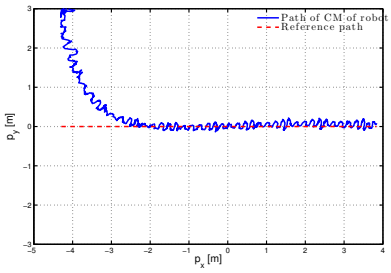

(a) Path of the CM

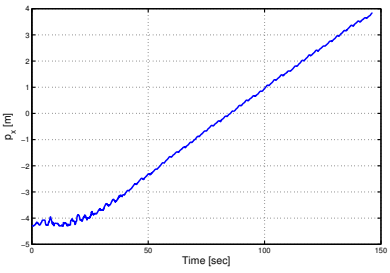

(b) Position along the path, p_x

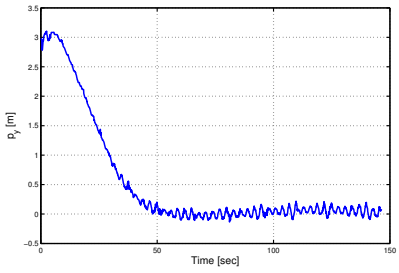

(c) Cross-track error, p_y

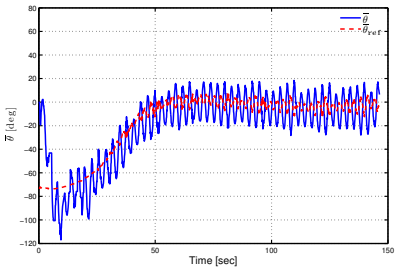

(d) Heading angle, $\overline{\theta}$

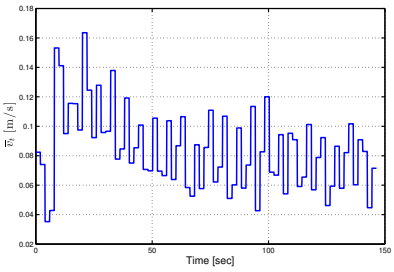

(e) Forward Velocity, $\overline{v}_t$

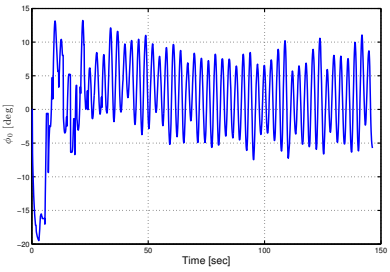

(f) Joint angle offset, ϕ_0

Figure 6.20: Eel-like motion: Straight line path following with the physical snake with the initial heading along the desired path (Second Trial).

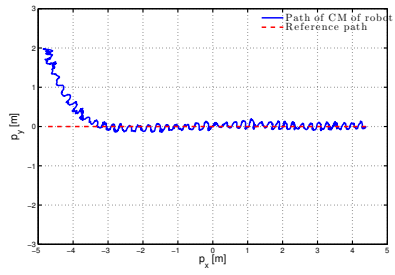

(a) Path of the CM

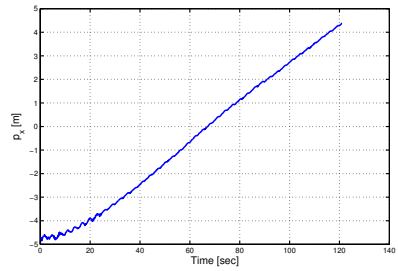

(b) Position along the path, p_x

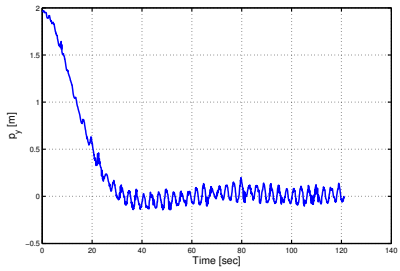

(c) Cross-track error, p_y

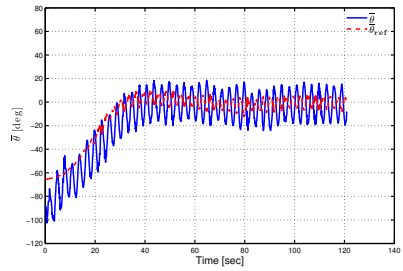

(d) Heading angle, $\overline{\theta}$

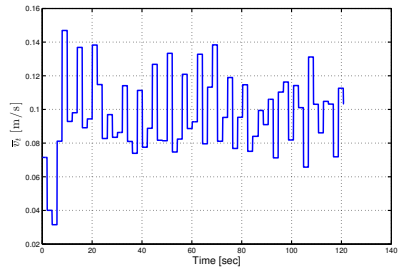

(e) Forward Velocity, $\overline{v}_t$

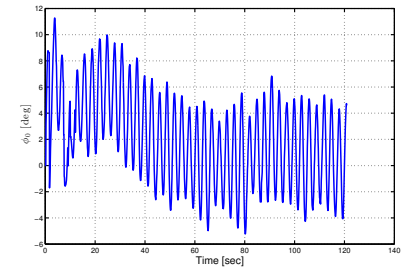

(f) Joint angle offset, ϕ_0

Figure 6.21: Eel-like motion: Straight line path following with the physical snake with initial heading towards the desired path (Third Trial).

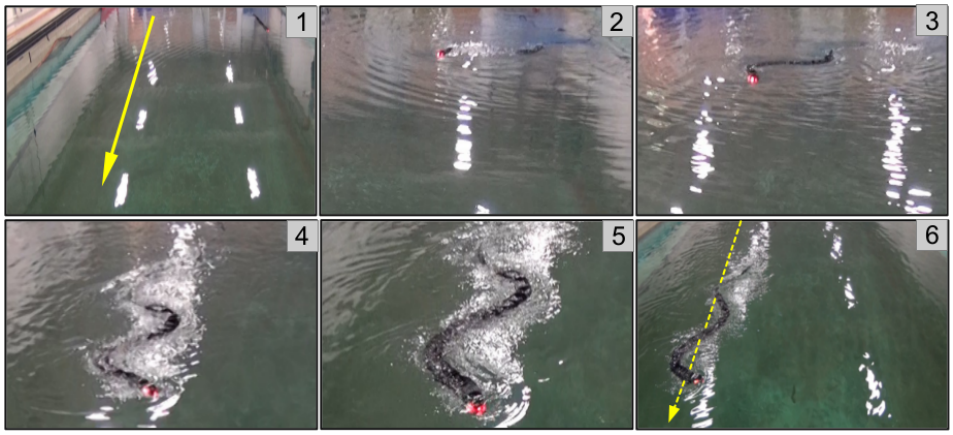

Figure 6.22: The motion of the underwater snake robot during path following for the experimental results presented in Fig. 6.16. The *yellow line* indicates the desired path, i.e. the global x axis.

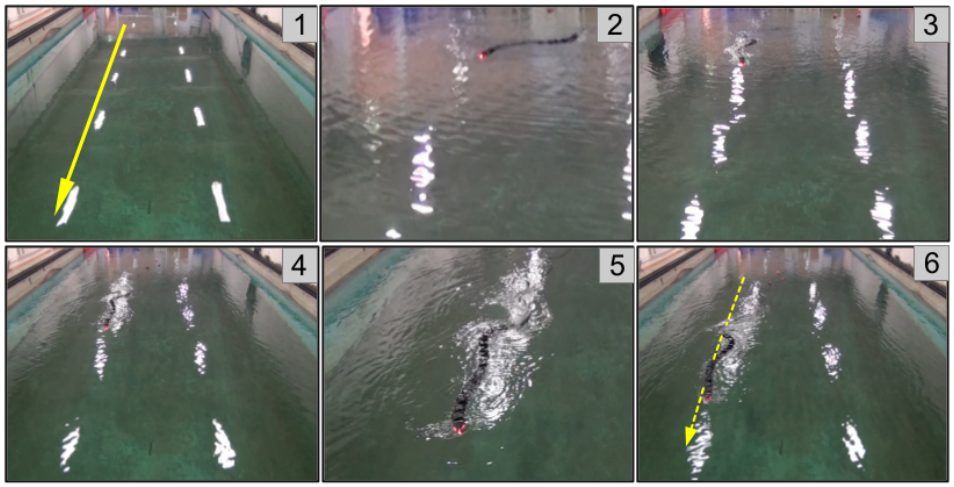

Figure 6.23: The motion of the underwater snake robot during path following for the experimental results presented in Fig. 6.19. The *yellow line* indicates the desired path, i.e. the global x axis.

that the robot converged nicely towards and moved along the desired path. This claim is supported by the plots of the cross-track error in Fig. 6.16(c) and Fig. 6.19(c), which shows that the cross-track error converges to and oscillates about zero.

6.4.4 Simulation Results

In order to perform a back-to-back comparison of real experimental and ideal simulation results, we simulate the model presented in Section 2.2 with the LOS path following controller proposed in Section 6.1 using similar parameters. In particular, we consider an underwater snake robot with $n = 9$ links, each one having length $2l = 0.18$ m and mass $m = 0.8$ kg, i.e. identical to the physical robot presented in Section 5.7. The hydrodynamic parameters c_t, c_n, μ_n λ_1, λ_2 and λ_3 are calculated for the fluid coefficients C_f, C_d and C_A as identified in Subsection 6.4.1. The joint PD controller (3.5) is used for each joint with parameters $k_p = 20$, $k_d = 5$, and the reference angles corresponding to the horizontal joint motion of the robot were calculated according to (3.3) with $n = 9$ by choosing $\mathrm{g}(i, n) = 1$ and $\mathrm{g}(i, n) = (n-i)/(n+1)$ for lateral undulation and eel-like motion respectively, with same gait parameters are presented in previous subsection. Furthermore, the control gain in (6.5) is $k_\theta = 0.4$ and $k_\theta = 0.6$ for lateral undulation and eel-like motion, respectively, while the guidance law parameters in (6.4) are chosen as $\Delta = 0.9$ similar to the experimental trials. The initial values of all states of the robot are set to zero except for the initial position of the center of mass, which is selected as $\mathbf{p}_{\mathrm{CM}}(0) = [-3.58, 1.89]$ and $\mathbf{p}_{\mathrm{CM}}(0) = [-4.20, 2.75]$ for lateral undulation and eel-like motion, respectively, i.e. same as the initial values presented for the cases shown in Fig. 6.16 and Fig. 6.19. The simulation results are shown in Fig. 6.24 and Fig. 6.25.

The results shown in Fig. 6.24 and Fig. 6.25 indicate that the qualitative behavior of the simulated system is similar to the behavior of the physical robot. In particular, from Fig. 6.16(a)-6.19(a) and Fig. 6.24(a)-6.25(a) it can be seen that the physical snake and the simulated snake follow almost the same path both for lateral undulation and eel-like motion patterns. The cross-track error converges and oscillates around zero in both motion patterns, as shown in Fig. 6.16(c)-6.19(c) and Fig. 6.24(c)-6.25(c). In Fig. 6.16(c)-6.19(c) the cross-track error has larger oscillations compared to the ideal case in Fig. 6.24(c)-6.25(c) and this was expected mainly due to the noise on the measurements in the experiments caused by different sensors i.e. the position measurement from the camera system and the joint angle measurements from the actuators. From Fig. 6.16(d)-6.19(d) and Fig. 6.24(d)-6.25(d), we see that in both cases the heading converges zero. The oscillations of the heading are larger in Fig. 6.16(d)-6.19(d) than in Fig. 6.24(d)-6.25(d) and this is again due to the inaccuracies of the different measurements from the sensors. Note that the heading is defined as the average of the link angles (2.2) and any inaccurate measurements from the encoders will produce errors and this is the main reason for the larger oscillations on the heading in the experimental results presented in Fig. 6.16(d)-6.19(d).

Remark 6.9: *Comparing the experimental results (Fig. (6.16,6.19)) with the simulated ones (Fig. 6.24-6.25), we see that the simulated model reaches higher velocities both for lateral undulation and eel-like motion. This is mainly due to the power supply cable that is attached on the robot. Note that in our simulations we do not have extra drag effects as the ones that are produced from the power supply cable of the robot that is used in our experiments. The effect of the this cable are more visible for the*

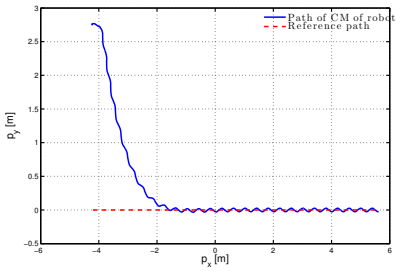

(a) Position of the CM of the robot

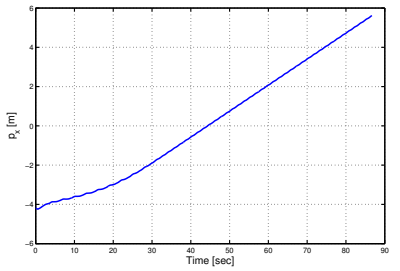

(b) Position along the path, p_x

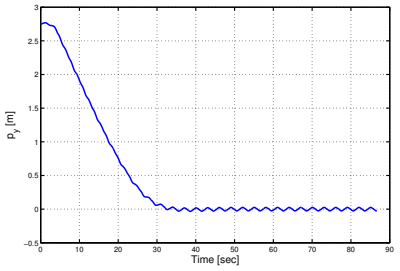

(c) Cross-track error, p_y

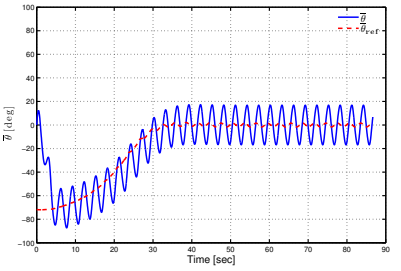

(d) Orientation of the robot

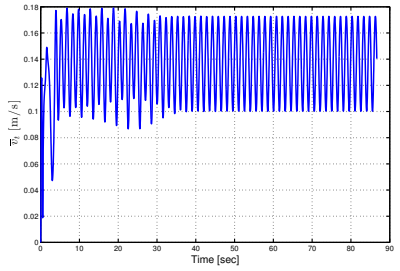

(e) Forward velocity, $\overline{v}_t$

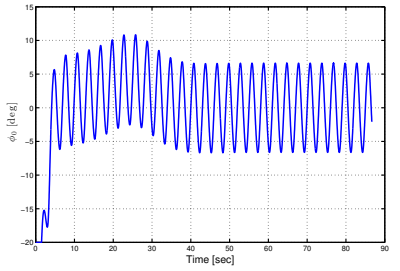

(f) Joint angle offset, ϕ_0

Figure 6.24: Simulation results for straight line path following for a snake robot with $n = 9$ links.

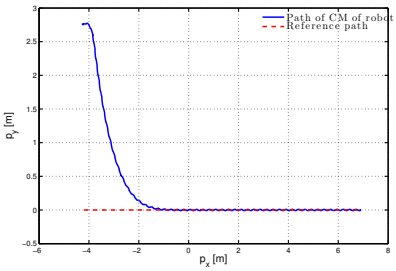

(a) Position of the CM of the robot

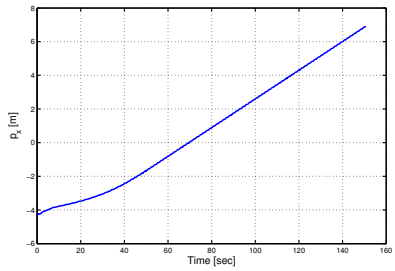

(b) Position along the path, p_x

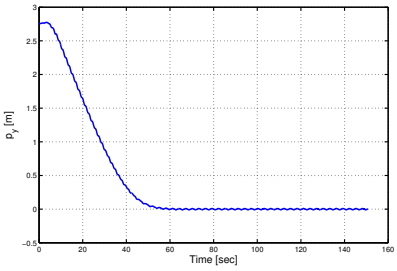

(c) Cross-track error, p_y

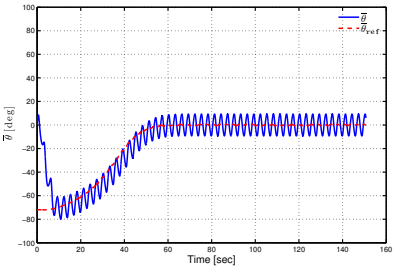

(d) Orientation of the robot

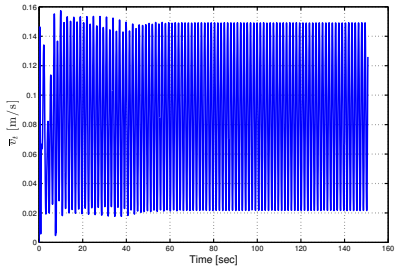

(e) Forward velocity, $\overline{v}_t$

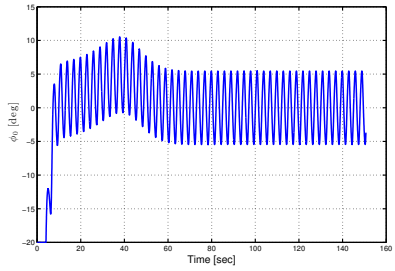

(f) Joint angle offset, ϕ_0

Figure 6.25: Simulation results for straight line path following for a snake robot with $n = 9$ links.

slower motions as the one achieved for the eel-like motion pattern (Fig. 6.19 and Fig. 6.25).

6.5 Experimental Investigation of I-LOS Path Following Controller

This section describes the experimental setup employed in order to investigate the performance of the integral LOS path following controller presented in Section 6.2, and the simulation and experimental results.

6.5.1 Experimental Setup

The performance of the guidance strategy presented in Section 6.2 was investigated experimentally for straight line paths. The experiments were performed in the North Sea Center Flume Tank in Hirtshals, Denmark [3]. The dimensions of the tank are L: 30 m, H: 6 m and W: 8 m and an installation of four propellers and motors of 64 kW in the tank provides the ability to generate water flow up to 1 m/sec. In addition, the tank is equipped with a state-of-the-art motion capture system from Qualisys [4], which provides accurate real time measurements of the position and orientation of underwater objects equipped with reflective markers.

The experiments were carried out using the underwater snake robot – Mamba (Fig. 5.15), with 18 identical joint modules mounted horizontally and vertically in an alternating fashion (see Section 5.7). During the experiments, the robot was moved according to a strictly horizontal motion pattern where the joints with vertical axis were constrained at zero degrees. The kinematics of the snake robot therefore corresponded to a planar snake robot with links of length $2l = 0.18$ m and mass $m \approx 0.8$ kg. During the experiments, the robot had a slightly positive buoyancy and was swimming near the water surface.

In order to measure the position and the orientation of the snake robot, reflective markers were attached on the tail part of the robot, as shown in Fig. 6.26. Although the robot was swimming on the surface of the tank, the markers were submerged in the tank approximately 0.5 m from the surface since the camera system was unable to track markers above 0.5 m from the surface. The global frame coordinates of the tail link and the absolute angle of the tail were measured using the camera-based motion capture system from Qualisys [4] installed in the tank. The camera system consisted of six cameras, which allow reflective markers to be tracked under water. The controller structure used in the experiments is illustrated in Fig. 6.27. The measured position and the absolute angle of the tail were received from an external computer where the Qualisys system [4] was connected, and afterwards these measurements were sent through UDP in *LabVIEW 2013* to another computer where the path following controller was implemented.

Knowing the position and the orientation of the tail of the robot, and also the individual joint angles, and by using the kinematics of the robot presented in Section 2.2, the center of mass position, $\mathbf{p}_{\mathrm{CM}}$ and the absolute link angles, $\boldsymbol{\theta}$ of the underwater snake robot were calculated. The I-LOS path following controller of the underwater snake robot was implemented on an external computer according to

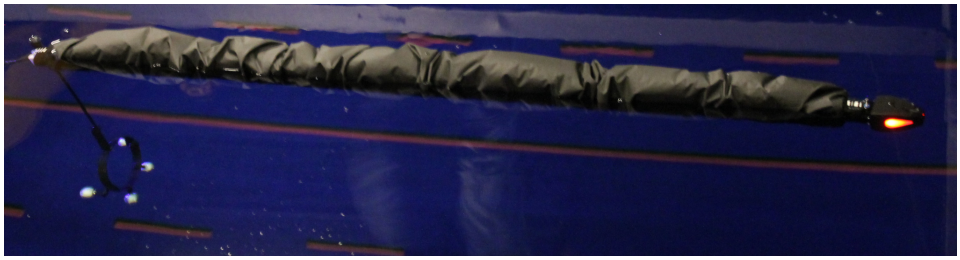

Figure 6.26: The underwater snake robot Mamba in the pool at SINTEF flume tank with the markers attached on the tail for position measurements.

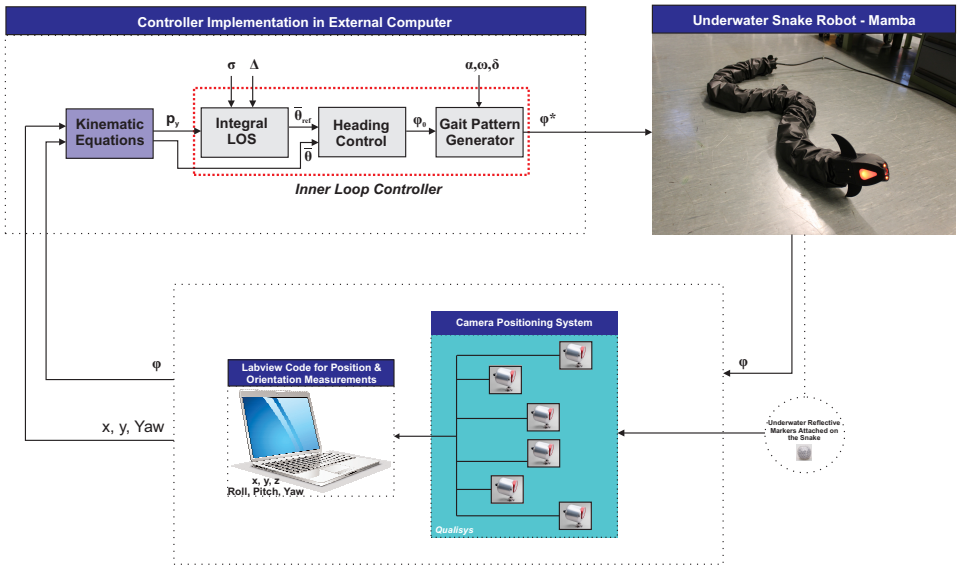

Figure 6.27: Illustration of the controller structure used in the experiments for I-LOS controller.

(3.1), (6.9), (6.10) and (6.5) for the lateral undulation gait pattern. The solutions of (6.10) were obtained by numerical integration in *LabVIEW 2013*, which was used as the development environment for the path following controller. The reference joint angles, computed by (3.1), were sent to the robot via a CAN bus and the joint angles were controlled according to a proportional controller implemented in the microcontroller of each joint module. As it is already mentioned in previous section, we did not implement the joint torque controller given by (3.5) since accurate torque control is not supported by the servo motors installed in the snake robot. The orientation of the robot was estimated according to (2.2), i.e. as the average of the individual link angles.

The I-LOS angle given by (6.9) was calculated with a look-ahead distance equal to the length of the robot, i.e. $\Delta = 1.6$ m [38] for fast convergence due to the

limited length of the tank, and $\sigma = 0.01$ [19]. Furthermore, the initial values of y_{int} were zero and the control gain in (6.5) was $k_\theta = 0.3$. The joint angle offset was saturated according to $\phi_0 = [-20^o, 20^o]$ in order to keep the joint reference angles within reasonable bounds with respect to the maximum allowable joint angles of the physical robot. The reference angles corresponding to the horizontal joint motion of the robot were calculated according to (3.1) with $n = 9$ and gait parameters $\alpha = 30^o$, $\delta = 40^o$ and $\omega = 90^o/s$. The reference angles corresponding to the vertical joint motion were zero in order to constrain the motion of the robot purely in the horizontal plane. Furthermore, the initial values of the link angles were set to zero, while the initial heading and position of the robot are presented in each trial.

6.5.2 Experimental Results

We investigated the performance of the proposed control strategy for a constant current in the inertial frame. Using the flow water speed generator this was set equal to $[-0.07\cos(45^o), -0.07\sin(45^o)]$ m/sec. This was achieved by defining the straight line path at a 45 degree angle with respect to the direction of the water flow and setting the water flow speed to 0.07 m/sec. The straight line path following controller was experimentally investigated from two different sets of initial conditions. In both trials, the robot was headed along the desired path (the x axis), and the initial distance from the CM to the desired path was -1.5728 m and -0.7661 m, respectively. In Fig. 6.28(d) and Fig. 6.29(d) we can see that (6.5) makes the heading angle converge to and oscillate about the desired heading angle given by (6.9) for lateral undulation. Note that the desired heading of the robot does not converge to oscillations about zero, but rather converges to a steady state constant value $\bar{\theta}_{ss}$ to compensate for the effect of the water current. Moreover, Fig. 6.28(c) and Fig. 6.29(c) show that the cross track error converges to and oscillates about zero. Finally, from Fig. 6.28(a) and Fig. 6.29(a), we can see that the center of mass of the underwater snake robot converges to the desired path for lateral undulation. Furthermore, the forward velocity of the robot is shown in Fig. 6.28(e)-6.29(e) and the joint angle offset is shown in Fig. 6.28(f)-6.29(f).

The visualisation in Fig. 6.30 for the results presented in Fig. 6.29 illustrates that the robot converged nicely towards and moved along the desired path. This claim is supported by the plots of the cross-track error in Fig. 6.29(c), which shows that the cross-track error converges to and oscillates about zero. Fig. 6.28-6.29 clearly show that the heading, the cross track error and the position of the robot have a steady state oscillatory behavior when the robot reaches the desired path.

6.5.3 Simulation Results

In order to perform a back-to-back comparison of real experimental and ideal simulation results, we simulate the model presented in Section 2.2 with the integral LOS path following controller proposed in Section 6.2 using similar parameters with the experiments. In particular, we consider an underwater snake robot with $n = 9$ links, each one having length $2l = 0.18$ m and mass $m = 0.8$ kg, i.e. identical to the physical robot presented in Section 5.7. The hydrodynamic parameters are $c_t = 0.4453$, $c_n = 15.84$, $\mu_n = 1.7106$, $\lambda_1 = 5.260410^{-8}$, $\lambda_2 = 0.0012$ and

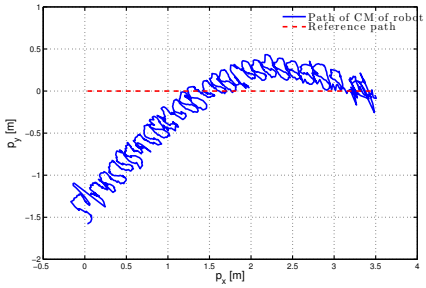

(a) Position of the CM of the robot

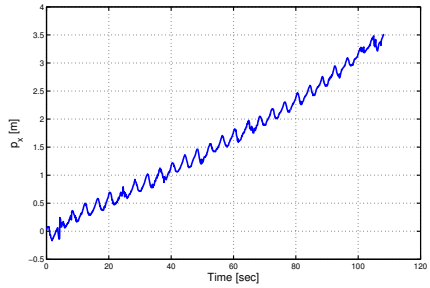

(b) Position along the path, p_x

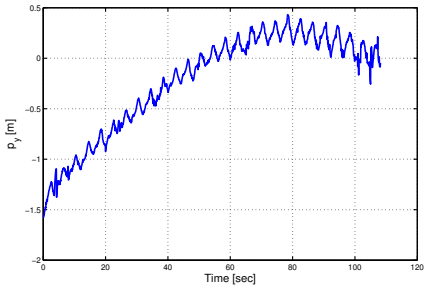

(c) Cross-track error, p_y

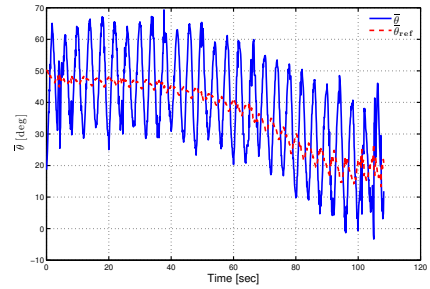

(d) Orientation of the robot

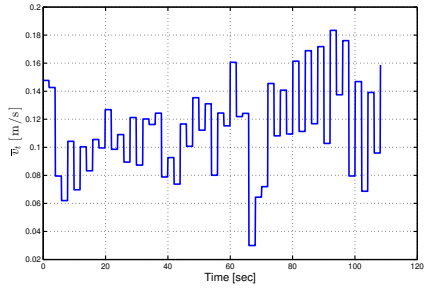

(e) Forward velocity, $\overline{v}_t$

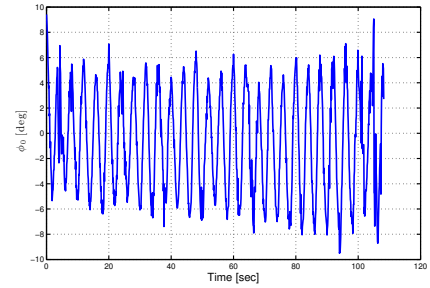

(f) Joint angle offset, ϕ_0

Figure 6.28: Straight line path following with the physical snake: First Trial.

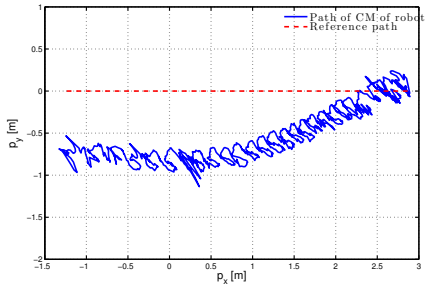

(a) Position of the CM of the robot

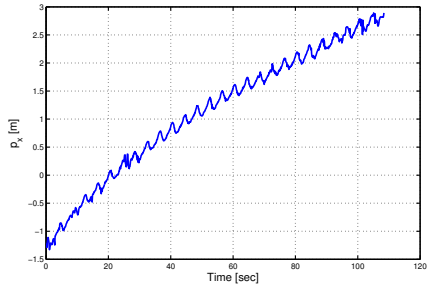

(b) Position along the path, p_x

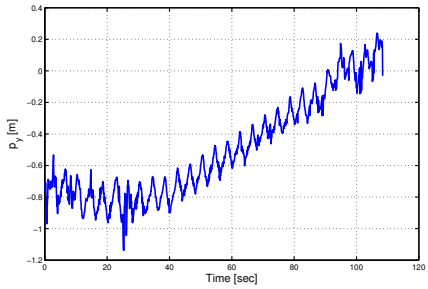

(c) Cross-track error, p_y

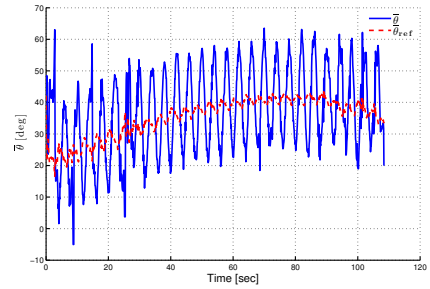

(d) Orientation of the robot

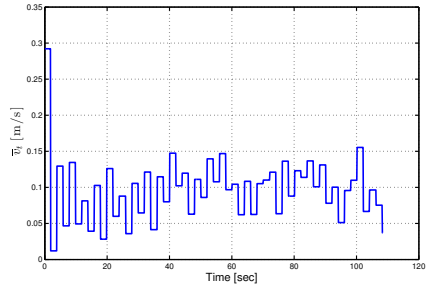

(e) Forward velocity, $\overline{v}_t$

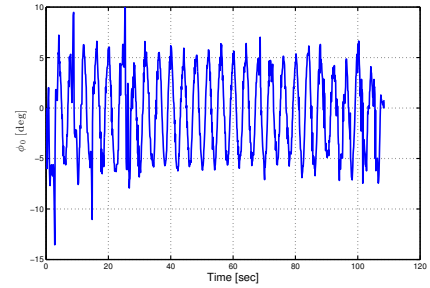

(f) Joint angle offset, ϕ_0

Figure 6.29: Straight line path following with the physical snake: Second Trial.

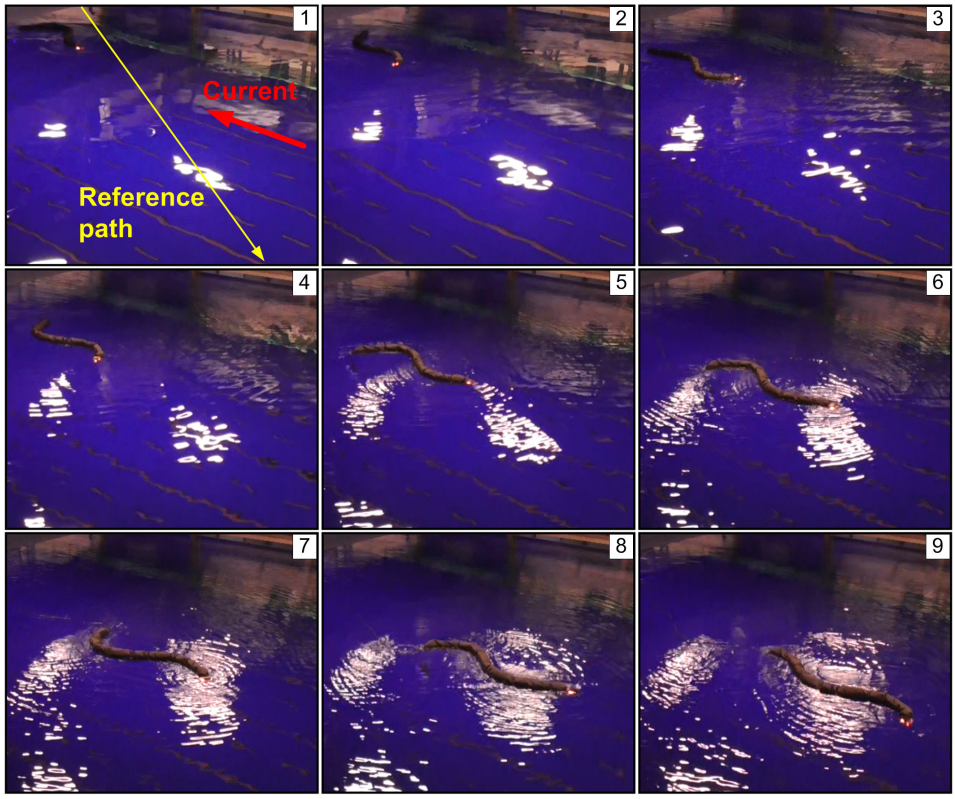

Figure 6.30: The motion of the underwater snake robot during path following for the experimental results presented in Fig. 6.29. The *yellow line* indicates the desired path, i.e. the global x axis, and the *red line* the constant irrotational current direction.

$\lambda_3 = 8.116010^{-5}$. The drag fluid parameters c_t and c_n are calculated for $C_d = 1.6$ and $C_f = 0.03$. Note that the fluid coefficients are not identified in the presence of current and thus we use the steady state values for the fluid parameters in this section. The values of a constant ocean current in the inertial frame are $[-0.17, -0.17]$ m/sec. The joint PD controller (3.5) is used for each joint with parameters $k_p = 20$, $k_d = 5$, and lateral undulation is achieved by choosing $\mathrm{g}(i, n) = 1$, with gait parameters $\alpha = 30^{\mathrm{o}}$, $\delta = 40^{\mathrm{o}}$ and $\omega = 90^{\mathrm{o}}$/s in (3.3). Furthermore, the control gain in (6.5) is $k_\theta = 0.3$, while the guidance law parameters in (6.9-6.10) are chosen as $\Delta = 1.6$ [38], and $\sigma = 0.08$ [19]. The initial values of all states of the robot are set to zero except for the initial position of the center of mass, which is selected as $\mathbf{p}_{\mathrm{CM}}(0) = [-1.2375, -0.7661]$, i.e. same as the initial values presented for the case shown in Fig. 6.29. The simulation results are shown in Fig. 6.31.

The results shown in Fig. 6.29 and Fig. 6.31 indicate that the qualitative behavior of the simulated system is similar to the behavior of the physical robot. In addition, tuning the values of the current for the simulated system, we also achieve

a good quantitative similarity between the simulated and experimental results. In particular, from Fig. 6.29(a) and Fig. 6.31(a) it can be seen that the physical snake and the simulated snake follow almost the same path. The cross track error converges and oscillates about zero in both cases in the same time horizon, as shown in Fig. 6.29(c) and Fig. 6.31(c). In Fig. 6.29(c) the cross-track error has larger oscillations compared to the ideal case in Fig. 6.31(c) and this was expected mainly due to the noise on the measurements in the experiments caused by different sensors i.e. the position measurement from the camera system and the joint angle measurements from the actuators. In addition, it is worth mentioning that the I-LOS was implemented in *Labview 2013* via numerical integration and the integration of noisy data produces errors that can cause these oscillations. From Fig. 6.29(d) and Fig. 6.31(d), we see that in both cases the heading converges to a constant steady state value of 38^o, approximately. The oscillation of the heading are larger in Fig. 6.29(d) than in Fig. 6.31(d) and this is again due to the inaccuracies of the different measurements from the sensors. Note that the heading is defined as the average of the link angles (2.2) and any inaccurate measurements from the encoders will produce errors and this is the main reason for the larger oscillations on the heading in the experimental results presented in Fig. 6.29(d).

Remark 6.10: *Note that although an ocean current with values* $[-0.07\cos(45^o), -0.07\sin(45^o)]$ *m/sec was generated in the flume tank, the experiments were performed on the surface of the flume tank where also surface effects and possibly also wave drift influenced the motion of the robot. Furthermore, the attachment system that is used for the markers on the tail of the robot also affects the motion of the robot. In addition, it is expected that the robot is influenced from other hydrodynamic effects which are produced through to the interaction of the robot and the surrounding fluid one the surface, and which are not taken into account in the proposed modeling approach for underwater snake robots presented in Section 2.2. The actual values of the total drift effects experienced by the snake robot are therefore not precisely known. In order to find an estimate of the total drift effects, we use that* $\bar{\theta}_{ss}$ *is directly related to the values of the drift effects that the system is experiencing, (see [19] for more details on this). We can thus find an estimate of the drift effects by tuning the ocean current (drift) parameters until they produce the same* $\bar{\theta}_{ss}$ *as observed in the experiments. This gives the resulting ocean drift values* $[-0.17, -0.17]$ *m/sec which are then used in the simulations. As we can see from Fig. 6.29 and Fig. 6.31, for these values there is a good match between the simulation and experimental results.*

Remark 6.11: *It is worth mentioning that results presented in Fig. 6.28-6.29 and Fig. 6.31 indicate that the proposed integral LOS path following controller successfully steered the underwater snake robot towards and along the desired straight path, compensating for the unknown hydrodynamic disturbances by keeping a constant non-zero heading. This makes the control strategy presented in Section 6.2 applicable for motion planning of underwater snake robots under the influence of constant irrotational ocean currents and other ocean drift effects.*

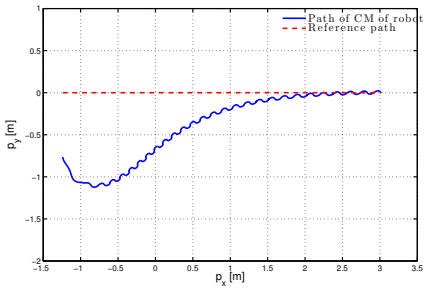

(a) Position of the CM of the robot

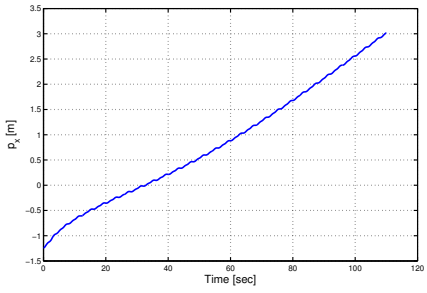

(b) Position along the path, p_x

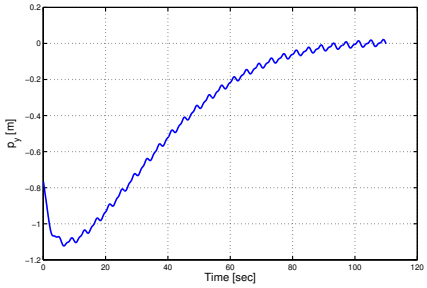

(c) Cross-track error, p_y

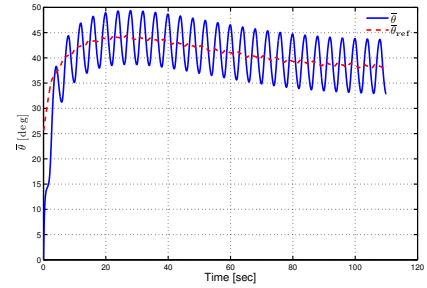

(d) Orientation of the robot

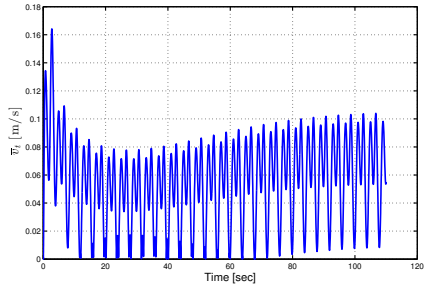

(e) Forward velocity, $\overline{v}_t$

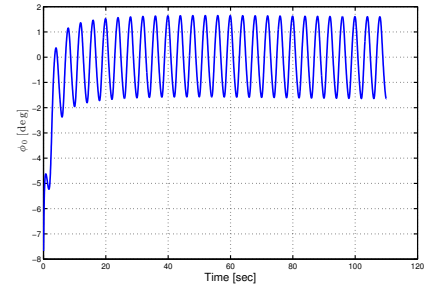

(f) Joint angle offset, ϕ_0

Figure 6.31: Simulation results for straight line path following with I-LOS guidance law for a snake robot with $n = 9$ links.

6.6 Waypoint Guidance Control of Underwater Snake Robots

In this section, we present a solution for path following control of underwater snake robots which combines the use of an artificial potential fields-based path planner with a new waypoint guidance strategy. A solution to the obstacle avoidance problem of an electric fish-like robot is presented in [119]. Another waypoint guidance strategy, where the waypoints are defined a priori, is proposed for a Carangiform swimmer in [49]. In addition, as opposed to [49] and [96] where the waypoints are chosen a priori, in this thesis the waypoints are derived using a path planner based on the artificial potential field method in order to also address the obstacle avoidance problems. Simulation results that illustrate the performance of the proposed guidance strategy both for lateral undulation and eel-like motions will be presented.

6.6.1 Artificial Potential Field (APF)

In this subsection, the artificial potential field (APF) method is applied to the obstacle avoidance problem of an underwater snake robot. The design of the path is an important step for the control of the robot. The objective is to determine the optimal path that should be followed in order to reach the goal of the mission while avoiding obstacles. Generally, path planners are divided into two categories; local path planners and global path planners [8]. In this thesis the artificial potential field method, which is introduced by [84], is used to derive the path for the underwater snake robot. In APF the robot moves in an area with a potential created by the obstacles and the target [8, 84]. The obstacles repel the robot, while the target attracts it. The potential functions are chosen so that the target position is a global minimum while the obstacles are maxima of the function. Denoting the repulsive potential from the ith obstacle by U_r^i, $i \in \{1, \cdots, o\}$, where o is the number of the obstacles, and the attractive potential from the goal position by U_a, the potential of the area can be expressed as [8]

$$U = U_a + \sum_{i=1}^{o} U_r^i. \tag{6.17}$$

It should be noted that, generally, in APF theory the obstacles are considered as points, without specific volume. However, it is obvious that the volume of the obstacles and the volume of the robot should be considered in order to derive the function for the potential. In this thesis, we follow a similar approach as described in [8], where the volume of the obstacles and the robot is set as the volume of a circle around the obstacles. Hence, the repulsive potential function is defined as [84]

$$U_r^i = K_{\text{rep}} \frac{1}{{d_o^i}^N - a_r^{N_o}}, \tag{6.18}$$

where K_{rep} is a positive gain constant which determines the intensity of the attractive potential, the parameter d_o^i denotes the distance to the ith obstacle, and a_r is the radius of the circle around the obstacle taking into account also the dimensions

of the robot. The radius of the circle that takes into account the dimension of the robot should be at least twice the amplitude of the sinusoidal motion of the robot. The parameter N_o is chosen equal to 2 and K_{rep} is chosen close to 1 in order to take into account only the local influence of the repulsive potential. The attractive potential function is defined as [84]

$$U_a = -K_{\text{att}} \frac{1}{d^{N_o}}, \tag{6.19}$$

where K_{att} is a positive gain constant which determines the intensity of the attractive potential, the parameter d denotes the distance to the goal and N_o is chosen equal to 2 in this study. It is worth to mention that increasing the parameter N_o will lead to a steeper curve of the attractive potential function. A gradient-based optimization method is used to derive the path [8]. In addition, we decide to increase the radius of the circle around the robot with a small value, in order to take into account the joint constraints of the robot, cf. [84]. When following the resulting path, the robot is moving towards the global minimum of the potential function (6.17). A simulation result of the described motion planning method is presented below for a space (8m $\times$ 8m) with obstacles (obstacle positions : $\{(1,1)\ (3,-2)\ (1,4)\ (4,2)\ (4,5)\}$) and a selected target (target position: $(7,5)$). The obstacles are rectangular shapes with dimensions (0.3×0.21). The simulation results are performed with the parameter $K_{\text{rep}} = 1$ giving the radius of the circumscribed circle around the obstacles and $K_{\text{att}} = 200$. Fig. 6.32(a) shows the described scenario, while in Fig. 6.32(b) the resulting potential is shown. Fig. 6.32(c) shows the resulting path that is created based on the obstacles and target scenario presented in Fig. 6.32(a).

Remark 6.12: *It should be noted that the disadvantage of this method is that there is a risk that the robot in some cases can be stuck at a local minimum. This problem can be solved using harmonic potential field as presented in [8], but in this thesis the typical non-harmonic potential method is chosen to avoid adding more complexity in our system.*

6.6.2 The Waypoint Guidance strategy

Future applications of snake robots will generally involve motion in challenging and unstructured environments [101]. It is worth to note that compared to traditional snake robots the underwater snake robots have the advantage of adaptability to aquatic environments. The most recent fields of interest include the integration of snake robots into underwater exploration, monitoring, and surveillance [69]. This brings the need for steering the robot to a specific target location(s) avoiding obstacles in the plane of motion. In these situations, it is generally less important to follow an exact curved path as long as the robot reaches the target(s) within a reasonable amount of time, avoiding obstacles in the environment. Waypoint Guidance (WPG) is the most widely used scheme in the field of autonomous underwater vehicles (AUVs) (see e.g. [38]), but has not been considered for motion control of underwater snake robots. It was shown in [96] how waypoint guidance can be used for ground snake robots, and based on these results we here propose a waypoint

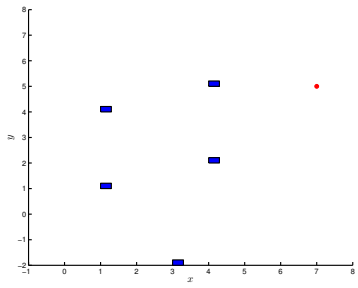

(a) Space with obstacles and target

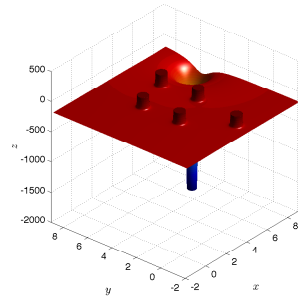

(b) The potential of the defined space

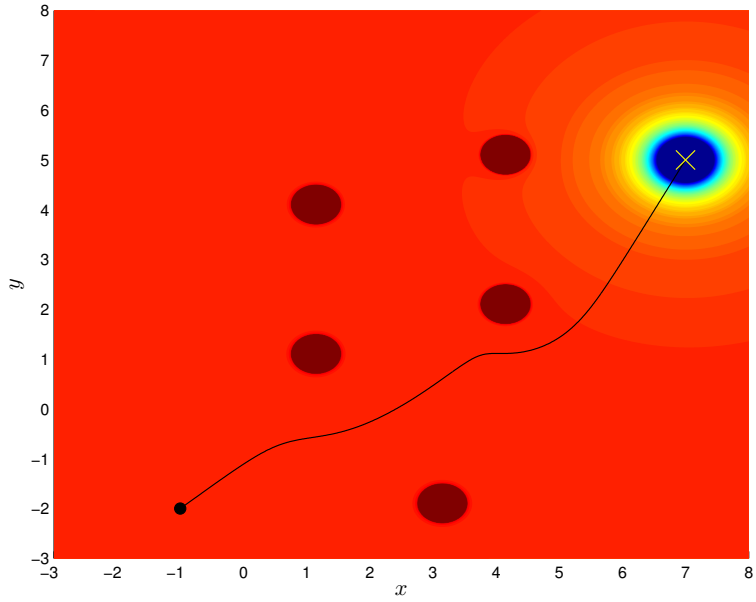

(c) Potential of the space and the derived path

Figure 6.32: Derived path for obstacle avoidance purposes using APF.

guidance strategy for underwater snake robots. The first version of the desired path is derived by the AFP as described in previous subsection.

Waypoint guidance can then be achieved between the start and end points of this path, $[x_d(t_o), y_d(t_o)]$ and $[x_d(t_f), y_d(t_f)]$, by splitting the path between the points into a number of waypoints $[x_d(k), y_d(k)]$ for $k = 1, 2, \cdots, N_w$, with N_w being the number of the waypoints. The waypoint guidance system switches from one waypoint to the next when the underwater snake robot reaches the vicinity of the current waypoint, i.e. when it comes within a circle of acceptance with radius r_{accept} of the current waypoint $[x_d(k), y_d(k)]$ (see e.g. [38]). The circle of acceptance is typically chosen as two times the length of the vehicle [38]. Note that the distance between the waypoints on the path derived by the path planner using APF should be sufficiently small in order to keep the straight line path approximation as close to the original path that the collision avoidance properties are kept. A disadvantage of the waypoint guidance method is that undesirable control energy consumption due to overshoot can occur during the change from one straight line path to the next. Therefore, selection of the reference path to follow is important to reduce the overshoot width of path and thus to decrease the control energy consumption. [140] employs turning simulations to determine modified waypoints to avoid overshoot. Waypoint guidance, and specifically LOS guidance is a key feature in the majority of guidance systems for marine vehicles [38], and we believe that this is a promising approach also for swimming snake robots.

In this thesis, an acceptance region is used, instead of the common approach of acceptance circle (see e.g. [96]). By this definition, it is guaranteed that the robot will reach the acceptance region of the current waypoint no matter how the waypoints are defined. The reason is that using an acceptance circle instead gives the risk that the robot misses a waypoint which is placed too close to the previous waypoint. A straight-line path following controller presented in Section 6.1 will be applied in order to steer the robot to the desired straight line path. The straight line defined as connections between the waypoints. As it is already mentioned, the path following control objective that is considered for the underwater snake robot is to make the robot converge to the desired straight line path and subsequently progress along the path at some nonzero forward velocity.

6.6.3 Simulation Study: Waypoint Guidance

This section presents simulation results in order to investigate the performance of the proposed waypoint guidance strategy for underwater snake robots. The dynamics was calculated using the *ode23tb* solver in *Matlab R2013b* with a relative and absolute error tolerance of 10^{-4}.

Implementation of guidance strategy

The efficacy of the proposed scheme has been examined through two different simulation studies; case 1 – the waypoint guidance strategy for a priori defined points and case 2 – the waypoint guidance strategy with obstacle avoidance. An underwater snake robot was considered with $n = 10$ links, each one having length $2l = 0.14$ m and mass $m = 0.6597$ kg. The initial values of all states of the robot

were set to zero for case 1, while the value for the initial position of the CM is selected as $p_{\mathrm{CM}}(0) = [-1, -2]$ in case 2. The hydrodynamic related parameters are set to $c_t = 0.2639$, $c_n = 8.4$, $\mu_n = 0.3958$, $\lambda_1 = 2.298810^{-7}$, $\lambda_2 = 4.310310^{-4}$ and $\lambda_3 = 2.262910^{-5}$ as discussed in Section 2.2. We do not take into account currents in the simulation, as handling currents will be a topic of future work. In addition, the radius of the acceptance circle (i.e. acceptance circle being a subset of the acceptance region) enclosing each waypoint is $r_{accept} = 0.8$. The joint PD controller (3.5) is used for each joint with parameters $k_p = 20$, $k_d = 5$, and lateral undulation or eel-like motion are achieved by moving the joints according to (3.1) or (3.2), respectively, with gait parameters $a = 30^{\mathrm{o}}$, $\delta = 40^{\mathrm{o}}$ and $\omega = 150^{\mathrm{o}}/\mathrm{s}$. Furthermore, the parameter $k_\theta = 0.3$ and the parameter $\Delta = 1.4$ m.

Simulation Results

The efficacy of the straight line path following controller is investigated via both simulation and experimental results in Section 6.4. In addition to this, in Fig. 6.33, we show that the joint angles converge exponentially to their reference values both for lateral undulation and eel-like motion patterns. Now, we will present simulation results for the two cases as mentioned at the beginning of this section.

Case 1– *The waypoint guidance strategy for a priori defined waypoints:* The proposed guidance strategy is then tested when having chosen a set of waypoints a priori. The chosen waypoints in global frame coordinates are (0 0), (3 0), (6 3), (6 8) and (0 8), respectively. The heading of the robot is presented in the Fig. 6.34(a)-6.35(a) and Fig. 6.34(b)-6.35(b) show the cross-track error. From Fig. 6.34(c)-6.35(c), we see that the robot achieves a smooth path towards each waypoint, and from Fig. 6.34(a)-6.35(a), we can see that the robot is able to follow the direction of the desired path. Fig. 6.34(b)-6.35(b) show the transient behavior discussed in Section 6.1, and show that the cross-track error oscillates around zero after each waypoint switching both for lateral undulation and eel-like motion, respectively. Fig. 6.34(c)-6.35(c) show the motion of the CM of the underwater snake robot.

Case 2– *The waypoint guidance strategy for obstacle avoidance using APF:* Finally, the proposed control strategy is tested in the case of an obstacle avoidance scenario. The heading of the robot is presented in the Fig. 6.36(a)-6.39(a). It may be noted that the cross-track error does not converge to zero (Figs 6.36(b)-6.39(b)) in all cases, because the waypoints are really close to each other, so there is not enough time to achieve zero convergence. In Fig. 6.36(c)-6.39(c), we can see that the robot manages to follow the desired path, derived using artificial potential field for obstacle avoidance purposes. As we can see from Fig. 6.36(b)-6.39(b), with larger subsampling step, we achieve better convergence results in cross-track error. This illustrates that a larger step in the subsampling process can give better results in cross-track error, but as the step is chosen larger the deviation between the original path and the straight line path becomes larger, and thus the risk for the robot to collide with an object increases. The important point is that, even if the cross-track error does not converge exactly to zero, the heading of the robot oscillates around zero (Fig. 6.36(a)-6.39(a)) and the robot manages to follow, with almost zero error, the desired path without colliding with any obstacle.

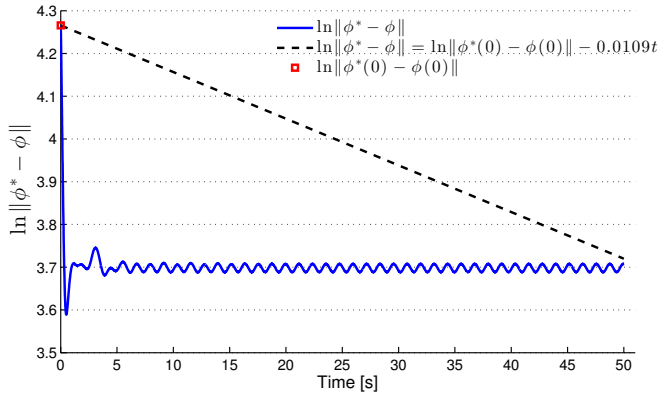

(a) Lateral Undulation

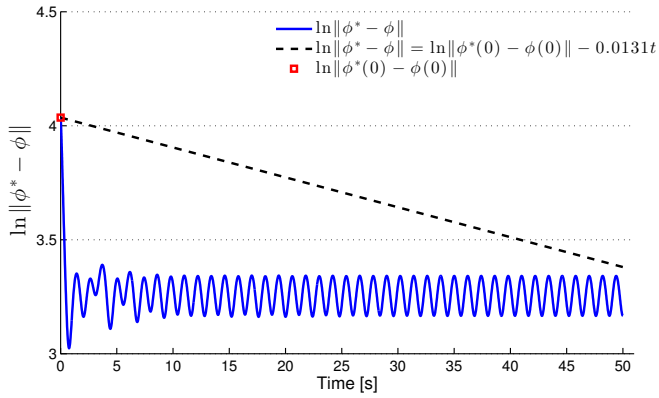

(b) Eel-like motion

Figure 6.33: Convergence of joint angles.

6.7 Chapter Summary

This chapter is summarized as follows:

- We have proposed a path following controller that enables the underwater snake robot to converge to straight line paths. The LOS guidance law is combined with a directional controller to steer the robot to the path.
- We have investigated the performance of the LOS path following controller through simulations and through experiments with the underwater snake robot Mamba, where it was shown that the proposed control strategy successfully steers the robot towards and along the desired path both for lateral undulation and eel-like motion patterns.
- Fluid parameter identification has been performed and simulation results

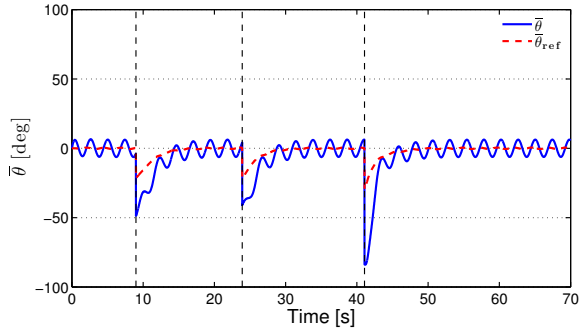

(a) Heading angle, $\bar{\theta}$

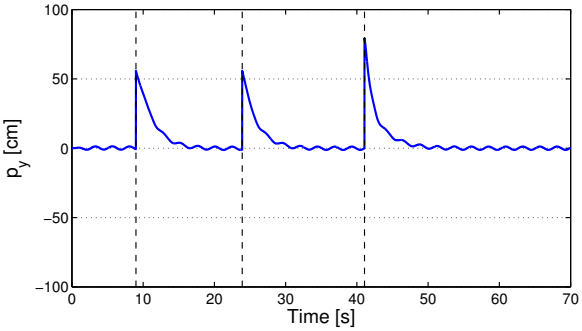

(b) Cross track error, p_y

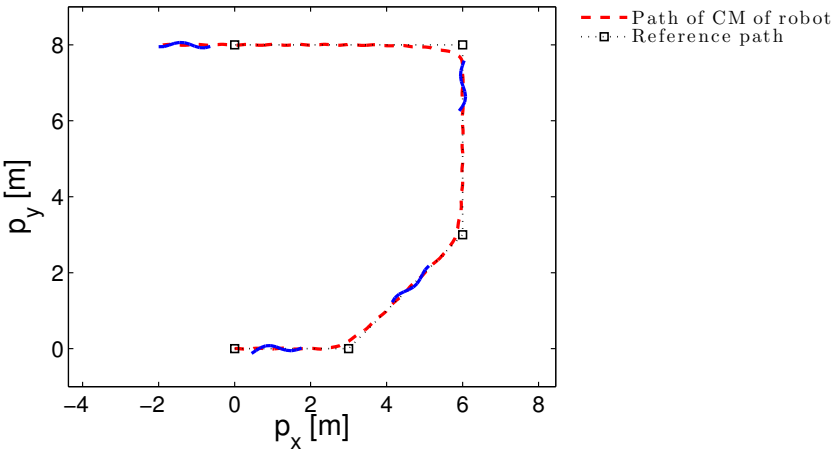

(c) Path of the robot

Figure 6.34: Path following of underwater snake robot during waypoint guidance for lateral undulation.

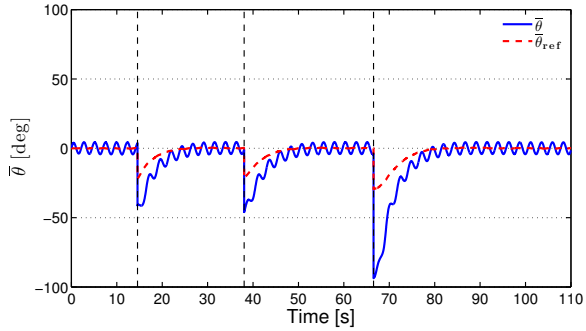

(a) Heading angle, $\bar{\theta}$

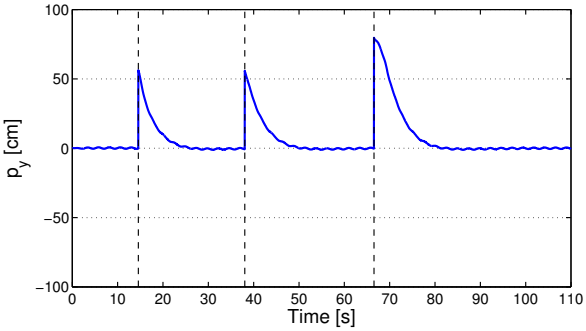

(b) Cross track error, p_y

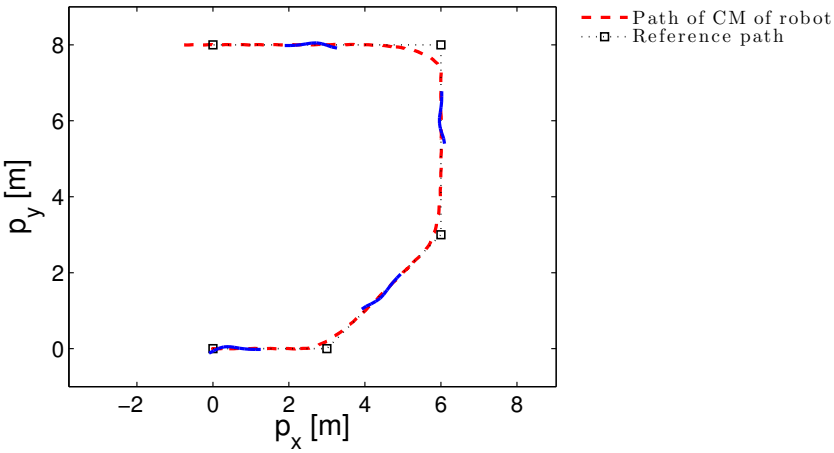

(c) Path of the robot

Figure 6.35: Path following of underwater snake robot during waypoint guidance for eel-like motion.

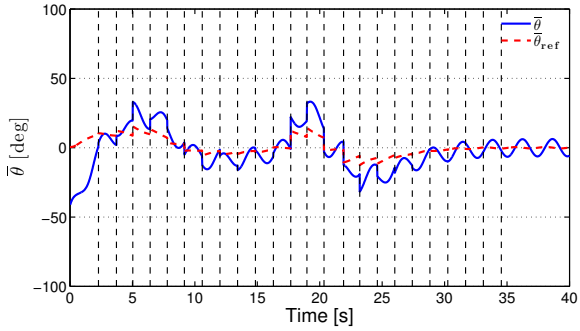

(a) Heading angle, $\bar{\theta}$

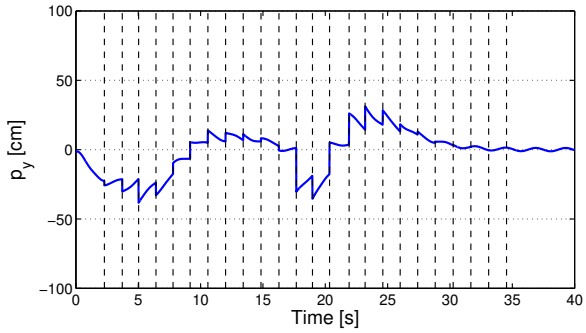

(b) Cross track error, p_y

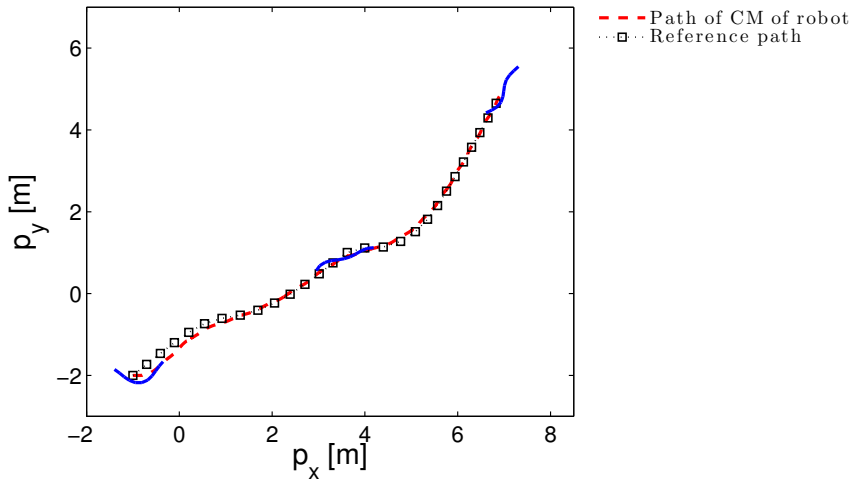

(c) Path of the robot

Figure 6.36: Path following of underwater snake robot during waypoint guidance for obstacle avoidance for lateral undulation: subsampling every 40 points –waypoints distance approximately 0.4 m.

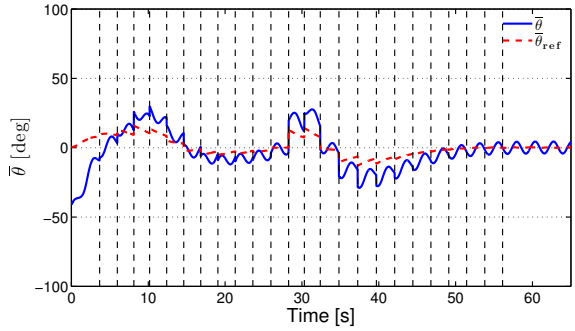

(a) Heading angle, $\bar{\theta}$

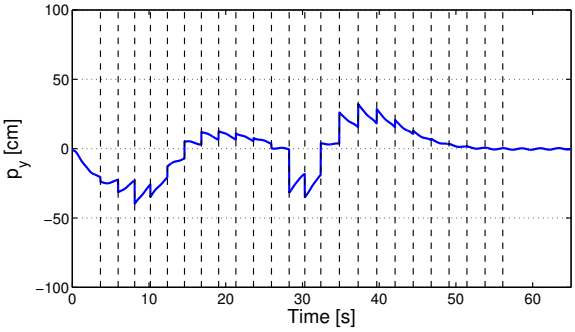

(b) Cross track error, p_y

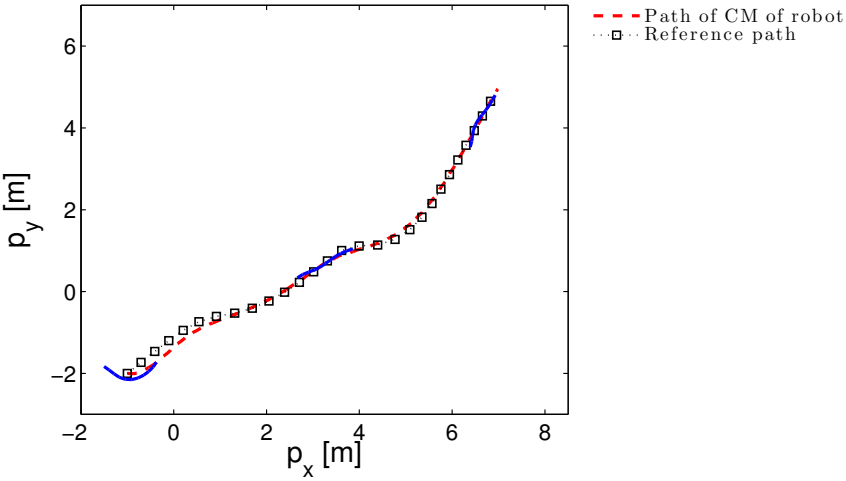

(c) Path of the robot

Figure 6.37: Path following of underwater snake robot during waypoint guidance for obstacle avoidance for eel-like motion: subsampling every 40 points –waypoints distance approximately 0.4 m.

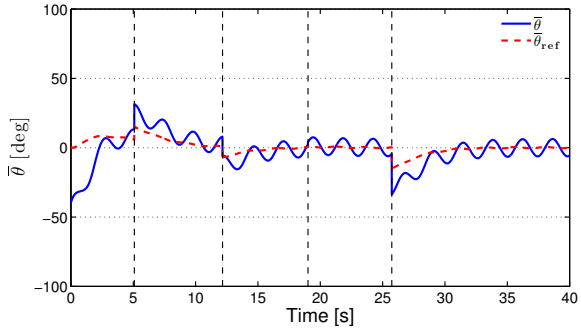

(a) Heading angle, $\bar{\theta}$

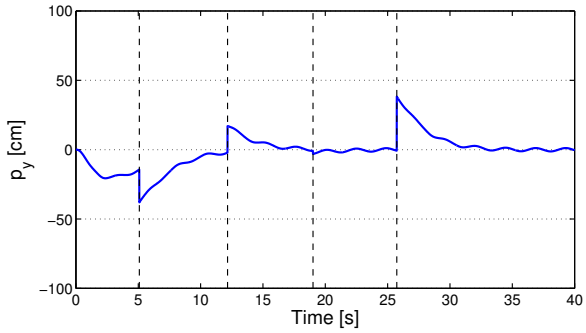

(b) Cross track error, p_y

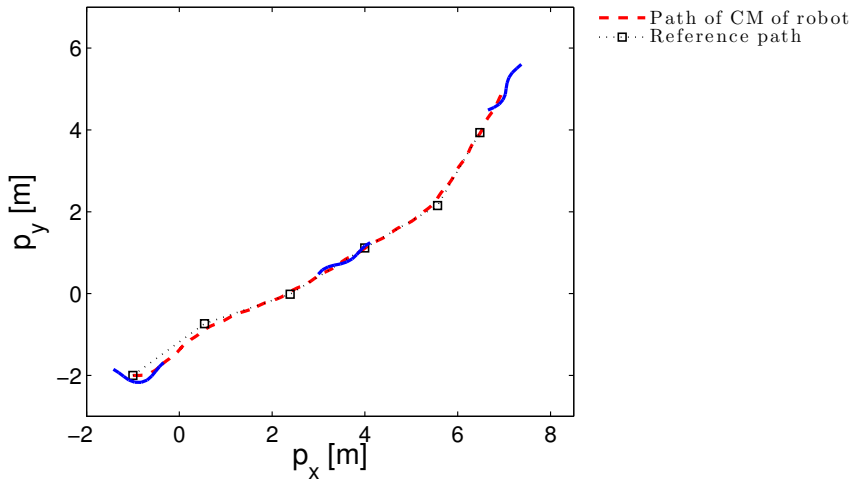

(c) Path of the robot

Figure 6.38: Path following of underwater snake robot during waypoint guidance for obstacle avoidance for lateral undulation: subsampling every 200 points–waypoints distance approximately 2 m.

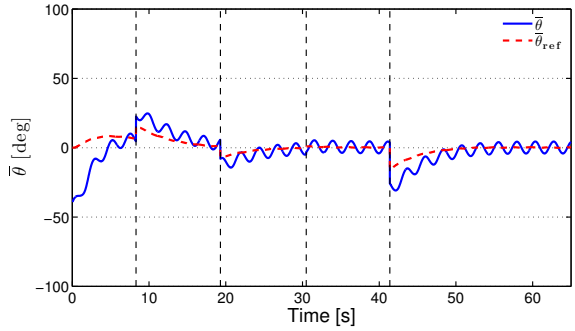

(a) Heading angle, $\bar{\theta}$

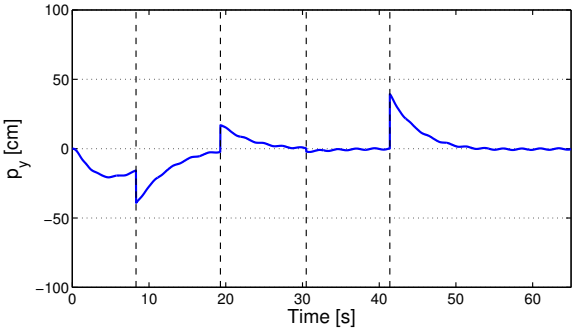

(b) Cross track error, p_y

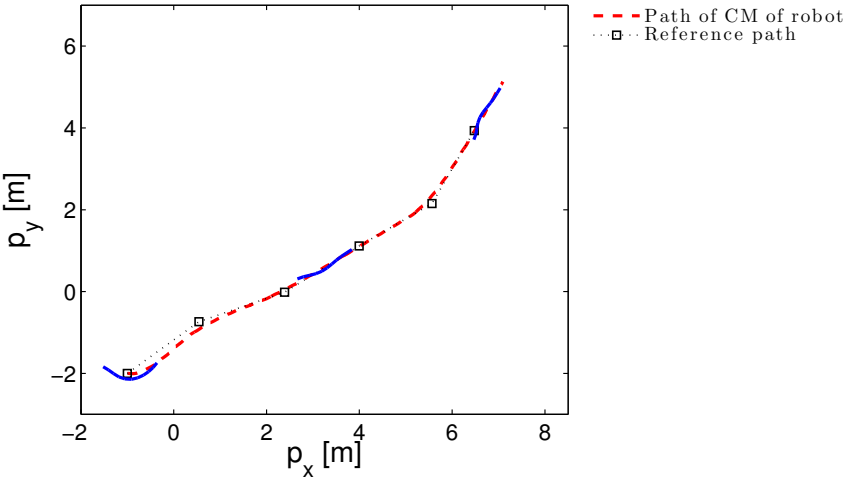

(c) Path of the robot

Figure 6.39: Path following of underwater snake robot during waypoint guidance for obstacle avoidance for eel-like motion: subsampling every 200 points–waypoints distance approximately 2 m.

based on the identified fluid coefficients are presented to obtain a back-to-back comparison with the motion of the physical robot during the experiments for the LOS path following control approach.

- We have proposed a straight line path following controller for underwater snake robots in the presence of constant irrotational currents of unknown direction and magnitude. The integral LOS guidance law is combined with a directional controller to steer the robot to the path, where the integral action in the guidance law produces a constant side-slip angle that allows the control system to compensate for the ocean current effect.
- We have analyzed the stability of the locomotion along the straight line path in the presence of current. By use of a Poincaré map, we have shown that all state variables of an underwater snake robot, except the position along the forward direction, trace out an exponentially stable periodic orbit when the I-LOS path following controller is applied.
- We have presented simulation and experimental results showing that the proposed I-LOS path following controller successfully steered the underwater snake robot towards and along the desired straight path, compensating the effects of currents. From the experimental results, it is shown that the underwater snake robot Mamba managed to orient itself and maintain a constant non-zero heading to compensate for the effect of the current forces.
- We have proposed a waypoint guidance control strategy for underwater snake robot along a path that was derived based on APF techniques in order to achieve collision free paths.
- We have presented simulation results illustrating the successful integration of the aforementioned strategy.

Chapter 7

Energy Efficiency of Underwater Snake Robots

Underwater snake robots provide a bio-inspired solution within underwater robotics. The long and slender structure of the robot provides superior capabilities for access through narrow openings and within confined areas. This is interesting for inspection and monitoring operations, for instance for subsea oil and gas installations and for marine archaeology. At the same time, a swimming snake robot carries manipulation capabilities as an inherent part of its body since it is essentially a mobile manipulator arm. Furthermore, bioinspired locomotion through oscillatory gaits, like lateral undulation and eel-like motion, is interesting from an energy efficiency point of view. To realize operational snake robots for such underwater applications, a number of different control design challenges must first be solved. An important control problem concerns the ability to achieve efficient motion with preferably a minimum amount of consumed energy in order to be able to undertake longer missions, and this is the topic of this chapter. Increasing the motion efficiency in terms of the achieved forward speed by improving the locomotion methods is a key issue for underwater robots. Furthermore, the energy efficiency is one of the main challenges for long-term autonomy of these systems. In this chapter, we will consider both these two aspects of efficiency. To this end, this chapter presents and experimentally investigates several fundamental properties of the velocity and the power consumption of an underwater snake robot both for lateral undulation and eel-like motion patterns. In particular, we investigate the relationship between the parameters of the gait patterns and the forward velocity for the different motion patterns for underwater snake robots. In addition, we compare the energy efficiency of underwater snake robots, which can provide both inspection and intervention capabilities and are thus interesting candidates for the next generation inspection and intervention AUVs, with those of the widely used robots for subsea operations which are the remotely operated vehicles (ROVs).

Note that in some cases these two aspects of efficiency can be conflicting. To this end, in this chapter we formulate a multi-objective optimization problem to minimize power consumption and maximize forward velocity. In particular, the optimal values of the gait parameters for the different motion patterns are calcu-

lated in the presence of trade-offs between power consumption and velocity. We present a weighted-sum method to combine power consumption and forward velocity optimization problems. Particle Swarm Optimization (PSO) is applied to obtain optimal gait parameters for different weighting factors. *Trade-off curves* or *Pareto fronts* are illustrated in a power consumption–forward velocity plane both for lateral and eel-like motion pattern. They give information on objective trade-offs and can show how improving power consumption is related to deteriorating the forward velocity along the trade-off curve.

Contributions of this Chapter: The first contribution of this chapter is the investigation of the issues that influence the performance of underwater snake robots, both when it comes to the achieved forward velocity (moving performance) and the energy efficiency (transportation performance). Based on the model of the underwater snake robot presented in Section 2.2, we present in this chapter simulation results in order to investigate the relationships between the parameters of the gait patterns, the consumed energy and the forward velocity for the different motion patterns for underwater snake robots. We initially present simulation result by investigating the power consumption of different motion patterns for underwater snake robots. Based on the results of this investigation, we present empirical rules to choose the values for the parameters of the motion gait pattern of underwater snake robots.

The second contribution of this chapter is to investigate the power consumption of different underwater robotic systems and pointing out the most efficient vehicle depending on the desired motion. In particular, we present simulation results in order to compare the power consumption of swimming snake robots with that of today's benchmark solution for subsea inspection, maintenance and repair, which are ROVs, and comparison results are thus obtained for the power consumption of underwater snake robots and ROVs. In this chapter, the energy index [123], is used in order to compare the energy efficiency of underwater snake robots compared with the widely used remotely operated vehicles. Comparison results are obtained for the total energy consumption and the cost of transportation of underwater snake robots and ROVs. The simulation results show that, with respect to the cost of transportation metric and the total consumed energy the underwater snake robots are more energy efficient for all the compared motion modes. To our best knowledge, a comparison of the consumed energy between underwater swimming snake robots and remotely operated vehicles have not been investigated in previous literature.

The third contribution of this chapter is the experimental investigation of properties presented in Proposition 7.1-7.2 regarding the relationship between the gait parameters and the power consumption for underwater snake robots. In particular, this chapter investigates the validity of the properties through experiments using the underwater snake robot Mamba. The experimental results support the empirical rules regarding the relationship between the gait parameters and the power consumption both for lateral undulation and eel-like motion patterns. To our knowledge, no research has been published investigating experimentally the power consumption of underwater

snake robots.

Finally, in this chapter, based on the complex model presented in Section 2.2, a multi-objective optimization problem is developed with the aim of maximizing the achieved forward velocity of the robot and minimizing the corresponding average power consumption of the system. As far as we know, investigation of efficient motion patterns by solving a multi-objective optimization problem has not been considered in previous literature. We therefore also consider the methodology of this chapter to be a contribution within the underwater snake robot literature. In particular, results are obtained for the two most common swimming patterns for underwater snake robot locomotion: lateral undulation and eel-like motion patterns. Furthermore, the proposed optimization framework is applied to obtain the parameters of the most efficient motion pattern, which can be used in the future for control and design of underwater snake robots.

Organization of this Chapter: This chapter is organized as follows. Section 7.1 presents the energy consumption analysis approach applied for underwater snake robots, while the energy consumption of ROVs is outlined in Section 7.2. Simulation results for the power consumption of underwater snake robots are presented in Section 7.3, followed by comparison simulation results regarding the energy consumption between underwater snake robots and ROVs in Section 7.4. Section 7.5 presents simulation and experimental results regarding the power consumption of underwater snake robots both for lateral undulation and eel-like motion patterns. The multi-objective optimization framework, followed by results obtained for an underwater snake robot are presented in Section 7.6. Finally, the chapter is summarized in Section 7.7.

Publications: The material in this chapter is based on the journal paper [72] and the conference papers [71], [74] and [75].

7.1 Energy Consumption of Underwater Snake Robots

In this section, we present the energy consumption analysis approach that is applied for underwater snake robots. In addition, we present a cost of transportation metric that makes it possible to obtain comparison results of the consumed energy for different systems (e.g. underwater snake robots with different number of links and mass, remotely operated vehicles (ROVs), etc.).

7.1.1 Energetics of underwater snake robots

For underwater snake robots, the propulsion is generated by the motion of the joints and its interaction with the surrounding fluid. The actuator torque input to the joints is thus transformed into a combination of joint motion and energy that is dissipated by the fluid. We assume that we have perfect joints and thus that the total amount of energy of the system (E_{s}) generated by this input is the sum of kinetic energy (E_{kinetic}) and the energy that is dissipated to the surrounding fluid (E_{fluid}) [135], [123]. The sum of these two is thus the total energy that is spent for

the propulsion of the robot:

$$E_{\mathrm{s}} = E_{\mathrm{kinetic}} + E_{\mathrm{fluid}} \tag{7.1}$$

where E_{s} is given by

$$E_{\mathrm{s}} = \int_0^T \left(\sum_{i=1}^{n-1} u_i(t)\dot{\phi}_i(t) \right) dt. \tag{7.2}$$

T is the time that corresponds to a complete swimming cycle, u_i is the actuation torque of joint i given by (3.5) and $\dot{\phi}_i$ is the joint's angular velocity defined as $\dot{\phi}_i = \dot{\theta}_i - \dot{\theta}_{i-1}$.

For a complete swimming cycle, T, the averaged power consumption, P_{avg}, is calculated as follows

$$P_{\mathrm{avg}} = \frac{1}{T} \int_0^T \left(\sum_{i=1}^{n-1} u_i(t)\dot{\phi}_i(t) \right) dt. \tag{7.3}$$

7.1.2 Efficient Motion

For underwater applications, it is important to find an optimum combination of different underwater vehicles or different motion modes, which lead to the lowest energy consumption. To compare the energy consumption of different vehicles, we need a suitable basis for comparison. In this thesis, in order to compare vehicles with different dimensions and characteristics, a dimensionless quantity is used. Generally, the energy index (cost of transportation) quantifies the energy efficiency of a vehicle, or of a robotic system in our case, from one place to another. The cost of transportation has been used in a wide range of applications in order to define the most energy efficient motion of different systems [123]. In this chapter, the cost of transportation is defined as

$$COT = \frac{\text{Energy}}{\text{Mass} \times g \times \text{Distance}}. \tag{7.4}$$

Cost of transportation is non-dimensional and it quantifies how much energy is applied to a system of a specified mass in order to move the system a defined distance (the ratio between the consumed energy and the transferred weight times the covered distance). Using the energy index approach, the vehicle is operated without taking into account the kind of propulsion system that is implemented inside. This coefficient is useful for the comparison of different types of transportation, since it gives an indication of the required power to a system and the effective power. A similar approach is used in order to indicate the relationship between the mechanical index and the energy index of different transformation modes for ships in [123]. In particular, the purpose of the case study in [123] was to investigate the issues that could influence both the moving performance and the transportation performance of ships. In this chapter, we will use the energy index in order to investigate the energy efficiency of underwater snake robots with different links and to obtain comparison results for the energy consumption between underwater snake robots and ROVs.

7.2 Energy Consumption of Remotely Operated Vehicles

In this section, we present the energy consumption analysis approach that is applied for remotely operated vehicles (ROVs). In addition, the kinematics and dynamics of a remotely operated vehicle (ROV) are discussed.

7.2.1 Dynamic Model of Remotely Operated Vehicle

We now briefly present a model of the kinematics and dynamics of a remotely operated vehicle (ROV). A more detailed presentation of the model can be found in [38]. The dynamics of ROVs are highly nonlinear due to the coupling of the rigid body dynamics and the hydrodynamic forces on the vehicle. The equation of motion of a remotely operated vehicle can be written as

$$\mathbf{M}_{\mathrm{r}}\ddot{\mathbf{q}} + \mathbf{C}_{\mathrm{r}}(\dot{\mathbf{q}})\dot{\mathbf{q}} + \mathbf{D}_{\mathrm{r}}(\dot{\mathbf{q}})\dot{\mathbf{q}} + g(\mathbf{x}_{\mathrm{r}}) = \boldsymbol{\tau}_{\mathrm{r}}, \tag{7.5}$$

$$\dot{\mathbf{x}}_{\mathrm{r}} = \mathbf{J}_r(\mathbf{x}_{\mathrm{r}})\dot{\mathbf{q}}, \tag{7.6}$$

where $\boldsymbol{\tau}_{\mathrm{r}} \in \mathbb{R}^k$ is the vector of control forces and moments, $\mathbf{q} \in \mathbb{R}^k$ is a vector of virtual coordinates and $\dot{\mathbf{q}} = [u_r, \nu_r, w_r, p_r, q_r, r_r]^T$ is the body-fixed linear and angular velocity vector. The earth-fixed position and angle vector is defined as $\mathbf{x}_{\mathrm{r}} = [x_r, y_r, z_r, \phi_r, \theta_r, \psi_r]^T \in \mathbb{R}^k$. $\mathbf{M}_{\mathrm{r}}$ is a $k \times k$ system inertia matrix, $\mathbf{C}_{\mathrm{r}}(\dot{\mathbf{q}})$ is a $k \times k$ matrix of centrifugal and Coriolis terms, $\mathbf{D}_{\mathrm{r}}(\dot{\mathbf{q}})$ is a $k \times k$ matrix of hydrodynamic damping terms, $g(\mathbf{x}_{\mathrm{r}})$ is a $k \times 1$ vector including restoring forces and moments and $\mathbf{J}_r(\mathbf{x}_{\mathrm{r}})$ is a $k \times k$ kinematic transformation matrix, which is a function of the angles ϕ_r, θ_r, ψ_r. A more detailed presentation of these terms are given in [38].

7.2.2 Energetics of Remotely Operated Vehicles

Similarly to the underwater snake robots, the total amount of energy of ROVs (E_{total}) is the sum of kinetic energy (E_{kinetic}) and the energy that is dissipated to the surrounding fluid (E_{fluid}). For an ROV the power is the input to the system that is generated through the actuator forces and torques applied to the system. The total amount of the energy that is spent for the propulsion of the vehicle is given by

$$E_{\mathrm{r}} = \int_0^{T_{\mathrm{r}}} \boldsymbol{\tau}_{\mathrm{r}}(t)\dot{\mathbf{q}}(t)\, dt, \tag{7.7}$$

where T_{r} is the a complete time to achieve a specified motion. In addition, the average power consumption for ROVs, P^r_{avg}, is given by the following expression

$$P^r_{\mathrm{avg}} = \frac{1}{T_r}\int_0^{T_{\mathrm{r}}} \boldsymbol{\tau}_{\mathrm{r}}(t)\dot{\mathbf{q}}(t)\, dt. \tag{7.8}$$

7.3 Simulation Study for Underwater Snake Robots

In this section, simulation results are presented for underwater snake robots model derived in Section 2.2 moving a distance of 4 m both for lateral undulation and eel-like motion patterns. Note that these results are derived for zero current velocity, since the current effects have not been considered in this chapter. The models were implemented in *Matlab R2013b*. The dynamics was calculated using the *ode23tb* solver with a relative and absolute error tolerance of 10^{-4}.

7.3.1 Simulation parameters

We consider snake robots with respectively $n = 5$, $n = 10$, $n = 20$ links, each one having length $2l = 2 \times 0.14$ m. The mass of each link is $m = 0.6597$ kg and is chosen so to fulfil the neutrally buoyant assumption. The initial values of the states of the snake robot were set to initial reference values at $t = 0$ with its heading along the inertial x axis. The hydrodynamic parameters are $c_t = 0.2639$, $c_n = 8.4$, $\mu_n = 0.3958$, $\lambda_1 = 2.298810^{-7}$, $\lambda_2 = 4.310310^{-4}$ and $\lambda_3 = 2.262910^{-5}$. The joint PD controller (3.5) is used for each joint with parameters $k_p = 200$, $k_d = 5$, and lateral undulation and eel-like motion are achieved by choosing (3.1) and (3.2), respectively. The gait pattern parameters are presented in each simulation result.

7.3.2 Simulation results

Simulation results are presented for lateral undulation and eel-like motion pattern for the underwater snake robots of different lengths. In particular, simulation results for the forward velocity $\bar{v}_t$, the averaged power consumption, P_{avg}, and the cost of transportation for a constant amplitude $\alpha = 20^o$ are presented for lateral undulation and eel-like motion in Fig. 7.1-7.2 and Fig. 7.3-7.4, respectively. Fig. 7.1 and Fig. 7.3 show that by increasing the phase shift δ there is an increase of the forward velocity until a value of δ_{max} where the system reaches the maximum velocity. After this value, an additional increase of this parameter causes a decrease in the forward velocity. It is worth noting that, for different values of ω, the forward velocity has a similar behavior, and that δ_{max} is approximately the same for all values of omega. In addition, we see that for different number of links, n, the value of δ_{max} is not the same. Increasing the number of the links, we see that δ_{max} decreases, and also that the maximum velocity reached at δ_{max} increases. The δ_{max} values for $n = 5$, $n = 10$ and $n = 20$ links are $\delta_{max} = 30^o$, $\delta_{max} = 20^o$ and $\delta_{max} = 20^o$ respectively, for lateral undulation (Fig. 7.1) and $\delta_{max} = 40^o$, $\delta_{max} = 20^o$ and $\delta_{max} = 10^o$ for eel-like motion (Fig. 7.3), for almost all values of ω except the very high frequency values. Note that for $n = 10$ and $n = 20$ links the maximum phase shift δ_{max} has the same value (Fig. 7.1), which shows that for $n > 10$, we can choose $\delta_{max} = 20^o$ in order to reach the maximum forward velocity.

From Fig. 7.2(a) and Fig. 7.4(a), we see that the average power consumption is decreasing by increasing δ, while also the cost of transportation is decreasing (Fig. 7.2(b) and Fig. 7.4(b)) both for lateral undulation and eel-like motion patterns. In addition, we can see that for δ_{max}, which makes the robot reach the maximum velocity, an additional increment of the δ does not significantly affect the cost of

transportation, in particular for the longer snake robots. Furthermore, Fig. 7.2(a) and Fig. 7.2(b) show that the average power consumption increases and the motion of the system is less energy efficient when the frequency ω increases. Thus, we see that when choosing the parameter ω there is a trade-off between the maximum velocity on the one side and the power consumption and cost of transportation on the other. The discussion above indicates that for a constant value of the amplitude, a good choice of parameters is $\delta = \delta_{max}$. In particular, it is more efficient to make the compromise by choosing the values of δ and ω to reach a desired maximum speed of the robot while simultaneously we minimize the cost of transportation. In addition, we can easily conclude that smaller values than δ_{max} should not been considered since for these values the averaged power consumption is increased, the robot does not reach the maximum velocity, and the motion is less energy efficient. Furthermore, the frequency ω should be chosen as a trade-off between maximum forward velocity and power consumption.

Simulation results for the forward velocity $\bar{v}_t$, the averaged power consumption, P_{avg}, and the cost of transportation for a constant frequency $\omega = 70^o/\text{s}$ are presented for lateral undulation and eel-like motion in Fig. 7.5-7.6 and Fig. 7.7-7.8, respectively. From Fig. 7.5 and Fig. 7.7, we can see that increasing the amplitude parameter α the robots manage to move faster, and also that increasing the parameter α increases the average power consumption (Fig. 7.6(a) and Fig. 7.8(a)). Fig. 7.5 and Fig. 7.7 show that also keeping the frequency constant and varying the amplitude α, there exists a δ_{max} that gives a maximum forward velocity, and comparing Fig. (7.1,7.5) with Fig. (7.3,7.7) we see that the value of δ_{max} is the same for $\alpha > 20^o$. Fig. 7.6(b) and Fig. 7.8(b) show that both for lateral undulation and eel-like motion patterns, if we choose $\delta = \delta_{max}$ to get the maximum velocity then the cost of transportation is almost the same for all values of α. Hence, we can conclude that for a constant value of $\omega = 70^o/\text{s}$ and for $\delta = \delta_{max}$, we can choose the value of α in order to maximize the forward velocity of the robot and still keep the energy efficiency of the system.

In Fig. 7.9-7.10 and Fig. 7.11-7.12, simulation results for the forward velocity $\bar{v}_t$, the averaged power consumption, P_{avg}, and the cost of transportation for specified phase offset values $\delta = 35^o$, $\delta = 15^o$ and $\delta = 15^o$ for $n = 5$, $n = 10$ and $n = 20$ links, are presented for lateral undulation and eel-like motion, respectively. From Fig. 7.9 and Fig. 7.11, we can see that by increasing the parameter ω the forward velocity is increasing. In particular, the forward velocity is almost linearly increasing with the frequency ω for all different values of α. It is interesting to note, however, that the forward velocity increases with increasing amplitudes α for the short snake robot, while as the number of links increase, this is inversed such that for $n = 20$ links the forward velocity decreases with increasing amplitudes α. This show us that for a normal length snake robot of 10 links or more, we need to choose smaller values of the α to achieve the highest forward velocity of the system. Hence the forward velocity given a constant ω and a constant δ depends on the amplitude of the motion pattern and the number of the links. However, we can see that the average power consumption (Fig. 7.10(a) and Fig. 7.12(a)) increases when increasing the parameters α and ω. The cost of transportation presented in Fig. 7.10(b) and Fig. 7.12(b) for lateral undulation and eel-like motion show that the cost of transportation increases when increasing the parameter ω and by increasing

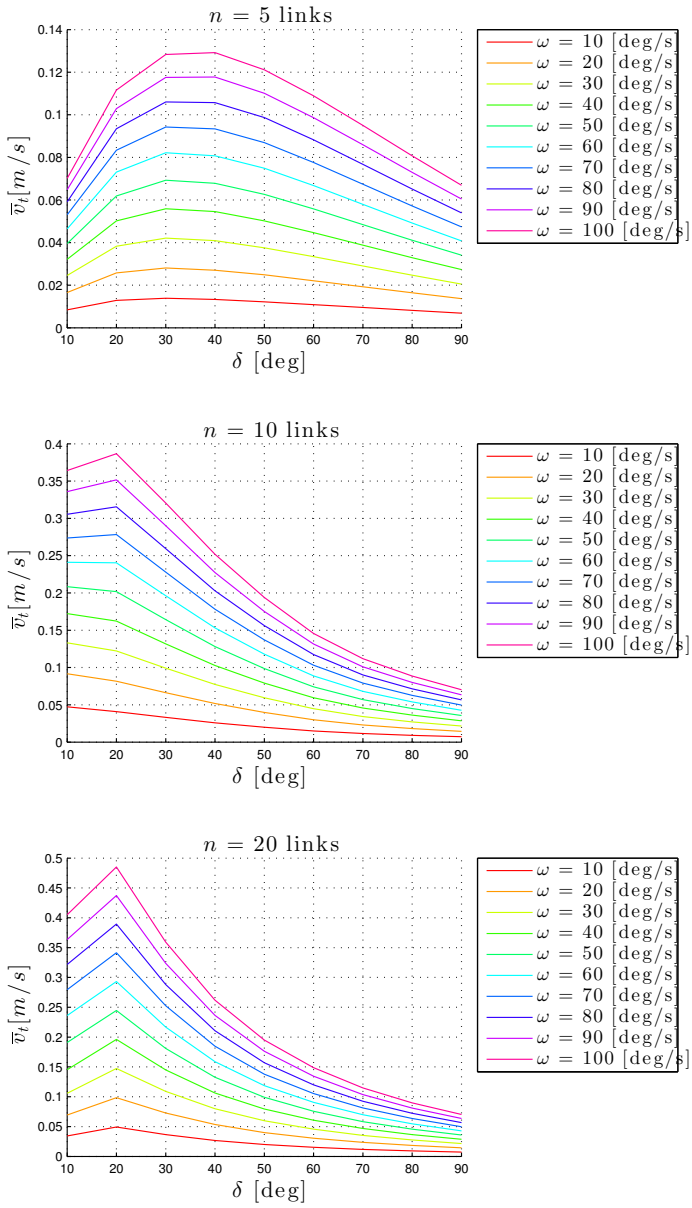

Figure 7.1: Forward velocity of underwater snake robot locomotion for lateral undulation motion pattern with constant amplitude $\alpha = 20^o$.

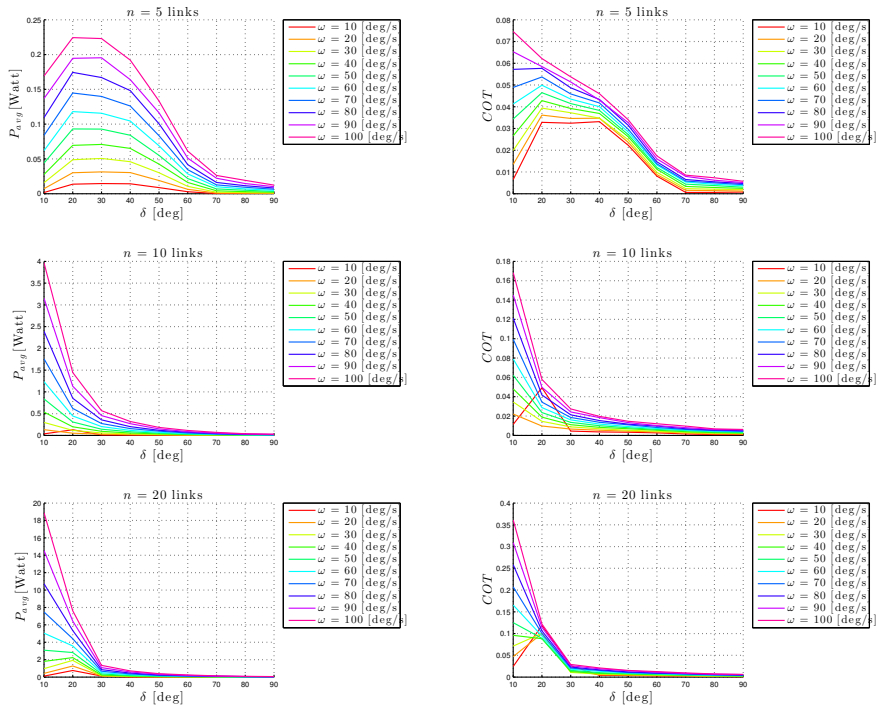

(a) Averaged power consumption (b) Cost of transportation

Figure 7.2: Simulation results for the lateral undulation motion pattern with constant amplitude $\alpha = 20^o$.

the amplitude α.

From Fig. 7.2(b)-7.12(b), we see that by increasing the number of the links the cost of transportation is increased both for lateral undulation and eel-like motion. This higher cost of transportation of underwater snake robots for high number of actuation points were expected since by increasing the number of the links we need $n-1$ servo motors for the joint actuation. In order to reduce the actuation points and thus increase the energy efficiency, the underwater swimming robots should adapt not only the shape and the motion patterns of the biological fish but, in addition, the actuation strategies and the compliant bodies properties should be considered.

Proposition 7.1 and Proposition 7.2 summarize the above discussion. This rules can be used in order to choose the parameters of the gait patterns for underwater snake robots to achieve energy efficient motion while reaching the fastest possible forward velocity based on the previous analysis.

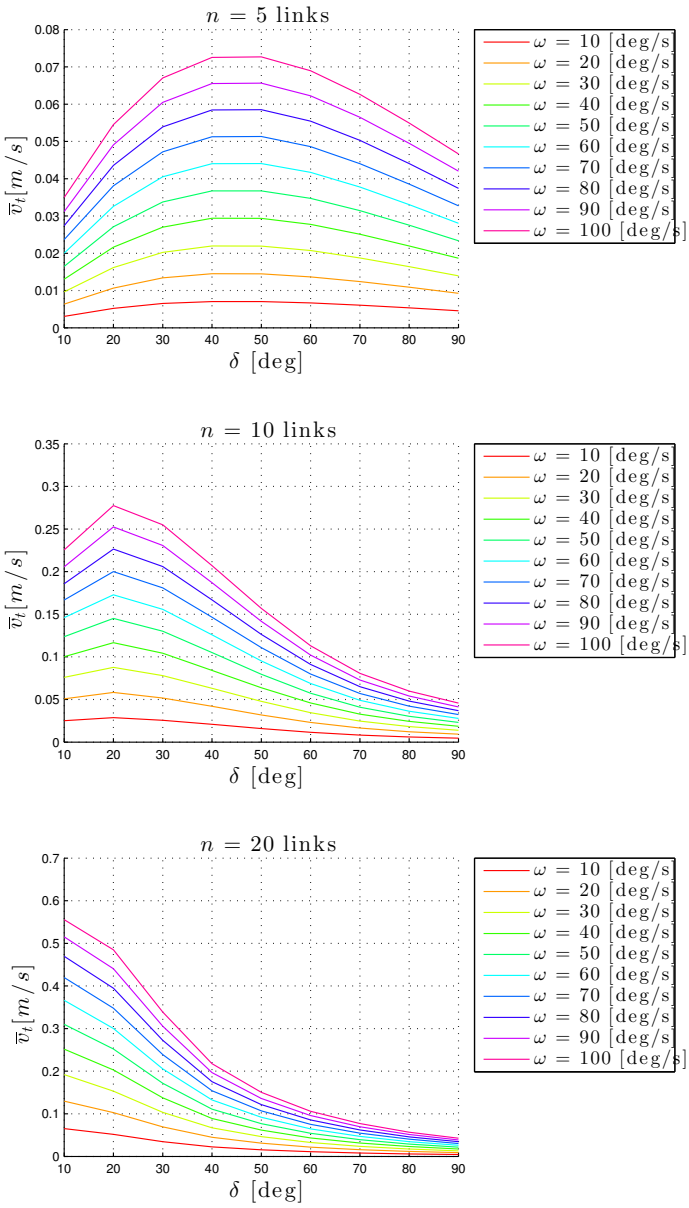

Figure 7.3: Forward velocity of underwater snake robot locomotion for the eel-like motion pattern with constant amplitude $\alpha = 20^o$.

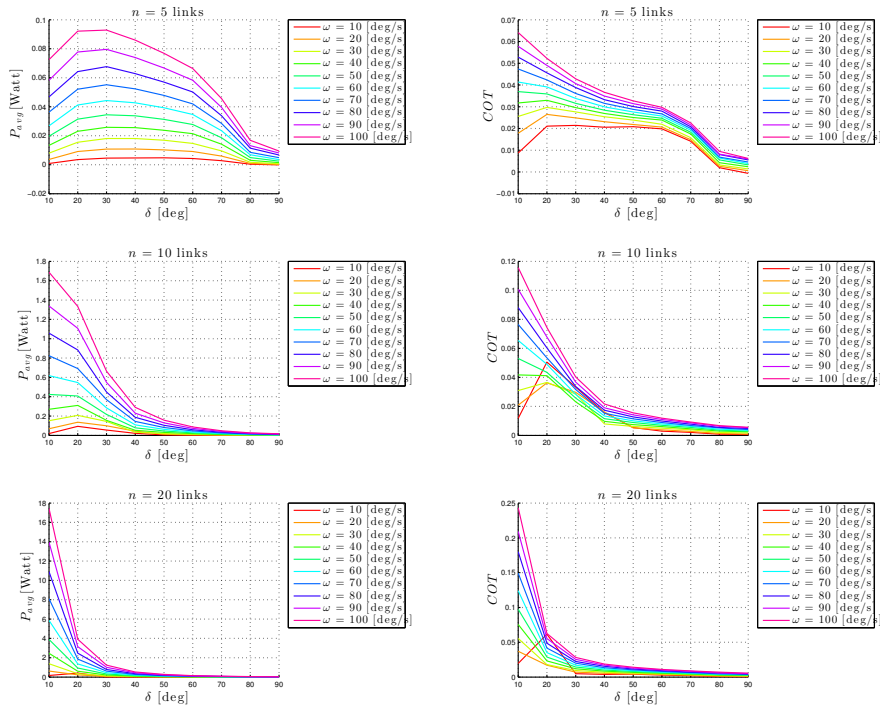

(a) Averaged power consumption (b) Cost of transportation

Figure 7.4: Simulation results for the eel-like motion pattern with constant amplitude $\alpha = 20^o$.

Proposition 7.1: Given an underwater snake robot with n links described by (2.33,2.38) which is controlled by (3.5) with the joint reference angles given by (3.3). The following rules hold for the forward velocity:

- The forward velocity increases by increasing the parameter ω, when α is kept constant.
- The forward velocity increases by increasing the parameter α as long as ω is constant.
- The forward velocity increases by increasing the parameter ω and by increasing the amplitude α, as long as δ is constant.
- Furthermore, there exists a value of the phase shift, δ_{max}, that gives the maximum forward velocity. The forward velocity increases with increasing δ for $\delta < \delta_{max}$, and decreases with δ when $\delta > \delta_{max}$. The maximum forward velocity is achieved when $\delta = \delta_{max}$ as long as α and ω are constant.

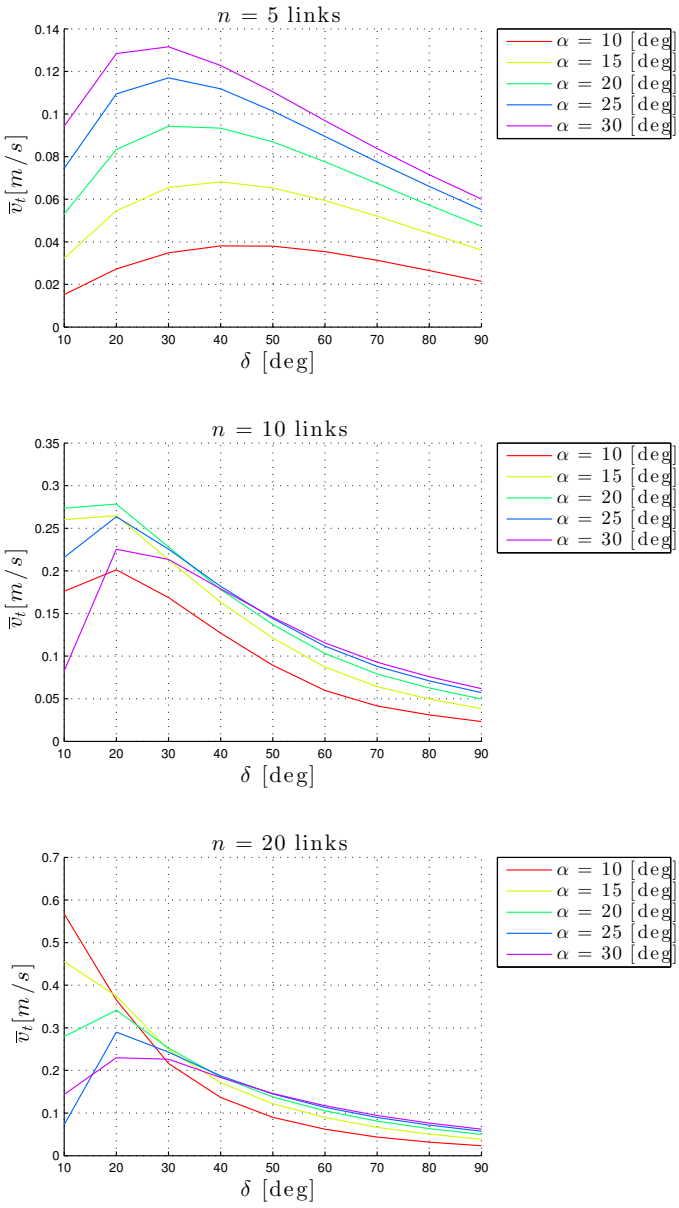

Figure 7.5: Forward velocity of underwater snake robot locomotion for the lateral undulation motion pattern with constant frequency $\omega = 70^o/\text{s}$.

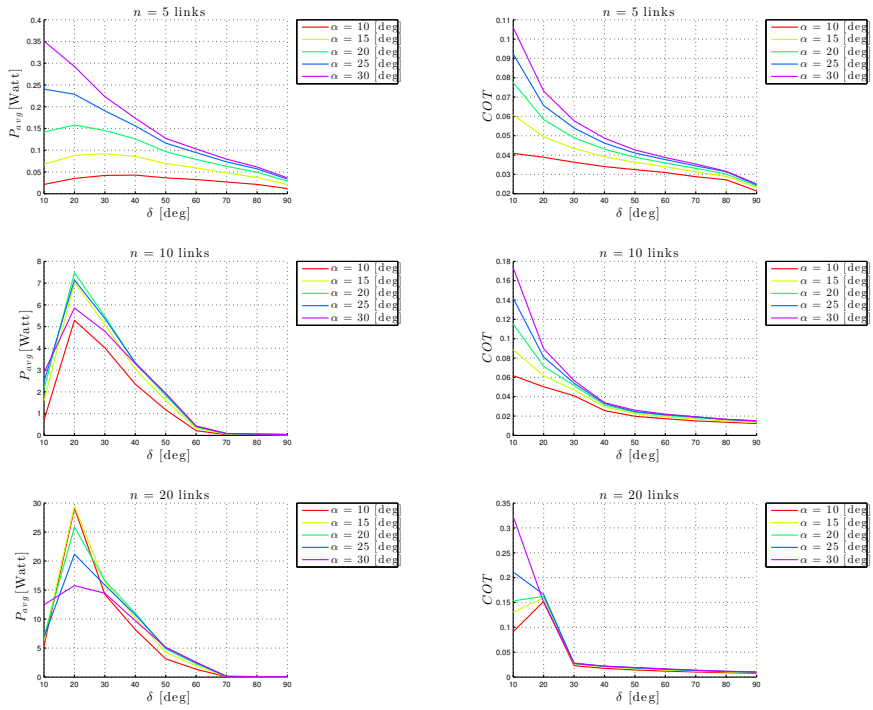

(a) Averaged power consumption (b) Cost of transportation

Figure 7.6: Simulation results for the lateral undulation motion pattern with constant frequency $\omega = 70^o/\text{s}$.

Proposition 7.2: Given an underwater snake robot with n links described by (2.33,2.38) which is controlled by (3.5) with the joint reference angles given by (3.3). The following rules hold for the average power consumption:

- The average power consumption decreases by increasing the parameter δ as long as α and ω are constant, and it increases by increasing the parameter ω as long as α and δ are constant.
- The average power consumption decreases by increasing the parameter δ as long as α and ω are constant and increases by increasing the parameter α as long as ω and δ are constant.
- The average power consumption increases by increasing the parameter ω and by increasing the amplitude α, when δ is constant

Remark 7.1: *Note that, in addition to results presented in Section 5.6, in this section, we presented simulation results for a wider range of the gait parameters and we proposed empirical rules for efficient motion of underwater snake robots based*

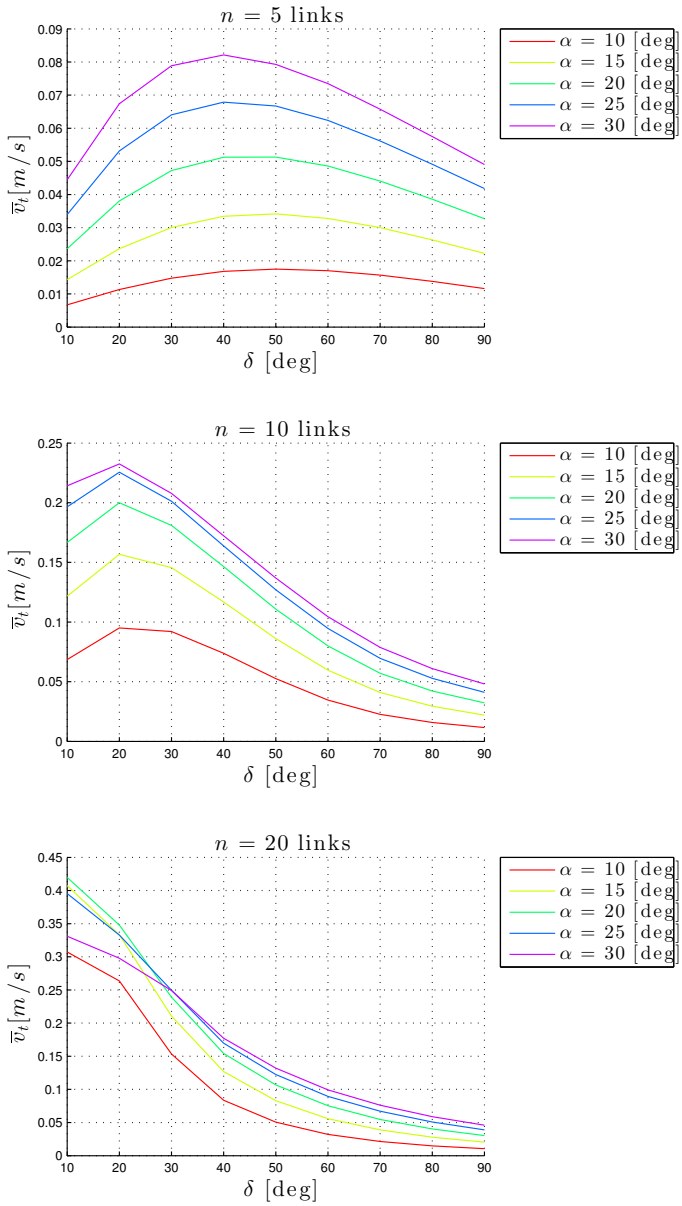

Figure 7.7: Forward velocity of underwater snake robot locomotion for the eel-like motion pattern with constant frequency $\omega = 70^o/\text{s}$.

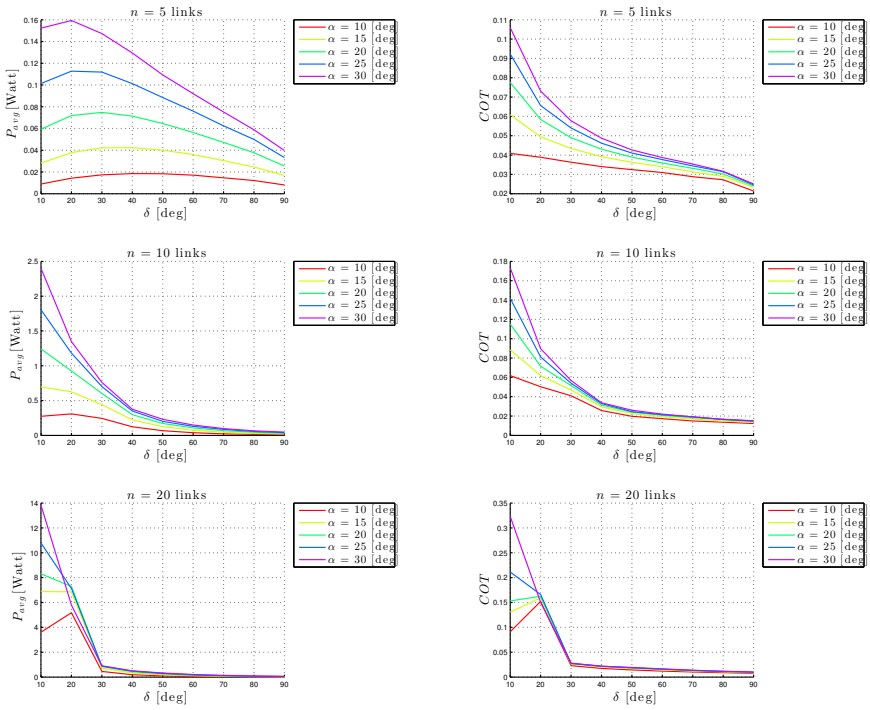

(a) Averaged power consumption

(b) Cost of transportation

Figure 7.8: Simulation results for the eel-like motion pattern with constant frequency $\omega = 70^o/\text{s}$.

on the complex model presented in Section 2.2. Note that the experimental results presented in 5.8 are in accordance with the properties in Proposition 7.1. Furthermore, experimental results will be presented in Section 7.5 in order to investigate the validity of the fundamental properties for underwater snake robot locomotion presented in Proposition 7.2.

7.4 Comparison Simulation Study with Remotely Operated Vehicle

In this section, simulation results are presented for underwater snake robots and ROV reaching the distance of 4 m. The models were implemented in *Matlab R2013b*. The dynamics was calculated using the *ode23tb* solver with a relative and absolute error tolerance of 10^{-4}. The parameters of the simulated underwater snake robots are presented in Section 7.3, while the parameters of the simulated ROV

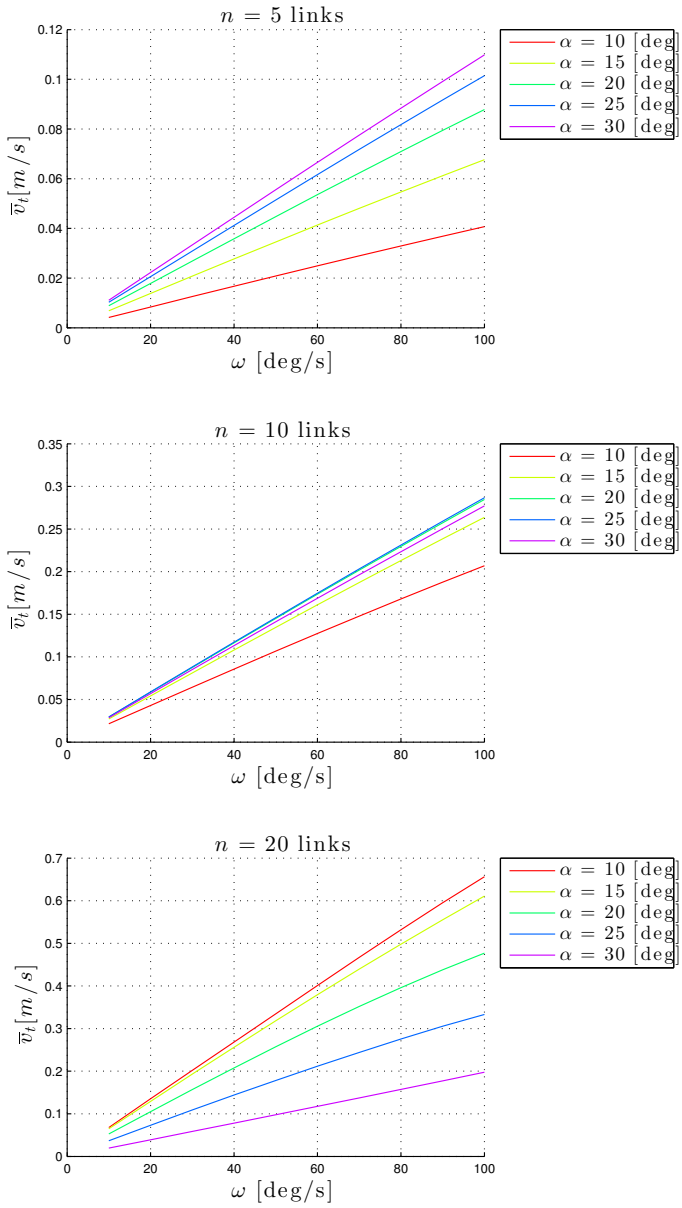

Figure 7.9: Forward velocity of underwater snake robot locomotion for the lateral undulation motion pattern with specified phase offset $\delta = 35^o$, 15^o, 15^o.

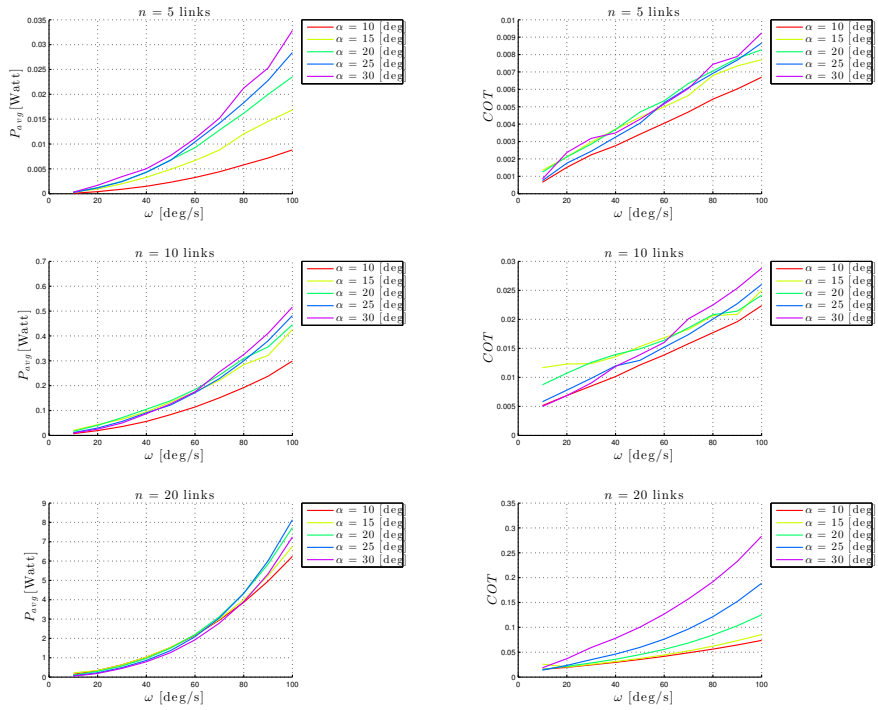

(a) Averaged power consumption

(b) Cost of transportation

Figure 7.10: Simulation results for the lateral undulation motion pattern with specified phase offset $\delta = 35^o$, 15^o, 15^o.

are presented in the following subsection.

7.4.1 Simulation parameters for ROV

We now present simulation results for a fairly typical model of a ROV. The mass of the ROV is $m_r = 3184$ kg with the volume of the vehicle being $V_r = 3.2$ and the vehicle is neutrally buoyant. The location of the center of gravity (CG) and the center of buoyancy are given by $r_g = [-0.00234, 0.00301, -0.02119]^T$ and $r_b = [0.12, 0, 0.197]^T$, respectively. The mass matrix, which includes the added mass effects, is given by $\mathbf{M}_{RB} = 1.1 m_r \mathbf{I}_r$. The inertia matrix, $\mathbf{I}_r$, the system inertia matrix, $\mathbf{M}_r$, and the damping matrix, $\mathbf{D}_r$, are defined in the following vector and matrices

$$\mathbf{I}_r = \begin{bmatrix} 1964.2 & 0 & -120 \\ 0 & 3209.2 & 7 \\ -120 & 7 & 3031.2 \end{bmatrix},$$

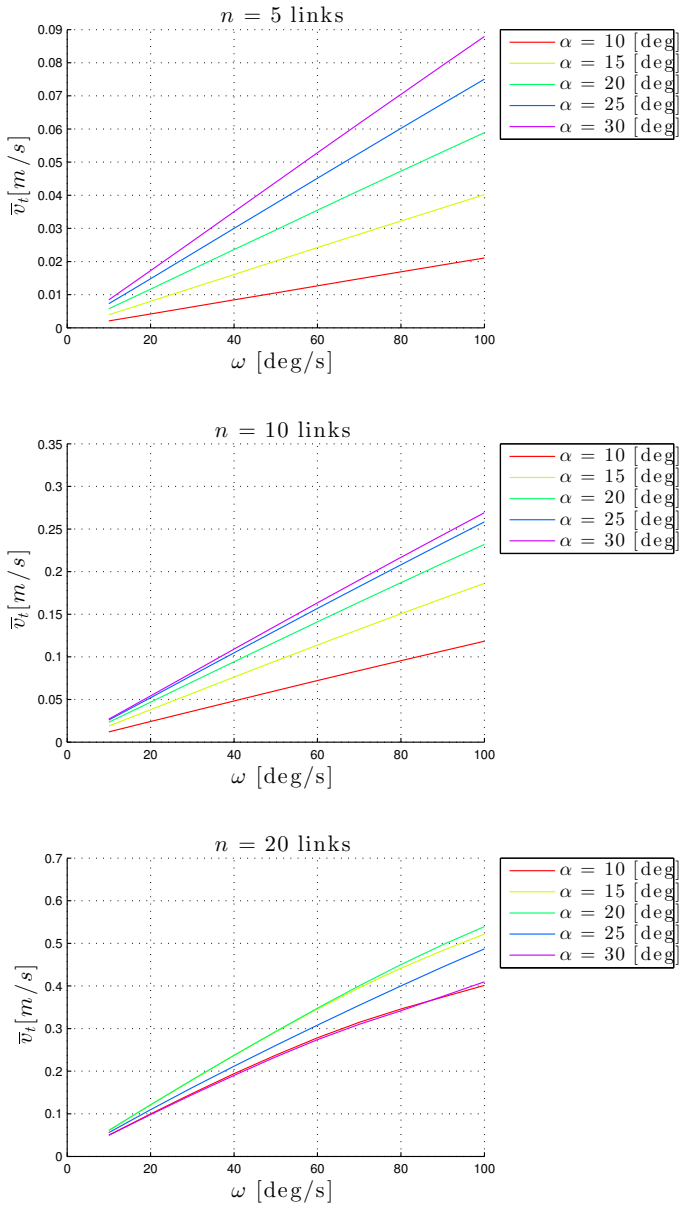

Figure 7.11: Forward velocity of underwater snake robot locomotion for the eel-like motion pattern with specified phase offset $\delta = 35^o$, 15^o, 15^o.

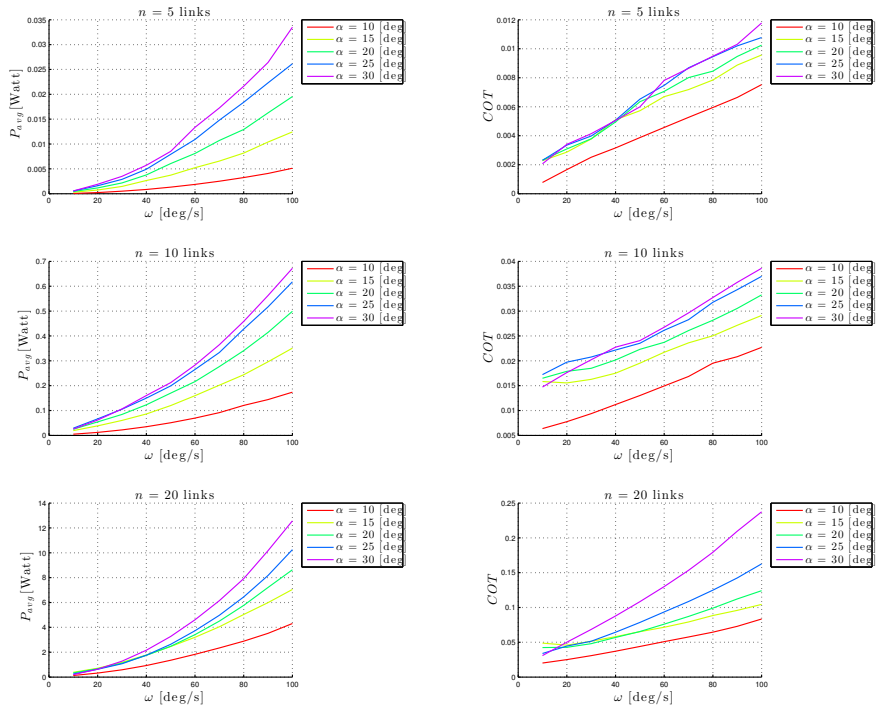

(a) Energy consumption

(b) Cost of transportation

Figure 7.12: Simulation results for the eel-like motion pattern with specified phase offset $\delta = 35^o,\ 15^o,\ 15^o$.

$$\mathbf{M}_r = \begin{bmatrix} 3502.4 & 0 & 0 & 0 & -67.5 & -9.6 \\ 0 & 3502.4 & 067.5 & 0 & -7.5 & \\ 0 & 0 & 3502.4 & 9.6 & 7.5 & 0 \\ 0 & 67.5 & 9.6 & 1964.2 & 0 & -120 \\ -67.5 & 0 & 7.5 & 0 & 3209.2 & 7 \\ -9.6 & -7.5 & 0 & -120 & 7 & 3031.2 \end{bmatrix},$$

$$\mathbf{D}_r = \text{diag}\left(1321, 2525, 2525, 192, 192, 192\right).$$

By using the MSS toolbox in Matlab, the centrifugal and Coriolis matrix, $\mathbf{C}_{\text{r}}(\dot{\mathbf{q}})$, is calculated for the ROV model. The initial values of the states of the ROV are chosen to be $[0, 0, -2, 0, 0, 0]^T$ and the vehicle is freely moved by applying the input $\boldsymbol{\tau}_{\text{r}} = [\tau_x, 0, 0, 0, 0, 0]^T$.

7.4.2 Simulation results

In Fig. 7.13-7.15 simulation results are presented based on the model of the ROV presented in Section 7.2. The system is freely moved with τ_x taking values in the range $[2 \cdot 10^3, 8 \cdot 10^3]$ N, to reach the distance of 4 m. Using (7.7) and (7.4), the total energy consumption and the cost of transportation are calculated. The maximum velocities that are achieved for different values of the input torque are presented in Fig. 7.13. From Fig. 7.14, we can see that the maximum energy is consumed for the maximum achieved forward velocity as it was expected. From Fig. 7.15, we can conclude that faster motions are not energy efficient and from a power consumption perspective, the vehicle is preferred to move the given distance of 4 m at the minimum possible velocity.

In addition, simulation results are presented in Fig. 7.16 - Fig. 7.19 for underwater snake robots of different length both for lateral undulation and eel-like motion patterns. Using (7.2) and (7.4), the total energy consumption and the cost of transportation are calculated. Fig. 7.16 and Fig. 7.18 present the total power consumption for lateral undulation and eel-like motion, respectively. In Fig. 7.17 and Fig. 7.19 the cost of transportation is presented both for lateral undulation and eel-like motion. In addition, the minimum and the maximum values of the total energy consumption and the cost of transportation are given in Table 7.1 - 7.2 for the simulation results presented in Fig. 7.16 - 7.19. From Table 7.1 - 7.2, we can see that the eel-like motion pattern is more energy efficient for snake robots with $n > 10$ links while lateral undulation is more energy efficient for snake robot with $n < 10$ links. In addition, we see that by increasing the number of links the total energy consumption and thus the cost of transportation are increased both for lateral undulation and eel-like motion, as were expected since by increasing the number of links n we need more $(n-1)$ servo motors for the joint actuation.

Comparing these results with the results for the ROV presented in Fig. 7.13-7.15, we can conclude that the underwater snake robots are more energy efficient by considering the cost of transportation as the metric. In particular, for the ROV the minimum and maximum values of the cost of transportation are 6.6743 and 1.8068, respectively, and the more energy efficient motion is achieved for the lowest velocities of the ROV. Even for the lowest velocities of the ROV the underwater snake robots are more energy efficient using COT as the metric. In addition, we see from Fig. 7.14 that the minimum and the maximum total energy consumption for ROV to move the 4 m distance are $2.2574 \cdot 10^5$ and $8.3389 \cdot 10^5$ Joule, respectively. Comparing this result with the total energy consumption of the underwater snake robots presented in Table 7.1-7.2, we see that for the snake robots locomotion the total energy required to cover a distance of 4m is less than for the ROV. For any values of the parameters of the gait pattern, both for lateral undulation and eel-like motion patterns, the underwater snake robot consumes less total energy than the remotely operated vehicle for the same task.

To conclude, the underwater snake robots consume less total energy traversing the given distance than the ROV and they are more energy efficient compare to the ROV by considering the cost of transportation as the metric. Note that the light weight and small cross-section works in favour of the energy efficiency of the snake robots. Furthermore, we see from the simulations that both systems

Table 7.1: Maximum and minimum values for the lateral undulation motion pattern.

n	Max E_s	Min E_s	Max COT	Min COT
5 (Fig. 7.16(a) and Fig. 7.17(a))	1.1967	0.1094	0.0092	$8.4544 \cdot 10^{-4}$
5 (Fig. 7.16(b) and Fig. 7.17(b))	14.8801	2.4304	0.1150	0.0188
5 (Fig. 7.16(c) and Fig. 7.17(c))	9.6530	0.7368	0.0746	0.0057
10 (Fig. 7.16(a) and Fig. 7.17(a))	7.4588	1.2927	0.0288	0.0050
10 (Fig. 7.16(b) and Fig. 7.17(b))	139.3753	2.9180	0.5384	0.0113
10 (Fig. 7.16(c) and Fig. 7.17(c))	43.5805	1.5911	0.1684	0.0061
20 (Fig. 7.16(a) and Fig. 7.17(a))	146.6482	9.7953	0.2833	0.0189
20 (Fig. 7.16(b) and Fig. 7.17(b))	347.7708	4.7240	0.6717	0.0091
20 (Fig. 7.16(c) and Fig. 7.17(c))	186.9369	3.1348	0.3611	0.0061

Table 7.2: Maximum and minimum values for the eel-like motion pattern.

n	Max E_s	Min E_s	Max COT	Min COT
5 (Fig. 7.18(a) and Fig. 7.19(a))	1.5244	0.2668	0.0118	0.0021
5 (Fig. 7.18(b) and Fig. 7.19(b))	13.7142	3.2400	0.1060	0.0250
5 (Fig. 7.18(c) and Fig. 7.19(c))	8.2996	0.8076	0.0641	0.0062
10 (Fig. 7.18(a) and Fig. 7.19(a))	9.9969	3.8121	0.0386	0.0147
10 (Fig. 7.18(b) and Fig. 7.19(b))	44.8714	3.9287	0.1733	0.0152
10 (Fig. 7.18(c) and Fig. 7.19(c))	29.9615	1.4559	0.1157	0.0056
20 (Fig. 7.18(a) and Fig. 7.19(a))	122.9098	15.9880	0.2374	0.0309
20 (Fig. 7.18(b) and Fig. 7.19(b))	167.2808	5.2576	0.3231	0.0102
20 (Fig. 7.18(c) and Fig. 7.19(c))	125.9718	2.9053	0.2433	0.0056

are more energy efficient when they move at lower velocities, and it may thus be that the property that the snake robot system moves at lower velocities than the ROV contributes to making it more energy efficient. In this case, we need to pay the penalty of achieving slower motion (more time required to achieve the same travelled distance).

Based on this analysis, we see that ROVs and swimming snake robots have different advantages and can be used for different tasks. ROVs have an advantage when it comes to carrying heavy payload sensors because of their considerable size. The ROV also achieves faster motion (less time required to achieve the same travelled distance) than the snake robots. Swimming snake robots, on the other hand, are more slender and flexible structures, and thus have an advantage with respect to maneuverability and access to narrow environments. The consequences for subsea structures or divers in case of a collision are also significantly reduced compared to those of a working class ROV. In addition, the total energy consumption and the cost of transportation are significantly lower for these lightweight structures. Furthermore, for monitoring of biological systems and also other surveillance tasks, the quiet motion of the snake robots is an advantage with respect to the thruster-driven propulsion of the ROVs.

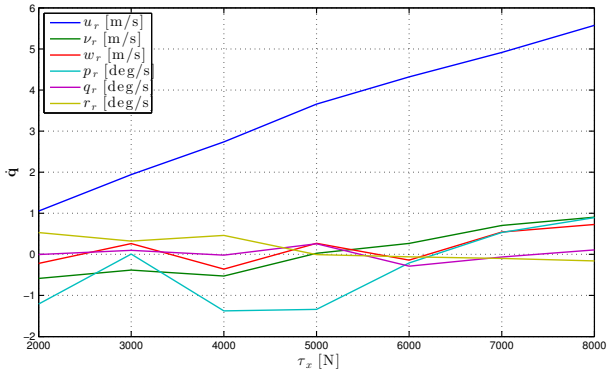

Figure 7.13: Simulation results for the velocities of the ROV.

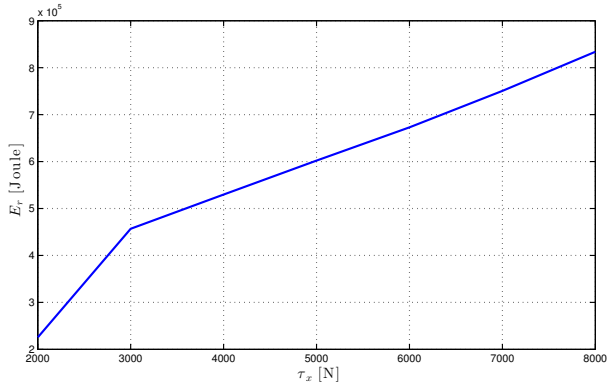

Figure 7.14: Simulation results for the total energy consumption of the ROV.

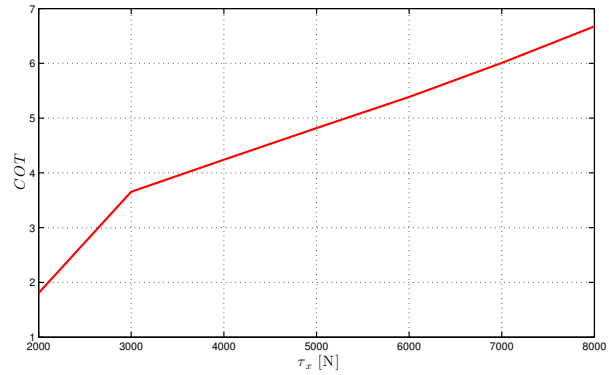

Figure 7.15: Simulation results for the cost of transportation of the ROV.

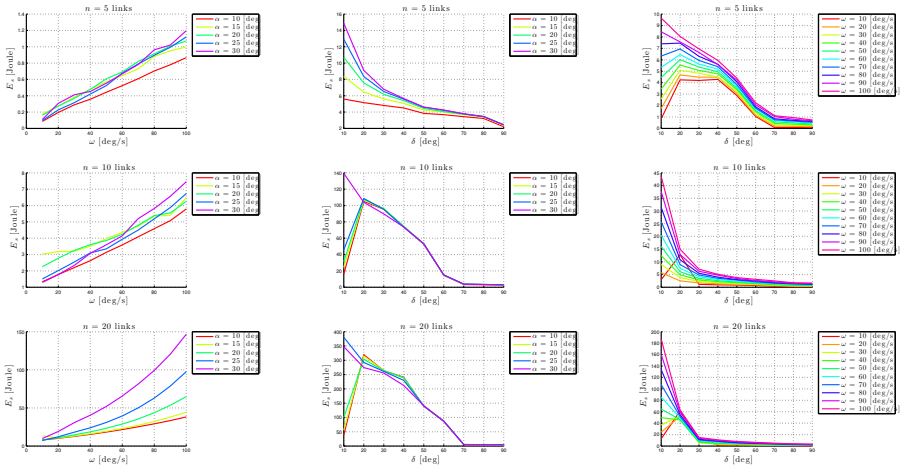

(a) For specified phase offset $\delta = 35^o,\ 15^o,\ 15^o$ (b) For constant $\omega = 70^o/\text{s}$ (c) For constant $\alpha = 20^o$

Figure 7.16: Total energy consumption for the lateral undulation motion pattern.

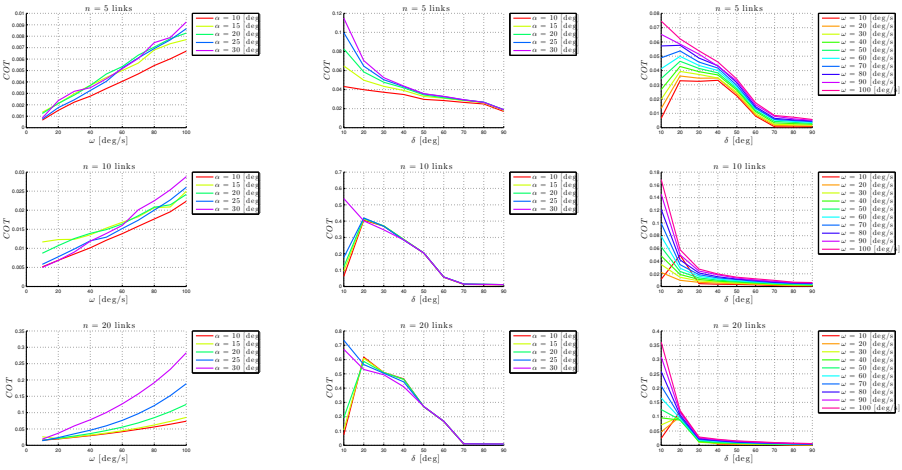

(a) For specified phase offset $\delta = 35^o,\ 15^o,\ 15^o$ (b) For constant $\omega = 70^o/\text{s}$ (c) For constant $\alpha = 20^o$

Figure 7.17: Cost of transportation for the lateral undulation motion pattern.

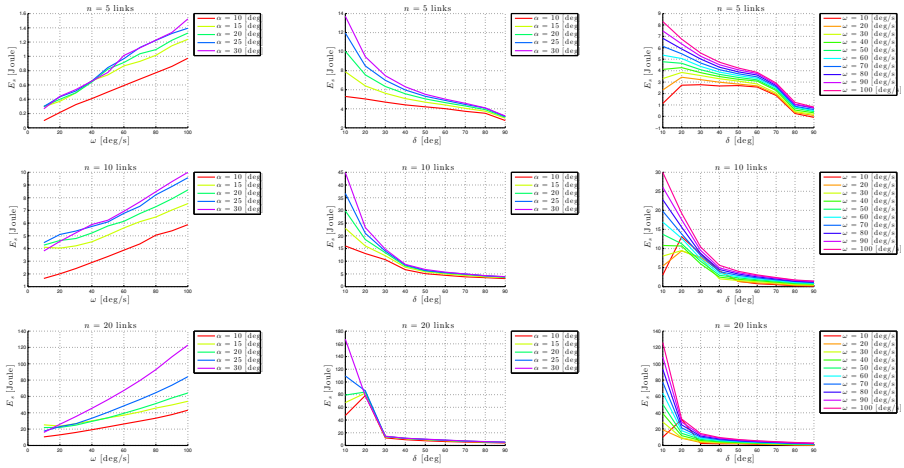

(a) For specified phase offset $\delta = [35^o\ 15^o\ 15^o]$ (b) For constant $\omega = 70^o/\text{s}$ (c) For constant $\alpha = 20^o$

Figure 7.18: Total energy consumption for the eel-like motion pattern.

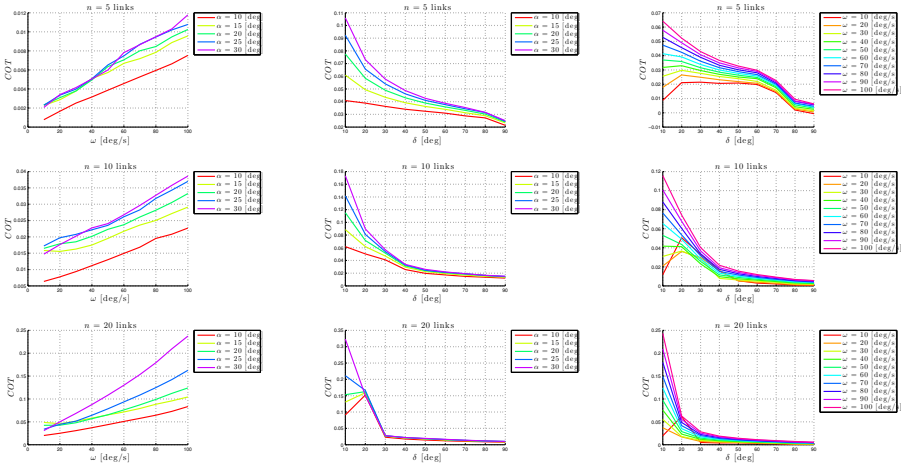

(a) For specified phase offset $\delta = [35^o\ 15^o\ 15^o]$ (b) For constant $\omega = 70^o/\text{s}$ (c) For constant $\alpha = 20^o$

Figure 7.19: Cost of Transportation for the eel-like motion pattern.

7.5 Experimental Study for Underwater Snake Robots

In this section, we present simulation and experimental results regarding the energy consumption for underwater snake robots. In particular, we present simulation and experimental results for the average power consumption of an underwater snake robot. The experimental results are obtained by running experiments with the underwater snake robot Mamba, while the simulation results are obtained by using the complex model of the robot described in Section 2.2. The experimental setup is presented in Section 5.7.

The simulations results shown in Fig. 7.20 and Fig. 7.21 are obtained for the underwater snake robot parameters as presented in Section 5.8. These parameters are identical to the characteristics of the physical robot Mamba that is used for the experiments (see for more details Section 5.7), except for the fluid parameters for which theoretical values are considered. In particular, the hydrodynamic related parameters c_t, c_n, μ_n λ_1, λ_2 and λ_3 for the elliptic section with major and minor diameters $2a = 2 \cdot 0.055$ m and $2b = 2 \cdot 0.05$ m, respectively, $\rho = 1000$ kg/m^3 and for the fluid coefficients set to $C_f = 0.03$, $C_D = 2$, $C_A = 1$, $C_M = 1$ were calculated by using equations derived in Section 2.2. In Fig. 7.20 simulation results are presented for the average power consumption of the robot for the lateral undulation motion pattern and in Fig. 7.21 simulation results are shown for the eel-like motion pattern. Note that for the simulation results presented in Fig. 7.20 and Fig. 7.21, the average power consumption is calculated as in (7.3), while for the experimental results the average power consumption is calculated by using the following equation

$$P_{\text{avg}} = V I_{\text{avg}}, \tag{7.9}$$

where $V = 35(V)$ and $I_{\text{avg}}(A)$ is the average current that is measured by using the high performance industrial logging multimeter FLUKE 289 [6]. The multimeter was connected to the power box on the tip of the power supply cable that is used for our experiments with Mamba. We measured and saved the current values for a wide range of the values of the gait parameters both for lateral undulation and eel-like motion patterns. Note that this multimeter has the ability to measure the values for a certain time, store all the measured data and, in addition, provide data regarding of the average, the maximum and the minimum values of the current.

As we can see from Fig. (7.20(a),7.20(b)) and Fig. (7.21(a),7.21(b)), by increasing the parameter α the average power consumption is increased both for the simulated robot and the physical robot for lateral undulation and eel-like motion pattern, respectively. In addition, it is easily seen that for constant values of the parameters α and δ by increasing ω the power consumption is increased both for lateral undulation and eel-like motion patterns (Fig. (7.20(c),7.20(d)) and Fig. (7.21(c),7.21(d))). In addition, in Fig. (7.20(e),7.20(f)) and Fig. (7.21(e),7.21(f)), we see that by keeping the values for α and ω constant and increase of the value of δ results in a decrease of the average power consumption for both investigated motion patterns. The simulation and the experimental results presented in this section are thus in accordance with the properties in Proposition 7.2.

Remark 7.2: Please note that for the physical robot we are able to measure the total average power consumption that is required for the motion of the robot, the electronics

installed inside the joints of the robot and also the power that is required for the servomotors, while for the simulated robot we assume the links to be perfect and thus consuming significantly less power. Hence, there is a difference of magnitude between the simulated power consumption and the physical power consumption and thus for the results presented in Fig. 7.20 and Fig. 7.21 we are able to obtain only a qualitative comparison of the power consumption of the simulated and the physical robot. This is mostly because an accurate model of the servo motor has not been considered for the simulation results and the power required from the electronics are not taken into account. As it is already mentioned in Section 5.7, each joint module of the robot is actuated by a Hitec servo motor (HSR 5990TG), which are high gain servomotors and consume a lot of power in order to allow precise control of angular position, velocity and acceleration. The comparison is thus qualitative and not quantitative. However, the obtained qualitative comparison results presented in this section validate the properties presented in Proposition 7.2.

7.6 Multi-Objective Optimization of Gait Parameters

This section presents an optimization framework to investigate the efficient motion of the underwater snake robot model presented in Section 2.2. In particular, we formulate this problem and propose a method to solve the multi-objective optimization problem. In order to address optimization of both the power consumption and the forward velocity, a combination of the goals are proposed as a single objective function. Therefore, we formulate the problem as a constrained optimization problem subject to constraints. There exist two types of optimization algorithms to solve this kind of problem: gradient-based methods and derivative free algorithms. Generally, gradient-based algorithms are faster than derivative free ones. However, gradient-based algorithms are susceptible to getting trapped in local optima, meaning that the optimized solution depends on the initial points [87]. Therefore, derivative free and stochastic methods, which have the ability to avoid local solutions, have received attention in problems with highly non-smooth objective functions containing multiple optima. Consequently, as also mentioned in [135], derivative free and stochastic methods are an appropriate choice for the motion optimization.

We depict the optimization framework in Fig. 7.22, consisting of the plant (the underwater snake robot model), a joint actuation controller, and an optimizer. The optimizer requires the simulation of the model in order to evaluate the objective function for different gait parameters. The constraints defining the feasible region are also inputs of the optimizer. The joint actuation controller consists of the gait pattern generator given by (3.3) and joint control as defined in (3.5), which are discussed in Section 3.1 and Section 3.2, respectively. In the following, the optimizer is discussed in detail.

7.6.1 Optimization problem formulation

An optimization problem is the minimization or maximization of a function from all feasible solutions. The goal of motion optimization is to minimize energy consumption and to maximize the forward velocity, simultaneously. This type of op-

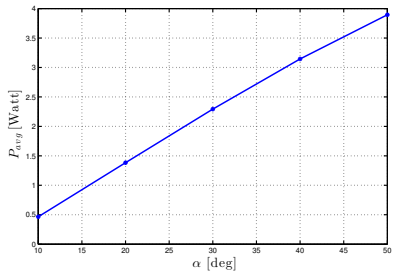

(a) Simulation: $\omega = 120^o/\text{s}$ and $\delta = 30^o$

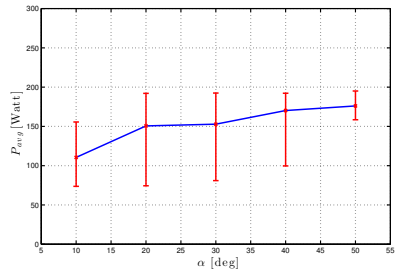

(b) Experiments: $\omega = 120^o/\text{s}$ and $\delta = 30^o$

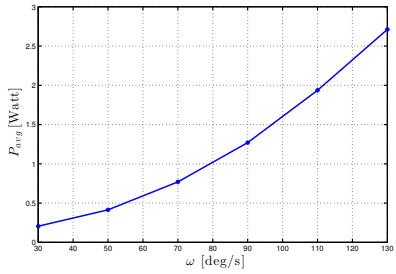

(c) Simulations: $\alpha = 30^o$ and $\delta = 30^o$

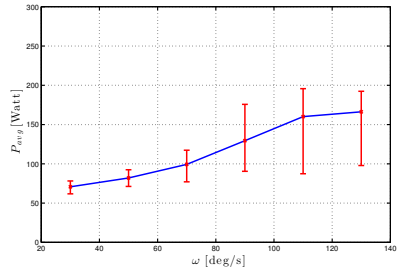

(d) Experiments: $\alpha = 30^o$ and $\delta = 30^o$

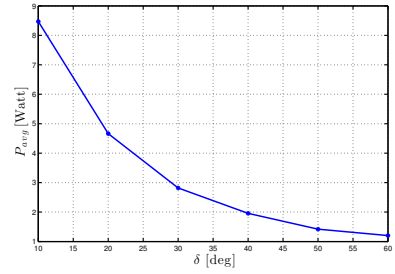

(e) Simulations: $\alpha = 30^o$ and $\omega = 120^o/\text{s}$

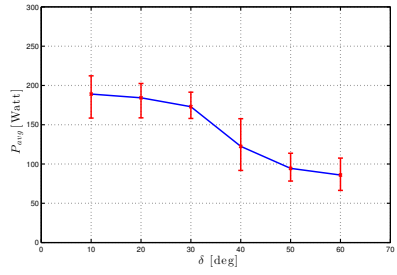

(f) Experiments: $\alpha = 30^o$ and $\omega = 120^o/\text{s}$

Figure 7.20: Lateral Undulation: The average power consumption, P_{avg} [W].

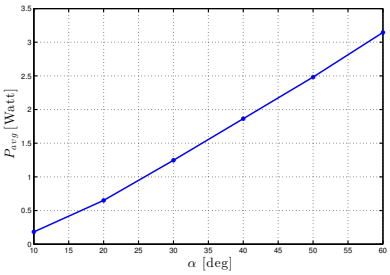

(a) Simulations: $\omega = 120^o/\text{s}$ and $\delta = 30^o$

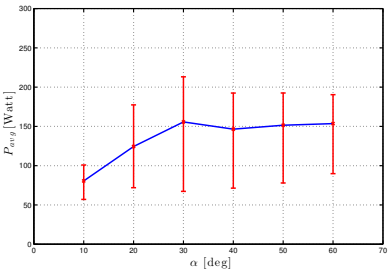

(b) Experiments: $\omega = 120^o/\text{s}$ and $\delta = 30^o$

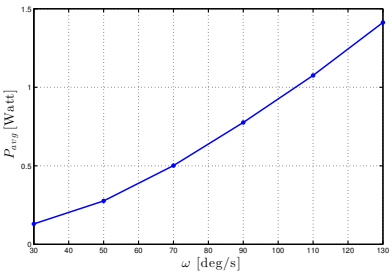

(c) Simulations: $\alpha = 30^o$ and $\delta = 30^o$

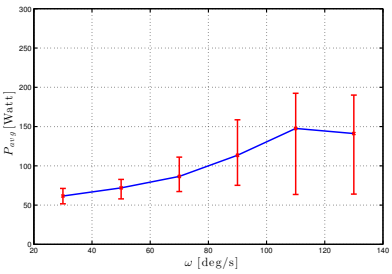

(d) Experiments: $\alpha = 30^o$ and $\delta = 30^o$

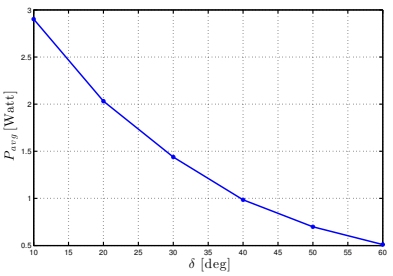

(e) Simulations: $\alpha = 30^o$ and $\omega = 120^o/\text{s}$

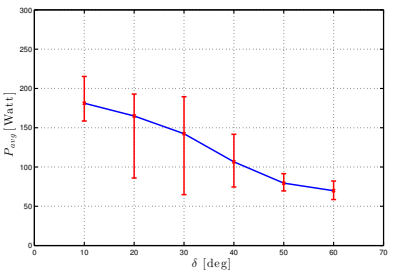

(f) Experiments: $\alpha = 30^o$ and $\omega = 120^o/\text{s}$

Figure 7.21: Eel-like motion: The average power consumption, P_{avg} [W].

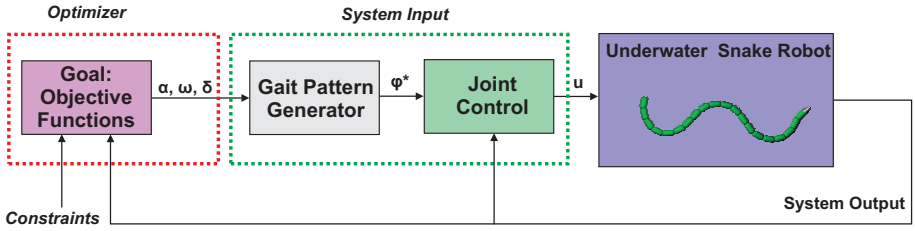

Figure 7.22: Illustration of the optimization framework.

timization problem which involves more than one objective function is known as multi-objective optimization [115]. In the following, both the energy consumption and the forward velocity are formulated and an approach to combine these two goals is introduced.

As it is already mentioned at the beginning of this chapter, for underwater snake robots, the propulsion is generated by the motion of the joints and its interaction with the surrounding fluid. In this section, we assume that the joints are ideal and thus the total amount of energy of the system (E_s) generated by this input is the summation of kinetic energy (E_kinetic) and the energy that is dissipated to the surrounding fluid (E_fluid) as it is defined in Section 7.1. The averaged power consumption,P_avg, that will be optimized in this section is calculated for a complete swimming cycle T by (7.3). In addition, the forward velocity for a complete swimming cycle T is defined as

$$\bar{v} = \frac{\sqrt{(p_x(T) - p_x(0))^2 + (p_y(T) - p_y(0))^2}}{T}, \tag{7.10}$$

where the initial and the final points are used to calculate the travelled distance of the robot. The optimization problem can be formulated by

$$\min_{\alpha,\omega,\delta} J_\mathrm{opt} = [P_{avg}, -\bar{v}], \tag{7.11a}$$

$$\text{s.t: } \mid \phi_i^* \mid \leq \phi_i^{max}, \mid \dot{\phi}_i^* \mid \leq \dot{\phi}_i^{max}, \mid u_i \mid \leq u_i^{max}, \tag{7.11b}$$

$$0 \leq \alpha \leq \alpha^{max}, 0 \leq \omega \leq \omega^{max}, 0 \leq \delta \leq \delta^{max}, \tag{7.11c}$$

where (7.11b) gives the physical constraints of the joints due to the servo motors and the physical design of the snake, and (7.11c) expresses the possible range of the parameters of the sinusoidal motion pattern (3.3).

Generally, in multi-objective optimization such as (7.11), there does not exist a single global solution to optimize all objective functions simultaneously. Particularly in this case, the objective functions are often in conflict, meaning that maximizing the velocity results in increasing the power consumption and vice versa. A solution is called Pareto optimal [115] of optimization problem (7.11), if there does not exist another point such that power consumption can be decreased in value without degrading the forward velocity or the forward velocity can be increased without enhancing power consumption. The Pareto frontier or efficient frontier is the collection of Pareto optimal solutions. For bi-objective functions (e.g., (7.11)),

the frontier can be expressed in Cartesian coordinates. An efficient way to generate the Pareto frontier is the weighted-sum method that combines both objective functions in a single criterion function [142]

$$J_{\text{bal}} = w_p(P_{\text{avg}})_{sc} - w_v(\bar{v})_{sc}, \tag{7.12}$$
$$w_p = 1 - w_v, \tag{7.13}$$

where $(P_{\text{avg}})_{sc}$ and $(\bar{v})_{sc}$ are scaled values of the power consumption and forward velocity, respectively, and w_p and w_v are the weighting factors of respectively the power consumption and the forward velocity. The solution is always the Pareto frontier, if the coefficients are positive. In order to plot the Pareto frontier, one can find the solutions for different values of w_p varying from 0 to 1 (and w_v changing from 1 to 0) using a small step size Δw_p. Therefore, the optimization problem (7.11) can be transformed to a new optimization problem by replacing the objective function J_{opt} to J_{bal} in (7.12). In order to find the solution of the new optimization problem for specific weighting factors, an optimization algorithm is required. In the following PSO is introduced as a proper optimization method for motion optimization.

7.6.2 PSO algorithm

The PSO algorithm is a population-based probabilistic algorithm first introduced by Kennedy and Eberhart in 1995 [76]. The PSO algorithm exploit a set of potential solutions to the optimization problem. Each potential solution is called a particle, and the set of particles is named a population. The first population is randomly initialized using a random number generator. The location of each particle in the new generation is determined by PSO update equations, which mimic the social behavior of members of bird flocks or fish schools.

Consider an unconstrained nonlinear problem where the objective function $f(\mathbf{x})$ must be minimized. Let $\mathbf{x}_i(k)$ denote the ith particle of the kth generation, and $\boldsymbol{\nu}_i(k)$ represent its velocity. The update equations for all $i \in \{1, 2, \cdots, n_p\}$ and $k \in \mathbb{N}$ are as follows:

$$\boldsymbol{\nu}_i(k+1) = \boldsymbol{\nu}_i(k) + c_1\rho_1(k)(\mathbf{p}_{l,i}(k) - \mathbf{x}_i(k)) + c_2\rho_2(k)(\mathbf{p}_{g,i}(k) - \mathbf{x}_i(k)), \tag{7.14a}$$
$$\mathbf{x}_i(k+1) = \mathbf{x}_i(k) + \boldsymbol{\nu}_i(k+1), \tag{7.14b}$$

where $c_1, c_2 \in \mathbb{R}^+$, $\rho_1(k), \rho_2(k) \sim U(0,1)$ are uniformly distributed random numbers between 0 and 1, $\boldsymbol{\nu}_i(0) \triangleq \mathbf{0}$, $\mathbf{p}_{l,i}(k)$ is the best location of the ith particle over all generations, and $\mathbf{p}_{g,i}(k)$ is the location for the best particle over all generations,

$$\mathbf{p}_{l,i}(k) \triangleq \underset{\mathbf{x} \in \{\mathbf{x}_i(j)\}_{j=0}^{k}}{\arg\min} \; f(\mathbf{x}), \tag{7.15a}$$
$$\mathbf{p}_{g,i}(k) \triangleq \underset{\mathbf{x} \in \{\{\mathbf{x}_i(j)\}_{j=0}^{k}\}_{i=1}^{n_p}}{\arg\min} \; f(\mathbf{x}). \tag{7.15b}$$

Therefore, c_1 and c_2 are named cognitive and social acceleration terms, respectively. In this section, we use the *von Neumann* neighborhood topology which has the

best performance among other topologies such as *lbest* and *gbest* [77]. In the von Neumann neighborhood topology, each particle has 4 neighborhoods which are defined by special enumeration.

The performance of the PSO algorithm can be improved by introducing an inertia weight. In this case for $\mathbf{x}_i(k) \in \mathbb{R}^{n_c}$ the velocity equation (7.14a) is replaced by

$$\begin{aligned}\hat{\boldsymbol{\nu}}_i(k+1) =& w(k)\boldsymbol{\nu}_i(k) + c_1\rho_1(k)(\mathbf{p}_{l,i}(k) - \mathbf{x}_i(k)) \\ &+ c_2\rho_2(k)(\mathbf{p}_{g,i}(k) - \mathbf{x}_i(k)), \qquad (7.16a)\\ \nu_i^j(k+1) =& \text{sign}(\hat{\nu}_i^j(k+1))\ \min\{|\hat{\nu}_i^j(k+1)|, \nu_{max}^j\}, \quad j \in \{1, 2, \cdots, n_c\}, \qquad (7.16b)\\ \nu_{max}^j =& \lambda(u_{iw}^j - l_{iw}^j), \qquad (7.16c)\\ w(k) =& w_0 - \frac{k}{K}(w_0 - w_1). \qquad (7.16d)\end{aligned}$$

where the maximum velocity gain λ is a scalar, $\mathbf{l}_{iw}, \mathbf{u}_{iw} \in \mathbb{R}^{n_c}$ are, respectively, the lower and upper bound of the independent variables, w_0, w_1 are the initial and final inertia weights, respectively, K is the maximum number of generations.

Remark 7.3: *As stated before, the optimizer only requires the plant to evaluate the objective function. Therefore, the proposed multi-objective optimization framework can be considered as a general tool for investigating motion efficiency of different dynamic models of swimming and ground snake robots controlled by sinusoidal motion patterns such as (3.3). Moreover, the approach can also be used for optimizing gaits of biped robots by introducing new proper optimization variables.*

7.6.3 Optimization Study

We now present optimization results both for lateral undulation and eel-like motion. The dynamic model presented in Section 2.2 is implemented in *Matlab R2013b*. The time evolution is calculated using the *ode23tb* solver with a relative and absolute error tolerance of 10^{-4}. The PSO is implemented using *GenOpt* which is developed by Lawrence Berkeley National Laboratory and is written in *java*. *GenOpt* runs multiple simulations in parallel to reduce computation time and allows using any simulation software to evaluate the cost function [133].

Parameters of the underwater snake robot

We consider an underwater snake robot with $n = 10$ links, each one having length $2l = 0.18$ m and mass $m = 0.8$ kg, i.e. identical to the physical robot Mamba presented in Section 5.7. The initial values of the states of the snake robot were set to initial reference values at $t = 0$. The hydrodynamic related parameters c_t, c_n, μ_n λ_1, λ_2 and λ_3 for the elliptic section with major and minor diameters $2a = 2 \cdot 0.055$ m and $2b = 2 \cdot 0.05$ m, respectively, $\rho = 1000$ kg/m^3 and for the fluid coefficients set to $C_f = 0.03$, $C_D = 2$, $C_A = 1$, $C_M = 1$ were calculated by using equations derived in Section 2.2. In these simulations a joint PD-controller (3.5) was used with parameters $k_p = 20$, $k_d = 5$, while lateral undulation or eel-like motion were achieved by moving the joints according to (3.3) by choosing $\text{g}(i, n) = 1$ and

number of particles	n_p	16
number of generations	n_g	20
cognitive acceleration	c_1	2.8
social acceleration	c_2	1.2
max velocity gain	λ	0.5
initial inertia weight	w_0	1.2
final inertia weight	w_1	0

Table 7.3: PSO parameters.

$g(i, n) = (n - i)/(n + 1)$, respectively. Note that current effects have not been considered in this study.

Optimization parameters

The PSO parameters are given in Table 7.3. It was suggested in [117] to use a population size of about $5n_c$ for $\mathbf{x}_i(k) \in \mathbb{R}^{n_c}$, where $n_c = 3$ in this case study. Different numbers of generations are tested and we conclude that PSO finds the optimal point in less than 20 generations. The inertia weights are chosen based on the suggestion in [91], the maximum of velocity gain, λ is commonly set to 0.5 [133] and the accelerations are chosen such that $c_1 + c_2 = 4$ [78].

The values of the physical constraints of the joints due to the servo motors in (7.11b) are set to $u_i^{max} = 2300$ Nm, $\phi_i^{max} = 90^o$, $\dot{\phi}_i^{max} = 429^o$/s, while the range of the parameters of sinusoidal motion pattern in (7.11c) are set to $\alpha^{max} = 90^o$, $\omega^{max} = 210^o$/s and $\delta^{max} = 90^o$. Furthermore, the join offset is set $\phi_0 = 0$. The step size for changing the weights, Δw_p, is equal to 0.05. In the first step, we optimize the velocity regardless of the power consumption which means $w_p = 0, w_v = 1$ in (7.13), and the maximum values of the velocity and the power consumption are obtained and can be used to scale the objective functions for the next sets of weights. In the next step, we start to reduce the weight of the velocity w_v, while increasing the power consumption weight w_p. Note that the initial value of PSO in the first step are defined based on expert knowledge, and the optimal value of each step is used as the initial guess of the next step. For instance, the initial value of the optimization problem where $w_p = 0.05, w_v = 0.95$ is the optimal value of the first step optimization problem where $w_p = 0, w_v = 1$.

In this thesis, PSO is implemented within a distributed computing framework consisting of 12 computing cores. In order to obtain a Pareto optimal point, $n_p \times n_g = 16 \times 20 = 320$ simulation runs are required. Distributing the simulation runs among 12 nodes results in a speedup factor larger than one. For this case study, the computation time to obtain a Pareto optimal point was about 65 minutes.

Results

We now present the results of the proposed multi-objective optimization is presented both for lateral undulation and eel-like motion patterns for the underwater snake robot with parameters as shown in Subsection 7.6.3; and the optimal forward

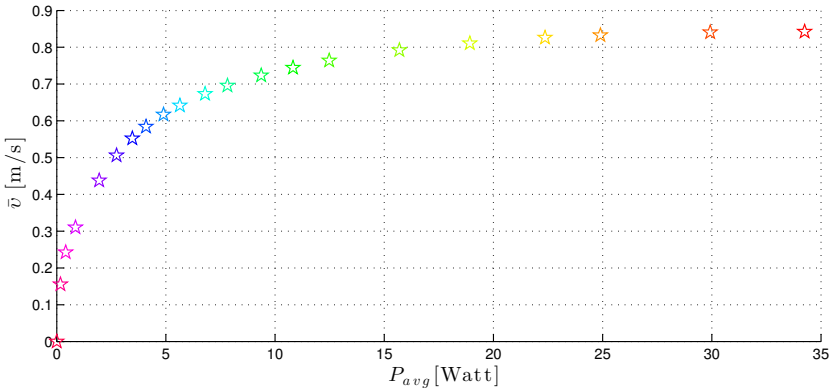

Figure 7.23: Pareto front for lateral undulation.

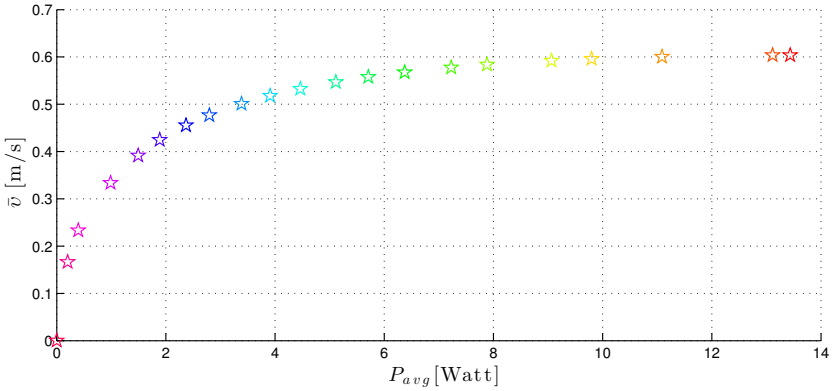

Figure 7.24: Pareto front for eel-like motion pattern.

velocity, $\bar{v}$, and the optimal average power consumption, P_{avg}, are illustrated with the corresponding gait parameters.

Pareto fronts are presented in Fig. 7.23-7.24 for lateral undulation and eel-like motion pattern, respectively. One can observe, as it was expected, that the maximum power is consumed in the case of achieving maximum velocity, and minimum power consumption (equal to zero) occurs for zero forward velocity. In the case of the motionless condition, the objective function is to minimize the power consumption regardless of the velocity ($w_p = 1, w_v = 0$); thus the optimal gait pattern parameter $\alpha = 0$, and two other parameters ω and δ are not effective. The underwater snake robot investigated in this section achieved maximum forward velocity $\bar{v} = 0.84$ m/s and $\bar{v} = 0.60$ m/s for lateral undulation and eel-like motion, respectively, with the corresponding maximum average power consumption of $P_{\text{avg}} = 34.25$ W and $P_{\text{avg}} = 13.44$ W.

Furthermore, the Pareto front presented in Fig. 7.23 illustrates that the average

power consumption of the robot can be decreased significantly from $P_{\text{avg}} = 34.25$ W to $P_{\text{avg}} = 18.92$ W by slightly decreasing the achieved forward velocity from $\bar{v} = 0.84$ m/s to $\bar{v} = 0.81$ m/s for the lateral undulation. This means that a 44.76% decrease of the average power consumption can be obtained, while the forward velocity is only reduced by 3.57%. For the eel-like motion pattern, Fig. 7.24 shows that the power consumption is decreased from $P_{\text{avg}} = 13.44$ W to $P_{\text{avg}} = 7.88$ W, if we choose to pay a marginal penalty by decreasing the forward velocity from $\bar{v} = 0.60$m/s to $\bar{v} = 0.58$m/s. Therefore, the average power consumption can be reduced by 41.37% in the eel-like motion pattern while the corresponding forward velocity is decreased only by 3.33%. Therefore, decision makers can choose the optimal gait pattern parameters such that a significant reduction of the power consumption only results in a slight reduction of the forward velocity.

Remark 7.4: *Note that the Pareto fronts shown in Fig. 7.23-7.24 can be considered as a useful tool to make the trade-off between the power consumption and the forward velocity. Therefore, based on the Pareto front, a proper set of gait parameters of the swimming robot can be chosen considering the requirement of the control strategies and the available power of the system.*

Fig. 7.25-7.27 and Fig. 7.28-7.30 show how the average power consumption and the forward velocity vary for different optimal values of the gait parameters in (3.3) for lateral undulation and eel-like motion patterns, respectively. In addition, the 2D projections of the 3D plots presented in Fig. 7.25(a)- 7.30(a), for forward velocity and power consumption, are presented in Fig. (7.25(b),7.30(b)) and Fig. (7.25(c),7.30(c)) for the investigated motion patterns. As it was expected, the maximum velocity is achieved for the set of weighting factor w_v=1 and $w_p = 0$. The maximum forward velocity $\bar{v} = 0.84$ m/s is achieved for the gait parameters $\alpha = 44.01^o$, $\omega = 210^o$/s and $\delta = 15.14^o$ for lateral undulation, while for eel-like motion pattern the robot achieves maximum forward velocity $\bar{v} = 0.60$ m/s for the gait parameters $\alpha = 59.24^o$, $\omega = 209.98^o$/s and $\delta = 26.20^o$. The maximum velocity is achieved when ω is at the maximum value for both patterns, while the optimal values of α and δ, however, are different for each pattern. Fig. 7.25-7.27 and Fig. 7.28-7.30 show that an increase of the parameter δ results in a decrease of the forward velocity and power consumption for lateral undulation and eel-like motion pattern, respectively. Furthermore, the optimal value of parameter α is greater than 30^o for lateral undulation and greater than 50^o for eel-like motion pattern in all weighting sets. These observations are important not only for control purposes but also for formulating the constraints for further optimization investigations in future.

Remark 7.5: *By setting the parameter ω to the maximum value, as is the case for almost all Pareto optimal points, we can reduce the dimension of the search space, n_c, to 2. In this case, the parameter ω is eliminated from the optimization problem and the parameters α and δ are the optimization decision variables. It can also be embedded in the design of swimming snake robots such that the maximum possible value for the parameter ω should be considered when the actuation mechanisms for the joint modules is chosen. This provides motivation for high frequency actuation solutions for future work in control and design of swimming robots.*

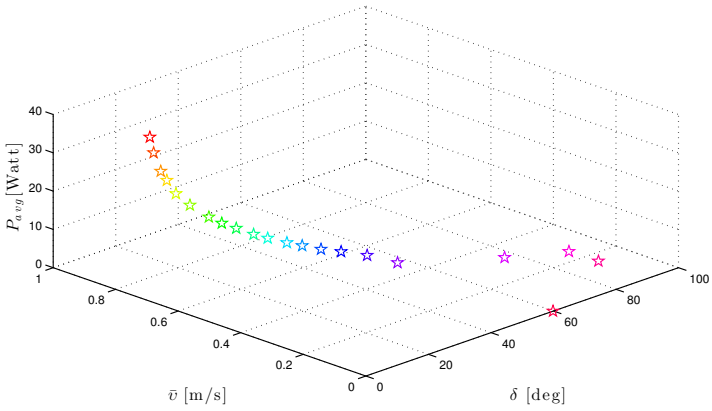

(a) 3D plot for the forward velocity and the average power consumption.

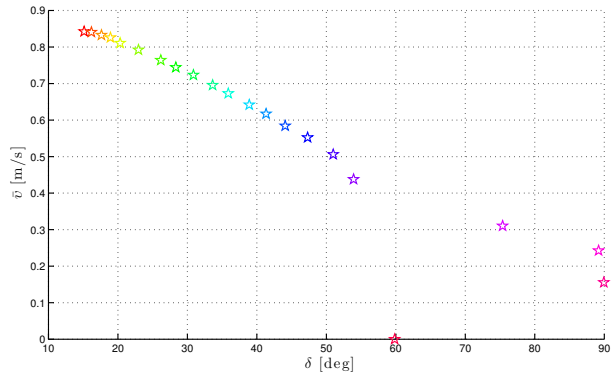

(b) 2D plot for the forward velocity, $\bar{v}$

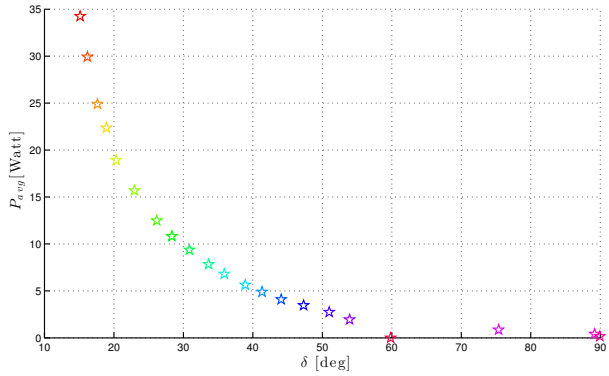

(c) 2D plot for the average power consumption, P_{avg}

Figure 7.25: Optimal solution of lateral undulation motion pattern for the gait parameter δ.

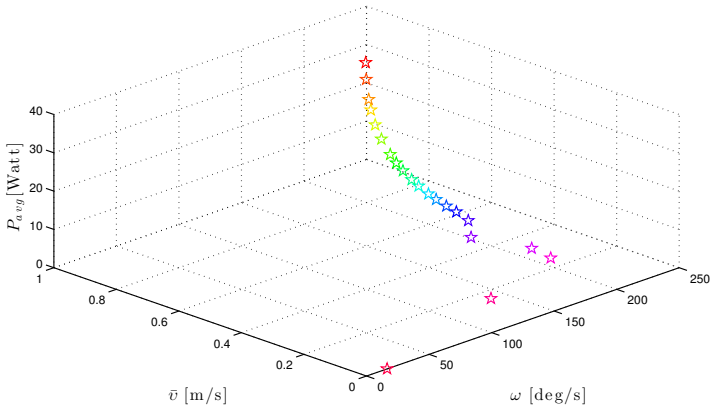

(a) 3D plot for the forward velocity and the average power consumption.

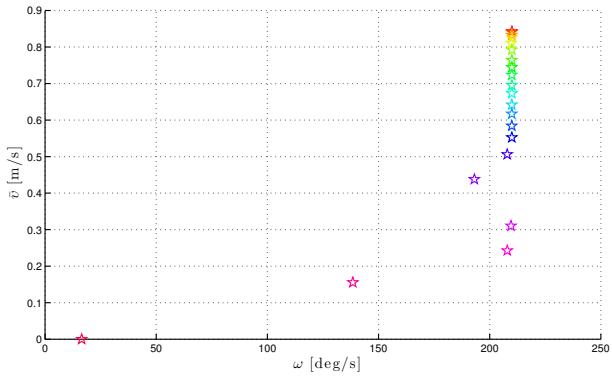

(b) 2D plot for the forward velocity, $\bar{v}$

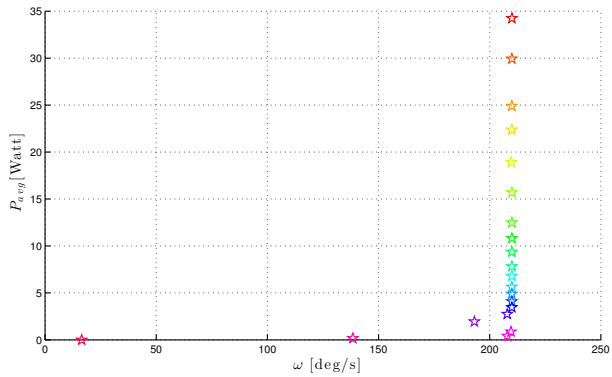

(c) 2D plot for the average power consumption, P_{avg}

Figure 7.26: Optimal solution of lateral undulation motion pattern for the gait parameter ω.

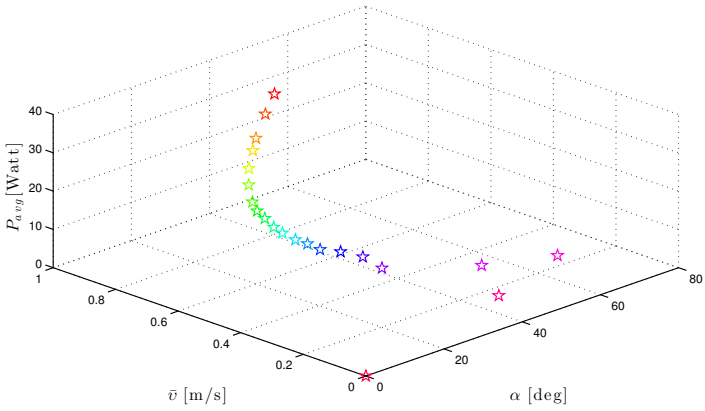

(a) 3D plot for the forward velocity and the average power consumption.

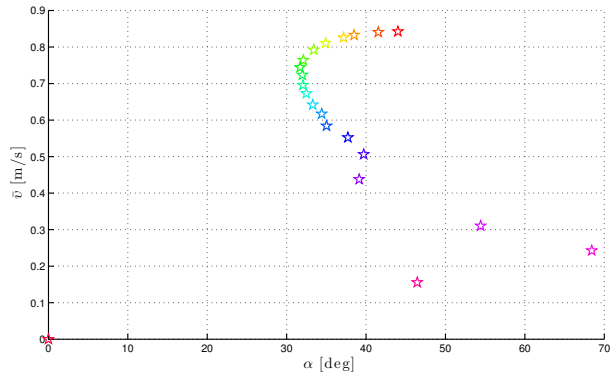

(b) 2D plot for the forward velocity, $\bar{v}$

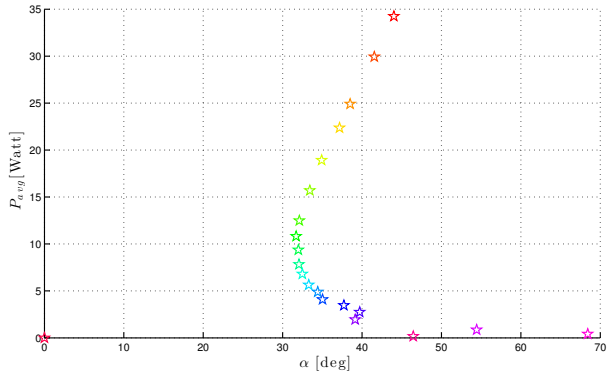

(c) 2D plot for the average power consumption, P_{avg}

Figure 7.27: Optimal solution of lateral undulation motion pattern for the gait parameter α.

7.7 Chapter Summary

- We have investigated the issues that influence the performance of underwater snake robots, both when it comes to the achieved forward velocity (moving performance) and the energy efficiency (transportation performance).
- We have presented simulation results in order to investigate the relationships between the parameters of the gait patterns, the consumed energy and the forward velocity for the motion patterns lateral undulation and eel-like motion for underwater snake robots.
- Based on the simulation studies, we have presented empirical rules to choose the values for the parameters of these motion gait patterns of underwater snake robots in Proposition 7.1-7.2.
- We have investigated the power consumption of different underwater robotic systems and pointing out the most efficient vehicle depending on the desired motion.
- We have presented simulation results in order to compare the power consumption of swimming snake robots with that of today's benchmark solution for subsea inspection, maintenance and repair, which are ROVs, and comparison results are thus obtained for the power consumption of underwater snake robots and ROVs.
- We have compared the energy efficiency of underwater snake robots with the energy efficiency of the widely used remotely operated vehicles (ROVs). Comparison results have been obtained for the total energy consumption and the cost of transportation of underwater snake robots and ROVs, which show that with respect to the cost of transportation metric and the total consumed energy the underwater snake robots are more energy efficient for all the compared motion modes.
- The properties regarding the energy efficiency of underwater snake robots presented in Proposition 7.1-7.2 have been investigated via simulation studies and have been validated via experimental results by using the underwater snake robot, Mamba. The experimental results supported the theoretical findings regarding the relationship between the gait parameters, the velocity and the power consumption both for lateral undulation and eel-like motion patterns.
- We have developed an effective multi-objective optimization scheme to obtain optimal gait parameters for underwater snake robots. The proposed optimization method constitutes a general tool to investigate the motion efficiency of different dynamic models of swimming snake robots controlled by sinusoidal motion patterns.
- PSO has been applied to obtain the Pareto optimal gait parameters in the presence of trade-offs between the the power consumption and the forward velocity. Pareto fronts showed how improving efficiency with respect to the power consumption is related to deteriorating efficiency in terms of the forward velocity along the trade-off curve. Decision makers can consider the

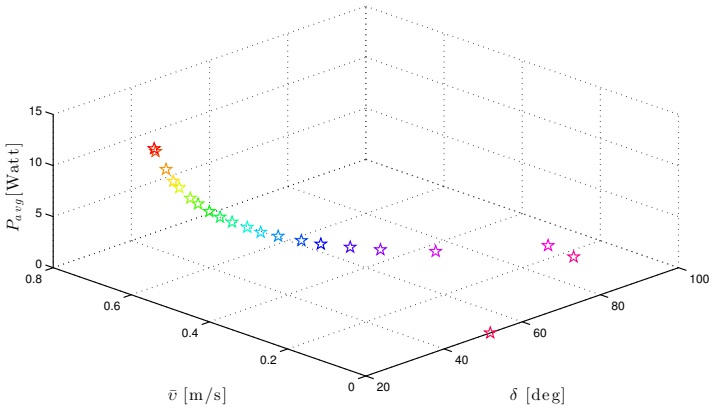

(a) 3D plot for the forward velocity and the average power consumption.

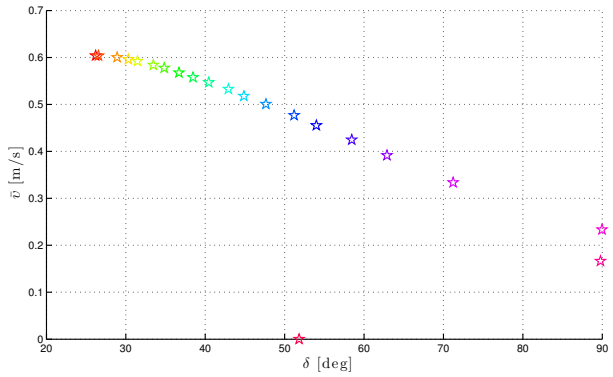

(b) 2D plot for the forward velocity, $\bar{v}$

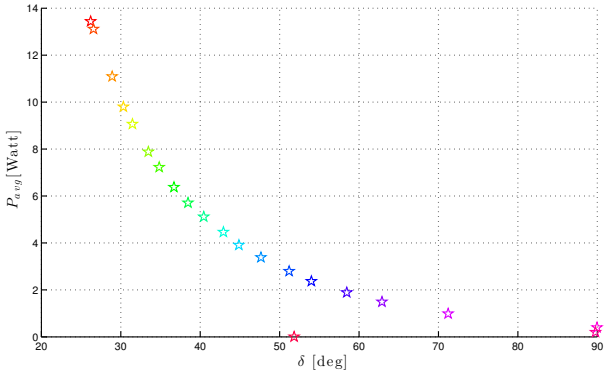

(c) 2D plot for the average power consumption, P_{avg}

Figure 7.28: Optimal solution of eel-like motion pattern for the gait parameter δ.

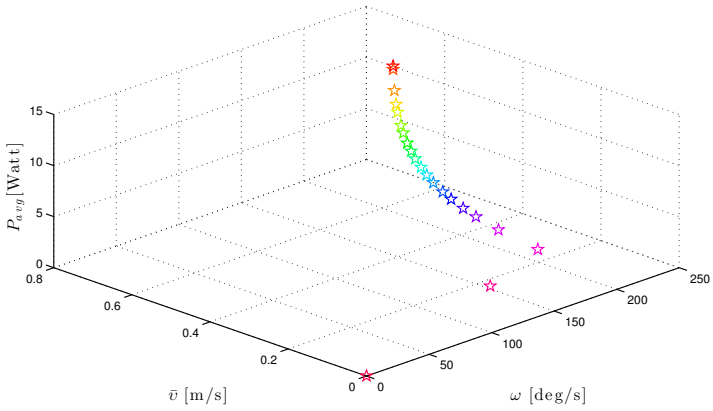

(a) 3D plot for the forward velocity and the average power consumption.

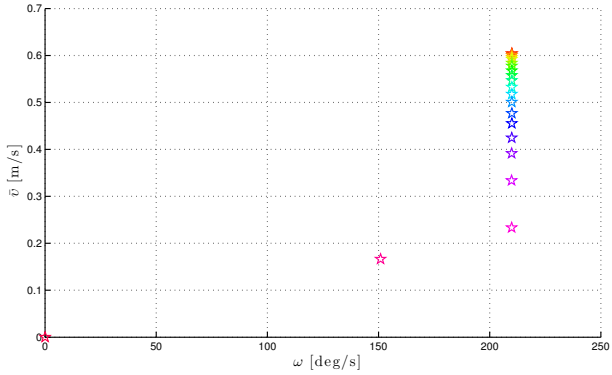

(b) 2D plot for the forward velocity, $\bar{v}$

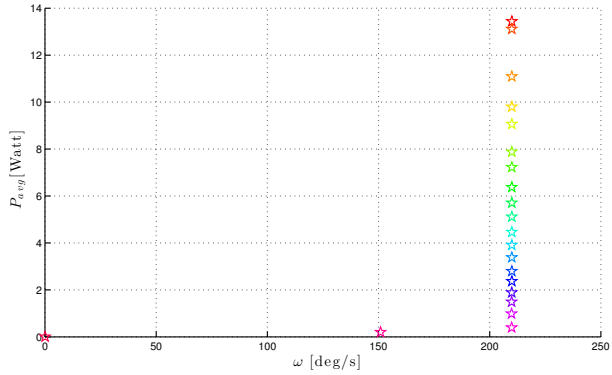

(c) 2D plot for the average power consumption, P_{avg}

Figure 7.29: Optimal solution of eel-like motion pattern for the gait parameter ω.

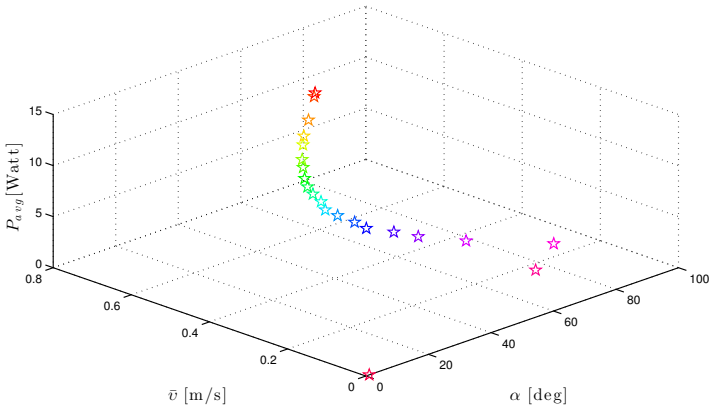

(a) 3D plot for the forward velocity and the average power consumption.

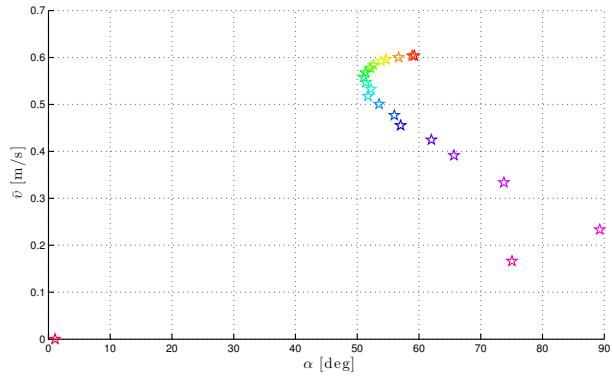

(b) 2D plot for the forward velocity, $\bar{v}$

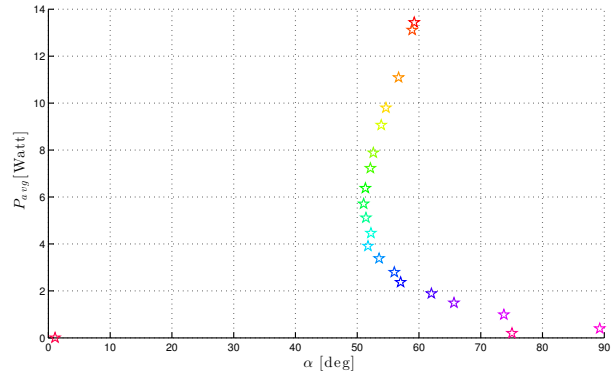

(c) 2D plot for the average power consumption, P_{avg}

Figure 7.30: Optimal solution of eel-like motion pattern for the gait parameter α.

Pareto front as an informative tool to specify the preferred Pareto optimal point.

- Results have been obtained for the two most common swimming patterns for underwater snake robot locomotion: lateral undulation and eel-like motion patterns. Interesting insights about the optimal swimming gait parameters, which are significant for the control and design of underwater snake robot, have been obtained.

Chapter 8

Conclusions and Future Challenges

8.1 Conclusions

In this section, we present the conclusions of each chapter of the thesis.

Conclusions of Chapter 2

In Chapter 2, we presented mathematical models aimed at control design, of an underwater snake robot fully submerged and swimming in virtual horizontal and vertical planes. The links of the robot are influenced by hydrodynamic and hydrostatic forces. These presented models include a hydrodynamic model of underwater snake robot considering the combination of linear and nonlinear drag forces, the added mass effect, the fluid moments and current effects. In addition, this chapter presented a hydrostatic model for underwater snake robots swimming in a virtual vertical plane taking into account the hydrostatic forces due to the buoyancy and gravity. The proposed models are derived in a closed-form avoiding the numerical evaluations of drag effects and are thus particularly well-suited for model-based control design schemes both for motion in horizontal and vertical planes.

Conclusions of Chapter 3

In the first part of the Chapter 3, we presented a general sinusoidal motion pattern which can be used to describe a broad class of motion patterns for underwater snake robot locomotion including lateral undulation and eel-like motion. In the second part, we presented an extensive analysis of the complex model of a fully immersed underwater snake robot moving in a virtual horizontal plane. Based on this analysis, a set of essential properties that characterize the overall motion of underwater snake robots were presented and in addition to this, the hydrodynamic effects which are essential for the overall behavior of the swimming snake robot were identified. Finally, this chapter presented propositions regarding the turning motion of an underwater snake robot and the relative displacement of the links during both lateral undulation and eel-like motion patterns.

Conclusions of Chapter 4

In Chapter 4, we presented a control-oriented model of an underwater snake robot moving in a virtual horizontal plane that is well-suited for control design and stability analysis. The proposed model, which takes into account the added mass effects, the linear drag forces, and the torques due to the added mass and linear drag forces, is significantly less complex than the existing models on underwater snake robots. In addition, this chapter presented simulation results both for lateral undulation and eel-like motion to support the claim that the proposed control-oriented model has the same essential properties as the more complex model of the underwater snake robot.

Conclusions of Chapter 5

We used averaging theory to reveal new fundamental properties of underwater snake robot locomotion that are useful from a motion planning perspective. In particular, we developed an averaged model of the velocity dynamics of an underwater snake robot influenced by added mass effects and linear drag forces during general sinusoidal motion gait patterns, which is well-suited for stability analysis and motion planning purposes. We also showed that the average velocity of an underwater snake robot following sinusoidal motion gait patterns converges exponentially to a steady-state velocity as a function of the gait parameters.

A set of essential relationships between the steady state velocity and the amplitude, the frequency, the phase shift and the offset of the joint motion for the case of general sinusoidal motion gait patterns was presented. In particular, it was shown that the average forward velocity of an underwater snake robot, influenced both by added mass and linear drag effects, and under any sinusoidal gait pattern: 1) is a function of the amplitude of the sinusoidal motion pattern, 2) depends on a linear and a nonlinear term of the gait frequency and 3) depends on the phase shift between the joints. The derived properties are general and provide a useful tool for achieving faster forward motion by selecting the most appropriate motion pattern and the best combination of the gait parameters. This chapter also presented simulation results both for lateral undulation and eel-like motion in order to support the theoretical findings. The chapter presented experimental results using the underwater snake robot Mamba to validate the derived properties of the velocity dynamics.

Conclusions of Chapter 6

In Chapter 6, we presented solutions to the path following control problem for biologically inspired swimming snake robots. In the first part of this chapter, we presented a line-of-sight (LOS) guidance law, which was combined with a sinusoidal gait pattern and a directional controller that steers the robot towards and along the desired path. The performance of the proposed path following controller was investigated through simulations and through experiments with the underwater snake robot Mamba. In addition, this chapter presented a simple fluid parameter identification approach for underwater snake robots. Based on the identified fluid

coefficients, we presented simulation results for the LOS path following controller in order to obtain a back-to-back comparison with the motion of the physical robot during the experiments.

The second part of this chapter presented a straight line path following controller for underwater snake robots in the presence of constant irrotational currents of unknown direction and magnitude. The integral line-of-sight (I-LOS) guidance law is combined with a directional controller to steer the robot to the path, where the integral action in the guidance law produces a constant side-slip angle that allows the control system to compensate for the ocean current effect. In addition, we analyzed the stability of the locomotion along the straight line path in the presence of current. By use of a Poincaré map, we proved that all state variables of an underwater snake robot, except the position along the forward direction, trace out an exponentially stable periodic orbit when the I-LOS path following controller is applied. We presented simulation and experimental results showing that the proposed I-LOS path following controller successfully steered the underwater snake robot towards and along the desired straight path, compensating the effects of currents.

Finally, this chapter presented a waypoint guidance control strategy for underwater snake robot along a path that was derived based on APF techniques in order to achieve collision free paths.

Conclusions of Chapter 7

In Chapter 7, we investigated the issues that influence the performance of underwater snake robots, both when it comes to the achieved forward velocity and the energy efficiency. This chapter presented results by considering both these two aspects of efficiency since the energy efficiency is one of the main challenges for long-term autonomy of underwater robots. In particular, we presented simulation results in order to investigate the relationships between the parameters of the gait patterns, the consumed energy and the forward velocity for the different motion patterns for underwater snake robots. Based on the simulation studies, this chapter presented empirical rules to choose the values for the parameters of the motion gait pattern of underwater snake robots.

This chapter also presented comparison results regarding the energy efficiency of underwater snake robots compared to the energy efficiency of the widely used remotely operated vehicles (ROVs). Comparison results have been obtained for the total energy consumption and the cost of transportation of underwater snake robots and ROVs, which show that with respect to the cost of transportation metric and the total consumed energy the underwater snake robots are more energy efficient for all the compared motion modes. The properties regarding the energy efficiency of underwater snake robots were investigated via simulation studies and have been validated via experimental results by using the underwater snake robot Mamba. The experimental results supported the theoretical findings regarding the relationship between the gait parameters, the velocity and the power consumption both for lateral undulation and eel-like motion patterns.

Finally, this chapter presented an effective multi-objective optimization scheme to obtain optimal gait parameters for underwater snake robots. The proposed op-

timization method constitutes a general tool to investigate the motion efficiency of different dynamic models of swimming snake robots controlled by sinusoidal motion patterns. PSO were applied to obtain the Pareto optimal gait parameters in the presence of trade-offs between the the power consumption and the forward velocity. Results presented for the two most common swimming patterns for underwater snake robot locomotion: lateral undulation and eel-like motion patterns. Interesting insights about the optimal swimming gait parameters, which are significant for the control and design of underwater snake robot, were presented.

8.2 Future Challenges in Underwater Snake Robots

In this thesis, we tried to give answers to problems that concern the modeling, control and energy efficiency of underwater snake robots. However, the results presented in this thesis have the potential to get extended or combined in order to get an even better understanding of these systems. To this end, this section presents some topics of future work that can be considered as open challenges within modeling, control and energy efficiency of underwater snake robots.

Dynamic Modeling Challenges

Considering the rapid research development in the field of bio-inspired robotics, the proposed closed-form models of underwater snake robots in this thesis can be used for stability analysis and control design by various research groups working on biologically inspired swimming robots. Although the complex model of an underwater snake robot presented in this thesis is in closed-form and is thus better suited for modern model-based control design schemes than models that involves numerical calculations, the dynamic models that are proposed in this thesis considered underwater snake robots swimming in a 2D plane of 3D. The majority of the realtime applications of underwater snake robots demands motion in 3D plane, and even though motion in any tilted horizontal plane will cover several of these applications, it is natural to extend the modeling approaches from 2D to 3D. Hence, it will be interesting to extend both the complex and the control-oriented model to 3D, in order to provide the possibility to use them for depth control purposes in the future. In addition, further development of the control-oriented model proposed in this thesis, to be able to capture the nonlinear drag forces and current effects, will be beneficial for further analysis and the control design of underwater snake robot locomotion. Moreover, an extension of the complex model by including a model of a caudal tail at the last link of the robot, to mimic the biological creatures and investigate the propulsion efficiency of underwater snake robots with and without a caudal tail, we expect to provide really interesting outcomes.

Furthermore, the majority of the results presented in this thesis uses theoretical values of the fluid coefficients. In this thesis, preliminary results were obtained regarding the experimental identification of the fluid coefficients based on a trial and error fitting process for the complex model presented in Section 2.2. These coefficients were used to investigate the efficacy of the path following controller presented in Section 6.1 by comparing the experimental results with the simulated ones. However, it would be really interesting to apply another more accurate method in order

to obtain a more precise online fluid coefficient identification with and without the current effects by using either the force/torque sensors installed inside the modules of the underwater snake robots, Mamba, or through computational fluid dynamic (CFD) methods.

Control Design Challenges

As we have already mentioned, various control design challenges must be solved in order to realize operational swimming robots for underwater tasks. Throughout this thesis we presented straight line path following control approaches which were derived based on the complex dynamic model for the underwater snake robot. In particular, we proposed LOS and integral LOS path following controllers for underwater snake robots. In addition, we validated all the presented approaches through extensive numerical simulations and through experiments with the physical underwater snake robot Mamba, both for lateral undulation and eel-like motion patterns. Initial results for general path following in 2D, considering a waypoint guidance approach, were presented in this thesis, while it will be interesting to investigate the validity of the proposed control strategies for general curved paths in the future. Moreover, a waypoint guidance strategy that also takes into account the current effects, remains a topic of future work. Another interesting topic for future work concerns the possibility to extend the proposed control approaches to 3D and thus be able to investigate depth control strategies for underwater snake robots. An experimental investigation of path following of underwater snake robots in 3D plane is necessary in order to realize underwater snake robots for challenging real time subsea operations.

In this thesis, through simulations and experiments, we showed that the proposed I-LOS path following controller successfully steered the underwater snake robot towards and along the desired straight path, compensating the effects of currents. From the experimental results, it was shown that the robot managed to orient itself and maintain a constant non-zero heading to compensate for the effects of the current forces. In addition, based on the Poincaré map approach, we proved that all state variables of an underwater snake robot, except from the position along the forward direction, trace out an exponentially stable periodic orbit when the I-LOS path following controller was applied. However, a formal stability proof for the proposed control strategies remains as a topic of future work. Furthermore, based on the simulation and experimental results for the proposed control strategies presented in this thesis, we can argue that the system is controllable. However, it would be interesting to perform a formal controllability and stabilisability analysis of the proposed complex and control-oriented models, in the future.

Energy Efficiency Challenges

Investigation of the energy efficiency is one of the main challenges for long-term autonomy of underwater snake robots. This thesis presented and experimentally investigated fundamental properties of the achieved velocity and the power consumption of an underwater snake robot for the two most common motion patterns for swimming snake-like robots: lateral undulation and eel-like motion patterns.

In particular, we investigated the relationship between the parameters of the gait patterns and the achieved forward velocity for the different motion patterns for underwater snake robots. In addition, we investigated the properties regarding the energy efficiency of underwater snake robots. This thesis presented experimental results which allow only a qualitative comparison regarding the properties for an efficient motion of underwater snake robots. It is interesting to investigate other methods in order to obtain also quantitative results for underwater snake robot locomotion. In addition, it will be interesting to investigate the efficiency of other sinusoidal motion patterns for these systems in the future.

Throughout this thesis, we investigated the energy efficiency of underwater snake robots, not only based on simulation results but experimentally validated as well, using the underwater snake robot Mamba. It will be interesting to furthermore perform an analytical study regarding the power consumption properties for these systems in the future. In Chapter 5, we derived an analytical relationship for the averaged velocity dynamics that can be used to select the most appropriate motion pattern to achieve the desired velocity requirements. Similar studies for the energy consumption requirements will provide interesting inputs for the efficiency of underwater snake robots. In addition, this thesis presented results regarding the efficiency of these systems considering two main aspects of efficient locomotion: increase of the forward speed by improving the locomotion methods while decreasing the consumed energy. In this thesis, we considered both these two aspects of efficiency, which in some cases can be conflicting. To this end, we formulated a multi-objective optimization problem to minimize power consumption and maximize forward velocity at the same time. In the future, a more general optimization framework can be employed which will include other design parameters of underwater snake robots (e.g., the number of the links) as optimization variables.

References

[1] URL http://www.mscsoftware.com/Products/CAE-Tools/Adams.aspx.

[2] Marine cybernetics laboratory (MC-lab). URL http://www.ntnu.no/imt/lab/cybernetics.

[3] Sintef fisheries and aquaculture flume tank. URL http://www.sintef.no/home/Fisheries-and-Aquaculture/About-us/Laboratories/SINTEF-Fisheries-and-aquaculture-flume-tank/.

[4] Qualisys–motion capture systems. URL http://www.qualisys.com.

[5] URL http://www.cyberbotics.com/.

[6] Multimeter, fluke289, 2015. URL http://www.fluke.com/fluke/r0en/digital-multimeters/advanced-multimeters/fluke-289.htm?pid=56061.

[7] M. Alamir, M. El Rafei, G. Hafidi, N. Marchand, M. Porez, and F. Boyer. Feedback design for 3D movement of an eel-like robot. In *Proc. IEEE International Conference on Robotics and Automation (ICRA)*, pages 256–261, Roma, Apr. 10-14 2007.

[8] I. Arvanitakis and A. Tzes. Trajectory optimization satisfying the robot's kinodynamic constraints for obstacle avoidance. In *Proc. 20th Mediterranean Conference on Control Automation (MED)*, pages 128–133, Barcelona, Spain, July 3-6 2012.

[9] J. Ayers, C. Wilbur, and C. Olcott. Lamprey robots. In *Proc. International Symposium on Aqua Biomechanisms*, 2000.

[10] J. Bak-Coleman, A. Court, D. Paley, and S. Coombs. The spatiotemporal dynamics of rheotactic behavior depends on flow speed and available sensory information. *The Journal of Experimental Biology*, 216(21):4011–4024, 2013.

[11] J. Blair and T. Iwasaki. Optimal gaits for mechanical rectifier systems. *IEEE Transactions on Automatic Control*, 56(1):59–71, 2011.

[12] I. Borazjani and F. Sotiropoulos. On the role of form and kinematics on the hydrodynamics of self-propelled body/caudal fin swimming. *The Journal of Experimental Biology*, 213(1):89–107, 2010.

[13] J. Borenstein and Y. Koren. The vector field histogram-fast obstacle avoidance for mobile robots. *IEEE Transactions on Robotics and Automation*, 7 (3):278–288, 1991.

[14] E. Borhaug, A. Pavlov, and K. Pettersen. Integral LOS control for path following of underactuated marine surface vessels in the presence of constant ocean currents. In *Proc. 47th IEEE Conference on Decision and Control (CDC)*, pages 4984–4991, Cancun, Dec. 9-11 2008.

[15] F. Boyer, M. Porez, and W. Khalil. Macro-continuous computed torque algorithm for a three-dimensional eel-like robot. *IEEE Transactions on Robotics*, 22(4):763 –775, 2006.

[16] F. Boyer, M. Porez, A. Leroyer, and M. Visonneau. Fast dynamics of an eel-like robot-comparisons with navier-stokes simulations. *IEEE Transactions on Robotics*, 24(6):1274–1288, 2008.

[17] F. Boyer, D. Chablat, P. Lemoine, and P. Wenger. The eel-like robot. *CoRR*, abs/0908.4464, 2009.

[18] C. Breder. The locomotion of fishes. *Zoologica*, 4:159–297, 1926.

[19] W. Caharija, K. Pettersen, A. Sorensen, M. Candeloro, and J. Gravdahl. Relative velocity control and integral line of sight for path following of autonomous surface vessels: Merging intuition with theory. *Part M: Journal of Engineering for the Maritime Environment*, 228(2):180–191, 2013.

[20] F. Candelier, M. Porez, and F. Boyer. Note on the swimming of an elongated body in a non-uniform flow. *Journal of Fluid Mechanics*, 716:616–637, 2013.

[21] J. Carling, T. Williams, and G. Bowtell. Self-propelled anguilliform swimming: simultaneous solution of the two-dimensional navier-stokes equations and newton's laws of motion. *Journal of Experimental Biology*, 201(23): 3143–3166, 1998.

[22] J. Chen, W. O. Friesen, and T. Iwasaki. Mechanisms underlying rhythmic locomotion: body-fluid interaction in undulatory swimming. *Journal of Experimental Biology*, 214(4):561–574, 2011.

[23] S. Chen, J. Wang, and X. Tan. Target-tracking control design for a robotic fish with caudal fin. In *Proc. 32nd Chinese Control Conference (CCC)*, pages 844–849, Xi'an, July 26-28 2013.

[24] H. Choset, K. M. Lynch, S. Hutchinson, G. Kantor, W. Burgard, L. E. Kavraki, and S. Thrun. *Principles of Robot Motion: Theory, Algorithms, and Implementations.* MIT Press, 2005.

[25] A. Cohen, P. Holmes, and R. Rand. The nature of the coupling between segmental oscillators of the lamprey spinal generator for locomotion: A mathematical model. *Journal of Mathematical Biology*, 13(3):345–369, 1982.

[26] J. Colgate and K. Lynch. Mechanics and control of swimming: A review. *IEEE Journal of Oceanic Engineering*, 29(3):660–673, 2004.

[27] A. Crespi and A. J. Ijspeert. AmphiBot II: An Amphibious Snake Robot that Crawls and Swims using a Central Pattern Generator. In *Proc. 9th International Conference on Climbing and Walking Robots (CLAWAR)*, pages 19–27, Brussels, Belgium, Sept. 2006.

[28] A. Crespi and A. J. Ijspeert. Online optimization of swimming and crawling in an amphibious snake robot. *IEEE Transaction on Robotics*, 24(1):75–87, 2008.

[29] A. Crespi, A. Badertscher, A. Guignard, and A. Ijspeert. Swimming and crawling with an amphibious snake robot. In *Proc. IEEE International Conference on Robotics and Automation (ICRA)*, pages 3024–3028, Barcelona, Spain, Apr. 18-22 2005.

[30] A. Crespi, D. Lachat, A. Pasquier, and A. J. Ijspeert. Controlling swimming and crawling in a fish robot using a central pattern generator. *Autonomous Robots*, 25(1-2):3–13, 2008.

[31] R. Crespi, A. Badertscher, A. Guignard, and A. J. Ijspeert. Amphibot I: an amphibious snake-like robot. *Robotics and Autonomous Systems*, 50(4): 163–175, 2005.

[32] O. Egeland and J. T. Gravdahl. *Modeling and Simulation for Automatic Control*. Marine Cybernetics, Trondheim, 2002.

[33] O. Ekeberg. A combined neuronal and mechanical model of fish swimming. *Biological Cybernetics*, 69(5-6):363–374, 1993.

[34] M. El Rafei, M. Alamir, N. Marchand, M. Porez, and F. Boyer. Multivariable constrained control approach for a three-dimensional eel-like robot. In *Proc. IEEE/RSJ International Conference on Intelligent Robots and Systems (IROS)*, pages 3152–3157, Nice, France, Sept. 22-26 2008.

[35] M. El Rafei, M. Alamir, N. Marchand, M. Porez, and F. Boyer. Motion control of a three-dimensional eel-like robot without pectoral fins. *Proc. 17th IFAC World Congress*, 17(1):750–755, 2008.

[36] O. Faltinsen. *Sea loads on ships and offshore structures*. Cambridge University Press Cambridge; New York, 1990.

[37] S. Fan and C. Woolsey. Underwater vehicle control and estimation in nonuniform currents. In *Proc. American Control Conference (ACC)*, pages 1400–1405, Washington, DC, June 17-19 2013.

[38] T. I. Fossen. *Handbook of Marine Craft Hydrodynamics and Motion Control*. John Wiley & Sons, Ltd, 2011.

[39] E. Fredriksen and K. Y. Pettersen. Global κ-exponential way-point maneuvering of ships: Theory and experiments. *Automatica*, 42(4):677 – 687, 2006.

[40] G. Gallot, O. Ibrahim, and W. Khalil. Dynamic modeling and simulation of a 3-d hybrid structure eel-like robot. In *Proc. IEEE International Conference on Robotics and Automation (ICRA)*, pages 1486 –1491, Roma, Apr. 10-14 2007.

[41] J. Gray. Studies in animal locomotion. *The Journal of Experimental Biology*, 10(1):88–104, 1933.

[42] J. Gray. Directional control of fish movement. *Proc. Royal Society of London. Series B, Containing Papers of a Biological Character*, 113(781):115–125, 1933.

[43] J. Gray. The mechanism of locomotion in snakes. *The Journal of Experimental Biology*, 23(2):101–120, 1946.

[44] S. Grillner. On the generation of locomotion in the spinal dogfish. *Experimental Brain Research*, 20(5):459–470, 1974.

[45] S. Grillner and S. Kashin. On the generation and performance of swimming in fish. In *Proc. Neural Control of Locomotion*, pages 181–201, New York, 1976.

[46] S. Grillner and T. Matsushima. The neural network underlying locomotion in lamprey-synaptic and cellular mechanisms. *Neuron*, 7(1):1–15, 1991.

[47] S. Grillner, P. Wallen, and L. Brodin. Neuronal network generating locomotor behavior in lamprey: circuitry, transmitters, membrane properties and simulation. *Annual Review of Neuroscience*, 14:169–199, 1991.

[48] S. Grillner, T. Deliagina, O. Ekeberg, A. El Manira, R. Hill, A. Lansner, G. Orlovsky, and P. Wallen. Neural networks that co-ordinate locomotion and body orientation in lamprey. *Trends in Neurosciences*, 18(6):270–279, 1995.

[49] J. Guo. A waypoint-tracking controller for a biomimetic autonomous underwater vehicle. *Ocean Engineering*, 33(17-18):2369 – 2380, 2006.

[50] N. Guskova, G. V. Makhortykh, and M. G. Shcheglova. Inertia and drag of elliptic cylinders oscillating in a fluid. *Fluid Dynamics*, 33(1):91–95, 1998.

[51] S. Hirose. *Biologically Inspired Robots: Snake-Like Locomotors and Manipulators*. Oxford University Press, 1993.

[52] S. Hirose and E. F. Fukushima. Snakes and strings: new robotics components for rescue operations. In *Proc. 41st SICE Annual Conference*, volume 1, pages 338–343, Osaka, Japan, Aug. 5-7 2002.

[53] D. Hu, J. Nirody, T. Scott, and M. Shelley. The mechanics of slithering locomotion. *Proc. National Academy of Sciences*, 106(25):10081–10085, 2009.

[54] H. Igarashi and M. Kakikura. Path and posture planning for walking robots by artificial potential field method. In *Proc. IEEE International Conference on Robotics and Automation (ICRA)*, volume 3, pages 2165–2170, New Orleans, LA USA, Apr. 26-May 1 2004.

[55] A. Ijspeert. Central pattern generators for locomotion control in animals and robots: a review. *Neural Networks*, 21(4):642–653, 2008.

[56] A. Isidori. *Nonlinear Control Systems (Communications and Control Engineering)*. Springer: New York, 1995.

[57] B. C. Jayne. Swimming in constricting (elaphe g. guttata) and nonconstricting (nerodia fasciata pictiventris) colubrid snakes. *Copeia*, 1:195–208, 1985.

[58] C. Jordan. Coupling internal and external mechanics to predict swimming behavior: A general approach. *American Zoologist*, 36(6):710–722, 1996.

[59] D. Jung, P. Pott, T. Salumae, and M. Kruusmaa. Flow-aided path following of an underwater robot. In *Proc. IEEE International Conference on Robotics and Automation (ICRA)*, pages 4602–4607, Karlsruhe, Germany, May 6-10 2013.

[60] M. J. Kanter and S. Coombs. Rheotaxis and prey detection in uniform currents by lake michigan mottled sculpin (cottus bairdi). *The Journal of Experimental Biology*, 206(1):59–70, 2003.

[61] S. Kashin, A. Feldman, and G. Orlovsky. Locomotion of fish evoked by electrical stimulation of the brain. *Brain Research*, 82(1):41–47, 1974.

[62] E. Kelasidi and A. Tzes. Serpentine motion control of snake robots for curvature and heading based trajectory - parameterization. In *Proc. IEEE 20th Mediterranean Conference on Control Automation (MED)*, pages 536–541, Barcelona, Spain, July 3-6 2012.

[63] E. Kelasidi, K. Y. Pettersen, J. T. Gravdahl, and P. Liljebäck. Guidance of Underwater Snake Robots, Patent Application No. 1417625.9, Sept. 25 2014.

[64] E. Kelasidi, P. Liljebäck, K. Y. Pettersen, and J. T. Gravdahl. Integral line-of-sight guidance for path following control of underwater snake robots: Theory and experiments. In *IEEE Transactions on Robotics*, 2014. (Submitted).

[65] E. Kelasidi, K. Pettersen, and J. Gravdahl. Modeling of underwater snake robots moving in a vertical plane in 3D. In *Proc. IEEE/RSJ International Conference on Intelligent Robots and Systems (IROS)*, pages 266–273, Chicago, Illinois, Sept. 14-18 2014.

[66] E. Kelasidi, K. Y. Pettersen, and J. T. Gravdahl. A waypoint guidance strategy for underwater snake robots. In *Proc. IEEE 22nd Mediterranean Conference on Control and Automation*, pages 1512–1519, Palermo, Italy, June 16-19 2014.

[67] E. Kelasidi, K. Y. Pettersen, and J. T. Gravdahl. A control-oriented model of underwater snake robots. In *Proc. IEEE International Conference on Robotics and Biomimetics (ROBIO)*, pages 753–760, Bali, Indonesia, Dec. 5-10 2014.

[68] E. Kelasidi, K. Y. Pettersen, and J. T. Gravdahl. Stability analysis of underwater snake robot locomotion based on averaging theory. In *Proc. IEEE International Conference on Robotics and Biomimetics (ROBIO)*, pages 574–581, Bali, Indonesia, Dec. 5-10 2014.

[69] E. Kelasidi, K. Y. Pettersen, J. T. Gravdahl, and P. Liljebäck. Modeling of underwater snake robots. In *Proc. IEEE International Conference on Robotics and Automation (ICRA)*, pages 4540–4547, Hong Kong, China, May 31-June 7 2014.

[70] E. Kelasidi, K. Y. Pettersen, P. Liljebäck, and J. T. Gravdahl. Integral line-of-sight for path-following of underwater snake robots. In *Proc. IEEE Multi-Conference on Systems and Control*, pages 1078 – 1085, Juan Les Antibes, France, Oct. 8-10 2014.

[71] E. Kelasidi, M. Jesmani, K. Y. Pettersen, and J. T. Gravdahl. Multi-objective optimization for efficient motion of underwater snake robots. In *Proc. The First International Symposium on Swarm Behavior and Bio-Inspired Robotics (SWARM)*, Kyoto, Japan, Oct. 28-30 2015.

[72] E. Kelasidi, P. Liljebäck, K. Y. Pettersen, and J. T. Gravdahl. Experimental investigation of efficient locomotion of underwater snake robots for lateral undulation and eel-like motion patterns. In *Robotics and Biomimetics*, 2015. (Accepted).

[73] E. Kelasidi, P. Liljebäck, K. Y. Pettersen, and J. T. Gravdahl. Biologically inspired swimming snake robots: Modeling, control and experimental investigation. In *IEEE Robotics and Automation Magazine*, 2015. (Conditionally Accepted).

[74] E. Kelasidi, K. Y. Pettersen, and J. T. Gravdahl. Energy efficiency of underwater robots. In *Proc. 10th IFAC Conference on Manoeuvring and Control of Marine Craft (MCMC)*, Copenhagen, Denmark, Aug. 24-26 2015.

[75] E. Kelasidi, K. Y. Pettersen, and J. T. Gravdahl. Energy efficiency of underwater snake robot locomotion. In *Proc. 23th Mediterranean Conference on Control Automation (MED)*, Torremolinos, Spain, June 16-19 2015.

[76] J. Kennedy and R. Eberhart. Particle swarm optimization. In *Proc. IEEE International Conference on Neural Networks*, pages 1942–1948, Perth, WA, Nov. 27-Dec. 1 1995.

[77] J. Kennedy and R. Mendes. Population structure and particle swarm performance. In *Proc. Congress on Evolutionary Computation (CEC)*, pages 1671–1676, Honolulu, HI, May 12-17, 2002.

[78] J. Kennedy, R. C. Eberhart, and Y. Shi. *Swarm Intelligence*. Morgan Kaufmann Publishers, 2001.

[79] S. Kern and P. Koumoutsakos. Simulations of optimized anguilliform swimming. *The Journal of Experimental Biology*, 209(24):4841–4857, 2006.

[80] H. K. Khalil. *Nonlinear Systems*. 3rd ed. Prentice Hall, 2002.

[81] W. Khalil. Dynamic modeling of robots using recursive newton-euler techniques. In *Proc. International Conference on Informatics in Control, Automation and Robotics (ICINCO)*, pages 19–31, Funchal, Madeira-Portugal, June 15-18 2010.

[82] W. Khalil, G. Gallot, O. Ibrahim, and F. Boyer. Dynamic modeling of a 3-d serial eel-like robot. In *Proc. IEEE International Conference on Robotics and Automation (ICRA)*, pages 1270 – 1275, Barcelona, Spain, Apr. 18-22 2005.

[83] W. Khalil, G. Gallot, and F. Boyer. Dynamic modeling and simulation of a 3-D serial eel-like robot. *IEEE Transactions on Systems, Man, and Cybernetics, Part C: Applications and Reviews*, 37(6):1259–1268, 2007.

[84] O. Khatib. Real-time obstacle avoidance for manipulators and mobile robots. In *Proc. IEEE International Conference on Robotics and Automation (ICRA)*, volume 2, pages 500–505, St. Louis, Missouri, March 25-28 1985.

[85] K. Klaka, J. Penrose, R. Horsley, and M. Renilson. Hydrodynamic tests on a plate in forced oscillation. *Ocean Engineering*, 34(8-9):1225 – 1234, 2007.

[86] T. Knutsen, J. Ostrowski, and K. McIsaac. Designing an underwater eel-like robot and developing anguilliform locomotion control. *NSF Summer Undergraduate Fellowship in Sensor Technologies, Tamara Harvard University*, pages 119–142, 2004.

[87] S. Koziel and X.-S. Yang, editors. *Computational Optimization, Methods and Algorithms*, volume 356. Springer-Verlag Berlin Heidelberg, 2011.

[88] M. Kruusmaa, P. Fiorini, W. Megill, M. De Vittorio, O. Akanyeti, F. Visentin, L. Chambers, H. El Daou, M.-C. Fiazza, J. Jezov, M. Listak, L. Rossi, T. Salumae, G. Toming, R. Venturelli, D. Jung, J. Brown, F. Rizzi, A. Qualtieri, J. Maud, and A. Liszewski. Filose for svenning: A flow sensing bioinspired robot. *IEEE Robotics Automation Magazine*, 21(3):51–62, 2014.

[89] P. D. Kuo and D. Grierson. Genetic algorithm optimization of escape and normal swimming gaits for a hydrodynamical model of carangiform locomotion. In *Proc. Genetic and Evolutionary Computation Conference (GECCO)*, pages 170–177, Chicago, IL, July 12-16 2003.

[90] L. Lapierre and B. Jouvencel. Path following control for an eel-like robot. In *Proc. MTS/IEEE International Conference Oceans*, volume 1, pages 460–465, Brest, France, June 20-23 2005.

[91] E. C. Laskari, K. E. Parsopoulos, and M. N. Vrahatis. Particle swarm optimization for minimax problems. In *Proc. Congress on Evolutionary Computation (CEC)*, pages 1576–1581, Honolulu, HI, May 12-17 2002.

[92] S. LaValle. *Planning Algorithms*. UK: Cambridge University Press, 2006.

[93] B. Li, S. Yu, S. Ma, and Y. Wang. An amphibious snake-like robot with novel gaits on ground and in water. In *Proc. IASTED International Conference Intelligent Systems and Control (ISC 2011)*, pages 100–105, Calgary, AB, July 11-13 2011.

[94] M. J. Lighthill. Aquatic animal propulsion of high hydro-mechanical efficiency. *Journal of Fluid Mechanics*, 44(2):265–301, 1970.

[95] M. J. Lighthill. Large-amplitude elongated-body theory of fish locomotion. *Proc. Royal Society of London. Series B. Biological Sciences*, 179(1055):125–138, 1971.

[96] P. Liljebäck and K. Y. Pettersen. Waypoint guidance control of snake robots. In *Proc. IEEE International Conference on Robotics and Automation (ICRA)*, pages 937–944, Shanghai, China, May 9-13 2011.

[97] P. Liljebäck, K. Pettersen, Ø. Stavdahl, and J. Gravdahl. Stability analysis of snake robot locomotion based on averaging theory. In *Proc. 49th IEEE Conference on Decision and Control (CDC)*, pages 1977–1984, Atlanta, GA, Dec 15-17 2010.

[98] P. Liljebäck, K. Pettersen, Ø. Stavdahl, and J. Gravdahl. A simplified model of planar snake robot locomotion. In *Proc. IEEE/RSJ International Conference on Intelligent Robots and Systems (IROS)*, pages 2868–2875, Taipei, Oct. 18-22 2010.

[99] P. Liljebäck, K. Pettersen, Ø. Stavdahl, and J. Gravdahl. Controllability and stability analysis of planar snake robot locomotion. *IEEE Transactions on Automatic Control*, 56(6):1365–1380, 2011.

[100] P. Liljebäck, K. Y. Pettersen, Ø. Stavdahl, and J. T. Gravdahl. A review on modelling, implementation, and control of snake robots. *Robotics and Autonomous Systems*, 60(1):29–40, 2012.

[101] P. Liljebäck, K. Y. Pettersen, Ø. Stavdahl, and J. T. Gravdahl. *Snake Robots: Modelling, Mechatronics, and Control*. Springer-Verlag, Advances in Industrial Control, 2013.

[102] P. Liljebäck, Ø. Stavdahl, K. Pettersen, and J. Gravdahl. Mamba - a waterproof snake robot with tactile sensing. In *Proc. International Conference on Intelligent Robots and Systems (IROS)*, pages 294–301, Chicago, IL, Sept. 14-18 2014.

[103] S. Ma. Analysis of snake movement forms for realization of snake-like robots. In *Proc. IEEE International Conference Conference on Robotics and Automation (ICRA)*, volume 4, pages 3007–3013, Detroit, MI USA, May 10-15 1999.

[104] K. McIsaac and J. Ostrowski. Open-loop verification of motion planning for an underwater eel-like robot. In D. Rus and S. Singh, editors, *Experimental Robotics VII*, volume 271 of *Lecture Notes in Control and Information Sciences*, pages 271–280. Springer Berlin - Heidelberg, 2001.

[105] K. McIsaac and J. Ostrowski. Experiments in closed-loop control for an underwater eel-like robot. In *Proc. IEEE International Conference on Robotics and Automation (ICRA)*, pages 750–755, Washington DC, May 12-18 2002.

[106] K. McIsaac and J. Ostrowski. Motion planning for anguilliform locomotion. *IEEE Transactions on Robotics and Automation*, 19(4):637–625, 2003.

[107] K. McIsaac and J. Ostrowski. A framework for steering dynamic robotic locomotion systems. *International Journal of Robotics Research*, 22(2):83–97, 2003.

[108] K. Melsaac and J. Ostrowski. A geometric approach to anguilliform locomotion: modelling of an underwater eel robot. In *Proc. International Conference on Robotics and Automation (ICRA)*, volume 4, pages 2843–2848, Detroit, MI, May 10-15 1999.

[109] K. Morgansen, P. Vela, and J. Burdick. Trajectory stabilization for a planar carangiform robot fish. In *Proc. IEEE International Conference on Robotics and Automation (ICRA)*, pages 756–762, Washington, DC, May 12-18 2002.

[110] K. Morgansen, B. Triplett, and D. Klein. Geometric methods for modeling and control of free-swimming fin-actuated underwater vehicles. *IEEE Transactions on Robotics*, 23(6):1184–1199, 2007.

[111] J. Morison, J. Johnson, and S. Schaaf. The force exerted by surface waves on piles. *Journal of Petroleum Technology*, 2(5):149–154, 1950.

[112] J. J. Myers, C. Halm, and R. McAllister. *Handbook of Ocean and Underwater Engineering*. McGraw Hill, New York, 1969.

[113] J. Newman. *Marine Hydrodynamics*. MIT Press, 1977.

[114] M. P. Païdoussis. 8 solitary cylindrical structures in axial flow. In *Slender Structures and Axial Flow*, volume 2 of *Fluid-Structure Interactions*, pages 787 – 1032. Academic Press, 2003.

[115] V. Pareto. *Manual of political economy*. A. M. Kelley, 1906.

[116] T. Parker and L. Chua. *Practical numerical algorithms for chaotic systems*. Springer Verlag, Berlin, 1989. ISBN 9780387966885.

[117] K. Parsopoulos and M. Vrahatis. Recent approaches to global optimization problems through particle swarm optimization. *Natural Computing*, 1(2-3): 235–306, 2002.

[118] T. Paul, T. Krogstad, and J. Gravdahl. UAV formation flight using 3d potential field. In *Proc. 16th Mediterranean Conference on Control and Automation (MED)*, pages 1240–1245, Ajaccio, France, Jun. 25 - 27 2008.

[119] M. Porez, V. Lebastard, A. Ijspeert, and F. Boyer. Multi-physics model of an electric fish-like robot: Numerical aspects and application to obstacle avoidance. In *Proc. IEEE/RSJ International Conference on Intelligent Robots and Systems (IROS)*, pages 1901–1906, San Francisco, CA, Sept. 25-30 2011.

[120] M. Porez, F. Boyer, and A. J. Ijspeert. Improved lighthill fish swimming model for bio-inspired robots: Modeling, computational aspects and experimental comparisons. *The International Journal of Robotics Research*, 33(10): 1322–1341, 2014.

[121] J. Sanders, F. Verhulst, and J. Murdock. *Averaging Methods in Nonlinear Dynamical Systems (Applied Mathematical Science)*, volume 59. Springer, 2007.

[122] T. Sarpkaya and M. Storm. In-line force on a cylinder translating in oscillatory flow. *Applied Ocean Research*, 7(4):188–196, 1985.

[123] W. Shi, D. Stapersma, and H. Grimmelius. Comparison study on moving and transportation performance of transportation modes. *International journal of energy and environment*, 2(4):106–120, 2008.

[124] C. Stefanini, S. Orofino, L. Manfredi, S. Mintchev, S. Marrazza, T. Assaf, L. Capantini, E. Sinibaldi, S. Grillner, P. Wallen, and P. Dario. A novel autonomous, bioinspired swimming robot developed by neuroscientists and bioengineers. *Bioinspiration & Biomimetics*, 7(2):025001, 2012.

[125] T. Takayama and S. Hirose. Amphibious 3d active cord mechanism "helix" with helical swimming motion. In *Proc. IEEE/RSJ International Conference on Intelligent Robots and Systems (IROS)*, volume 1, pages 775 – 780, Lausanne, Switzerland, Sept. 30-Oct. 2 2002.

[126] G. Taylor. Analysis of the swimming of long and narrow animals. *Proc. Royal Society of London. Series A. Mathematical and Physical Sciences*, 214 (1117):158–183, 1952.

[127] A. A. Transeth and K. Y. Pettersen. Developments in snake robot modeling and locomotion. In *Proc. 9th International Conference on Control, Automation, Robotics and Vision (ICARCV)*, pages 1–8, Singapore, Dec. 5-8 2006.

[128] E. Tytell. The hydrodynamics of eel swimming: I. wake structure. *The Journal of Experimental Biology*, 207:1825–1841, 2004.

[129] E. Tytell. The hydrodynamics of eel swimming: II. effect of swimming speed. *Journal of Experimental Biology*, 207:3265–3279, 2004.

[130] P. A. Vela, K. A. Morgansen, and J. W. Burdick. Underwater locomotion from oscillatory shape deformations. In *Proc. 41st IEEE Conference on Decision and Control (CDC)*, volume 2, pages 2074–2080, Las Vegas, USA, Dec. 10-13 2002.

[131] J. Wang, S. Chen, and X. Tan. Control-oriented averaging of tail-actuated robotic fish dynamics. In *Proc. of American Control Conference (ACC)*, pages 591–596, Washington, DC, June 17-19 2013.

[132] E. Westervelt and J. Grizzle. *Feedback Control of Dynamic Bipedal Robot Locomotion (Control and Automation Series)*. CRC PressINC, 2007. ISBN 9781420053722.

[133] M. Wetter. Genopt-a generic optimization program. In *Proc. 7th International Conference of the International Building Performance Simulation Association Conference (IBPSA)*, pages 601–608, Rio de Janeiro, Brazil, Aug. 13-15 2001.

[134] F. White. *Fluid Mechanics*. McGraw-Hill series in mechanical engineering. McGraw-Hill Higher Education, 2003.

[135] A. Wiens and M. Nahon. Optimally efficient swimming in hyper-redundant mechanisms: control, design, and energy recovery. *Bioinspiration & Biomimetics*, 7(4):046016, 2012.

[136] C. Wilbur, W. Vorus, Y. Cao, and S. Currie. *Neurotechnology for biomimetic robots, chapter A Lamprey-Based Undulatory Vehicle*. Bradford/MIT Press, 2002.

[137] T. Williams. Phase coupling by synaptic spread in chains of coupled neuronal oscillators. *Science*, 258(5082):662–665, 1992.

[138] H. Yamada, S. Chigisaki, M. Mori, K. Takita, K. Ogami, and S. Hirose. Development of amphibious snake-like robot ACM-R5. In *Proc. 36th International Symposium on Robotics*, Tokyo, Japan, 2005.

[139] C. Ye, S. Ma, B. Li, and Y. Wang. Locomotion control of a novel snake-like robot. In *Proc. IEEE/RSJ International Conference on Intelligent Robots and Systems (IROS)*, pages 925–930 vol.1, Sendai, Japan, Sept. 28-02 2004.

[140] D. Yeo. *Design of AUV Tracking System Using the Sliding Mode Control and The Optimal Control Theory*. PhD thesis, MS Thesis, Department of Naval Architecture and Ocean Engineering, Seoul National University, Korea, 1999.

[141] S. Yu, S. Ma, B. Li, and Y. Wang. An amphibious snake-like robot: Design and motion experiments on ground and in water. In *Proc. International Conference on Information and Automation (ICIA)*, pages 500 –505, Zhuhai, China, Jun. 22-24 2009.

[142] L. Zadeh. Optimality and non-scalar-valued performance criteria. *IEEE Transactions on Automatic Control*, 8(1):59–60, 1963.

[143] C. Zhou, Z. Cao, S. Wang, and M. Tan. The dynamic analysis of the backward swimming mode for biomimetic carangiform robotic fish. In *Proc. IEEE/RSJ International Conference on Intelligent Robots and Systems (IROS)*, pages 3072 –3076, Nice, France, Sept. 22-26 2008.

[144] L. Zhu, Z. Chen, and T. Iwasaki. Oscillation, orientation, and locomotion of underactuated multilink mechanical systems. *IEEE Transactions on Control Systems Technology*, 21(5):1537–1548, 2013.

[145] Q. Zhu, M. Moser, and P. Kemp. Numerical analysis of a unique mode of locomotion: vertical climbing by pacific lamprey. *Bioinspiration & Biomimetics*, 6(1):016005, 2011.

[146] Z. Zuo, Z. Wang, B. Li, and S. Ma. Serpentine locomotion of a snake-like robot in water environment. In *Proc. IEEE International Conference on Robotics and Biomimetics (ROBIO)*, pages 25–30, Bangkok, Thailand, Feb. 21-26 2009.